UNIVERSITÉ DU QUÉBEC À MONTRÉAL

SIMULATION DES PROCESSUS MICROPHYSIQUES ET DES TYPES DE PRÉCIPITATIONS HIVERNALES LORS DE LA TEMPÊTE DE VERGLAS DE JANVIER 1998 EN UTILISANT LA PRÉVISION DE LA FRACTION LIQUIDE

THÈSE
PRÉSENTÉE
COMME EXIGENCE PARTIELLE
DU DOCTORAT EN SCIENCES DE LA TERRE ET DE L'ATMOSPHÈRE

PAR
MÉLISSA CHOLETTE

FÉVRIER 2020

UNIVERSITY OF QUEBEC AT MONTREAL

SIMULATION OF MICROPHYSICAL PROCESSES AND WINTER PRECIPITATION TYPES DURING THE 1998 ICE STORM USING A PREDICTED LIQUID FRACTION

DISSERTATION
PRESENTED
AS PARTIAL REQUIREMENT
OF THE DOCTORATE IN EARTH AND ATMOSPHERIC SCIENCES

BY
MÉLISSA CHOLETTE

FEBRUARY 2020

UNIVERSITÉ DU QUÉBEC À MONTRÉAL
Service des bibliothèques

Avertissement

La diffusion de cette thèse se fait dans le respect des droits de son auteur, qui a signé le formulaire *Autorisation de reproduire et de diffuser un travail de recherche de cycles supérieurs* (SDU-522 – Rév.07-2011). Cette autorisation stipule que «conformément à l'article 11 du Règlement no 8 des études de cycles supérieurs, [l'auteur] concède à l'Université du Québec à Montréal une licence non exclusive d'utilisation et de publication de la totalité ou d'une partie importante de [son] travail de recherche pour des fins pédagogiques et non commerciales. Plus précisément, [l'auteur] autorise l'Université du Québec à Montréal à reproduire, diffuser, prêter, distribuer ou vendre des copies de [son] travail de recherche à des fins non commerciales sur quelque support que ce soit, y compris l'Internet. Cette licence et cette autorisation n'entraînent pas une renonciation de [la] part [de l'auteur] à [ses] droits moraux ni à [ses] droits de propriété intellectuelle. Sauf entente contraire, [l'auteur] conserve la liberté de diffuser et de commercialiser ou non ce travail dont [il] possède un exemplaire.»

REMERCIEMENTS

Avec ces quelques lignes, je souhaite remercier plusieurs personnes qui m'ont aidée, accompagnée et encouragée à réaliser ce projet. D'abord, mes premiers remerciements vont à ma directrice de thèse Julie M. Thériault pour son soutien, son implication et son aide tout au long du projet. Julie, merci beaucoup de m'avoir dirigée avec tant de dynamisme, j'espère que nous continuerons d'entretenir des liens professionnels dans l'avenir.

I would also like to acknowledge my collaborators, Jason Milbrandt and Hugh Morrison, without them, I would probably still be thinking about how to change the P3 equations. I am very grateful for our meetings in which I learned a lot and from your comments during the writing of the manuscripts. Thank you.

Je remercie René Laprise de m'avoir transmis l'intérêt et la curiosité pour la recherche scientifique et surtout de m'avoir conseillé d'entreprendre ce doctorat.

Je remercie Frédérik Toupin, Delphine Person, Georges Huard, Adelina Alexandru, Élisabeth Lindsay et les autres membres de ce département pour votre aide et votre disponibilité quand j'avais des questions ou des problèmes.

Je remercie les membres du comité de devis de recherche, Julie M. Thériault, René Laprise et Frédérick Chosson, qui ont jugé pertinente ma place dans ce programme. Je remercie les membres du comité d'évaluation, Julie M. Thériault, René Laprise, Philippe Gachon et Danahé Paquin-Ricard pour leur lecture attentive et leurs commentaires.

Dominic Matte, merci pour ton écoute, tes conseils et ton soutien moral. J'espère du fond du cœur que nos carrières vont se croiser quelque part, parce que c'est un plaisir de travailler avec toi et de partager notre environnement de travail en écoutant la musique de Luce.

Un énorme merci à Julie M. Thériault et aux Fonds de recherche du Québec – Nature et technologies (FQRNT) pour les soutiens financiers si précieux tout au long de ce projet.

Merci à Frédérick Chosson d'avoir toujours cru en ce projet et pour nos conversations à des moments importants pour moi.

Juris Almonte and Arlett Chacón thank you very much for your help with the English grammar and the wording.

Je remercie ma famille pour leur accompagnement et leur patience. Finalement, un immense merci à Stéphanie Mayer, merci pour ton soutien inconditionnel, #rocktusais…

TABLES DES MATIÈRES

LISTE DES FIGURES

Figure Page

LISTE DES TABLEAUX

LISTE DES ACRONYMES

ATL-O	The point delimiting the Atlantic Ocean from the coast for the cross-section used in the Chapter III
CAR	Caribou meteorological station
CCSM4	Community Climate System Model
CMIP5	Coupled Model Intercomparison Project Phase 5
COSMO	Consortium for Small-scale Modeling
CPCM	Convection-Permitting Climate Models
CUR	Simulation of the 1998 Ice Storm using NARR as driven data
GCM	Global Climate Model
GYX	Gray meteorological station
M90	Refers to Mitra *et al.* (1990) citation
MA	Massachusetts
ME	Maine
MM15	Refers to Morrison and Milbrandt (2015) citation
MM16	Refers to Milbrandt and Morrison (2016) citation
NARR	North American Regional Reanalysis
NB	New Brunswick
NH	New Hampshire
NWP	Numerical Weather Prediction

NY	New York
OBS	Refers to observation
ON	Ontario
P3	Predicted Particle Properties
P3_MOD	Predicted Particle Properties scheme including the predicted bulk liquid fraction
P3_ORIG	Predicted Particle Properties scheme without the predicted bulk liquid fraction
PGW	Simulation of the 1998 Ice Storm using NARR perturbed by the Pseudo-Global-Warming approach
PSD	Particle Size Distribution
QC	Quebec
RCP	Representative Concentration Pathway
RMSE	Root mean square error
SLRV	St. Lawrence River Valley
VT	Vermont
WMJ	Maniwaki meteorological station
WRF	Weather and Research Forecasting model
YHU	Saint-Hubert surface station
YMX	Mirabel surface station
YOW	Ottawa international airport
YQB	Quebec Jean-Lesage international airport
YUL	Montreal Pierre-Elliott-Trudeau international airport

LISTE DES SYMBOLES ET DES UNITÉS

$A_d(D)$	P3_ORIG's projected area-D relationship for ice	m^2
$A_d(D_x)$	Projected area-D_x relationship for mixed-phase particles, D_x can be D_p or D_d	m^2
$A_{i,wet}$	Forcing term for supersaturation due to vertical motion	$kg\ kg^{-1}\ s^{-1}$
$A_{liq}(D_p)$	Projected area-D_p of liquid drops ($F_{i,liq} = 1$)	m^2
$A_t(D_p, F_{i,liq})$	Projected area relationship of the whole particle in P3_MOD	m^2
$B_{i,rim}$	Rime volume mixing ratio of ice	$m^3\ kg^{-1}$
$C(D_d, F_{i,liq})$	Capacitance for the melting of the ice core of mixed-phase particles	m
$C_d(D_x)$	Capacitance of dry ice ($F_{i,liq} = 0$), D_x can be D_p or D_d	m
$C(D_p, F_{i,liq})$	Capacitance for the condensation/evaporation and refreezing of mixed-phase particles	m
$C_{liq}(D_x)$	Capacitance of liquid drops ($F_{i,liq} = 1$), D_x can be D_p or D_d	m
D	Maximum dimension of ice particles in P3_ORIG	m
D^*	Melting critical diameter	m

D_{cr}	Threshold diameter separating graupel/hail from partially rimed non-spherical ice particles	m
D_d	Maximum dimension of the ice core of mixed-phase particles	m
D_{eq}	Spherical drop equivalent diameter	m
D_{gr}	Threshold diameter separating unrimed non-spherical ice particles from graupel/hail	m
D_m	Mean mass-weighted diameter	cm
$\left.\frac{dm_{ice}}{dt}\right\|_{melting}$	The mass melting rate of a particle	kg s^{-1}
$\left.\frac{dm_{tot}}{dt}\right\|_{freezing}$	The mass refreezing rate of a particle	kg s^{-1}
D_p	Dimension of mixed-phase particles	m
D_r	Rain (T>0°C) or freezing rain (T<0°) mean mass-weighted diameter	mm
D_{th}	Threshold diameter separating small spherical ice particles from unrimed non-spherical ice particles	m
D_v	Diffusivity of water vapor in air	m^2 s^{-1}
$F_d(D_d)$	Ventilation factor of dry ice ($F_{i,liq} = 0$)	-
$F(D_d, F_{i,liq})$	Ventilation factor for the melting of ice cores in mixed-phase particles	-
$F(D_p, F_{i,liq})$	Ventilation factor of the whole mixed-phase particles	-
$F_{i,liq}$	Bulk liquid mass fraction	-
$F_{i,rim}$	Bulk rime mass fraction	-

$F_{liq}(D_d)$	Ventilation factor of liquid drops ($F_{i,liq} = 1$)	-
g	Gravitational acceleration	$m\ s^{-2}$
k_a	Thermal conductivity of air	
L_e, L_f and L_s	Latent heats of evaporation, fusion and sublimation, respectively	$J\ K^{-1}\ kg^{-1}$
$m_d(D)$	Mass-D relationship of ice particles in P3_ORIG	kg
$m_d(D_x)$	Mass-D_x relationship of the ice core component of mixed-phase particles, D_x can be D_p or D_d	kg
$m_{liq}(D_p)$	Mass-D_p relationship of liquid drops ($F_{i,liq} = 1$)	kg
$m_t(D_p, F_{i,liq})$	Mass-D_p relationship of the whole mixed-phase particles	kg
N_0, $N_{0,core}$, $N_{0,p}$	PSD intercept parameter in P3_ORIG, for the ice cores in P3_MOD, and for the whole particles in P3_MOD, respectively	$kg^{-1}\ m^{-(1+\mu)}$
$N_{i,tot}$	Total ice number mixing ratio	kg^{-1}
$N_{l,evp}$	$N_{i,tot}$ sink term of evaporation of $q_{i,liq}$	$kg^{-1}\ s^{-1}$
N_{rain}	Rain number mixing ratio	kg^{-1}
$N_{r,mlt}$	$N_{i,tot}$ (N_{rain}) sink (source) term of melting	$kg^{-1}\ s^{-1}$
q_{cloud}	Cloud mass mixing ratio	$kg\ kg^{-1}$
$q_{i,dep}$	Vapor deposition mass mixing ratio	$kg\ kg^{-1}$
$q_{i,ice}$	Ice mass mixing ratio	$kg\ kg^{-1}$
$q_{i,liq}$	Liquid mass mixing ratio accumulated on ice	$kg\ kg^{-1}$
$Q_{i,mlt}$	$q_{i,liq}$ source term of melting	$kg\ kg^{-1}\ s^{-1}$
$q_{i,rim}$	Rime mass mixing ratio	$kg\ kg^{-1}$

$q_{i,tot}$	Total mass mixing ratio of ice and mixed-phase particles	kg kg^{-1}
$Q_{l,coll,c}$	$q_{i,liq}$ source term of collection with cloud droplets	kg kg^{-1} s^{-1}
$Q_{l,coll,r}$	$q_{i,liq}$ source term of collection with raindrops	kg kg^{-1} s^{-1}
$Q_{l,dep}$	$q_{i,liq}$ source/sink term of vapor transfer	kg kg^{-1} s^{-1}
$Q_{l,frz}$	$q_{i,liq}$ sink term of refreezing	kg kg^{-1} s^{-1}
$Q_{l,shd}$	$q_{i,liq}$ sink term of shedding	kg kg^{-1} s^{-1}
$Q_{l,wgrth}$	$q_{i,liq}$ source term of wet growth	kg kg^{-1} s^{-1}
Q_{mlt}	Total melting source term: $Q_{r,mlt}+Q_{i,mlt}$ for P3_MOD and $Q_{r,mlt}$ for P3_ORIG	kg kg^{-1} s^{-1}
q_{rain}	Rain mass mixing ratio	kg kg^{-1}
$Q_{r,mlt}$	q_{rain} source term of melting	kg kg^{-1} s^{-1}
$q_{s,0}$	Saturated water vapor mixing ratio	kg kg^{-1}
q_v	Water vapor mixing ratio	kg kg^{-1}
Re, Re_d and Re_r	Reynolds number for calculating $F(D_p, F_{i,liq})$, $F_d(D_d)$ and $F_{liq}(D_d)$, respectively	-
Sc	Schmidt number	-
t	Time	min
T	Air temperature	°C
T_0	Freezing point (0°C)	°C
T_d	Dew point temperature	°C
u	3D wind vector	m s^{-1}
V_m, V_N	Mass- and number-weighted mean fall speeds, respectively	m s^{-1}
$V_t(D)$	Terminal velocity-D relationship of P3_ORIG	m s^{-1}

$V_t(D_p, F_{i,liq})$	Terminal velocity relationship of P3_MOD	$m\ s^{-1}$
$V_t(D_x, F_{i,liq} = 0)$	Terminal velocity relationship when $F_{i,liq} = 0$, D_x can be D_d or D_p.	$m\ s^{-1}$
$V_t(D_x, F_{i,liq} = 1)$	Terminal velocity relationship when $F_{i,liq} = 1$, D_x can be D_d or D_p.	$m\ s^{-1}$
X_d, X_p and X_r	Best numbers for calculating $F_d(D_d)$, $F(D_p, F_{i,liq})$ and $F_{liq}(D_d)$, respectively	-
z	Height	km
α_{va}	Coefficient for unrimed non-spherical ice particle mass	$kg\ m^{-\beta va}$
β_{va}	Coefficient for unrimed non-spherical ice particle mass	-
Γ_l	Psychrometric correction associated with the latent heating/cooling	-
Δt	Time step	s
ΔT	Air temperature difference	°C
$\delta_{t=0}$	Supersaturation at the beginning of the time step	$kg\ kg^{-1}$
λ, λ_{core} and λ_p	PSD slope parameter in P3_ORIG, for the ice cores in P3_MOD, and for the whole particles in P3_MOD, respectively	m^{-1}
μ, μ_{core} and μ_p	PSD shape parameter in P3_ORIG, for the ice cores in P3_MOD, and for the whole particles in P3_MOD, respectively	-
υ	Dynamic viscosity of air	$Pa\ s^{-1}$
ρ	Mass-weighted mean particle density	$kg\ m^{-3}$

ρ_a	Air density	kg m^{-3}
ρ_g	Graupel/hail density	kg m^{-3}
ρ_i	Density of solid ice	kg m^{-3}
$\rho_{i,rim}$	Rime density	kg m^{-3}
ρ_{ur}	Density of the unrimed component of ice particles between D_{gr} and D_{cr}	kg m^{-3}
ρ_w ($\rho_{w,g}$)	Liquid water density	kg(g) m^{-3}
τ_c, $\tau_{i,wet}$, τ_r and τ	Relaxation time scale of cloud, mixed-phase ice, rain and total ice for evaporation/condensation in P3_MOD, respectively	-

RÉSUMÉ

La zone de transition de précipitation des tempêtes hivernales se caractérise par une évolution spatio-temporelle de plusieurs types de précipitations, tels que la neige, la neige mouillée, le grésil, la pluie verglaçante et la pluie. Le givrage de la pluie verglaçante sur les infrastructures et les accumulations rapides de grésil et de neige mouillée peuvent, entre autres, provoquer des bris majeurs des lignes de distribution et de transport d'électricité et, ainsi, engendrer des coûts économiques majeurs. Il existe encore plusieurs défis en ce qui concerne l'étude et la simulation des types de précipitations dans la zone de transition lorsque les températures sont proches de 0°C. Ces défis sont notamment liés à la nécessité de connaître l'évolution des particules en phase mixte et au manque d'outils permettant de simuler explicitement les processus microphysiques de ces particules. L'objectif de la thèse est d'étudier les processus microphysiques et les types de précipitations simulés d'une tempête hivernale extrême dans le climat actuel comme dans le contexte du réchauffement climatique en utilisant la prévision de la fraction liquide. La fraction liquide est définie comme le rapport de la masse d'eau liquide sur la masse totale d'une particule en phase mixte. Pour atteindre l'objectif, des simulations à haute résolution d'une tempête hivernale extrême sont faites en combinaison avec le développement d'une nouvelle approche pour prévoir la fraction liquide des particules en phase mixte dans un schéma de microphysique.

Le premier chapitre décrit et teste une nouvelle approche pour inclure la prévision de la fraction liquide dans le schéma de microphysique « bulk » *Predicted Particle Properties*. Il est d'abord démontré que le processus de fonte partielle des flocons de neige proposé par cette nouvelle approche se compare bien à un modèle de référence basé sur la théorie et les observations. Ensuite, le schéma incluant la prévision de la fraction liquide est comparé à la version originale (sans la prévision de la fraction liquide) en utilisant un modèle de nuage colonne. Il est démontré que la prévision de la fraction liquide permet de représenter, d'une part, plusieurs comportements importants des propriétés des hydrométéores, comme l'augmentation de la densité des particules en fonte, et, d'autre part, de nouvelles rétroactions entre la température de l'air et les changements de phase des processus microphysiques de regel et de transfert de vapeur d'eau. La prévision de la fraction liquide affecte les proportions de la masse de pluie et de neige mouillée dans la couche de fonte notamment en favorisant la production de neige mouillée aux dépens de la pluie.

Le deuxième chapitre utilise la paramétrisation développée dans le premier chapitre pour étudier les impacts de la prévision de la fraction liquide sur la simulation des types de précipitations d'une tempête hivernale. Pour ce faire, des simulations numériques avec le modèle atmosphérique *Weather Research and Forecasting* de la tempête extrême de pluie verglaçante du 4 au 10 janvier 1998 sont faites avec et sans la prévision de la fraction liquide. L'accent est mis sur la comparaison des types de précipitations et des propriétés microphysiques simulés. Il est démontré que l'impact principal de la prévision de la fraction liquide est une diminution générale de l'accumulation totale de pluie verglaçante associée notamment à une augmentation de l'accumulation totale de neige et grésil. La diminution de pluie verglaçante est maximale dans les régions où les particules de glace en altitude sont givrées et la hauteur de la couche de fonte est élevée.

Le troisième chapitre a pour objectif d'étudier les impacts d'une atmosphère plus chaude sur la simulation des types de précipitations d'une tempête hivernale en utilisant la prévision de la fraction liquide. Pour cela, l'approche du *Pseudo-Global-Warming* est employée pour la simulation de la même tempête qu'au deuxième chapitre. Cette approche consiste à modifier les variables météorologiques fournies aux conditions initiales et aux frontières latérales avec des perturbations climatiques calculées à partir de projections climatiques d'un modèle climatique global couplé. Les distributions à la surface et en altitude des types de précipitations des deux simulations sont comparées. Les résultats montrent qu'en général la pluie verglaçante et la neige mouillée sont changées en pluie, alors que la neige et le grésil deviennent plutôt un mélange de pluie verglaçante, de grésil et de pluie. Or, ces résultats restent variables pour les accumulations de pluie verglaçante (grésil) de moins de 20 mm (15 mm). De plus, il est démontré que la présence montagneuse des Appalaches affecte l'emplacement des couches de fonte et de regel en altitude. Il existe donc des régions sur lesquelles des quantités importantes de pluie verglaçante sont accumulées dans les deux simulations.

En conclusion, l'approche basée sur la physique développée dans cette thèse pour la prévision de la fraction liquide est novatrice et permet de simuler explicitement les propriétés et les processus microphysiques des particules en phase mixte. Ces particules sont importantes pour les formations de plusieurs types de précipitations, tels que le grésil et la pluie verglaçante. La recherche présentée dans cette thèse contribue à une meilleure compréhension physique de la simulation des types de précipitations d'une tempête hivernale lorsque les températures sont proches de 0°C dans l'objectif ultime de contribuer aux prévisions numériques du temps hivernal.

Mots clés : simulations numériques, tempête hivernale, grésil, pluie verglaçante, fraction liquide, réchauffement climatique

ABSTRACT

The precipitation type transition region associated with winter storms is characterized by a temporal evolution of many precipitation types such as snow, wet snow, ice pellets, freezing rain and rain. Surface icing caused by freezing rain and wet snow, as well as the fast accumulation of ice pellets, can lead to devastating consequences to society, such as power outages. Several scientific challenges remain in studying the precipitation types occurring in a transition region because it involves knowing the evolution of mixed-phase particles when the temperatures are near 0°C. There is a need to develop tools allowing to explicitly represent the microphysical processes associated with mixed-phase particles. The objective is to study the microphysical processes and the precipitation types simulated during an extreme winter storm under current and warmer climates using the prediction of the liquid fraction. The liquid fraction is defined as the ratio of the liquid water mass to the total mass of a mixed-phase particle. The approach is to make high-resolution simulations of an extreme winter storm combined with the development of a new approach to predict the liquid fraction of mixed-phase particles in a bulk microphysics scheme.

The first chapter aims at describing and testing a new parameterization to include the predicted bulk liquid fraction into the Predicted Particle Properties bulk microphysics scheme. First, it is shown that the process of partial melting of snow proposed by this new approach compares well with a benchmark model based on theories and observations. Second, the scheme including the predicted liquid fraction is compared to the original version (without the predicted liquid fraction) using a column cloud model. The predicted liquid fraction allows the description of most winter precipitation types and their properties, such as the fall speed and the density, as well as the simulation of key feedback mechanisms between phase changes and air temperature from new microphysical processes of refreezing and water vapor transfer. The predicted liquid fraction affects the mass proportions of rain (freezing rain) and wet snow (ice pellets) in the melting (refreezing) layer by simulating more wet snow (ice pellets) instead of rain (freezing rain).

The second chapter uses the parameterization developed in the first chapter to study the impacts of the predicted liquid fraction on the simulation of the precipitation types produced during a winter storm. To do this, numerical simulations with the Weather

Research and Forecasting (WRF) model of the extreme freezing rain storm from 4 to 10 January 1998 are conducted with and without the predicted liquid fraction. The focus is on the similarities and differences in simulated precipitation types and microphysical processes. The main impact of predicting the liquid fraction is a general decrease of the total accumulated freezing rain associated with an overall increase of snow and ice pellets. The decrease of freezing rain is maximum where ice particles aloft are rimed and both the melting and the refreezing layers are deep.

The third chapter aims to study the impacts of a warmer atmosphere on the simulation of a winter storm precipitation types using the predicted liquid fraction. To do that, the Pseudo-Global-Warming approach is used for simulating the same storm as the second chapter. This approach consists of modifying the meteorological variables provided as initial and lateral boundaries conditions with climate perturbations from a coupled global cliamte model projection. The distributions of precipitation types at the surface and aloft between the two simulations are compared. The results show that, in general, freezing rain and wet snow are changed to rain, while snow and ice pellets are changed to a mixture of freezing rain, ice pellets and rain. However, these results remain variable for freezing rain (ice pellets) accumulations less than 20 mm (15 mm). Also, it is shown that the orography affects the location of the melting and refreezing layers aloft, and therefore, it exists some region where significant amounts of freezing rain are accumulated in both simulations.

In conclusion, the physically based approach developed in this thesis to predict the liquid fraction is innovative and allows explicit simulations of mixed-phase particles' properties and microphysical processes. These particles are important to the formation of many precipitation types, such as ice pellets and freezing rain. The scientific research of this thesis contributes to a better physical understanding of the simulated microphysical processes of precipitation types during a winter storm when temperatures are near 0°C, with ultimate goal to contribute improving winter weather forecasting.

Key words: numerical simulations, winter storm, ice pellets, freeing rain, liquid fraction, climate warming

CONTRIBUTIONS À LA SCIENCE

La nouvelle approche développée dans cette thèse pour la prévision de la fraction liquide des particules en phase mixte ainsi que les résultats obtenus par les simulations de la tempête hivernale extrême de janvier 1998 avec et sans l'approche du *Pseudo-Global-Warming* apportent les contributions techniques et scientifiques ci-dessous.

Contributions techniques :

- Développement d'une approche unique et novatrice basée sur la physique pour la prévision de la fraction liquide des particules en phase mixte dans un schéma microphysique « bulk ».
- Première simulation numérique de la tempête extrême de pluie verglaçante de janvier 1998 avec la simulation explicite des processus microphysiques associés aux formations de grésil et de pluie verglaçante.
- Première simulation numérique qui emprunte l'approche du *Pseudo-Global-Warming* pour l'étude d'une tempête hivernale de pluie verglaçante et de grésil en utilisant la prévision de la fraction liquide.

Contributions scientifiques :

- Suivre l'évolution de la fraction liquide permet de faire la distinction des proportions de neige mouillée et de pluie dans la couche de fonte, et de grésil et de pluie verglaçante dans la couche de regel en raison de la simulation explicite de nouveaux processus microphysiques clés, tels que la fonte partielle, le regel et le transfert de vapeur d'eau. Cela affecte donc les proportions de la masse des différents types de précipitations à la surface notamment, par exemple, en favorisant de la neige mouillée aux dépens de la pluie lorsque la température de surface est entre 0°C et 2°C.

- La prévision de la fraction liquide conduit à une diminution générale de l'accumulation totale de pluie verglaçante pouvant aller jusqu'à ~25 mm en fonction des conditions atmosphériques en altitude dans le cadre de l'événement de pluie verglaçante de janvier 1998. La diminution d'accumulation de pluie verglaçante est maximale dans les régions où un mélange de grésil et de pluie verglaçante est obtenu avec la prévision de la fraction liquide.
- Il existe plusieurs endroits, tels que le nord-est de la Vallée-du-Saint-Laurent et le centre du Maine, pour lesquels l'accumulation totale de pluie verglaçante demeure élevée, voire augmentée dans l'expérience du *Pseudo-Global-Warming* de l'événement de pluie verglaçante de janvier 1998.
- La topographie du sud du Québec, notamment la Vallée-du-Saint-Laurent bordée par les Appalaches au sud et les Laurentides au nord, affecte la distribution des types de précipitations dans la zone de transition et la position des couches de fonte et de regel en altitude.

CONTRIBUTIONS DES AUTEUR.ES

Cette thèse est une série de trois articles scientifiques. Le premier article est publié dans la revue *Journal of the Atmospheric Sciences*, le deuxième est soumis à *Monthly Weather Review* et le dernier sera soumis au journal *Atmospheric Research*.

Je suis l'auteure principale des trois articles scientifiques. J'ai développé et implanté une nouvelle approche physique pour la prévision de la fraction liquide dans le schéma de microphysique *Predicted Particle Properties* (P3). J'ai également fait les simulations numériques et rédigé les articles. L'une des coauteur.es sur les trois articles est ma directrice Julie M. Thériault. Elle m'a conseillée sur le contenu scientifique et a contribué à l'analyse des résultats et à l'écriture des articles. Deux des articles de la thèse (le premier et le deuxième) ont deux autres coauteurs : Jason A. Milbrandt Ph. D. (*Atmospheric and Oceanic Sciences*) et Hugh Morrison Ph. D. (*Astrophysical, Planetary, and Atmospheric Sciences*). Jason A. Milbrandt est chercheur à la division Centre de Recherche en Prévision Numérique du Temps à Environnement et Changement Climatique Canada à Dorval au Québec et Hugh Morrison est chercheur au *National Center for Atmospheric Research* à Boulder au Colorado. Ces chercheurs ont développé le schéma de microphysique P3 avec lequel j'ai travaillé durant cette thèse en y ajoutant, notamment, la fraction liquide pour la prévision explicite des particules en phase mixte. Ils m'ont conseillée sur les approches scientifique et technique et ils ont contribué à la rédaction des deux articles.

INTRODUCTION

To improve prediction of the impacts of many winter storms,
it is therefore necessary to better understand
the precipitation-type transition region.
(Stewart 1992, p. 287)

En 1992, Stewart mentionnait que : « pour améliorer la prévision des impacts des nombreuses tempêtes hivernales, il faut avoir une meilleure compréhension de la zone de transition de précipitation » (traduction libre). Il existe dans cette citation trois éléments interconnectés auxquels sont, encore aujourd'hui, associés des défis importants en recherche dans le domaine des sciences de l'atmosphère. Le premier élément concerne la compréhension de la zone de transition de précipitation et des processus microphysiques qui la gouvernent. Le deuxième élément porte sur l'amélioration des prévisions des types de précipitations de la zone de transition. Le troisième élément est associé à la prévision des impacts des tempêtes hivernales et des différents types de précipitations. Dans le cadre de cette recherche doctorale, les objectifs poursuivis s'organisent autour de ces trois éléments.

Cette introduction générale s'organise en trois temps. Premièrement, un état des lieux des connaissances des dernières décennies sera présentée et permettra de saisir les différents enjeux associés à la simulation des différents types de précipitations hivernales dans la zone de transition. Deuxièmement, l'objectif principal de la thèse et les sous-questions qui structurent les trois chapitres seront précisés. Troisièmement, une présentation succincte des trois chapitres de la thèse sera faite.

0.1 Revue de littérature

La revue de littérature s'intéresse aux trois éléments suivants : les définitions des types de précipitations dans la zone de transition d'une tempête hivernale; la simulation de ces types de précipitations et la représentation des particules en phase mixte; et l'étude des types de précipitations hivernales dans le contexte du réchauffement climatique mondial.

0.1.1 Définition des types de précipitations dans la zone de transition

La zone de transition de précipitation lors du passage d'une tempête hivernale se caractérise par une évolution temporelle de plusieurs types de précipitations (Stewart 1985; Stewart and King 1987; Stewart and King 1990; Stewart 1992). Généralement bordée par de la neige d'un côté et de la pluie de l'autre côté, la zone de transition de précipitation peut s'étendre de quelques kilomètres à une centaine de kilomètres (Stewart 1992). Les types de précipitations dans la zone de transition varient selon la phase des particules. Il y a la phase solide qui comprend la neige, la neige roulée et le grésil; la phase liquide qui est la pluie; la phase surfondue associée à la pluie verglaçante; et, finalement, la phase mixte qui est la neige mouillée (Stewart 1992; Thériault *et al.* 2006; Thériault and Stewart 2010; Thériault *et al.* 2010). Les accumulations rapides de grésil et de neige mouillée dense ainsi que le givrage de la pluie verglaçante sur les infrastructures peuvent entraîner des bris majeurs des réseaux électriques, des interruptions des moyens de transports aériens et routiers, l'endommagement de la végétation et des blessures chez la population (par exemple :

Lecompte *et al.* 1998; King and Laplante 2005; Chang *et al.* 2007; Kringlebotn Nygaard *et al.* 2013).

Les tempêtes caractérisées d'une zone de transition de précipitation sont assez fréquentes dans l'est du Canada et particulièrement dans le sud du Québec (Cortinas *et al.* 2004; Bresson *et al.* 2017; McGray *et al.* 2019). Les analyses climatologiques ont révélé que la Vallée-du-Saint-Laurent, l'estuaire et le Golfe du Saint-Laurent jusqu'à Terre-Neuve sont les régions dans l'est du Canada ayant les plus grandes fréquences annuelles de pluie verglaçante et de grésil (Stuart and Isaac 1999; Cortinas *et al.* 2004; Groisman *et al.* 2016; Bresson *et al.* 2017; Matte *et al.* 2018; McGray *et al.* 2019). Par exemple, selon Cortinas *et al.* (2004), les médianes du nombre d'heures étaient de 40 heures/an pour la pluie verglaçante et de 30 heures/an pour le grésil dans le sud du Québec pour la période de 1976 à 1990. Pour la même région, mais pour la période de 1980 à 2014, Bresson *et al.* (2017) ont montré une médiane du nombre d'heures qui se situe entre 45 et 60 heures/an pour la pluie verglaçante et entre 35 et 55 heures/an pour le grésil. En général, les épisodes de pluie verglaçante et de grésil sont de courtes durées, c'est-à-dire moins de 4 heures (par exemple : Cortinas *et al.* 2004); or, il arrive que la tempête perdure plusieurs jours (Lecompte *et al.* 1998; Milton and Bourque 1999). L'orientation sud-ouest/nord-est et les configurations physiographiques de la Vallée-du-Saint-Laurent font en sorte qu'il s'agit d'un endroit propice pour la persistance des épisodes de pluie verglaçante en raison du maintien de l'air froid dans les bas niveaux et la canalisation par la pression des vents dans la vallée (Laflamme and Périard 1998 ; Stuart and Isaac 1999; Cortinas *et al.* 2004; Carrera *et al.* 2009; Ressler *et al.* 2012).

Les conditions propices à la formation de pluie verglaçante et de grésil sont généralement obtenues avec le passage d'un front chaud. Ce dernier provoque le soulèvement graduel de l'air chaud au-dessus d'une couche d'air froid, permettant ainsi la formation d'une inversion de température nécessaire aux formations de grésil et de pluie verglaçante (par exemple : Stewart *et al.* 1990). La Fig. 0.1b montre une coupe verticale idéalisée d'un front chaud avec la formation d'une couche de fonte en altitude qui superpose une couche de regel en surface bordée par de la neige d'un côté et de la pluie de l'autre. Alors que le nuage en altitude peut être composé de plusieurs types de précipitations en phase solide provenant des différents stades de croissance d'un cristal de glace (Fig. 0.1a) (Macklin 1962; Browning *et al.* 1963; Pruppacher and Klett 1997; Milbrandt and Morrison 2013), le type de précipitation observé à la surface dépend grandement des trois facteurs suivants : les propriétés de la glace entrant dans la couche de fonte, l'épaisseur et la température maximale de la couche de fonte, et la présence ou non d'une couche de regel en surface.

L'épaisseur et la température maximale de la couche de fonte détermineront le taux de fonte des particules qui peut être partiel pour former de la neige mouillée ou bien complet pour former une goutte de pluie (Stewart 1992 ; Zerr 1997). Quant à lui, le taux de fonte varie si la particule de glace en fonte est petite ou grosse, sphérique ou non sphérique et givrée ou non givrée (Rasmussen and Pruppacher 1982; Rasmussen *et al.* 1984a,b; Fujiyoshi 1986; Leinonen and von Lerber 2018). La présence d'une couche d'air froid dans les bas niveaux est nécessaire pour le regel des particules partiellement fondues de la couche de fonte (Pruppacher and Klett 1997; Zerr 1997) et pour le givrage de la pluie verglaçante sur les surfaces. La température minimale de la couche de regel permet aussi de déterminer s'il y aura formation de petits cristaux de glace (Hallett and Mossop 1974) qui peuvent collecter la pluie surfondue pour former du grésil et changer ainsi le type de précipitation à la surface de pluie verglaçante à grésil (Hogan 1985; Carmichael *et al.* 2011; Barszcz *et al.* 2018).

Comme l'illustre la Fig. 0.1b, les types de précipitations dans la zone de transition sont associés à plusieurs processus microphysiques de changements de phase qui forment ou dégradent une particule en phase mixte. Il y a, entre autres, la fonte (partielle ou complète) de la composante solide de la particule, le regel de la composante liquide et le transfert de la vapeur d'eau sur les particules. À leur tour, ces processus affectent la température de l'air, par exemple, en refroidissant (réchauffant) l'air ambiant lors de l'absorption (dégagement) de chaleur latente associée à la fonte (au regel) (Stewart *et al.* 1984; Donaldson and Stewart 1993; Lackmann *et al.* 2002; Stewart *et al.* 2015). Ainsi, pour un point fixe au sol, le type de précipitation observé lors du passage d'une tempête hivernale dépend grandement du profil vertical de température et peut changer rapidement de neige, à grésil, à pluie verglaçante et à pluie.

0.1.2 Simulation des types de précipitations

Les principales incertitudes en lien avec les prévisions numériques des types de précipitations hivernales proviennent d'une part de la validation des prévisions avec des observations peu abondantes (Reeves 2016) et, d'autre part, de la représentation des différents types de précipitations et de leurs évolutions dans les modèles (Ralph *et al.* 2005; Reeves *et al.* 2014). Bien que les conditions synoptiques associées aux tempêtes hivernales peuvent être similaires, chaque tempête a ses propres caractéristiques de température, d'humidité et de types de précipitations (par exemple : Rauber *et al.* 1994; Petrolito 2005; Ramos da Silva *et al.* 2006; Descurieux 2010; Hosek *et al.* 2011; Finch 2011; Arnott and Chamberlain 2014; Kumjian and Schenkman 2014).

Il existe plusieurs méthodes pour la prévision des types de précipitations dans les modèles. D'abord, il y a les méthodes implicites qui utilisent les profils verticaux de température et d'humidité des sorties de modèle pour déterminer de manière diagnostique les types de précipitations à la surface (Baldwin and Contorno 1993; Cantin and Bachand 1993; Ramer 1993; Czys *et al.* 1996; Bourgouin 2000; Reeves *et al.* 2014; Benjamin *et al.* 2016). Ces méthodes sont favorisées pour des simulations d'emblée coûteuses numériquement (Matte *et al.* 2018). Or, considérant que les processus microphysiques impliqués dans la formation et la sédimentation des types de précipitations sont souvent associés à des échelles spatiotemporelles petites, une méthode dite explicite est davantage utilisée en prévision numérique du temps (Reeves *et al.* 2014). Cette méthode implique l'utilisation de schémas de microphysique des nuages et de la précipitation pour représenter les processus microphysiques dans les modèles (Milbrandt and Yau 2005; Thompson *et al.* 2008; Morrison *et al.* 2009).

Les schémas de microphysique sont composés d'un ensemble d'équations qui résout de manière pronostique des variables microphysiques pertinentes en fonction d'une distribution de taille des particules. Généralement, les variables microphysiques utilisées sont les rapports de mélange en masse et la concentration en nombre des hydrométéores. Il existe deux types de schémas de microphysique : les schémas « bin » et les schémas « bulk ». Les schémas « bulk » intègrent les équations sur toute la distribution de taille des particules, tandis que les schémas « bin » discrétisent la distribution de taille en plusieurs bandes de diamètres. Les schémas « bin » sont donc généralement très coûteux numériquement et la plupart des schémas utilisés en prévision numérique du temps sont de type « bulk ».

Les schémas « bulk » divisent en catégories les différents types de précipitations. Par exemple, pour la précipitation en phase solide, le schéma « bulk » de Milbrandt and Yau (2005) sépare les différentes formes que peuvent avoir les particules de glace en trois catégories : les petits cristaux de glace sphériques, les flocons de neige (agrégats) et les grosses particules givrées. Il y a aussi une catégorie pour la vapeur d'eau, et deux catégories pour la phase liquide : la pluie et les gouttelettes de nuage. Afin d'assurer une continuité dans l'évolution des types de précipitations, l'approche « bulk » traditionnelle nécessite l'insertion de taux de conversions artificiels entre les différentes catégories de précipitations en phase solide. Or, depuis environ dix ans, une nouvelle technique, qui ne nécessite plus de conversions artificielles, est appliquée à certaines paramétrisations microphysiques. Il s'agit d'une méthode qui marque l'évolution des propriétés microphysiques des particules en phase solide (Hashino and Tripoli 2007; Morrison and Grabowski 2008b; Morrison and Milbrandt 2015). Cette approche a été généralisée dans le schéma de microphysique *Predicted Particle Properties* (P3) de Morrison and Milbrandt (2015). P3 permet de simuler plusieurs propriétés « bulk » des particules de glace à travers toutes les étapes de croissance (Fig. 0.1a) et de détérioration de ces particules en utilisant une seule catégorie dite « libre » de particules en phase solide.

La principale limitation de la plupart des schémas de microphysique demeure que les particules en phase mixte ne sont pas considérées, alors que ces dernières sont nécessaires notamment lors de la formation de neige mouillée et de grésil. Les raisons qui justifient d'ignorer les particules en phase mixte dans les schémas sont (1) les ajouts de complexité et de coût de calcul (Thériault *et al.* 2006) et (2) les manques de compréhension et d'observation des processus microphysiques associés aux formations et aux évolutions des particules en phase mixte (Szyrmer and Zawadzki 1999 ; Thériault *et al.* 2010). Par exemple, alors que les observations de Fujiyoshi (1986) montrent une accumulation de l'eau de fonte sur la particule pour former une particule en phase mixte, les schémas de microphysique transfèrent immédiatement en pluie l'eau de fonte produite en un pas de temps. De plus, le processus de regel (Hindmarsh *et al.* 2003; Gibson and Stewart 2007; Nagumo *et al.* 2019) d'une particule en phase mixte lors de son passage dans une couche d'air froid ou encore le processus par lequel la vapeur d'eau se condense sur ou s'évapore de la particule en phase mixte sont complètement négligés dans les schémas. En négligeant ces processus, les interactions entre les changements de phase et la température de l'air ne sont pas explicitement simulées. À leur tour, ces changements de température affectent la quantité de vapeur d'eau présente dans l'air, qui elle, affecte les processus microphysiques calculés.

La propriété qui permet de décrire l'évolution des particules en phase mixte se nomme la fraction liquide (Mitra *et al.* 1990; Szyrmer and Zawadzki 1999). Cette dernière est le rapport entre la masse d'eau et la masse totale de la particule en phase mixte. Une fraction liquide de 0 représente une particule en phase solide, comme un flocon de neige, tandis qu'une fraction liquide de 1 est la phase liquide, comme une goutte de pluie. Quelques études numériques ont permis l'implantation de la fraction liquide explicite dans des paramétrisations microphysiques afin de mieux représenter les différents taux de fonte des particules. En prenant appui sur les relations expérimentales et théoriques de Mitra *et al.* (1990) et de Pruppacher and Klett (1997), l'étude de Szyrmer and Zadwazki (1999) a permis d'entreprendre les premières expériences de la simulation des différents taux de fonte en fonction de la fraction liquide. Par la suite, en s'appuyant sur les travaux de Szyrmer and Zadwazki (1999), d'autres études ont inclus l'ajout d'une fraction liquide explicite dans des paramétrisations microphysiques « bulk » (Thériault *et al.* 2006; Thériault *et al.* 2010; Thériault and Stewart 2010; Frick *et al.* 2013) et « bin » (Phillips *et al.* 2007; Geresdi *et al.* 2014; Reeves *et al.* 2016). Les résultats de ces études ont montré que l'ajout d'une fraction liquide explicite dans la paramétrisation microphysique permet de mieux décrire les différents taux de fonte des particules et, par le fait même, la simulation de nouveaux types de précipitations, comme le grésil (Thériault *et al.* 2010) et la neige mouillée (Frick *et al.* 2013). Cependant, seulement Frick *et al.* (2013) ont testé la prévision de la fraction liquide « bulk » avec un modèle atmosphérique complet pour l'étude d'une tempête de neige mouillée, Thériault *et al.* (2010) et Szyrmer and Zadwadzi (1999) ont utilisé des simulations à une et deux dimensions, respectivement.

0.1.3 Dans le contexte d'une atmosphère plus chaude

Étant donné que le type de précipitation obtenu à la surface dépend grandement du profil vertical de température, un changement de seulement 1°C peut changer le type observé et favoriser, par exemple, de la pluie verglaçante au lieu du grésil ou bien de la pluie à la place de neige mouillée (Frick *et al.* 2013). Cela soulève des questionnements sur le signe (augmentation ou diminution) du changement futur des événements incluant ces types de précipitations dans le contexte du réchauffement climatique (IPCC 2013; Kämäräinen *et al.* 2018).

Plusieurs recherches ont porté sur l'étude des impacts du réchauffement climatique sur l'occurrence des événements de pluie verglaçante dans le futur (Cheng *et al.* 2007; Cheng *et al.* 2011; Lambert and Hansen 2011; Jeong and Sushama 2018; Matte *et al.* 2018). Par exemple, Cheng *et al.* (2011) ont utilisé une méthode de mise à l'échelle statistique aux stations d'observation des différents modèles climatiques globaux pour étudier le changement d'occurrence des événements de pluie verglaçante sur l'est du Canada vers la fin du XXI^{e} siècle. Ils ont trouvé une augmentation (une diminution) de la fréquence des événements de pluie verglaçante lors des mois d'hiver (des mois d'automne et de printemps) pour la région du sud du Québec. Pour leur part, Lambert and Hansen (2011) ont utilisé une méthode de post-traitement appliquée aux sorties du modèle canadien du climat couplé pour diagnostiquer les occurrences de pluie verglaçante à la fin du XXI^{e} siècle sur l'Amérique du Nord. Leur étude suggère des migrations vers le nord de l'isotherme 0°C et des précipitations verglaçantes, ce qui occasionne une réduction de l'occurrence de pluie verglaçante dans le sud du Québec. Klima and Morgan (2015) ont fait des expériences idéalisées en perturbant avec plusieurs scénarios les profils verticaux de température historiques obtenus des radiosondages aux États-Unis incluant ceux de Maniwaki au Québec. Leurs résultats principaux abondent dans le sens d'une transition vers le nord de la pluie verglaçante et d'une augmentation de la pluie verglaçante durant les mois d'hiver dans le sud du Québec. Finalement, Matte *et al.* (2018) ont utilisé plusieurs algorithmes de diagnostic des types de précipitations appliqués à des projections climatiques du Modèle Régional Canadien du Climat à ~15 km de résolution spatiale. Selon cette étude, une diminution du nombre d'heures et du nombre d'événements de pluie verglaçante dans le sud du Québec pour la fin du XXI^{e} siècle est obtenue.

Ces résultats contracdictoires témoignent d'un haut niveau d'incertitude quant à l'évolution des précipitations verglaçantes dans le futur. Par exemple, un premier résultat abonde en faveur d'une diminution des épisodes de pluie verglaçante due au déplacement vers le nord de l'isotherme 0°C et de la zone de transition de précipitation en raison d'un climat plus chaud (Lambert and Hansen 2011; Matte *et al.* 2018). Tandis qu'un résultat opposé suggère une augmentation de la pluie verglaçante (Cheng *et al.* 2011), en raison notamment d'une atmosphère plus humide et un accroissement de l'occurence des précipitations liquides et surfondues aux dépens des précipitations solides (par exemple : Jeong and Sushama 2018).

Les techniques pour évaluer les changements futurs des événements météorologiques à grands impacts, comme les tempêtes de pluie verglaçante, dans le contexte du réchauffement climatique sont limitées, car l'utilisation des schémas de microphysique est encore trop coûteuse numériquement pour des projections climatiques à long terme (par exemple : Prein *et al.* 2015; Matte *et al.* 2018). Toutefois, il existe une technique qui permet d'étudier les impacts d'une atmosphère plus chaude sur ces événements locaux du passé récent. Cette technique est appelée *Pseudo-Global-Warming* et a été originalement développée par Schär *et al.* (1996). Cette approche consiste à modifier les conditions initiales et aux frontières latérales d'une simulation à haute résolution spatiale d'un événement météorologique d'intérêt avec des perturbations climatiques calculées à partir de résultats de projections climatiques d'un modèle climatique global. Cette expérimentation permet d'étudier les impacts des perturbations de température et d'humidité sur un événement météorologique d'intérêt ayant les mêmes caractéristiques synoptiques qu'au moment de son passage dans le passé. L'approche du *Pseudo-Global-Warming* a été utilisée, entre autres, pour étudier l'épaisseur de la neige au sol (Hara *et al.* 2008), les bandes de pluie (Kawase *et al.* 2009), les chutes de neige (Rasmussen *et al.* 2011), le bilan hydrologique (Rasmussen *et al.* 2014; Liu *et al.* 2017), la pluie intense (Taniguchi et Sho 2015; Prein *et al.* 2017), les ouragans

(Gutmann *et al.* 2018) et les événements convectifs (Liu *et al.* 2017; Prein *et al.* 2017; Rasmussen *et al.* 2017). L'aspect intéressant est que cette approche offre une alternative pour étudier les impacts d'une atmosphère plus chaude sur un phénomène météorologique local en utilisant une microphysique détaillée pour simuler les types de précipitations et les processus microphysiques.

En résumé, les défis interconnectés présentés ci-dessus demeurent des sujets de recherches scientifiques d'actualité en lien avec la simulation des types de précipitations dans la zone de transition d'une tempête hivernale. Par ailleurs, pour prévoir les impacts découlant des tempêtes hivernales de pluie verglaçante dans le climat actuel comme dans le climat futur, il importe de mieux comprendre les processus microphysiques qui gouvernent les différents types de précipitations et les particules en phase mixte. Une solution immédiate à ces enjeux passe par l'élaboration d'un outil de paramétrisation permettant la simulation explicite des processus microphysiques associés aux particules en phase mixte avec la prévision de la fraction liquide. Enfin, l'idéal serait que cet outil puisse être utilisé à la fois en prévision numérique du temps et à la fois en mode climat.

0.2 Objectif poursuivi et questions de recherche

L'objectif central de la thèse est d'étudier les processus microphysiques et les types de précipitations simulés lors d'une tempête hivernale extrême, dans le climat actuel comme dans le contexte d'une atmosphère plus chaude, en utilisant la prévision de la fraction liquide. Plus spécifiquement, les trois chapitres de la thèse visent à répondre aux questions suivantes :

(1) Quels sont les effets de la prévision de la fraction liquide sur la représentation des propriétés des hydrométéores, telles que la vitesse de chute, la densité et les proportions en masse des différentes phases (solide, mixte, surfondue et liquide) ?

(2) Quels sont les impacts de la prévision de la fraction liquide sur la simulation des types de précipitations d'une tempête hivernale extrême ?

(3) Quelles sont les conséquences d'une atmosphère plus chaude sur la simulation des types de précipitations de la zone de transition d'une tempête hivernale extrême ?

0.3 Présentation des trois chapitres de la thèse

Chaque chapitre se présente sous la forme d'article scientifique.

Le premier chapitre est intitulé : « *Parameterization of the bulk liquid fraction on mixed-phase particles in the Predicted Particle Properties (P3) scheme: Description and idealized simulations* ». Cet article scientifique est publié dans la revue *Journal of the Atmospheric Sciences* (Cholette *et al.* 2019). Il vise à développer et tester une nouvelle paramétrisation qui inclut la prévision de la fraction liquide des particules en phase mixte dans un schéma de microphysique. Cette étape est primordiale pour la suite de la thèse, car sans outil permettant de décrire les processus microphysiques importants de ces particules, la simulation des types de précipitations hivernales dans la zone de transition, tels que le grésil et la neige mouillée, demeure implicite. Dans un premier temps, la nouvelle approche pour l'implantation de la fraction liquide dans le schéma de microphysique P3 est décrite. Dans un deuxième temps, avec pour objectif de valider la paramétrisation, le processus proposé de la fonte partielle des flocons de neige est comparé avec celui d'un modèle de référence basé sur la littérature et les observations de Mitra *et al.* (1990). Finalement, le schéma incluant la prévision de la fraction liquide est comparé à la version originale en utilisant un modèle de nuage colonne (à une dimension : la verticale) dans le but d'examiner les effets de la prévision de la fraction liquide sur la simulation des propriétés des hydrométéores.

Le deuxième chapitre s'intitule : « *Impacts of predicting the liquid fraction on mixed-phase particles in simulations of the precipitation types produced during 1998 Ice Storm* ». Il a pour objectif d'utiliser la paramétrisation développée dans le premier chapitre afin d'étudier les impacts de la prévision de la fraction liquide sur la simulation des types de précipitations lors d'une tempête hivernale extrême. Pour ce faire, des simulations numériques sont faites avec le modèle atmosphérique *Weather Research and Forecasting* (WRF; Skamarock and Klemp 2008) couplé au schéma P3 avec et sans la prévision de la fraction liquide. La tempête choisie est l'événement extrême de janvier 1998, qualifié ainsi à cause de sa durée et ses très grandes accumulations de neige, pluie verglaçante et pluie. Elle a été choisie pour deux raisons. La première raison est le caractère unique de cette tempête : elle est considérée comme l'un des désastres naturels les plus coûteux du dernier siècle au Canada (Lecompte *et al.* 1998). Elle a duré 6 jours et de 50 à 100 mm de pluie verglaçante se sont accumulés sur les surfaces du sud du Québec et du nord-est des États-Unis. Cela a encouru des dépenses de près de 4,4 M$ US en dommages, dont environ 70% de ces coûts au Canada (Risk and Management Solutions 2008). La deuxième raison repose sur le fait que cette tempête est bien documentée (Laflamme et Périard 1998; Lecompte *et al.* 1998; Milton and Bourque 1999; Cober *et al.* 2001; Gyakum and Roebber 2001; Roebber and Gyakum 2003; Henson *et al.* 2007; Henson *et al.* 2011), toutefois, cette tempête n'a jamais été simulée à haute résolution avec une paramétrisation microphysique explicite des particules en phase mixte. Les simulations avec et sans la prévision de la fraction liquide sont comparées afin de comprendre les impacts des processus microphysiques associés aux particules en phase mixte sur la simulation des types de précipitations et de leurs propriétés verticales.

Le troisième chapitre a pour titre : « *Changes in precipitation type distributions during the 1998 Ice Storm simulated under warmer conditions* ». L'objectif est d'étudier les impacts d'une atmosphère plus chaude sur la simulation des types de précipitations de la tempête de janvier 1998 en utilisant la prévision de la fraction liquide des particules en phase mixte. L'approche du *Pseudo-Global-Warming* est appliquée à la simulation WRF de la tempête. Cette approche modifie les conditions initiales et aux frontières latérales de température, d'humidité, de vents et de pression avec des perturbations climatiques calculées à partir de projection climatique. Les types de précipitations de la zone de transition des simulations avec et sans le réchauffement du *Pseudo-Global-Warming* sont comparés à la surface et dans la verticale.

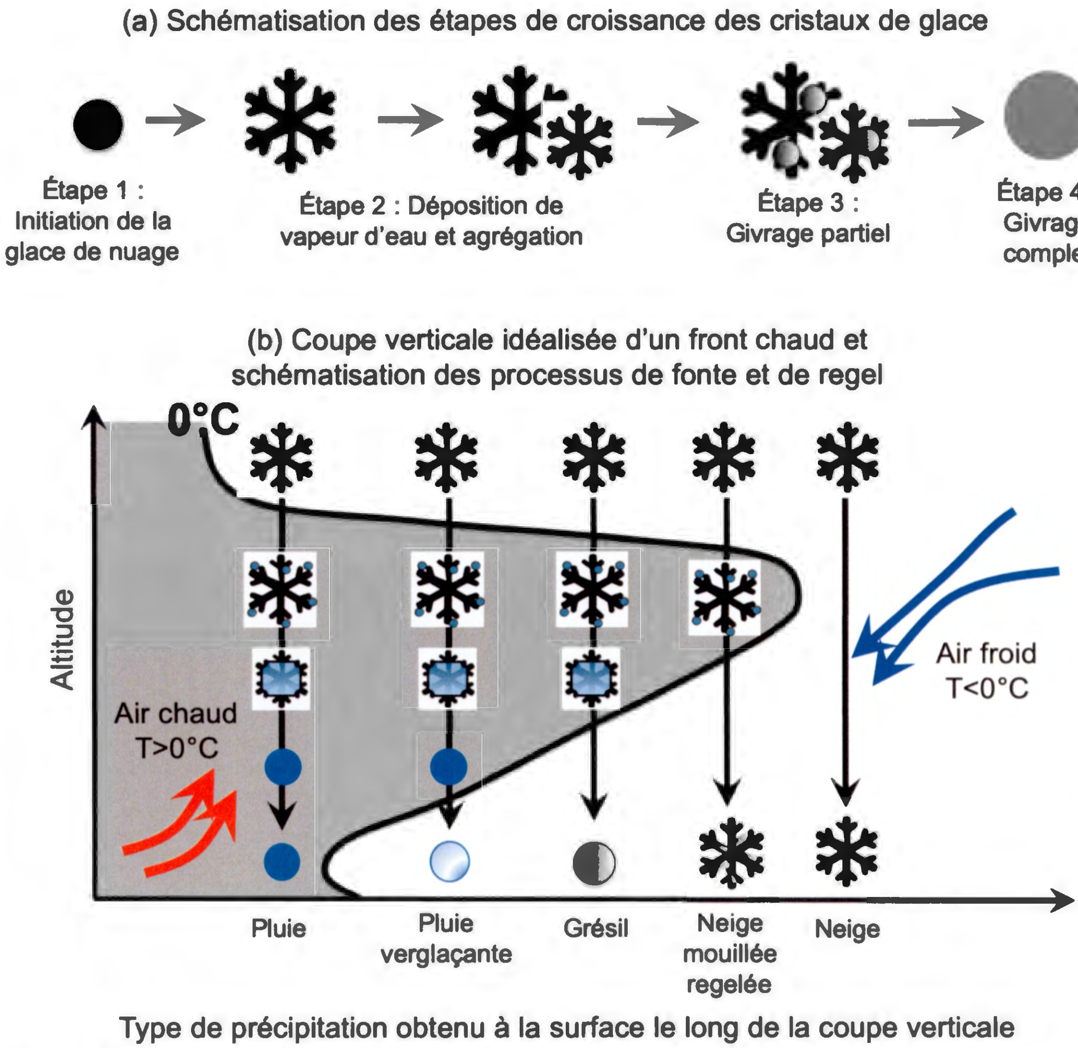

Figure 0.1 (a) Étapes de croissance d'un cristal de glace : 1) initiation de la glace de nuage, 2) croissance par déposition de vapeur d'eau et agrégation, 3) croissance par givrage partiel et 4) croissance par givrage complet. (b) Coupe verticale idéalisée d'un front chaud et schématisation de l'évolution des particules lors des processus de fonte d'un flocon de neige non givré et de regel. (Figure adaptée de Thériault *et al.* 2006).

CHAPITRE I

PARAMETERIZATION OF THE BULK LIQUID FRACTION ON MIXED-PHASE PARTICLES IN THE PREDICTED PARTICLE PROPERTIES (P3) SCHEME: DESCRIPTION AND IDEALIZED SIMULATIONS

This chapter is presented in the format of a scientific article published in the *Journal of the Atmospheric Sciences*. The detailed reference is:

Cholette, M., Morrison, H., Milbrandt, J.A., and Thériault, J.M. (2019). Parameterization of the bulk liquid fraction on mixed-phase particles in the Predicted Particle Properties (P3) scheme: Description and idealized simulations. *Journal of the Atmospheric Sciences*, *76*(2), 561-582.

Abstract

Bulk microphysics parameterizations that are used to represent clouds and precipitation usually allow only solid and liquid hydrometeors. Predicting the bulk liquid fraction on ice allows an explicit representation of mixed-phase particles and various precipitation types, such as wet snow and ice pellets. In this paper, an approach for the representation of the bulk liquid fraction into the Predicted Particle Properties (P3) microphysics scheme is proposed and described. Solid phase microphysical processes, such as melting and sublimation, have been modified to account for the liquid component. New processes, such as refreezing and condensation of the liquid portion of mixed-phase particles, have been added to the parameterization. Idealized simulations using a one-dimensional framework illustrate the overall behavior of the modified scheme. The proposed approach compares well to a Lagrangian benchmark model. Temperatures required for populations of ice crystals to melt completely also agree well with previous studies. The new processes of refreezing and condensation impact both the surface precipitation type and feedback between the temperature and the phase changes. Overall, prediction of the bulk liquid fraction allows an explicit description of new precipitation types, such as wet snow and ice pellets, and improves the representation of hydrometeor properties when the temperature is near 0°C.

1.1 Introduction

The passage of a warm front can produce favourable environmental conditions for many winter precipitation types such as rain, freezing rain, ice pellets, wet snow and snow (Stewart 1985). In such situations, a temperature (T) inversion, characterized by a warm layer aloft with T>0°C (called the melting layer) and cold layer near the surface with T<0°C (called the refreezing layer), occurs (e.g., Lin and Stewart 1986; Hanesiak and Stewart 1995; Gyakum and Roebber 2001; Thériault *et al.* 2006; Carmichael *et al.* 2011). The precipitation types formed when the temperature is near 0°C involve several microphysical processes including melting, refreezing, vapor deposition, collection and wet growth. For example, when T>~0°C, wet snow is formed from the partial melting of snow during which the melted water tends to accumulate on the ice core to form mixed-phase particles (Fujiyoshi 1986). Ice pellets are formed by refreezing in cold layers of the partially melted particles from aloft (Gibson and Stewart 2007; Thériault and Stewart 2010; Carmichael *et al.* 2011). Freezing rain corresponds to the surface icing of supercooled raindrops present in cold layers originating from the total melting of snow in warm layers aloft. Often, several types of precipitation can coexist, and, for example, the amount of surface freezing rain can be greatly inhibited due to the collection in the cold layers between supercooled raindrops and solid hydrometeors, such as ice pellets (Hogan 1985; Carmichael *et al.* 2011; Barszcz 2017). When T<0°C, wet growth of graupel/hail and the shedding of accumulated liquid water can occur in conditions of high liquid water content, also involving the formation of mixed-phase particles (e.g., Phillips *et al.* 2014). In turn, the phase changes occurring with some of these processes impact the environmental temperature as, for example, the cooling induced by melting and evaporation (e.g., Lackmann *et al.* 2002) or the warming induced by refreezing and condensation (e.g., Thériault *et al.* 2006).

Most bulk microphysics schemes allow only for the representation of solid phase hydrometeors (e.g., snow, graupel, hail) and liquid phase hydrometeors (e.g., rain, cloud) (e.g., Milbrandt and Yau 2005; Thompson *et al.* 2008; Morrison *et al.* 2009). Mixed-phase hydrometeors, such as wet snow, are typically not represented. For example, instead of forming wet snow from partial melting, most schemes immediately transfer the melted water directly into the rain category. To represent the evolution of mixed-phase particles in microphysical parameterizations explicitly, it is necessary to track in space and time the liquid fraction of mixed-phase hydrometeors, defined as the ratio of liquid water mass to the total particle mass.

Some studies have experimented with an explicit parameterization of the liquid fraction. Based on the experimental and theoretical relationships developed by Mitra *et al.* (1990) (hereafter M90), the study of Szyrmer and Zawadzki (1999) predicted the liquid fraction in a bulk microphysics module. This scheme was coupled with a two-dimensional non-hydrostatic, fully compressible dynamic framework to evaluate the effects of partial melting on the simulated "bright band" parameters (Austin and Bemis 1950; Yokoyama and Tanaka 1984; Braun and Houze 1995; Fabry and Zawadzki 1995; Fabry and Szyrmer 1999). They showed that the description of the particle habit prior to melting (unrimed or rimed and spherical or non-spherical) influences the melting rate and the liquid fraction evolution. They also pointed out the relevance of predicting the liquid fraction for radar applications. Based on the Szyrmer and Zawadzki (1999) parameterization, Thériault and Stewart (2010) modified the Milbrandt and Yau (2005) scheme to include several winter precipitation type categories. The new categories were wet snow, almost completely melted snow, refrozen wet snow, and two types of ice pellets. They tested the scheme using a one-dimensional (1D) cloud model and showed good agreement with observations for several winter storms (Thériault *et al.* 2006; Thériault *et al.* 2010; Thériault and Stewart 2010). More recently, and also based on Szyrmer and Zawadzki (1999), Frick *et al.* (2013) implemented partial melting in a bulk microphysics scheme coupled with the Consortium for Small-scale Modeling (COSMO; Doms and Schättler 2002) mesoscale model. They clearly showed the potential of their parameterization to simulate wet snow; however, their parameterization did not include the refreezing process, which is necessary to produce ice pellets. The implementation of an explicit liquid fraction has also been tested using bin microphysics parameterizations (Phillips *et al.* 2007; Geresdi *et al.* 2014; Reeves *et al.* 2016). Walko *et al.* (2000) developed an algorithm to diagnose the liquid fraction in the Regional Atmospheric Modeling System, which can be used with larger numerical time steps and regional modeling.

Recently, the Predicted Particle Properties (P3) bulk microphysics scheme described in Morrison and Milbrandt (2015) (hereafter MM15) and Milbrandt and Morrison (2016) (hereafter MM16), was introduced. The P3 scheme completely abandons the use of pre-defined ice-phase categories and introduces the idea of "free" ice categories. With four prognostic variables per free category, important physical properties of ice can evolve realistically and smoothly in time and space and thus a wide range of ice particle types can be represented. Despite the conceptual improvement over traditional fixed-category schemes for representing ice, P3 is still limited in that it cannot represent ice particles that accumulate liquid water. To address this limitation, in this study the original P3 scheme is modified to include the prediction of the bulk liquid fraction of ice categories and thus allow the representation of mixed-phase particles.

This paper is organized as follows. Section 1.2 briefly describes the original P3 scheme. Section 1.3 describes the implementation of the bulk liquid fraction into P3. Section 1.4 shows a validation of the proposed melting parameterization compared to a Lagrangian benchmark model. Section 1.5 shows results from two idealized experiments using a one-dimensional modelling framework to illustrate the overall behavior of the new parameterization and compare with the original one. Section 1.6 gives concluding remarks.

1.2 Overview of the original P3 microphysics scheme

This section gives a brief overview of the original P3 microphysics scheme (hereafter referred to as P3_ORIG); further details are in MM15 and MM16. As in other bulk schemes, P3 has two liquid-phase categories, cloud and rain, both of which are two-moment, with prognostic mass and number mixing ratios for each. There is a user-specified number of free ice-phase categories, each with four prognostic variables. In this study, only the single-ice category configuration is discussed, but the modifications described below are general and can apply to multi-ice category configurations. The four prognostic ice variables are total ice mass ($q_{i,tot}$; kg kg^{-1}), total ice number ($N_{i,tot}$; kg^{-1}), rime mass ($q_{i,rim}$; kg kg^{-1}) and rime volume ($B_{i,rim}$; m^3 kg^{-1}) mixing ratios. One can calculate the vapor deposition ice mass ($q_{i,dep}$) from $q_{i,tot} - q_{i,rim}$. Several relevant bulk properties, including the rime mass fraction ($F_{i,rim} = q_{i,rim}/q_{i,tot}$), the bulk ice density, the bulk rime density ($\rho_{i,rim} = q_{i,rim}/B_{i,rim}$), the mean particle size, and the mean number- and mass-weighted fall speeds are derived from these four conserved prognostic variables.

The total number and ice mass mixing ratios are respectively given by

$$N_{i,tot} = \int_0^\infty N_0 D^\mu \exp(-\lambda D)\, dD \tag{1.1}$$

$$q_{i,tot} = \int_0^\infty m_d(D)\, N_0 D^\mu \exp(-\lambda D)\, dD \tag{1.2}$$

where D is the maximum dimension of the ice particles, $m_d(D)$ is the mass-dimension relationship, and the particle size distribution (PSD) is assumed to follow a gamma function (all symbols for variables and parameters are defined in the list of symbols). The gamma distribution is described by N_0, λ and μ, respectively being the intercept, slope and shape parameters. In P3 the shape parameter follows from the observational study of Heymsfield (2003): $\mu = 0.00191\, \lambda^{0.8} - 2$, where λ has units of m^{-1}. For a given combination of prognostic variables ($N_{i,tot}$, $q_{i,tot}$), to solve for the PSD intercept and slope parameters, the $m_d(D)$ is needed.

Similar to Morrison and Grabowski (2008b) the $m_d(D)$ follows specific power laws for various sizes dependent regimes (see MM15 for details):

$$m_d(D)=\begin{cases} \frac{\pi}{6}\rho_i D^3\ ; & \text{if } D\leq D_{th}\text{: small spherical ice particles} & (1.3a) \\ \alpha_{va} D^{\beta_{va}}; & \text{if } D_{th}<D\leq D_{gr}\text{: unrimed non-spherical ice} & (1.3b) \\ \frac{\pi}{6}\rho_g D^3\ ; & \text{if } D_{gr}<D\leq D_{cr}\text{: graupel/hail particles} & (1.3c) \\ \frac{\alpha_{va}\left(1+F_{i,rim}\right)}{1-F_{i,rim}} D^{\beta_{va}}\ ; & \text{if } D>D_{cr}\text{: partially rime non-spherical ice} & (1.3d) \end{cases}$$

where ρ_i = 917 kg m^{-3} is the density of bulk ice and ρ_g is the density of fully rimed ice (graupel/hail). The regimes are bounded by three threshold diameters

$$D_{th}=\left(\frac{\pi\rho_i}{6\alpha_{va}}\right)^{1/\beta_{va}-3} \tag{1.4a}$$

$$D_{gr}=\left(\frac{6\alpha_{va}}{\pi\rho_g}\right)^{1/3-\beta_{va}} \tag{1.4b}$$

$$D_{cr}=\left(\frac{6\alpha_{va}(1+F_{i,rim})}{\pi\rho_g(1-F_{i,rim})}\right)^{1/\beta_{va}} \tag{1.4c}$$

that can evolve within the PSD as a function of the ice regime. The parameters α_{va} and β_{va} are empirical constants, and herein we use default P3 values of α_{va} = 0.0121 kg m$^{-\beta_{va}}$ and β_{va} = 1.9 following Brown and Francis (1995), modified for the correction proposed by Hogan *et al.* (2012). D_{th} (1.4a) smoothly divides small spherical ice particles from unrimed non-spherical particles and is found by equating (1.3a) and (1.3b). This threshold is needed because extrapolation of the $m_d(D)$ relationship for unrimed non-spherical ice to sizes smaller than D_{th} would give particle densities larger than ρ_i, which is unphysical. D_{gr}, given by (1.4b), smoothly separates dense, unrimed, non-spherical ice particles from graupel/hail and is found by equating (1.3b) and (1.3c). This is the size at which the masses of a completely rime-filled particle (graupel/hail) and of an unrimed non-spherical ice particle are equal for a given diameter D. Finally, D_{cr} (1.4c) smoothly divides graupel/hail from partially rimed non-spherical ice and is obtained by equating (1.3c) and (1.3d). Physically this threshold originates directly from the assumption that the rime mass fraction does not vary with D, giving a critical size (D_{cr}) below which particles are completely filled in with rime.

The value of ρ_g is a $F_{i,rim}$-weighted average of the rime density ($\rho_{i,rim}$) and the density underlying the unrimed structure of the particle (ρ_{ur}) (see MM15 for details). Due to their complicated inter-relationship, the equations for D_{gr}, D_{cr}, ρ_g and ρ_{ur} are solved together by iteration (MM15; Dietlicher *et al.* 2018). The projected area-diameter relationship ($A_d(D)$) also follows specific power laws for various sizes dependent regimes consistent with the $m_d(D)$ relationship (MM15). The terminal velocity-diameter relationship ($V_t(D)$) is computed using $m_d(D)$ and $A_d(D)$ according to Mitchell and Heymsfield (2005).

Once the parameters for the PSD (N_0, λ and μ) and the $m_d(D)$, $A_d(D)$ and $V_t(D)$ relationships are obtained, all the microphysical process rates are integrated. This is done offline and the values are stored in lookup tables as a function of the normalized total ice mass $q_{i,tot}/N_{i,tot}$, the bulk rime density $\rho_{i,rim}$ and the bulk rime mass fraction $F_{i,rim}$.

1.3 Parameterization description of the bulk liquid fraction

1.3.1 Overview of the liquid mass mixing ratio

In order to simulate mixed-phase particles and $F_{i,liq}$ explicitly in P3, a new conserved prognostic variable, the liquid mass mixing ratio on ice particles ($q_{i,liq}$), has been added to P3_ORIG. The modified scheme will be referred to as P3_MOD. In P3_MOD,

$$q_{i,tot} = q_{i,ice} + q_{i,liq} = q_{i,rim} + q_{i,dep} + q_{i,liq} \tag{1.5}$$

where $q_{i,ice} = q_{i,rim} + q_{i,dep}$. The bulk rime mass and liquid mass fractions are thus defined by

$$F_{i,rim} = \frac{q_{i,rim}}{q_{i,ice}} = \frac{q_{i,rim}}{q_{i,rim} + q_{i,dep}} \tag{1.6}$$

$$F_{i,liq} = \frac{q_{i,liq}}{q_{i,tot}} = \frac{q_{i,liq}}{q_{i,rim} + q_{i,dep} + q_{i,liq}} \tag{1.7}$$

respectively. The conservation equation for $q_{i,liq}$ is

$$\frac{\partial q_{i,liq}}{\partial t} = -\mathbf{u}\cdot\nabla q_{i,liq} + \frac{1}{\rho_a}\frac{\partial(\rho_a V_m q_{i,liq})}{\partial z} + \Delta^*(q_{i,liq}) + \left.\frac{dq_{i,liq}}{dt}\right|_S \tag{1.8}$$

where t is time, ρ_a is the air density, $\mathbf{u}$ is the 3D wind vector, z is height, V_m is the mass-weighted fall speed (see section 1.7.6), $\Delta^*(q_{i,liq})$ is a subgrid-scale mixing operator and $\left.\frac{dq_{i,liq}}{dt}\right|_S$ is a source/sink term that includes various microphysical processes. The $q_{i,liq}$ microphysical tendency is

$$\left.\frac{dq_{i,liq}}{dt}\right|_S = Q_{i,mlt} + Q_{l,wgrth} + Q_{l,coll,r} + Q_{l,coll,c} + Q_{l,dep} - Q_{l,frz} - Q_{l,shd} \tag{1.9}$$

where $Q_{i,mlt}$ is the melting, $Q_{l,wgrth}$ the wet growth, $Q_{l,coll,r}$ ($Q_{l,coll,c}$) the collection of rain (cloud droplets), $Q_{l,shd}$ the shedding, $Q_{l,frz}$ the refreezing and $Q_{l,dep}$ is the vapor transfer. The latter can be a source term (condensation) or a sink term (evaporation). The source/sink terms are described in section 1.7. Note, the modified definitions of $q_{i,tot}$ and $F_{i,rim}$ in (1.5) and (1.6), respectively, are consistent with P3_ORIG since for $F_{i,liq} = 0$ these variables simply revert back to the original formulations in MM15.

1.3.2 Main assumptions

A major question when predicting $F_{i,liq}$ in bulk schemes is how the particle size evolves during melting. In traditional multi-moment bulk parameterizations the mean size of ice particles typically does not change during melting (e.g., Milbrandt and Yau 2005; Thompson *et al.* 2008; Morrison *et al.* 2009). This is a common closure assumption in order to calculate the decrease in number concentration during melting. However, observations show a decrease of size during melting for individual particles (Fujiyoshi 1986). This decrease can be captured by predicting $F_{i,liq}$. Past studies approximated the spherical drop equivalent diameter (D_{eq}) as a function of $F_{i,liq}$ and utilized a "melting critical diameter" (D^*), such as Thériault and Stewart (2010) and Szyrmer and Zawadzki (1999). The melting critical diameter determines the largest particles in the PSD that will melt completely within one time step, and it depends on $F_{i,liq}$. Thus, this method requires iterations to solve D_{eq} because of the interdependence of D^* and $F_{i,liq}$. This is one reason why this approach for the implementation of $F_{i,liq}$ has not been widely used in traditional bulk schemes designed with several solid precipitation categories.

Past theoretical and experimental studies have described the melting behavior of ice particles depending on their size and type. Rasmussen *et al.* (1984a) and Rasmussen and Pruppacher (1982) found that small spherical ice particles with $D<\sim 0.1$ cm melt quickly, in less than one minute, into liquid drops. Fujiyoshi (1986) showed that the liquid water produced by the melting of unrimed non-spherical ice particles accumulates to form wet snow. Rasmussen *et al.* (1984b) found that a portion of the liquid produced by the melting of large rimed ice particles (D>0.1 cm) is shed, while the rest is accumulated around the ice core. Leinonen and von Lerber (2018) showed that the melting of lightly-rimed crystals is similar to the melting of unrimed aggregates (no shedding), whereas the melting of moderately-rimed crystals is similar to the melting of graupel/hail (with shedding).

Based on Rasmussen *et al.* (1984a), all liquid water produced by the melting of small spherical ice particles ($D \leq D_{th}$) in P3_MOD is transferred to the rain category in one time step. Thus, it is assumed that D_{th} corresponds to the melting critical diameter in P3_MOD. For the parameter values of α_{va} and β_{va} used here, D_{th} is ~66 μm. Based on the studies discussed above, shedding during melting is considered when $F_{i,rim}>0$, detailed in section 1.7.5.

The simplest approach to describe the melting process is to assume that the liquid water is uniformly distributed around an ice core. For simplicity and due to a lack of detailed observations, ice cores are assumed to have the same properties (mass, projected area, capacitance, ventilation coefficient and so on) as in P3_ORIG. Melting decreases ice core mass $q_{i,ice}$ but not the total ice number $N_{i,tot}$, except for particles with $D \leq D_{th}$ that are transferred to the rain category as described above; thus, the mean size of ice cores decreases during melting. Because the bulk ice particle density increases with decreasing particle size in P3, this assumption is physically reasonable and implies a tendency towards small spherical ice cores with a density equal to ρ_i as particles melt.

According to the assumptions below, the most straightforward approach for the implementation of $F_{i,liq}$ into P3 is to separate processes based on whether they apply to the ice core embedded within the particle or the whole mixed-phase particle (liquid and ice). This way, each process can be integrated over the appropriate size distribution based on the microphysical process computed. It is assumed that melting depends directly on properties of the ice core embedded in mixed-phase particles. Thus, the bulk melting rate (detailed in the section 1.7.1) is calculated by integration over the PSD computed using the ice core diameter (D_d). Ice core PSD parameters $N_{0,core}$, μ_{core} and λ_{core} are computed using $q_{i,ice} = (1 - F_{i,liq})\, q_{i,tot}$ and $m_d(D)$ following (1.3a)-(1.3d). Note that sublimation/deposition processes also depend directly on properties of the ice core embedded in the whole particle, as explained in the section 1.7.4.

Other microphysical processes, such as refreezing, condensation/evaporation of the liquid component, self-collection, shedding and collection with other particle categories depend on properties of the whole particle (both the ice and liquid components). Bulk rates for these processes (also detailed in section 1.7) are calculated by integrating over the PSD computed using the full mixed-phase particle diameter (D_p). To compute the whole particle PSD parameters $N_{0,p}$, μ_p and λ_p, the mass-diameter relationship ($m_t(D_p, F_{i,liq})$) is needed. For simplicity and due to lack of observations, it is assumed that at a given D_p, $m_t(D_p, F_{i,liq})$ is calculated by a linear interpolation based on $F_{i,liq}$:

$$m_t(D_p, F_{i,liq}) = (1 - F_{i,liq}) m_d(D_p) + F_{i,liq}\, m_{liq}(D_p) \tag{1.10}$$

Here $m_d(D_p)$ is given by (1.3a) to (1.3d) and $m_{liq}(D_p) = \pi/6 \rho_w D_p^3$ ($\rho_w = 1000$ kg m^{-3}), evaluated over the full mixed-phase PSD (from 0 to ∞). $m_t(D_p, F_{i,liq})$ is used to solve the PSD parameters $N_{0,p}$, μ_p and λ_p over $q_{i,tot}$ defined by

$$q_{i,tot} = \int_0^\infty m_t(D_p, F_{i,liq})\, N_{0,p}\, D_p^{\mu_p} \exp(-\lambda_p D_p)\, dD_p \tag{1.11}$$

The linear interpolation of $F_{i,liq}$ for $m_t(D_p, F_{i,liq})$ is consistent with a density of the mixed-phase particle being equal to a $F_{i,liq}$-weighted average of the ice and liquid parts, which was also used by Szyrmer and Zawadzki (1999). Also, this approach is consistent with (1) assuming a constant $F_{i,liq}$ with diameter over the size distribution; (2) physically consistent behaviors in the limits of $F_{i,liq} = 0$ and $F_{i,liq} = 1$; (3) a mixed-phase particle density that must always be less than or equal to the density of a liquid drop with the same diameter; and (4) a straightforward computation of the size distribution parameters as a function of $F_{i,liq}$.

An approach similar to (1.10) is made for the projected area ($A_t(D_p, F_{i,liq})$) and for the terminal velocity ($V_t(D_p, F_{i,liq})$) relationships. These are, respectively,

$$A_t\left(D_p, F_{i,liq}\right)=\left(1-F_{i,liq}\right)A_d\left(D_p\right)+F_{i,liq}\, A_{liq}\left(D_p\right) \qquad (1.12)$$

where $A_d(D_p)$ is the P3_ORIG projected-area relationships and $A_{liq}(D_p) = \pi/4D_p^2$; and

$$V_t\left(D_p, F_{i,liq}\right)=\left(1-F_{i,liq}\right)V_t\left(D_p, F_{i,liq}=0\right)+F_{i,liq}\, V_t\left(D_p,F_{i,liq}=1\right) \qquad (1.13)$$

where $V_t(D_p, F_{i,liq} = 0)$ and $V_t(D_p, F_{i,liq} = 1)$ are given in section 1.8 (equations 1.26 and 1.28, respectively, but with D_d replaced by D_p). These expressions follow Mitchell and Heymsfield (2005) and Simmel *et al.* (2002), respectively.

The $V_t(D_p, F_{i,liq})$ of unrimed ice ($F_{i,rim} = 0$) and fully rimed ice ($F_{i,rim} = 1$) at four different values of $F_{i,liq}$ are shown in Figs. 1.1a-b, respectively. The terminal velocity increases with both the particle size D_p and $F_{i,liq}$ in agreement with the observations of M90 for unrimed ice (Fig. 1.1a). Direct comparison with the observed and experimental terminal velocities of M90 is, however, difficult because the M90 relationship can only be applied to unrimed ice particles. Also, the M90 fall speed relationship used a different ice core mass-dimension relationship compared to P3. There are no observations of terminal velocities of partially melted rimed (partially or fully) ice particles. Based on Rasmussen *et al.* (1984b), it is assumed that for large particles accumulated liquid water is shed. However, for unrimed and partially rimed ice the liquid water is retained and forms a shell, which flattens as the particles fall, thereby limiting the increase of fall speed with D_p similar to the behavior of large purely liquid drops. This is seen in Fig. 1.1b for particles larger than 0.4 cm.

1.4 Comparison with a benchmark melting model

1.4.1 Experimental design

A benchmark comparison of P3_MOD with a detailed Lagrangian model using the M90 microphysics parameterization is presented. It aims at illustrating differences between P3_MOD and M90 in the melting behavior of a population of ice particles. M90, Yokoyama and Tanaka (1984) and Matsuo and Sayso (1981) have evaluated the distance below the 0°C level for a single falling ice crystal to melt completely using a Lagrangian model with their respective melting equations. Here, this distance is evaluated for a population of unrimed non-spherical ice particles to calculate the evolution of melting particles as they fall, with comparison between the P3_MOD scheme and a Lagrangian model we developed with the M90 parameterization Two different populations of ice particles, shown in Fig. 1.2a, provide input boundary conditions. The first, PSD 1, includes a moderate number of large ice particles characterized by a total ice mass mixing ratio of $q_{i,tot} = 0.6$ g kg^{-1} and a total number mixing ratio of ice of $N_{i,tot} = 10\ 550$ kg^{-1}. The second, PSD 2, includes a larger number of small ice particles characterized by $q_{i,tot} = 0.65$ g kg^{-1} and $N_{i,tot} = 41\ 550$ kg^{-1}. Rimed particles are not included in this experiment because they are not accounted for in the M90 parameterization.

Both the Lagrangian benchmark and P3_MOD bulk model use the melting equation developed in section 1.7 (equation 1.16). To solve (1.16), both models use a temperature variation with height of 0.6°C/100 m as shown in Fig. 1.2b. For both models, melting is the only microphysical process included, and feedback between temperature and latent cooling during melting is neglected; the temperature profile is constant in time. The parameters L_e, L_f, k_a, D_v, $q_{s,0}$, q_v and ρ_a are computed with the air temperature and pressure, assuming hydrostatic balance. The atmosphere is saturated with respect to water.

The Lagrangian model solves (1.16) using the M90 parameterization. It is numerically integrated as an initial value problem using a simple Euler forward scheme with a time step of 1 s. The model is initialized by dividing the particle population into 10 000 particle sizes with varying D_d, covering a size range from 0.0001 cm to 2 cm. This provides the evolution of particle properties along vertical trajectories for each of the 10 000 initial sizes. Bulk properties of the model, such as $F_{i,liq}$ and $q_{i,ice}$, are calculated from these trajectories every meter below the 0°C level. The particle fall speed follows from M90 (Geresdi *et al.* 2014; see their equation 3).

P3_MOD solves bulk equations for the 1D (vertical) model prognostic variables as they evolve in time. Sedimentation is calculated using a simple first-order upwind approach using the mean number- and mass-weighted bulk fall speeds described in section 1.7.6. The equations are solved using a time step of 1 s and a vertical grid spacing of 1 m. Results for comparison with the Lagrangian model are taken after 10 min of simulation time.

1.4.2 Results

$F_{i,liq}$ and the $q_{i,ice}$ as a function of the distance below the 0°C level are shown in Figs. 1.3a-b, respectively. Overall, the Lagrangian benchmark model and P3_MOD give similar results. For a given T, differences in $F_{i,liq}$ between P3_MOD and the Lagrangian model are always smaller than 0.15, and relatively larger for small $F_{i,liq}$. The melting process in P3_MOD is somewhat slower than the Lagrangian model for

$F_{i,liq}$<0.6-0.7, leading to a slightly larger $q_{i,ice}$ in P3_MOD. This is compensated by slightly faster melting in P3_MOD for larger $F_{i,liq}$, so that the total distance for melting is nearly the same as in the Lagrangian model.

The small differences between P3_MOD and the Lagrangian model seen in Fig. 1.3 can be explained mainly by differences in the parameterization used for the melting equation associated with the capacitance $C(D_d, F_{i,liq})$ and ventilation coefficient $F(D_d, F_{i,liq})$ relationships. For the Lagrangian model, the M90 relationships are based on Pruppacher and Klett (1997). For P3_MOD, the relationships are given in section 1.8 (equations 1.23 and 1.24, respectively). Figure 1.4 shows comparisons between M90 and P3_MOD of the capacitance (Fig. 1.4a) and the ventilation coefficient (Fig. 1.4b) for unrimed ice ($F_{i,rim} = 0$). At a given D_d, the capacitance of P3_MOD is slightly smaller than M90, especially at low $F_{i,liq}$. Larger differences occur for the ventilation coefficient owing to its dependence on the terminal velocity parameterization in (1.16). For a given D_d, the ventilation coefficient of P3_MOD is greater (smaller) than M90 at low (high) $F_{i,liq}$. As detailed in section 1.8, the ventilation coefficient for P3_MOD is computed by linear interpolation as a function of $F_{i,liq}$ between the ventilation parameters for dry ice in P3_ORIG when $F_{i,liq} = 0$ and those corresponding to a liquid drop when $F_{i,liq}= 1$. On the other hand, in M90 the ventilation coefficient is computed using their experimental terminal velocity, which is small at low $F_{i,liq}$ and increases quickly at $F_{i,liq}$>0.7. Also seen in Fig. 1.3, the differences between P3_MOD and the Lagrangian model using M90 are larger for PSD 1 than for PSD 2, especially when $F_{i,liq}$ is small. This is because PSD 1 has a higher concentration of large particles, and differences in the ventilation coefficient parameterization between P3_MOD and M90 are greater for larger particles than smaller ones (Fig. 1.4b).

A comparison between M90 Lagrangian model and P3_MOD for the evolution of the PSDs as the two populations of ice particles fall below the 0°C is shown in Fig. 1.5. Note that the PSDs in Fig. 1.5 are shown as a function of the ice core diameter (D_d).

For both initial PSDs 1 and 2 from P3_MOD, the shape parameter of the gamma PSD remains unchanged and is equal to 0 at small liquid fractions. However, when the liquid fraction increases, the slope parameter increases, which leads to an increase of the shape parameter. This behavior is seen with PSD 2 at $F_{i,liq} = 0.9$. The intercept parameter also increases with $F_{i,liq}$ for both PSDs. In general, the three parameters of the PSD increase with the increasing $F_{i,liq}$ and their changes depend on the rime mass fraction and the values of $q_{i,tot}$ and $N_{i,tot}$ that characterize the PSD. The evolution of the PSDs for the P3_MOD simulations compares well to that using the M90 Lagrangian model, especially at low $F_{i,liq}$, and reflects the decrease of particle size and shift of the PSD towards smaller sizes during melting (Thériault *et al.* 2006; Thériault and Stewart 2010). Overall, these simulations suggest that P3_MOD behaves realistically compared to M90.

Instead of comparing with the Lagrangian M90 model, the P3_MOD melting process for $F_{i,rim} = 0$ could also be compared to the Thériault and Stewart (2010) bulk microphysics scheme. It is believed that results will be comparable, since they used the same parameterizations as M90. However, as the parameterizations are very different between Thériault and Stewart (2010) and P3_MOD, and the Thériault and Stewart (2010) scheme does not include the prediction of rime fraction, P3_MOD will only be compared to P3_ORIG in the following.

1.5 Idealized simulations using P3_MOD

1.5.1 Experimental design

Characteristics of the precipitation type are investigated using P3_MOD coupled with a simple 1D kinematic model. P3_MOD is compared to P3_ORIG to illustrate differences in the precipitation properties with the prediction of the $F_{i,liq}$ and the overall behavior of the modified scheme.

All 1D simulations are initialized with vertical profiles of temperature and water vapor mass mixing ratio for 50 vertical levels evenly spaced. The grid spacing is 60 m. The simulated period is 2 h and the time step is 1 s. Hydrostatic balance is assumed. The precipitation type characteristics are analyzed after 30 min of simulation time. A total ice mass mixing ratio of $q_{i,tot} = 0.265$ g kg^{-1} and total ice number mixing ratio of $N_{i,tot} = 5000$ kg^{-1} provide boundary conditions at the domain top. This corresponds to a snowfall rate of 1 mm h^{-1} when $F_{i,rim} = 0$. Sensitivity of the precipitation properties to variation of the $F_{i,rim}$ value specified at the domain top is also investigated. The initial $q_{i,rim}$, with a fixed bulk rime density of 900 kg m^{-3}, is systematically modified to increase the snowfall rate at the top of the column such that it reaches 2.7 mm h^{-1} when $F_{i,rim} = 1$; the increased snowfall rate for a given $q_{i,tot}$ occurs because the mass-weighted mean fall speed increases with $F_{i,rim}$. The vertical air motion is zero throughout the column.

Two observed vertical profiles of temperature and dew point temperature were used to initialize the 1D simulations, shown in Fig. 1.6. Case 1 (Fig. 1.6a) has a vertical profile that was measured by a Gondola during the *Science of Nowcasting Olympic Weather for Vancouver 2010* (SNOW-V10; Isaac *et al.* 2014) field campaign. It is characterized by melting near the surface. A rain-snow boundary was observed along Whistler Mountain at around 2300 UTC 7 March 2010 (Thériault *et al.* 2014), with a mixture of wet snow and rain at the base of the mountain. In this profile, the near surface melting layer is 500 m deep and the environmental conditions are sub-saturated with respect to liquid water in cold layers and at the melting layer top.

The case 2 (Fig. 1.6b) thermodynamic profile is based on observations obtained on 2315 UTC 1 February 1992 at St. John's, Newfoundland, Canada (Hanesiak and

Stewart 1995). It is associated with a melting layer atop a refreezing layer below. A mixture of ice pellets and some needles was reported at the surface around 2317 UTC, and a mixture of ice pellets, freezing rain and needles at around 2345 UTC. In the refreezing layer of this profile, the environmental conditions are near saturation with respect to liquid water, meaning that it is supersaturated with respect to ice. The top of the melting layer is sub-saturated with respect to liquid water.

1.5.2 Case 1 : Melting layer near the surface

Vertical profiles of the temperature, mass and number mixing ratios, liquid fraction, and mass-weighted density and fall speed after 90 min are shown in Fig. 1.7 for both P3_ORIG and P3_MOD. These results are for unrimed ice; that is $F_{i,rim} = 0$ at the domain top. The main microphysical processes (not shown) for both simulations are sublimation in the cold layers (T<0°C) and melting in the warm layers. Collection of rain and evaporation occur in the warm layer, with evaporation of melting ice neglected in P3_ORIG. In P3_MOD these processes are sources and sinks for the liquid component, $q_{i,liq}$. Collected rain in P3_ORIG is shed back to rain at temperatures above freezing, while in P3_MOD the collected rain is added to $q_{i,liq}$. The evaporation of $q_{i,liq}$ in P3_MOD cools the air near the top of the melting layer compared to P3_ORIG (Fig. 1.7a). The surface precipitation type formed in P3_ORIG is rain (Fig. 1.7b), while in P3_MOD there is a mixture of rain and almost completely melting ice (Fig. 1.7b), the latter characterized by a $F_{i,liq}$ of 0.98 (Fig. 1.7d). The total number mixing ratio of rain (Fig. 1.7c) is higher in P3_MOD compared to P3_ORIG because the source term for rain number concentration is parameterized differently. In P3_ORIG, the rain number source from melting is proportional to the respective changes in $q_{i,tot}$, while it is proportional to $q_{i,ice}$ in P3_MOD (section 1.7.1). Moreover, P3_ORIG calculates the number of raindrops formed by melting using a scaling factor of 0.2 to account for the rapid evaporation of small melting particles; that is, it assumes a proportion of one raindrop formed per five melted ice particles. No such scaling is applied in P3_MOD. Both mass-weighted density (Fig. 1.7e) and fall speed (Fig. 1.7f) are larger in P3_MOD compared to P3_ORIG in the melting layer, which has significant impacts on the melting time of particles; faster fall speeds mean less time to melt over a given distance.

Results from varying the rime mass fraction $F_{i,rim}$ specified at the domain top are shown in Figs. 1.8-1.9. Vertical profiles of $F_{i,liq}$ after 90 min (Fig. 1.8a) illustrate that at low $F_{i,rim}$, particles melt completely before reaching the surface. This is reflected by the percentages of surface precipitation types reaching the surface (Fig. 1.8b). The surface precipitation type is only rain using P3_ORIG for an initial $F_{i,rim} \leq 0.2$, while P3_MOD produces a mixture of rain and very wet ice with $F_{i,liq} > 0.95$. For initial values of $F_{i,rim} > 0.5$, both P3_ORIG and P3_MOD show a mixture of surface precipitation types. Differences between P3_ORIG and P3_MOD are mainly due to collection of rain, shedding and the production of faster falling particles by P3_MOD. For example, the collection of rain by partially melted ice increases with the specified $F_{i,rim}$ at the domain top because there is more shedding, which reduces the amount of rain reaching the surface in P3_MOD. Also, as seen in Fig. 1.9, an increase of the mean mass-weighted density (Fig. 1.9a) and the mean mass-weighted fall speeds (Fig. 1.9c) occurs in P3_MOD compared to P3_ORIG (Fig. 1.9b and Fig. 1.9d, respectively), which, as mentioned before, impacts the time spent by particles in the warm layer. The main added value of P3_MOD for this case is the ability to produce wet snow at the surface.

1.5.3 Case 2 : Melting layer aloft

Results for case 2, specifying $F_{i,rim} = 1$ at the domain top, are shown in Fig. 1.10. As for case 1, only melting cools the environmental air in P3_ORIG, while there is also cooling from evaporation of $q_{i,liq}$ in P3_MOD at the top of the melting layer (Fig. 1.10a).

In both P3_ORIG and P3_MOD, a mixture of supercooled raindrops and rimed ice is produced in the refreezing layer (Figs. 1.10b-c). Note that supercooled raindrops represent freezing rain as the surface temperature is <0°C in both P3_MOD and P3_ORIG. Note also that since $F_{i,rim} = 1$, the lines for $q_{i,tot}$ and $q_{i,rim}$ are superimposed for P3_ORIG. In P3_MOD, rimed ice is produced from the complete refreezing of partially melted ice particles aloft, which is the process forming ice pellets. The proportion of ice to the total precipitation is higher in P3_MOD compared to P3_ORIG due to the partial melting and the refreezing of partially melted ice, which is neglected in P3_ORIG. Values of $F_{i,liq}$ for partially melted ice entering the cold layer are ~0.8 and decrease below 1.2 km due to refreezing (Fig. 1.10d). The rime mass fraction (Fig. 1.10d) remains close to 1 and the rime density (Fig. 1.10e) to 900 kg m^{-3} at all heights, which follows from the parameterization of melting and refreezing as described in sections 1.7.1 and 1.7.2, respectively. The mass-weighted mean density (Fig. 1.10e) and fall speed (Fig. 1.10f) increase in the warm layer and slightly decrease in the cold layer, the latter associated with ice pellets.

The temporal evolutions of P3_MOD and P3_ORIG air temperature are shown in Figs. 1.11a-b, respectively. Cooling due to melting and warming due to refreezing are the main processes affecting temperature, giving profiles that tend toward a 0°C isothermal layer. P3_MOD is generally colder in the melting layer and warmer in the refreezing layer than P3_ORIG (Fig. 1.11c). The formation of ice pellets by refreezing in P3_MOD warms the air compared to P3_ORIG. Differences in the melting layer are associated with faster falling particles when $F_{i,liq}>0$ after the onset of melting in P3_MOD, which vertically extends the region where particles melt compared to P3_ORIG. In the cold layer, temperature differences are larger due to refreezing in P3_MOD, which does not occur in the P3_ORIG simulation.

Percentages of surface precipitation types from varying $F_{i,rim}$ at the domain top for case 2 are shown in Fig. 1.12. For $F_{i,rim} \leq 0.6$ at the domain top, both P3_MOD and

P3_ORIG produce only freezing rain at the surface over the entire period. For $F_{i,rim}\geq0.6$ at the model top, both P3_MOD and P3_ORIG show a mixture of ice and freezing rain. However, ice pellets formed from refreezing are the dominant precipitation type in P3_MOD when $F_{i,rim}>0.65$ at the model top, whereas freezing rain is the dominant type in P3_ORIG. The refreezing process in P3_MOD has a major impact on the precipitation types reaching the surface because the generation of ice pellets from refreezing leads to an increase in the collection of supercooled raindrops, in turn reducing freezing rain at the surface consistent with Barszcz *et al.* (2018).

1.6 Summary and conclusion

A new parameterization approach is proposed to predict the bulk liquid mass fraction of mixed-phase particles, $F_{i,liq}$, in the Predicted Particle Properties (P3) bulk microphysics scheme. The modified scheme, P3_MOD, can explicitly simulate the evolution of bulk mixed-phase particle properties, thus improving the representation of key microphysical processes such as melting, evaporation/condensation and refreezing. It also allows the explicit prediction of several winter precipitation types, such as freezing rain, ice pellets and wet snow due to the addition of a new prognostic variable, the bulk liquid mass mixing ratio accumulated on ice ($q_{i,liq}$).

P3_MOD produced comparable melting rates to a Lagrangian benchmark model based on the Mitra *et al.* (1990) melting parameterization which was developed from observations. This supports the viability of P3_MOD and its bulk representation of the melting behavior of ice particles. Prediction of the liquid fraction affects the mean fall speed and density of hydrometeors falling into a melting layer, which in turn impacts distributions of latent cooling as well as other microphysical processes such as collection and condensation/evaporation, compared to P3_ORIG. Predicting the liquid fraction also allows the refreezing of partially melted ice particles to be explicitly represented, which increases the formation of ice pellets and the ratio of ice pellets to supercooled rain compared to P3_ORIG. Finally, the sensitivity of surface precipitation characteristics to riming differs between P3_MOD and P3_ORIG. For a melting layer 500 m deep and a surface temperature of 2°C, an increase in rime mass fraction leads to an increase in the snow to liquid precipitation ratio in P3_MOD compared to P3_ORIG.

Overall, implementation of the bulk liquid fraction in P3 is a step forward toward better prediction of precipitation type and distribution when the temperature is near 0°C. Important precipitation types, such as ice pellets and hail, involve tracking mixed-phase particles. Forecasting these precipitation types will therefore benefit from the prediction of the bulk liquid fraction. Although the focus of this work is on improving the representation of wintertime mixed-phase precipitation, the parameterized microphysics in P3_MOD is general and thus the inclusion the predicted liquid fraction should also improve the simulation of hail through better representation of shedding during wet growth and melting. The effects of P3_MOD on the simulation of hail will be examined in a future study. Since P3_MOD only involves one additional prognostic variable per ice category, the additional computational cost is relatively small. It could be used in Numerical Weather Prediction (NWP) as well as in Convection-Permitting Climate models (CPCM).

Although the main objective of the paper was to describe the new approach for implementing $F_{i,liq}$ into P3, and we show that the approach is comparable to the detailed Lagrangian model, comparison with observations is needed to validate the new parameterization. Therefore, in future work, P3_MOD will be tested by simulating a freezing rain and ice pellets storm using a three-dimensional atmospheric model, with comparison to detailed observations.

Acknowledgments

The authors would like to thank the Canadian Network for Regional Climate and Weather Processes (CNRCWP) and the NSERC Discovery grant for funding this research. One of the authors (Mélissa Cholette) would like to thank the Fonds de Recherche du Québec – Nature et technologies (FQRNT) and the UQAM Faculty of Science for graduate fellowships. We would like to thank the three anonymous reviewers for their constructive comments.

1.7 Appendix: The microphysical process formulations

1.7.1 Melting

The melting source/sink is divided into two terms. The first term is the meltwater transferred to the rain category ($Q_{r,mlt}$) and the second is the meltwater accumulated on ice particles ($Q_{i,mlt}$):

$$Q_{r,mlt} = \int_0^{D_{th}} \left.\frac{dm_{ice}}{dt}\right|_{melting} N_{0,core} D_d^{\mu_{core}} \exp(-\lambda_{core} D_d)\, dD_d \tag{1.14}$$

$$Q_{i,mlt} = \int_{D_{th}}^{\infty} \left.\frac{dm_{ice}}{dt}\right|_{melting} N_{0,core} D_d^{\mu_{core}} \exp(-\lambda_{core} D_d)\, dD_d \tag{1.15}$$

where D_d is the maximum dimension of the ice core, and $\left.\frac{dm_{ice}}{dt}\right|_{melting}$ is the melting rate of a single particle. During melting $q_{i,rim}$ is reduced to maintain a constant rime mass fraction. The ice (rain) number sink (source) terms are proportional to the respective changes in $q_{i,ice}$: $N_{r,mlt} = Q_{r,mlt} N_{i,tot}/q_{i,ice}$. All remaining ice is transferred to the rain category when $F_{i,liq}$>0.99.

M90 developed an equation for the melting behavior of an individual non-spherical unrimed ice crystal based on observations (Fujiyoshi 1986), using the thermodynamic model of Mason (1956). Two processes control the melting rate. The first is latent heating/cooling associated with condensation/evaporation of water vapor at the particle's surface. The second is heat transfer from the environment to the particle surface, and from the surface to the embedded ice core. During the melting process, it is assumed that the particle surface temperature is T_0 = 273.15 K. The change of ice core mass from melting is

$$\left.\frac{dm_{ice}}{dt}\right|_{melting} = \frac{4\pi\, C(D_d, F_{i,liq})\, F(D_d, F_{i,liq})}{L_f} \left(D_v\, \rho_a L_e \left[q_v - q_{s,0}\right] + k_a[T - T_0]\right) \tag{1.16}$$

where D_v is the diffusivity of water vapor in air, L_f (L_e) is the latent heat of fusion (evaporation), k_a is the thermal conductivity of air, q_v is the water vapor mass mixing ratio, $q_{s,0}$ is the saturated water vapor mass mixing ratio at the surface of the particle, $C(D_d, F_{i,liq})$ is the capacitance (section 1.8; equation 1.23) and $F(D_d, F_{i,liq})$ is the ventilation coefficient (section 1.8; equation 1.24). The melting rate is treated in a simple way following most parameterizations (e.g., M90) that assumes the same ventilation coefficient and capacitance for both the latent term and the heat diffusion term in (1.16).

1.7.2 Refreezing

The refreezing process describes how the liquid water surrounding the ice core freezes when mixed-phase particles are transported to regions where T<0°C. The refreezing source/sink term ($Q_{l,frz}$) is

$$Q_{l,frz} = \int_0^{\infty} F_{i,liq} \left.\frac{dm_{tot}}{dt}\right|_{freezing} N_{0,p}\, D_p^{\mu_p} \exp(-\lambda_p D_p)\, dD_p \tag{1.17}$$

where D_p is the full mixed-phase particle diameter and $F_{i,liq} \left.\frac{dm_{tot}}{dt}\right|_{freezing}$ is the refreezing rate of a particle. $Q_{l,frz}$ is a mass transfer from $q_{i,liq}$ to $q_{i,rim}$ and the rime density of refreezing ice is assumed to be near solid bulk ice (900 kg m^{-3}), following other drop freezing process in P3_ORIG.

From Pruppacher and Klett (1997), assuming a quasi-steady state during the refreezing process and a surface particle temperature of $T_0 = 273.15$ K, the freezing rate equation is a balance between the latent heat of freezing and the conduction through the ice shell formed around the whole particle. The conduction through the ice shell is given by the conduction of heat between the surrounding air and the particle, and the heat exchange by evaporation/condensation at the particle surface

$$\left.\frac{dm_{tot}}{dt}\right|_{freezing} = \frac{-4\pi\, C(D_p, F_{i,liq})\, F(D_p, F_{i,liq})}{L_f} \left(D_v\, \rho_a L_s \left[q_v - q_{s,0}\right] + k_a[T - T_0]\right) \tag{1.18}$$

where, L_s is the latent heat of sublimation, $C(D_p, F_{i,liq})$ is the capacitance (section 1.8; equation 1.29) and $F(D_p, F_{i,liq})$ is the ventilation coefficient (section 1.8; equation 1.30).

1.7.3 Collection with liquid phase categories

It is assumed that rain ($Q_{l,coll,r}$) and cloud water ($Q_{l,coll,c}$) mass collected when $T \geq 0°C$ is transferred into $q_{i,liq}$. At $T<0°C$ and in the dry growth regime, the collected rain and cloud masses are assumed to freeze instantaneously and are transferred to $q_{i,rim}$, as in P3_ORIG (MM15). At $T<0°C$ and in the wet growth regime, calculated following Musil (1970), the total collected rain and cloud mass ($Q_{l,wgrth}$) is assumed to be a source for $q_{i,liq}$. Wet growth of hail is not the focus of the paper, however, prediction of $F_{i,liq}$ in P3_MOD presents an interesting possibility for improving the prediction of wet growth and shedding from hail.

The rain and cloud collection rates are parameterized using a collection kernel derived from the projected area and the terminal velocity relationships for rain and ice or mixed-phase particles, numerically integrated over the respective PSDs. The fall speed of cloud droplets is neglected in the kernel equation.

1.7.4 Vapor transfer

For simplicity, deposition/sublimation of ice in P3_MOD is allowed only when $F_{i,liq} = 0$ because liquid water is assumed to be distributed around the ice core when $F_{i,liq}>0$. The calculation of deposition/sublimation follows from P3_ORIG (see MM15). Note that the $F_{i,liq}$ threshold for sublimation/deposition versus condensation/evaporation processes can be modified easily in P3_MOD. For example, it could be increased to 0.2 as in Thériault and Stewart (2010). If so, then the sublimation/deposition process would be calculated using the ice core properties as for the melting process.

Vapor transfer of $q_{i,liq}$ ($Q_{l,dep}$), which represents the liquid mass of mixed-phase particles lost by evaporation or gained by condensation, is also computed with the quasi-analytic formulation for supersaturation of MM15, using liquid phase thermodynamic parameters. $Q_{l,dep}$ source/sink term when $F_{i,liq}>0$ is

$$Q_{l,dep} = \frac{A_{i,wet}\,\tau}{\tau_{i,wet}\Gamma_l} + \left(\delta_{t=0} - A_{i,wet}\tau\right)\frac{\tau}{\Delta t\,\tau_{i,wet}\Gamma_l}\left(1 - \exp\left(-\Delta t/\tau\right)\right) \tag{1.19}$$

where $\delta_{t=0}$ is the initial supersaturation, Δt is the time step and Γ_l the psychrometric correction associated with the latent heating/cooling. $A_{i,wet}$ is the change in δ due to vertical motion, turbulent mixing, and radiation. The overall supersaturation relaxation time scale in conditions when $F_{i,liq}>0$ (τ) is $\tau^{-1} = \tau_c^{-1} + \tau_r^{-1} + \tau_{i,wet}^{-1}$. The supersaturation relaxation time scale associated with mixed-phase particles ($\tau_{i,wet}$) is

$$\tau_{i,wet}^{-1} = \int_0^{\infty} 4\pi D_v \rho_a\, C(D_p, F_{i,liq})\, F(D_p, F_{i,liq})\, N_{0,p}\, D_p^{\mu_p} \exp(-\lambda_p D_p)\, dD_p \tag{1.20}$$

where τ_c and τ_r are the relaxation time scales for cloud and rain, respectively (Morrison and Grabowski 2008a). $C(D_p, F_{i,liq})$ and $F(D_p, F_{i,liq})$ are the capacitance (section 1.8; equation 1.29) and ventilation coefficient (section 1.8; equation 1.30) relationships. During the evaporation process (when $Q_{l,dep}<0$), which is computed gradually as a function of the liquid fraction, it is assumed that $N_{i,tot}$ decreases proportionally to the change in $q_{i,tot}$: $N_{l,evp} = Q_{l,dep}\, N_{i,tot}/q_{i,tot}$.

1.7.5 Shedding

Based on Rasmussen *et al.* (1984b), it is assumed that only ice particles with diameter larger than 9 mm within the PSD shed. The mass of $q_{i,liq}$ due to shedding ($Q_{l,shd}$) is given by the total integrated liquid mass of particles with D_p>9 mm within the PSD and interpolating as a function of $F_{i,rim}$, with no shedding when $F_{i,rim} = 0$ and all liquid mass (for D_p>9 mm) shed when $F_{i,rim} = 1$. The increase in the rain number mixing ratio from shedding assumes a mean raindrop diameter of 1 mm.

1.7.6 Sedimentation

The variables $q_{i,liq}$, $q_{i,tot}$, $q_{i,rim}$ and $B_{i,rim}$ use the total mass-weighted fall speed (V_m) for their sedimentation, while the number mixing ratio $N_{i,tot}$ uses the number-weighted fall speed (V_N,), given by, respectively,

$$V_m = \frac{\int_0^\infty V_t(D_p, F_{i,liq})\ m_t(D_p, F_{i,liq})\ N_{0,p}\ D_p^{\mu_p} \exp(-\lambda_p D_p)\, dD_p}{\int_0^\infty m_t(D_p, F_{i,liq})\ N_{0,p}\ D_p^{\mu_p} \exp(-\lambda_p D_p)\, dD_p} \tag{1.21}$$

$$V_N = \frac{\int_0^\infty V_t(D_p, F_{i,liq})\ N_{0,p}\ D_p^{\mu_p} \exp(-\lambda_p D_p)\, dD_p}{\int_0^\infty N_{0,p}\ D_p^{\mu_p} \exp(-\lambda_p D_p)\, dD_p} \tag{1.22}$$

$V_t(D_p, F_{i,liq})$ is given by (1.13) in section 1.3.2. An increase of both V_m and V_N occurs with increasing $F_{i,liq}$ in P3_MOD (see Fig. 1.1).

All integrations are done offline and the values are stored in lookup tables as a function of 50 values of normalized total ice mass $q_{i,tot}/N_{i,tot}$, 5 the bulk rime densities $\rho_{i,rim}$ (50, 250, 450, 650 and 900 kg m^{-3}), 4 bulk rime mass fractions $F_{i,rim}$ (0, 0.333, 0.667 and 1) and 4 bulk liquid mass fractions $F_{i,liq}$ (0, 0.333, 0.667 and 1).

1.8 Appendix : Capacitance and ventilation coefficient

1.8.1 Processes depending on the ice core properties

The capacitance $C(D_d, F_{i,liq})$ accounts for non-spherical shape of ice particles undergoing melting or deposition/sublimation. The capacitance is calculated simply by a linear interpolation based on $F_{i,liq}$ between the capacitance of an ice particle $C_d(D_d)$ when $F_{i,liq} = 0$ and that of a spherical drop $C_{liq}(D_d) = 0.5D_d$ when $F_{i,liq} = 1$, for a given D_d:

$$C(D_d, F_{i,liq}) = \left(1 - F_{i,liq}\right) C_d(D_d) + F_{i,liq}\, C_{liq}(D_d) \tag{1.23}$$

where $C_d(D_d)$ is function of the ice particle properties for each regime of the distribution as detailed in MM15.

The ventilation coefficient $F(D_d, F_{i,liq})$ for the melting calculation is also given by linear interpolation over $F_{i,liq}$ between the value for an ice particle $F_d(D_d)$ when $F_{i,liq} = 0$ from P3_ORIG and that of a liquid drop $F_{liq}(D_d)$ when $F_{i,liq} = 1$:

$$F(D_d, F_{i,liq}) = \left(1 - F_{i,liq}\right) F_d(D_d) + F_{i,liq}\, F_{liq}(D_d) \tag{1.24}$$

where $F_d(D_d)$ is (Thorpe and Mason 1966)

$$F_d(D_d) = \begin{cases} 1 & \text{if } D_d < 100\ \mu\text{m} \\ 0.65 + 0.44\, X_d & \text{if } D_d \geq 100\ \mu\text{m} \end{cases} \tag{1.25}$$

and $X_d = Sc^{1/3}\, Re_d^{1/2}$, $Re_d = V_t(D_d, F_{i,liq} = 0)\, D_d\, \rho_a / \upsilon$ is the Reynolds number, υ is the dynamic viscosity of air and Sc is the Schmidt number $Sc = \upsilon / (\rho_a D_v)$. The terminal velocity $V_t(D_d, F_{i,liq} = 0)$ follows Mitchell and Heymsfield (2005) with $F_{i,liq} = 0$, as in P3_ORIG:

$$V_t(D_d, F_{i,liq}=0)= a_1 \upsilon^{1-2b_1} \left(\frac{2g}{\rho_a}\right)^{b_1} \left(\frac{m_d(D_d)}{A_d(D_d)}\right)^{b_1} D_d^{2b_1-1}, \tag{1.26}$$

$$a_1 = c_2 \,(1 + c_1 X^{1/2})^{1/2} - 1/(X^{b_1})$$

$$b_1 = c_2 X^{1/2}/(2((1 + c_1 X^{1/2})^{1/2}\text{-}1)(1 + c_1 X^{1/2})^{1/2})$$

$$c_1 = 4/(5.83^2\; 0.6^{1/2})$$

$$c_2 = 5.83^2/4$$

$$X = 2\, g\rho_a/(\upsilon\rho_a)\; (m_d(D_d)/A_d(D_d))^{b_1}\; D_d^{2b_1-1}$$

$F_{liq}(D_d)$ is (Pruppacher and Klett 1997)

$$F_{liq}(D_d)= \begin{cases} 1 & \text{if } D_d\text{<}100\ \mu\text{m} \\ 0.78+0.28\ X_r & \text{if } D_d\geq 100\ \mu\text{m} \end{cases} \tag{1.27}$$

with $X_r = Sc^{1/3}\, Re_r^{1/2}$, $Re_r = V_t(D_d, F_{i,liq} = 1)\, D_d\, \rho_a / \upsilon$. $V_t(D_d, F_{i,liq} = 1)$ is the terminal velocity for $F_{i,liq} = 1$ and is computed using Simmel *et al.* (2002), Beard (1976) and Gunn and Kinzer (1949)

$$V_t(D_d, F_{i,liq}=1)= \begin{cases} 4579.4\ m^{2/3} & \text{if } D_d\leq 134.43\ \mu\text{m} \\ 49.62\ m^{1/3} & \text{if } D_d\text{<}1511.64\ \mu\text{m} \\ 17.32\ m^{1/6} & \text{if } D_d\text{<}3477.84\ \mu\text{m} \\ 9.17 & \text{if } D_d\text{>}3477.84\ \mu\text{m} \end{cases} \tag{1.28}$$

where $m = \pi/6\rho_{w,g}D_d^3$ and $\rho_{w,g} = 1$ g m^{-3} is the density of water.

Equations (1.23) and (1.24) are the formulations to express the capacitance and ventilation coefficient as a function of the ice core diameter, in contrast to those used in M90 that also depend on the real particle diameter. Although the capacitance and ventilation coefficient used for the latent heat term in the melting equation (1.16) should also depend on the liquid part of the particle, the melting equation is treated following most parameterizations (e.g., M90; Milbrandt and Yau 2005) that assumes the same ventilation coefficient and capacitance for both the latent heat term and the heat diffusion term in (1.16). Note also that the relationships for capacitance and ventilation coefficient differ for $F_{i,liq} = 0$ between M90 and P3 and the M90 coefficients are only for unrimed particles, which is why we use the P3 coefficients rather than M90.

1.8.2 Processes depending on properties of the entire particle

For condensation/evaporation and refreezing of mixed-phase particles with $F_{i,liq}>0$, the capacitance $C(D_p, F_{i,liq})$ is similar to (1.23) but uses the full particle diameter (D_p):

$$C(D_p, F_{i,liq})=(1-F_{i,liq})C_d(D_p)+ F_{i,liq}\, C_{liq}(D_p) \tag{1.29}$$

The ventilation coefficient $F(D_p, F_{i,liq})$ is (Thorpe and Mason 1966)

$$F(D_p, F_{i,liq})= \begin{cases} 1 & \text{if } D_p<100\ \mu m \\ 0.65+0.44\, X_p & \text{if } D_p\geq 100\ \mu m \end{cases} \tag{1.30}$$

where $X_p = Sc^{1/3}\, Re^{1/2}$, $Re = V_t(D_p, F_{i,liq})\, D_p\, \rho_a / \upsilon$ and $V_t(D_p, F_{i,liq})$ is given by (1.13), which uses D_p instead of D_d in (1.26) to (1.28).

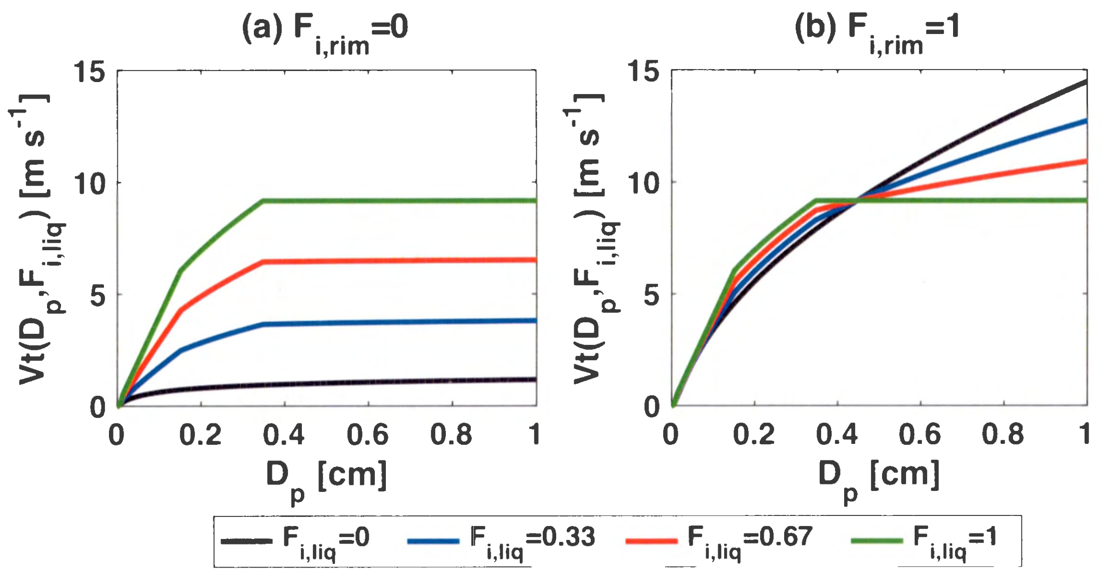

Figure 1.1 Terminal velocity of P3_MOD [$V_t(D_p, F_{i,liq})$, m s^{-1}] as a function of the full particle diameter [D_p, cm] when the bulk rime mass fraction [$F_{i,rim}$] is 0 for (a) and 1 for (b) and the bulk liquid mass fraction [$F_{i,liq}$] is 0 (black), 0.33 (blue), 0.67 (red) and 1 (green).

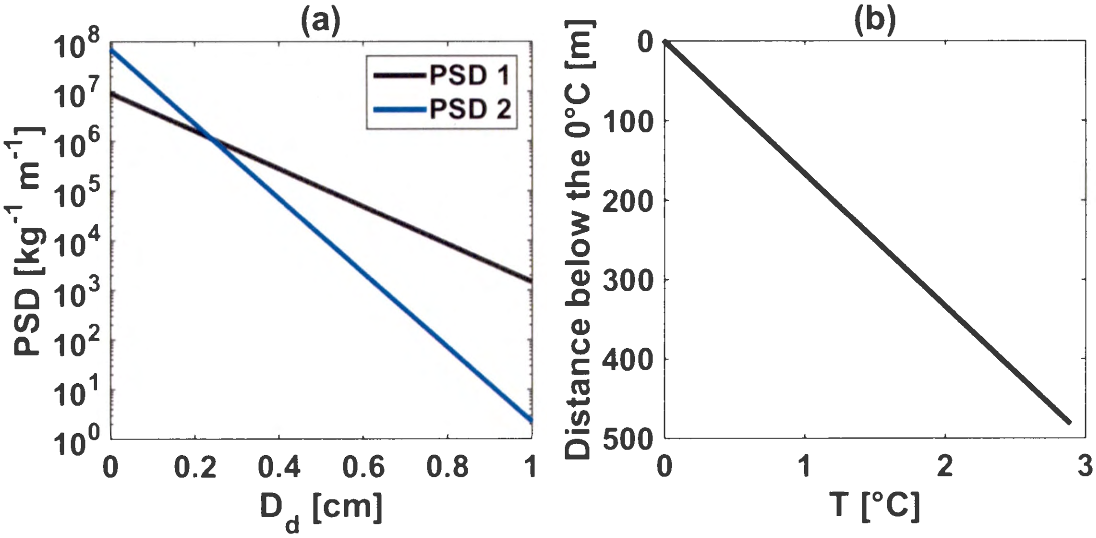

Figure 1.2 Initial conditions used for the melting rate tests comparing P3_MOD and the Lagrangian M90 model: (a) the initial particle size distribution PSD 1 (black, [kg^{-1} m^{-1}]) and PSD 2 (blue, [kg^{-1} m^{-1}]) and (b) the initial vertical profile of temperature [T, °C] below the 0°C.

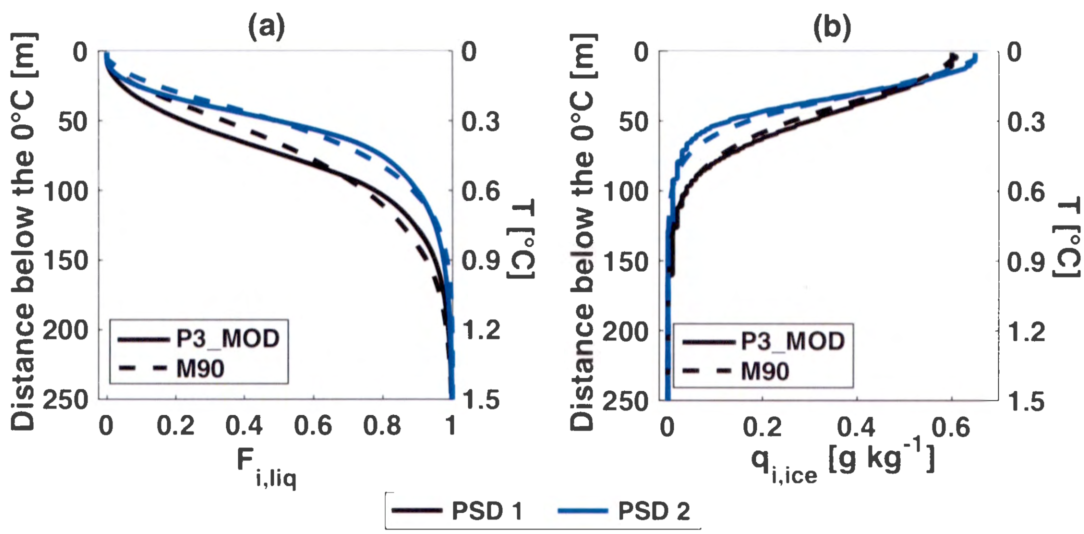

Figure 1.3 P3_MOD (solid) and the Lagrangian M90 model (dashed) variations below the 0°C of (a) the bulk liquid mass fraction [$F_{i,liq}$] and (b) the ice mass mixing ratio [$q_{i,ice}$, g kg^{-1}] for the initial PSD 1 (black) and the initial PSD 2 (blue).

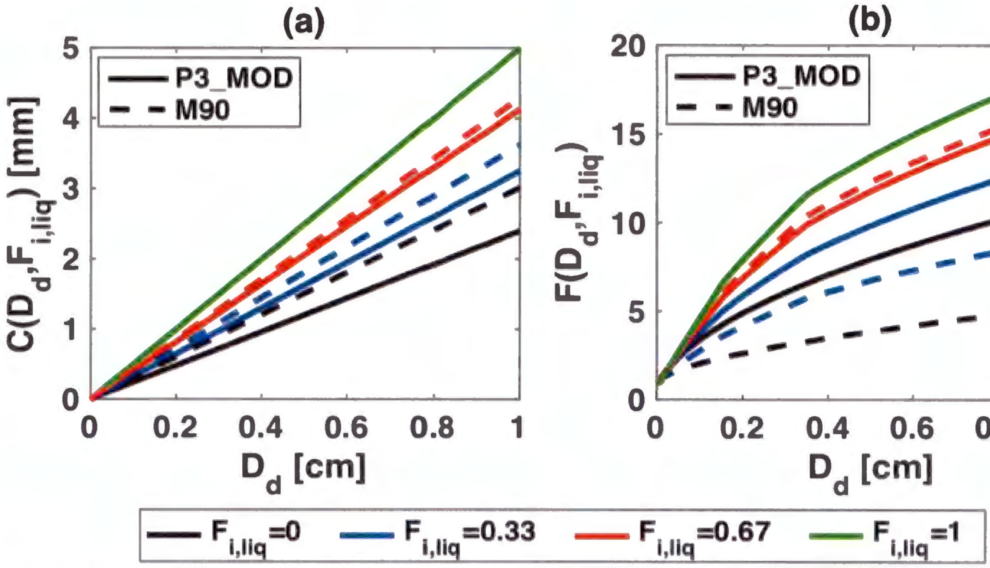

Figure 1.4 P3_MOD (solid) and the Lagrangian M90 model (dashed) (a) capacitance [$C(D_d, F_{i,liq})$, mm] and (b) ventilation coefficient [$F(D_d, F_{i,liq})$] as a function of the maximum dimension of the ice core [D_d, cm] when the bulk rime mass fraction is 0 and the bulk liquid mass fraction [$F_{i,liq}$] is 0 (black), 0.33 (blue), 0.67 (red) and 1 (green).

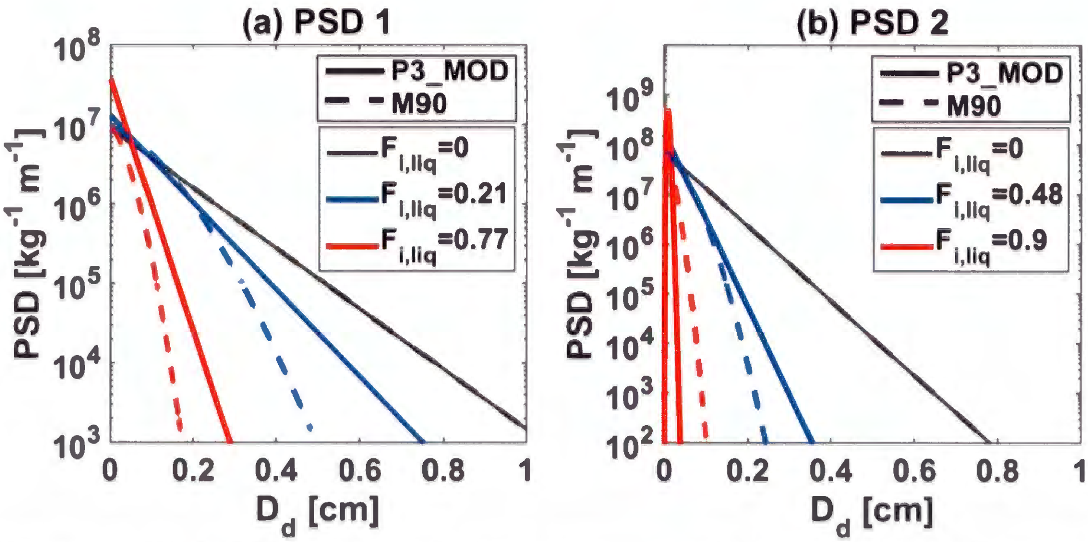

Figure 1.5 P3_MOD (solid) and the Lagrangian M90 model (dashed) vertical evolutions of the particle size distribution (PSD, [kg^{-1} m^{-1}]) below the 0°C for (a) initial PSD 1 and (b) initial PSD 2 at three different liquid mass fractions: (a) $F_{i,liq}$ = 0 (black), $F_{i,liq}$ = 0.21 (blue) and $F_{i,liq}$ = 0.77 (red), and (b) $F_{i,liq}$ = 0 (black), $F_{i,liq}$ = 0.48 (blue) and $F_{i,liq}$ = 0.9 (red). The three liquid mass fractions correspond to heights (temperatures) of 0 m (0°C), 50 m (0.3°C) and 100 m (0.6°C), respectively in P3_MOD.

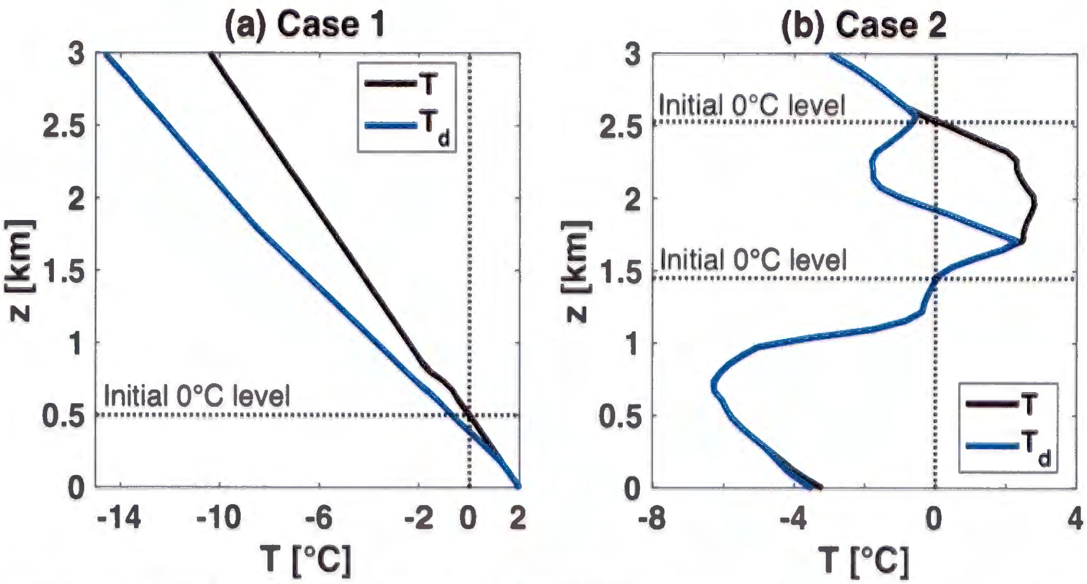

Figure 1.6 Initial vertical profiles of temperature (black, [T, °C]) and dew point temperature (blue, [T_d, °C]) for (a) Case 1 and (b) Case 2. The horizontal dotted lines show the initial 0°C levels.

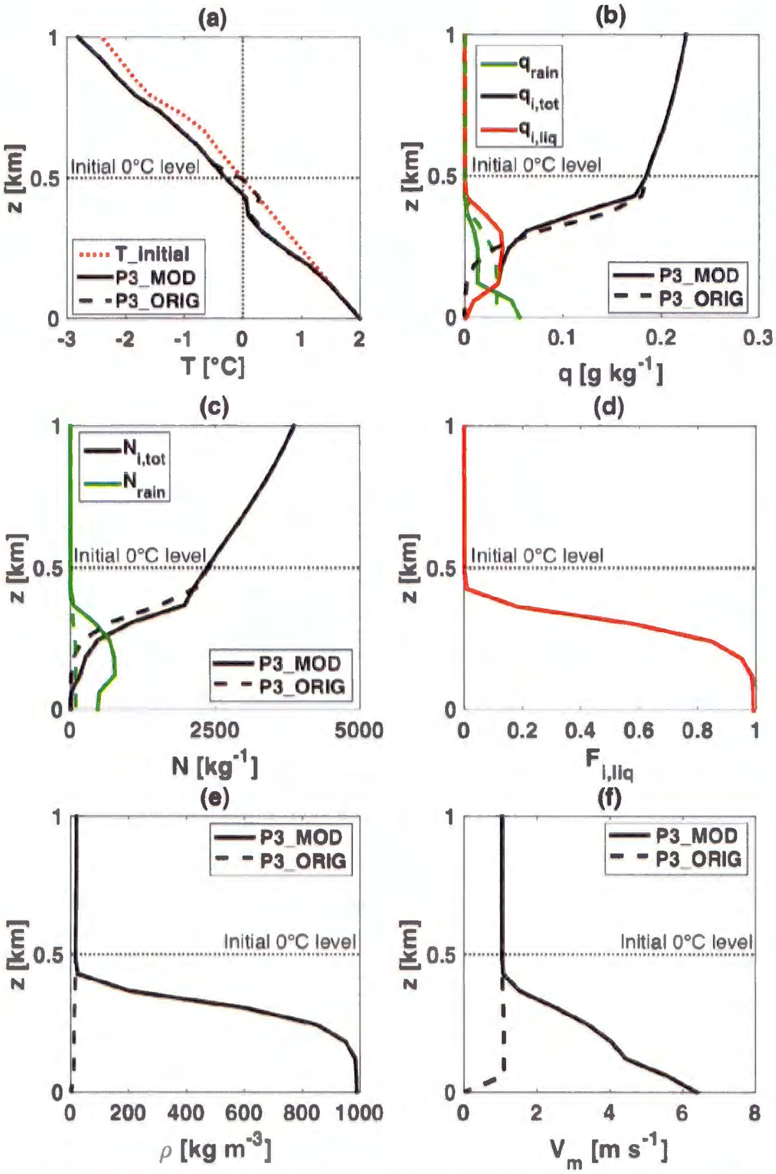

Figure 1.7 P3_MOD (solid) and P3_ORIG (dashed) vertical profiles of (a) temperature [T, °C], (b) mass mixing ratio [g kg^{-1}] of rain (green, [q_{rain}]), total ice (black, [$q_{i,tot}$]) and liquid on ice (red, [$q_{i,liq}$]), (c) number mixing ratio [N, kg^{-1}] of ice (black, [$N_{i,tot}$]) and rain (green, [N_{rain}]), (d) bulk liquid mass fraction of P3_MOD [$F_{i,liq}$], (e) mean mass-weighted density [ρ, kg m^{-3}], and (f) mean mass-weighted fall speed [V_m, m s^{-1}] produced at t = 90 min. The red dotted line in (a) shows the initial profile of temperature [T_initial, °C]. The horizontal dotted lines show the initial 0°C levels. The rime mass fraction at the model top is 0 for both P3_MOD and P3_ORIG.

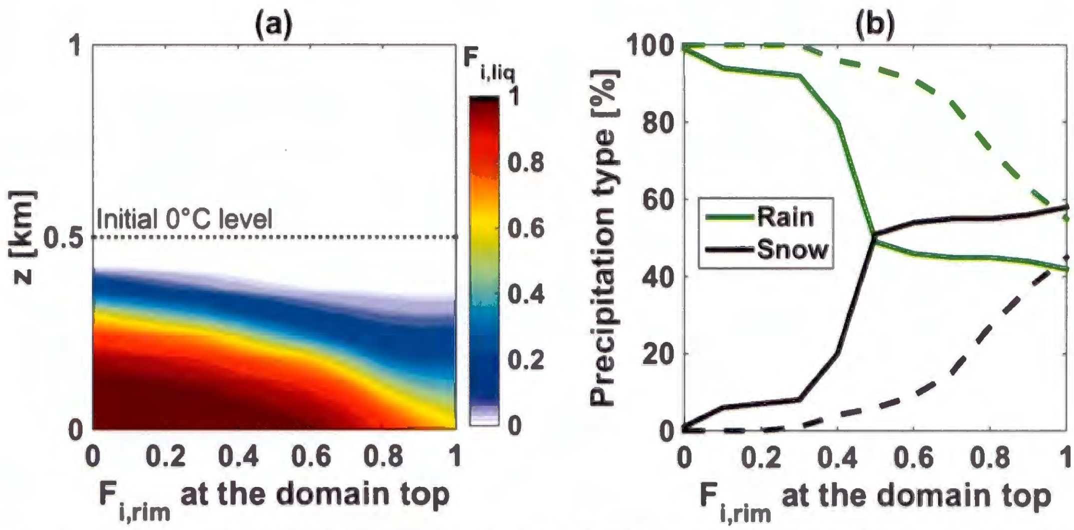

Figure 1.8 (a) Vertical evolution of the bulk liquid mass fraction (colors, [$F_{i,liq}$]) and (b) P3_MOD (solid) and P3_ORIG (dashed) surface precipitation type relative to the total surface precipitation [in %] of ice (black) and rain (green) produced at t = 90 min as a function of the rime mass fraction [$F_{i,rim}$] at the domain top. The horizontal dotted line in (a) shows the initial 0°C level.

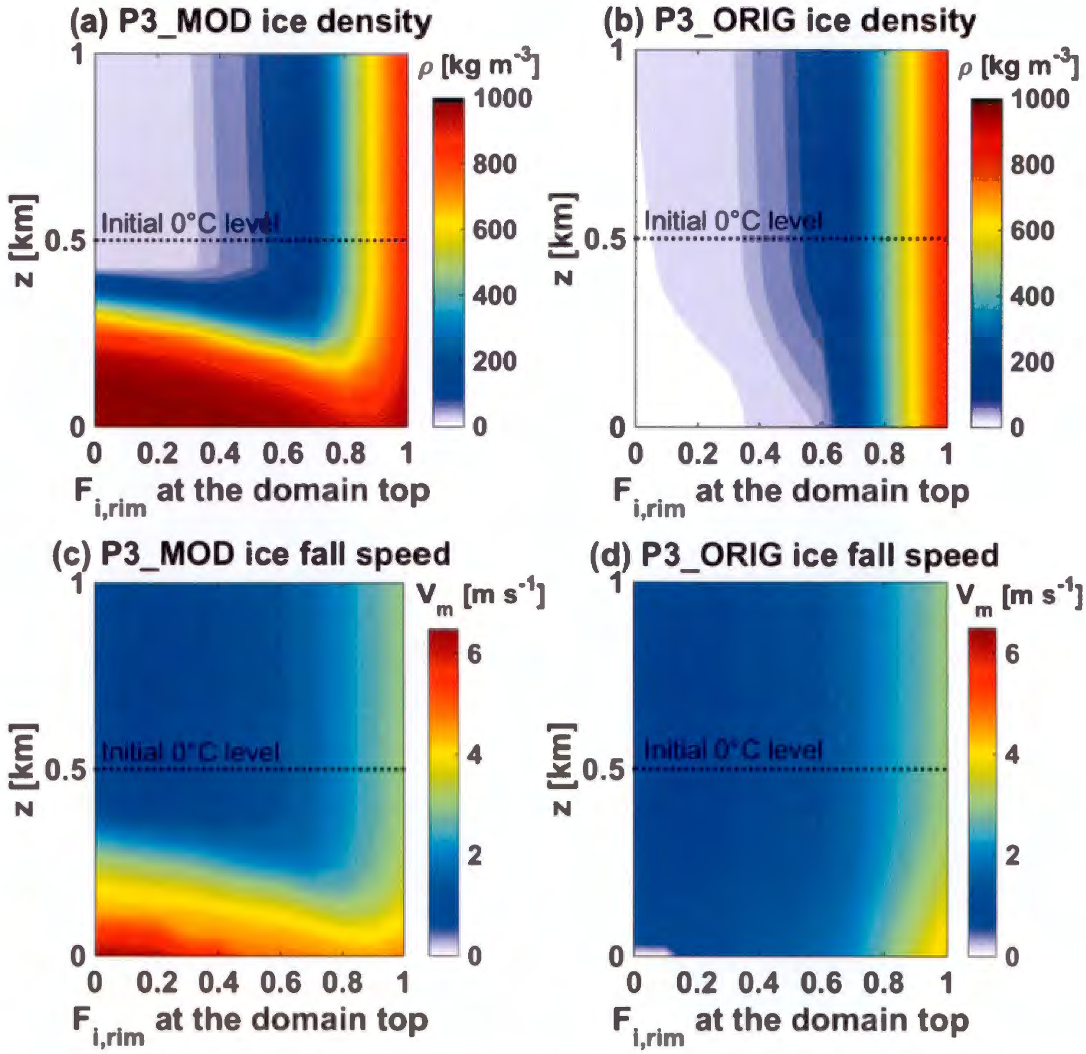

Figure 1.9 (a), (c) P3_MOD and (b), (d) P3_ORIG vertical evolutions of (a)-(b) the mean mass-weighted bulk density [ρ, kg m^{-3}] and (c)-(d) the mean mass-weighted fall speed [V_m, m s^{-1}] at t = 90 min as a function of the rime mass fraction [$F_{i,rim}$] at the domain top. The horizontal dotted lines show the initial 0°C levels.

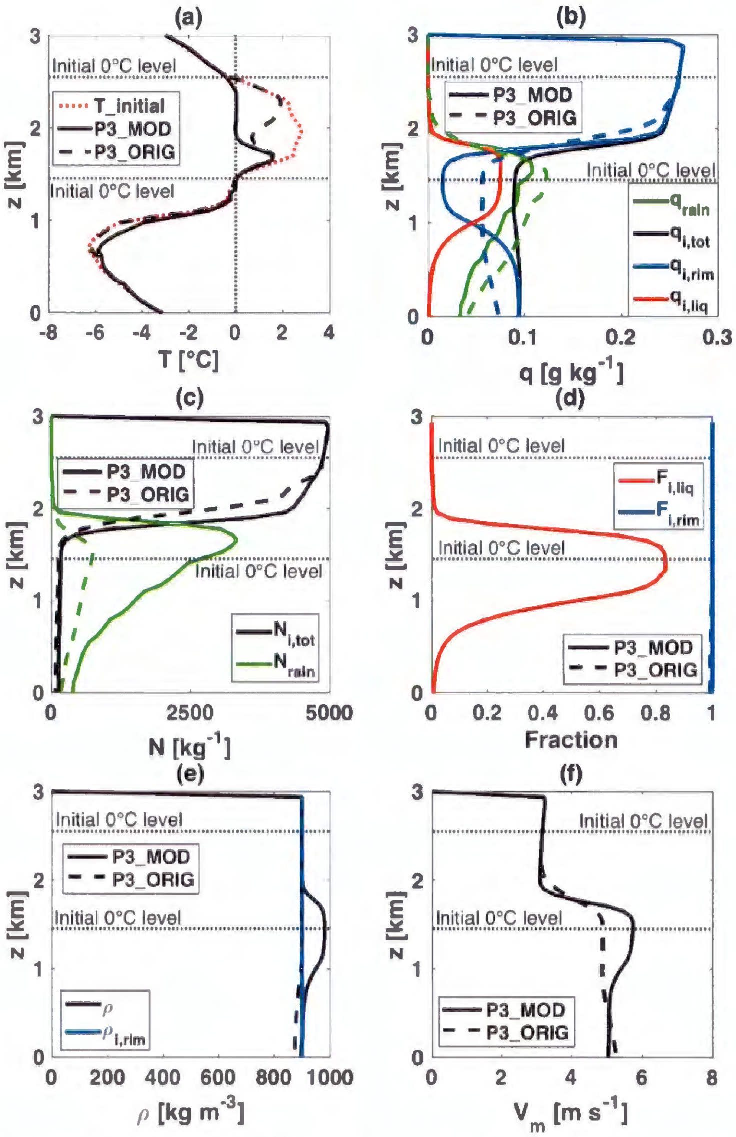

Figure 1.10 P3_MOD (solid) and P3_ORIG (dashed) vertical profiles of (a) temperature [T, °C], (b) mass mixing ratio [g kg^{-1}] of rain (green, [q_{rain}]), total ice (black, [$q_{i,tot}$]), rime on ice (blue, [$q_{i,rim}$]) and liquid on ice (red, [$q_{i,liq}$]), (c) number mixing ratio [N, kg^{-1}] of ice (black, [$N_{i,tot}$]) and rain (green, [N_{rain}]), (d) bulk liquid (red, [$F_{i,liq,}$]) and rime (blue, [$F_{i,rim}$]) mass fractions, (e) mean mass-weighted density (black, [ρ, kg m^{-3}]) and bulk rime density (blue, [$\rho_{i,rim}$, kg m^{-3}]), and (f) mean mass-weighted fall speed [V_m, m s^{-1}] produced at t = 90 min. The red dotted line in (a) shows the initial profile of temperature [T_initial, °C]. The horizontal dotted lines show the initial 0°C levels. The rime mass fraction at the domain top is 1 for both P3_MOD and P3_ORIG.

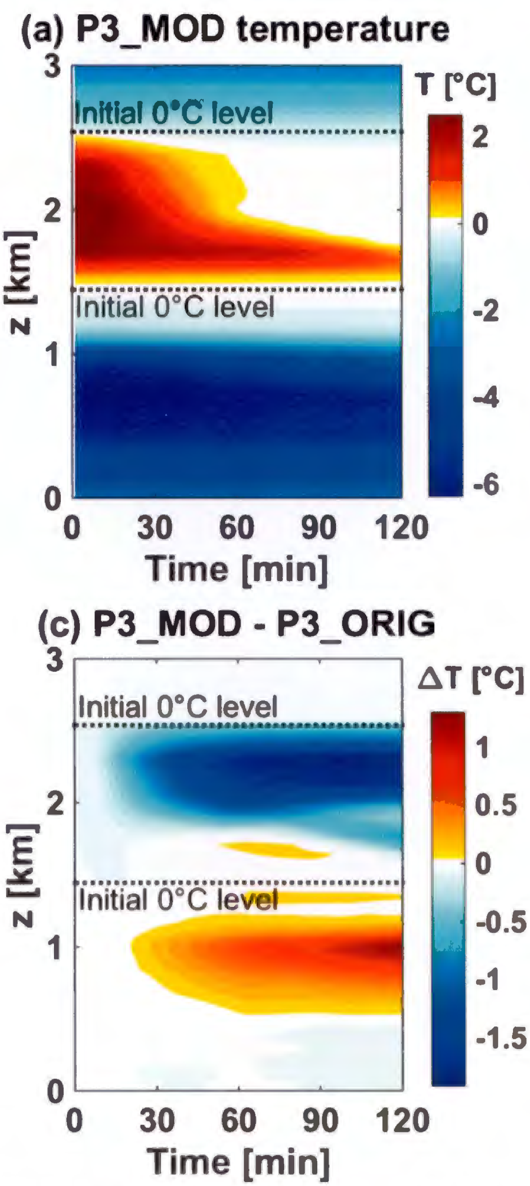

Figure 1.11 Temporal evolution of the vertical profiles of (a) P3_MOD temperature [T, °C], (b) P3_ORIG temperature [T, °C] and (c) P3_MOD–P3_ORIG temperature [ΔT, °C]. The horizontal dotted lines show the initial 0°C levels. The rime mass fraction at the domain top is 1 for both P3_MOD and P3_ORIG.

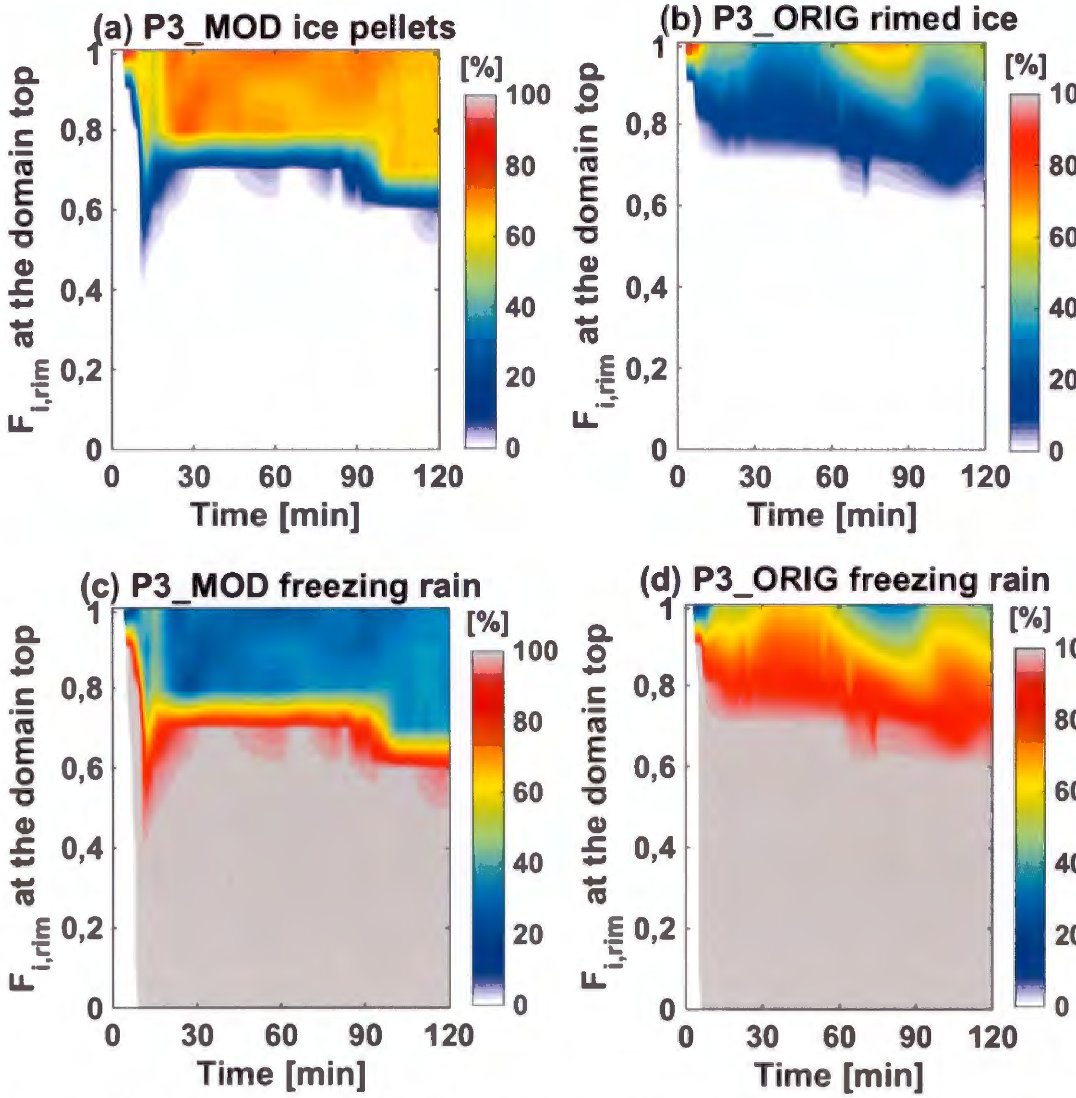

Figure 1.12 Temporal evolution of the surface precipitation type relative to the total surface precipitation [in %] of (a) P3_MOD ice pellets, (b) P3_ORIG rimed ice, (c) P3_MOD freezing rain and (d) P3_ORIG freezing rain as a function of the initial rime mass fraction [$F_{i,rim}$] at the domain top.

CHAPITRE II

IMPACTS OF PREDICTING THE LIQUID FRACTION ON MIXED-PHASE PARTICLES IN SIMULATIONS OF THE PRECIPITATION TYPES PRODUCED DURING THE 1998 ICE STORM

Submitted to *Monthly Weather Review*. The detailed reference is:

Cholette, M., Thériault, J.M., Morrison, H. and Milbrandt, J.A. (2019). Impacts of predicting the liquid fraction on mixed-phase particles in simulations of the precipitation types produced during the 1998 Ice Storm. *Submitted to Monthly Weather Review*.

Abstract

Prediction of the liquid fraction on mixed-phase particles has been recently added to the Predicted Particle Properties (P3) microphysics scheme. Mixed-phase particles are necessary to simulate key microphysical processes leading to winter precipitation types, such as ice pellets and freezing rain. To illustrate the impacts of predicting the bulk liquid fraction, the 1998 Ice Storm is simulated using the Weather Research and Forecasting (WRF) model with the modified and original versions of P3. The focus is on the comparison of simulated accumulated precipitation type characteristics between the two simulations. It is found that the parameterization of partial melting produces higher mass and number concentration mixing ratios of rain when the liquid fraction is predicted. This leads to smaller mean mass-weighted diameter of rain particles reaching the refreezing layer and the surface as well as a decrease in the freezing rain surface accumulation by up to 25 mm in some regions compared to when no liquid fraction is predicted. The increase in the fall speed and density and the decrease of the ice diameter during partial melting combined with the parameterization of the refreezing process lead to generally higher total solid surface precipitation rates and an increase of solid precipitation accumulations, in particular in regions of ice pellets accumulation compared to when no liquid fraction is predicted. Overall, the simulation of mixed-phase particles impacts the vertical and spatial distributions and properties of precipitation. This is a step forward in a better understanding of the processes producing many types of precipitation during a winter storm at near 0°C.

2.1 Introduction

During cold seasons, several types of precipitation such as snow, wet snow, ice pellets, freezing rain and rain can reach the surface when the temperatures are near 0°C (Stewart 1985; Stewart and King 1987; Stewart and King 1990; Stewart 1992; Stewart *et al.* 2015). Wet snow and freezing rain can lead to ice accumulation on surfaces causing major power outages, interruptions to land and air transportations, damage to vegetation and injuries to people (Lecompte *et al.* 1998; King and Laplante 2005; Chang *et al.* 2007; Kringlebotn Nygaard *et al.* 2013). An example is the 5–9 January 1998 Ice Storm during which snow, ice pellets and freezing rain fell over a widespread area in the northeastern United States and the eastern Canadian provinces. Nearly 100 mm of freezing rain has been accumulated at the surface in southern Quebec. This event is considered to be one of the costliest natural disasters in Canadian history (Lecompte *et al.* 1998).

Many types of precipitation may form while falling through a typical temperature profile composed of a warm layer aloft (T>0°C) and cold layer (T<0°C) below it, near the surface. While falling through the melting layer aloft, solid precipitation particles melt partially or completely. If they melt only partially upon reaching the top of the refreezing layer, the remaining ice fraction within the particles initiates freezing to produce ice pellets. In contrast, if particles melt completely, supercooled drops may not refreeze before reaching the surface, producing freezing rain. Supercooled drops in the refreezing layer can also interact with locally produced ice crystals to initiate freezing, which also produces ice pellets (Hallett and Mossop 1974). This process can reduce freezing rain at the surface (Carmichael *et al.* 2011; Barszcz *et al.* 2018).

Accurate prediction of freezing precipitations is challenging in numerical weather prediction (NWP) models because it involves the parameterization of mixed-phase particles formed when the temperatures are near 0°C (Frick *et al.* 2013). Main challenges are associated with the differentiation of the surface precipitation and their transition (Ralph *et al.* 2005; Reeves *et al.* 2014) as well as their validation with observations (Reeves 2016). The various local and synoptic environmental conditions of winter storms account for several feedback mechanisms that become important for the precipitation types forecasting (e.g., Rauber *et al.* 1994; Ramos da Silva *et al.* 2006; Petrolito 2005; Descurieux 2010; Hosek *et al.* 2011; Finch 2011; Kumjian and Schenkman 2014; Arnott and Chamberlain 2014). Small errors in temperature and humidity fields can lead to an incorrect prediction of the surface precipitation type (Thériault *et al.* 2010; Frick *et al.* 2013). Recently, there have been more efforts to improve forecasting of winter precipitation types, such as freezing rain and ice pellets (e.g., Hux *et al.* 2001; Cheng *et al.* 2004; Milbrandt *et al.* 2012; Kringlebotn Nygaard *et al.* 2013; Forbes *et al.* 2014; Benjamin *et al.* 2016; Ikeda *et al.* 2017; Thielke 2018; Gascón *et al.* 2018). However, most of these studies used diagnostic methods to determine the surface precipitation types and not the explicit prediction of mixed-phase particles.

To parameterize microphysical processes leading to freezing rain and ice pellets, it is necessary to predict partial melting of ice particles. Typically, hydrometeors composed of only solid (i.e., bulk snow, hail, graupel, cloud ice) and liquid (i.e., rain) are represented in most bulk microphysics schemes (e.g., Milbrandt and Yau 2005; Thompson *et al.* 2008; Morrison and Milbrandt 2015). The melted mass of solid hydrometeors is converted immediately to rain, leading to a sharp increase in fall speed (from ~1 m/s to ~5 m/s), which impacts the distributions of latent heating and the trajectories of precipitation (Henson *et al.* 2011). Moreover, gradual refreezing is not allowed in most schemes. Freezing is assumed to occur instantaneously when an ice nucleus is activated, whereas it is a gradual process as for melting (e.g., Hindmarsh *et al.* 2003; Gibson and Stewart 2007; Nagumo *et al.* 2019).

The explicit representation of mixed-phase particles involves tracking the bulk liquid fraction ($F_{i,liq}$, all symbols are defined in the list of symbols) of ice in a bulk microphysics scheme in time and space. $F_{i,liq}$ represents the liquid mass proportion of the mixed-phase particle distribution and is mainly driven by phase changes and interactions among particles. To predict $F_{i,liq}$, the liquid mass mixing ratio on ice particles ($q_{i,liq}$) must be included as a prognostic variable in the scheme. $q_{i,liq}$ is an extensive, conserved quantity that can be advected and diffused, whereas $F_{i,liq}$ is not. $F_{i,liq}$ is then calculated as the ratio of $q_{i,liq}$ and the total ($q_{i,tot}$) mass mixing ratio. Cholette *et al.* (2019) added $q_{i,liq}$ in the Predicted Particle Properties (P3) bulk microphysics scheme of Morrison and Milbrandt (2015) and Milbrandt and Morrison (2016). The P3 approach uses one "free" ice category instead of many separated solid categories. Several physical properties, such as the mean density (ρ), the rime density ($\rho_{i,rim}$), the mean dimension (D_m) and the rime mass fraction ($F_{i,rim}$), are predicted. The prediction of $F_{i,liq}$ in P3 was tested using a one-dimensional cloud model in Cholette *et al.* (2019).

Given that precipitation at near 0°C can lead to hazardous conditions, the objective is to show the impacts of predicting $F_{i,liq}$ in simulations of the precipitation types produced during a winter storm. To address this, high-resolution numerical simulations of the 1998 Ice Storm are conducted using both the modified P3 with the predicted $F_{i,liq}$ (Cholette *et al.* 2019) and the original P3 scheme (Milbrandt and Morrison 2016; Morrison and Milbrandt 2015). This particular storm is chosen because it is well documented (Laflamme and Périard 1998; Lecompte *et al.* 1998; Milton and Bourque 1999; Cober *et al.* 2001; Gyakum and Roebber 2001; Roebber and Gyakum 2003; Henson *et al.* 2007; Henson *et al.* 2011). The main focus is on the similarities and the differences in microphysical processes parameterized and simulated precipitation types with and without the predicted $F_{i,liq}$.

This paper is organized as follows. Section 2.2 describes the experimental design including the model configuration and the differences in the P3 schemes with and without $F_{i,liq}$. Section 2.3 gives an overview of the 1998 Ice Storm and the simulated precipitation types. Section 2.4 investigates the impacts of predicting $F_{i,liq}$ in simulated precipitation types, in particular freezing rain. Section 2.5 presents the conclusions.

2.2 Experimental Design

2.2.1 Model configuration

This study uses the Weather Research and Forecasting (WRF) model version 3.9.1.1 (Skamarock and Klemp 2008). WRF is a non-hydrostatic compressible atmospheric model. The domain of simulation, shown in Fig. 2.1, covers the region of southern Quebec extending from Lake Ontario to almost all of New Brunswick. It has 352 × 352 horizontal grid points and 3 km horizontal grid spacing. The red square in Fig. 2.1 shows the analysis domain which accounts for the spatial spinup of fine scales (e.g., Matte *et al.* 2017). The initial and lateral boundary conditions are provided by the North American Regional Reanalysis (NARR; Mesinger *et al.* 2006). This dataset is available every 3 h over North America at 32 km horizontal grid spacing. There are 56 vertical levels with a vertical grid spacing varying from 60–320 m in the first 2 km and from 320–340 m between 2 km and 16 km. The simulated period is from 0600 UTC 4 January 1998 to 0600 UTC 10 January 1998. The time step is 10 s and the model outputs are stored every 30 min.

Physics parameterizations include radiation, planetary boundary layer/turbulent mixing, and surface processes. Short-wave and long-wave radiation are calculated using the General Circulation Model version of the Rapid Radiative Transfer Model (Iacono *et al.* 2008) with a 10 s radiation time step. The Yonsei University nonlocal planetary boundary layer scheme of Hong *et al.* (2006) is employed. Surface processes are calculated using the 5-layers thermal diffusion scheme of Dudhia (1996). Two simulations have been performed using the Predicted Particle Properties bulk microphysics scheme (P3). The first simulation uses the original P3 scheme (Morrison and Milbrandt 2015), hereafter referred as P3_ORIG. The second simulation uses the modified P3 scheme including the predicted $F_{i,liq}$ (Cholette *et al.* 2019), hereafter referred as P3_MOD.

2.2.2 P3_MOD and P3_ORIG

This section summarizes the main differences between P3_MOD and P3_ORIG. More details can be found in Morrison and Milbrandt (2015) for P3_ORIG and in Cholette *et al.* (2019) for P3_MOD. Both schemes have two liquid categories: cloud and rain. The solid category is parameterized differently compared to most bulk microphysics schemes. Similar to Morrison and Grabowski (2008b), P3 evolves particle properties and bulk ice type for "free" categories using four prognostic variables per ice category. In contrast, most bulk schemes separate solid hydrometeors into categories corresponding to fixed ice types (e.g., snow, graupel and hail) and use artificially constrained conversions between the solid categories. P3 can include more than one ice category as detailed in Milbrandt and Morrison (2016), but the single ice category is used here. The P3_ORIG ice category four prognostic variables are: the total ice mass ($q_{i,tot}$ in kg kg^{-1}), the total number ($N_{i,tot}$ in kg^{-1}), the rime mass ($q_{i,rim}$ in kg kg^{-1}) and the rime volume ($B_{i,rim}$ in m^3 kg^{-1}) mixing ratios. P3_MOD has a fifth prognostic variable, the liquid on ice mass mixing ratio ($q_{i,liq}$ in kg kg^{-1}). Hence, the total ice mass mixing ratio is $q_{i,tot} = q_{i,rim} + q_{i,dep}$ in P3_ORIG and $q_{i,tot} = q_{i,rim} + q_{i,dep} + q_{i,liq}$ in P3_MOD, where $q_{i,dep}$ is the mass mixing ratio of vapor deposition growth. Several bulk properties, including the rime and liquid (for P3_MOD) mass fractions, the bulk density, the bulk rime density, the mean size, and the mean number and mass-weighted fall speeds are predicted from the conserved prognostic variables. The bulk rime mass fraction is

$F_{i,rim} = q_{i,rim}/(q_{i,rim} + q_{i,dep})$ and the liquid mass fraction of P3_MOD is $F_{i,liq} = q_{i,liq}/(q_{i,rim} + q_{i,dep} + q_{i,liq})$. All symbols are defined in the list of symbols.

Four regimes of ice particles give the particle size distribution (PSD) in P3 (see Morrison and Milbrandt 2015 Fig. 1 and Dietlicher *et al.* 2018 Fig. 1 for details). These are small spherical ice, unrimed non-spherical ice particles, partially rimed non-spherical ice particles and completely filled with rime spherical particles. The four regimes are smoothly separated by three threshold diameters that vary with the prognostic variables. Particle-diameter characteristics, such as mass, projected area, terminal velocity, capacitance, and ventilation coefficient relationships are calculated for each ice regime and depend on the four prognostic ice variables. In P3_MOD, these relationships also depend on $q_{i,liq}$.

The main assumptions for the implementation of $F_{i,liq}$ in P3_MOD are summarized as follows. First, the liquid fraction of particles does not vary with size and is given by the bulk liquid mass fraction ($F_{i,liq}$). Therefore, both the rime mass and liquid mass fractions are constant with sizes over a given PSD. Second, it is assumed that the liquid water in P3_MOD is uniformly distributed around an ice core. For simplicity and due to lack of observations, ice cores are assumed to have the same properties (mass, projected area, capacitance, ventilation coefficient and so on) as in P3_ORIG. Basically, it is assumed that some processes, such as melting, depend on the ice core properties while other processes, such as refreezing, depend on the whole mixed-phase particle.

The differences between P3_MOD and P3_ORIG in formulations of microphysical processes are summarized as follows. First, the melting source/sink term is divided into two terms in P3_MOD. The first term is the melted water transferred into rain from the melting of small spherical ice particles (Rasmussen *et al.* 1984a) and the second term is the melted water accumulated on ice (i.e., into $q_{i,liq}$) (Fujiyoshi 1986). In P3_ORIG, all the melted water produced in one time step is instantaneously transferred to rain mass (q_{rain}). A scaled number for rain source number mass mixing ratio (N_{rain}) of 0.2 is applied in P3_ORIG to account for rapid evaporation of small melting ice particles. No such scaling is applied in P3_MOD since evaporation/condensation of melting ice is a new process. When $F_{i,liq}$>0.99 in P3_MOD, all the remaining ice mass and number are transferred to rain.

Second, the refreezing process in P3_MOD gives the rate of accumulated water that refreeze on the particle when mixed-phase particles enter cold layers (T<0°C) (Pruppacher and Klett 1997). This process is not included in P3_ORIG. Third, at T>0°C, the mass of rain and cloud droplets that collides with ice is shed assuming a shed drop of 1 mm following Rasmussen *et al.* (1984b) in P3_ORIG, whereas, in P3_MOD, the collected liquid mass is accumulated in $q_{i,liq}$. Fourth, at T<0°C and in wet growth situations in P3_ORIG, not all of the collected liquid water is frozen some fraction is shed instead (Musil 1970). When wet growth conditions are diagnosed in P3_MOD, the collected rain and cloud mass is transferred to $q_{i,liq}$. Fifth, in P3_ORIG, shedding occurs with the collection and the wet growth processes when T<0°C while shedding from melting is not included. In P3_MOD, the total shedding from both melting and wet growth when $F_{i,rim}$>0 assumes that only particles with diameters >9 mm within the PSD are allowed to shed (Rasmussen *et al.* 1984b). Sixth, for simplicity, the deposition/sublimation in P3_MOD is allowed only when $F_{i,liq} = 0$ because liquid water is distributed evenly around the ice core. Otherwise, the particle would undergo condensation/evaporation of the liquid mass mixing ratio $q_{i,liq}$. Note that the sublimation/deposition and the condensation/evaporation processes can occur at any temperature in P3_MOD compared to P3_ORIG. In the latter the sublimation/deposition of ice is allowed only at T<0°C and the condensation/evaporation of melting particles is not included.

Lastly, the variables $q_{i,liq}$, $q_{i,tot}$, $q_{i,rim}$ and $B_{i,rim}$ use the total mass-weighted fall speed for their sedimentation, while $N_{i,tot}$ uses the number-weighted fall speed in both

P3_ORIG and P3_MOD. However, an increase in both fall speeds is expected with the increasing $F_{i,liq}$ in P3_MOD compared to P3_ORIG associated with the terminal velocity-diameter relationship (Cholette *et al.* 2019). The diagnostic variables, such as the mean mass-weighted density, the mean mass-weighted diameter, the reflectivity and the ice effective radius as well as the self-aggregation process are calculated using the $F_{i,liq}$ dependence in P3_MOD (Cholette *et al.* 2019). This means that the PSD accounts for both the dry and the liquid component of the ice. In P3_ORIG, these variables are computed only with the dry ice properties.

2.2.3 Result analysis

The impacts of predicting the liquid fraction in simulated precipitation types are investigated in a systematic manner. First, a description of the 1998 Ice storm is given including a brief description of the precipitation amounts and types produced only by P3_MOD. Second, a comparison with some observations showing that the model reproduced relatively well the spatial and vertical structures of the storm and the precipitation types over southern Quebec is given in the Appendix (section 2.6). Third, a more thorough comparison between P3_MOD and P3_ORIG is conducted. To do so, four sub-regions of 3600 km^2 into the domain of interest are defined. These are mainly chosen based on the different amounts and types of precipitation at the surface. Two sub-regions are located where the total accumulated freezing rain in P3_ORIG is >50 mm and the two others are located where the total solid accumulation in P3_ORIG is >25 mm. The comparison between P3_MOD and P3_ORIG is then conducted within those sub-regions. Lastly, the precipitation characteristics aloft, such as the mass mixing ratios, are analyzed with two cross-sections over the sub-regions.

To differentiate between ice particles, ice pellets and wet snow, we applied some assumptions. Ice pellets in P3_MOD are solid precipitation when the liquid fraction aloft is >0 and temperature of the lowest model level is <0°C. Wet snow is solid precipitation when the lowest model level liquid fraction is >0. Note that wet snow is a general terminology for wet ice, because ice can include snow, partially rimed ice and fully rimed ice. Also, the validation of those precipitation types with observation is difficult because ice pellets are usually reported with a mixture of snow or freezing rain and wet snow is reported as snow.

2.3 Case overview

2.3.1 Meteorological overview of the 1998 Ice Storm

The storm was from 4–10 January 1998. The successive passages of low-pressure systems and the quasi-stationary front extending from southern Ontario to the Maritime Provinces led to relatively warm and moist air flow aloft producing favourable conditions for freezing rain and ice pellets (Roebber and Gyakum 2003). The accumulated freezing rain extended from southeastern Ontario to Nova Scotia, including southern Quebec, Maine and New Brunswick. However, the maximum accumulated freezing rain was located in southern Quebec (110 mm at Acton-Vale). The accumulated precipitation types of Milton and Bourque (1999) (circles in Fig. 2.1) are shown in Fig. 2.2. This includes the total accumulated precipitation (Fig. 2.2a), liquid (rain and freezing rain; Fig. 2.2b), solid (snow and ice pellets; Fig. 2.2c) and freezing rain (Fig. 2.2d). Observed solid precipitation does not separate snow and ice pellets and a 10 cm-to-1 mm ratio is used (Milton and Bourque 1999). Near up to 120 mm of total precipitation and 100 mm of freezing rain accumulated over southern Quebec. The maxima of solid and freezing rain accumulations were located near Quebec City (YQB) and south-east Montreal (YUL), respectively.

Two periods of significant freezing rain accumulation occurred in southern Quebec (Henson *et al.* 2011). Figure 2.3 shows 12-hourly accumulated freezing rain (from Milton and Bourque 1999) as well as hourly observed ice pellets (data from http://weather.uwyo.edu/) at three surface stations within the St. Lawrence River Valley (SLRV) and at Ottawa (YOW). Note that observed hourly ice pellets were generally mixed with other precipitation types such as snow, freezing rain or freezing drizzle. The first icing period was from 0000 UTC 5 January to 2000 UTC 6 January and the second one was longer, from 1800 UTC 7 January to 0000 UTC 10 January. The precipitation type during the first icing period was mainly freezing rain, whereas during the second icing period, it was more of a mixture of freezing rain and ice pellets (Henson *et al.* 2011), in particular for northern stations of Mirabel (YMX) and Montreal (YUL). The second icing period was characterized by a more widespread region of precipitation and higher precipitation accumulations including freezing rain, in particular at YOW and YHU (Roebber and Gyakum 2003). For example, at YHU, 36 mm of freezing rain were accumulated during the first period, while 44 mm were accumulated during the second icing period (Fig. 2.3a).

Different synoptic conditions characterized the two icing periods. The first icing period was associated with frontogenesis within a baroclinic zone established with the approach of a trough whereas the baroclinic zone was associated with a well-developed cyclone during the second icing period (Roebber and Gyakum 2003). The low-level temperature in southern Quebec remained below 0°C during the two icing periods as shown in Figs. 2.4a-b. For both icing periods, northeasterly low-level winds contributed to maintaining the cold air near the surface in the SLRV and the Ottawa River Valley (Figs. 2.4a-b) (Roebber and Gyakum 2003; Milton and Bourque 1999). Windrose diagrams show that 10-m horizontal winds were always north-northeasterly and northeast-easterly during the storm at YUL and YQB, respectively (Fig. 2.4c-d) and stronger at YQB than at YUL. Low-level winds were ~1 m s^{-1} to 3 m s^{-1} higher during the second icing period compared to the first icing period (Henson *et al.* 2011). Also, a wind flow from the south at high elevation was obtained during the second icing period but that was not observed for the first icing period (Henson *et al.* 2011). Lastly, from Henson *et al.* (2011), the height of the upper and lower 0°C isotherms were lower during the first icing period compared to the second one. The thickness of the melting layer aloft during the first icing period was nearly constant while it varied during the second icing period.

2.3.2 Simulated precipitation types

To give a description of the precipitation amounts and types produced during the simulation of the storm, only the results from P3_MOD are discussed (Fig 2.5). The intensities and locations of the maxima total accumulated precipitation (Fig. 2.5a), solid precipitation (Fig. 2.5c), liquid precipitation (Fig. 2.5b) and freezing rain (Fig. 2.5g) are mainly similar to observations of Fig. 2.2 with some differences. The locations and maximum of total, solid and liquid accumulated precipitations are well reproduced by P3_MOD. The location of freezing rain maximum accumulation is shifted southwest compared to observation, but the maximum amount is well captured (113 mm). Maximum amounts of snow (Fig. 2.5d) are located east YQB and north of Maine, while maximum amounts of rain (Fig. 2.5h) are located near Quebec/Vermont border and into the Appalachians (NY).

Ice pellets (Fig. 2.5f) and wet snow (Fig. 2.5e) are also produced during the storm. First, a widespread region of ice pellets is being simulated during the storm. The maximum amount of ice pellets (~35 mm) is located ~60 km north of YUL. Only ~0.2 mm of ice pellets accumulated at YUL. Second, the maximum amount of wet snow is (~10 mm) located near west of YOW and was mainly accumulated during the second icing period.

Wet snow also occurred south-east Quebec and into the Green Mountains (VT) at different times but mainly at the beginning and the end of the simulated period.

Lastly, the amounts and types of precipitation differ during the two icing periods. First, accumulated precipitation is lower during the first icing period compared to the second one. For example, at YHU, 33 mm of freezing rain accumulated during the first icing period and 47 mm during the second one. Second, over the analysis domain, liquid, rain, freezing rain (Fig. 2.6a) and ice pellets (Fig. 2.6b) precipitation rates are higher during the second icing period compared to the first period. Third, the solid precipitation rates (Fig. 2.6b) are similar between the two icing periods, but generally lower compared to liquid precipitation rates. Fourth, ice pellets occurred at the beginning and the end of the first icing period, and mostly during the second icing period (Fig. 2.6b). Lastly, wet snow (Fig. 2.6b) mainly occurred during the first half of the second icing period (between 0600 UTC 8 January and 1500 UTC 8 January) when the low-level temperature became slightly >0°C near YOW.

2.4 Comparison between P3_MOD and P3_ORIG

The impacts of predicting $F_{i,liq}$ on simulated precipitation amounts and types are investigated in this section. The differences between P3_MOD and P3_ORIG in accumulated freezing rain and solid precipitation are shown in Fig. 2.7. There is an overall decrease of freezing rain in P3_MOD, while a general increase in solid precipitation is obtained. In Maine (ME), a decrease up to 25 mm of freezing rain is obtained in P3_MOD compared to P3_ORIG. Maximum differences between P3_MOD and P3_ORIG are obtained where a mixture of ice pellets and freezing rain is obtained in P3_MOD (Fig. 2.5f).

To investigate differences between P3_MOD and P3_ORIG in precipitation properties aloft and at the surface, four sub-regions have been chosen into the domain of interest (squares in Fig. 2.7). The precipitation characteristics and associated temperature fields were analyzed in those sub-regions and presented in the following sub-sections.

2.4.1 Differences in accumulated precipitation

The sub-region-averaged total accumulated precipitation types are shown in Fig. 2.8. Sub-region A is associated with mainly freezing rain whereas sub-region B is associated with a mixture of precipitation but mainly freezing rain. Sub-region C is located north of sub-region A and mainly solid precipitation occurred with some ice pellets and freezing rain. Finally, the fourth sub-region (D) is located northwest of sub-region B and has nearly same accumulations at the surface as sub-region C. According to Lecompte *et al.* (1998), 40-60 mm and 20-40 mm of freezing rain were reported at B and D, respectively, leading to a model overestimation in all sub-regions. The accumulated ice pellets (Fig. 2.5f) in P3_MOD are 4.2 mm, 7.7 mm and 5.9 mm for sub-regions B, C and D, respectively.

The temporal evolution of the sub-regions-averaged 0°C-isotherm, freezing rain and ice pellets rates as well as the difference between P3_MOD and P3_ORIG in accumulated precipitation are shown in Fig. 2.9. For the sub-regions A and B, the two icing periods are similar (listed in Table 2.1). Ice pellets are obtained in P3_MOD at the beginning of each icing period and at the end of the second one in the sub-region B associated with a lower freezing rain rate in P3_MOD compared to P3_ORIG. Larger differences between P3_MOD and P3_ORIG are obtained during the first half of the second icing period for sub-regions A and B. This is when the precipitation rate is higher and the melting layer is deep (between 1500 m and 2000 m) enough to melt ice completely producing freezing rain. The second icing period is similar in sub-regions C and D while shorter in sub-region C. Note that sub-region D has no first icing period at all (Table 2.1). Most of changes in accumulated freezing rain between P3_MOD and P3_ORIG in sub-regions C and D occurred when ice pellets are produced. This is when the depth and the maximum temperature of the melting layer are <1000 m and <2°C, respectively (Zerr 1997). For the sub-region D, the small increase of accumulated freezing rain occurs at the beginning of the second icing period (from 1200 UTC 8 January to 0000 UTC 9 January). It could also be due to a slightly deeper and warmer melting layer in P3_MOD compared to P3_ORIG. The difference between the two simulations are, however, very small. For instance, the upper 0°C-level of the melting layer in P3_MOD is lower by about 15 m compared to P3_ORIG, and the maximum temperature of the melting layer warmer by about 0.15°C.

2.4.2 Vertical structure of the particle size distributions

The vertical structure of particle size distribution (PSD) is investigated because it can impact the melting and refreezing rates of particles (Thériault *et al.* 2010). For example, smaller particles will tend to melt faster than larger ones. The focus is on the second icing period because larger differences between P3_MOD and P3_ORIG are obtained then (Fig. 2.9). However, the difference between the two icing periods will also be discussed in this section in regard to the mean ice size distribution aloft the melting layer.

Figure 2.10a shows time-averaged over the second icing period (see Table 2.1) of the sub-region-averaged vertical profiles of temperature for both simulations. For sub-regions A and B, ice has melted completely producing freezing rain at the surface. Sub-regions C and D are associated with deeper and colder refreezing layers compared to the sub-regions A and B. In general, the vertical temperature profiles produced by P3_MOD and P3_ORIG are similar, with some small differences. P3_MOD is slightly colder above the maximum temperature of the melting layer whereas it is slightly warmer below it.

The mean PSDs (Figs. 2.10b-f) at different heights (i.e., top of the melting layer, at the bottom of the melting layer and at the surface) are shown in Figs. 2.10b-f. Note that only ice size distributions of sub-regions C and D are shown in Figs. 2.10d and f) since ice melted completely into sub-regions A and B.

First, the shape parameter of all ice distributions (Figs. 2.10b, d and f) is zero. The ice mean mass-weighted diameters at the top of the melting layer are similar between P3_MOD and P3_ORIG (near ~0.2 cm) with slightly smaller values for P3_MOD in all sub-regions. The higher mean mass-weighted diameter of ice aloft is obtained in sub-region B during the second icing period with mean value of ~0.24 cm for both P3_MOD and P3_ORIG. This corresponds to higher precipitation rates (Fig. 2.9). Second, at the bottom of the melting, which also corresponds to the top of the refreezing layer, the P3_MOD ice distributions (Fig. 2.10d) are shifted towards smaller mean diameters with respect to the ice distributions above the melting layer of Fig. 2.10b. In contrast, in P3_ORIG those ice distributions are similar. This is the result of predicting the bulk liquid fraction because the mean ice mass-weighted diameter decreases with partial melting of P3_MOD, while it is not in P3_ORIG (Cholette *et al.* 2019). Thirdly, the mean ice diameter in P3_MOD increases while falling in the refreezing layer while it remains mainly constant in P3_ORIG (Fig. 2.10f). This increase in P3_MOD is mainly due to the refreezing process, which transfers mass but not concentration from $q_{i,liq}$ to $q_{i,rim}$, thus changing the rime mass fraction gradually. Higher mean ice diameters lead to higher precipitation rates and accumulated solid precipitation, in particular in the sub-region C.

The difference in ice size distribution aloft during the first (not shown) and second icing periods explains the difference in the surface precipitation rate. The slope and the intercept parameters above the melting layer are smaller during the second icing period, leading to higher mean particle sizes. Therefore, the second icing period ice PSDs aloft are generally characterized by higher $q_{i,tot}$, smaller $N_{i,tot}$, higher $F_{i,rim}$ and higher $\rho_{i,rim}$.

The rain and freezing rain size distributions (Figs. 2.10c and e) produced by P3_MOD have higher slope and intercept parameters compared to P3_ORIG. The mean mass-weighted diameter of rain and freezing rain (D_r) is always smaller in P3_MOD compared to P3_ORIG in all sub-regions. The maximum decrease of P3_MOD mean mass-weighted diameter of freezing rain at the surface compared to P3_ORIG is ~0.2 mm in sub-region B. This difference is mainly associated with the parameterization of the melting process. In particular, in updating N_{rain}, which is higher in P3_MOD compared to P3_ORIG (Cholette *et al.* 2019). The production of smaller raindrops diameters is associated with lower precipitation rate, which explains the lowest amount of accumulated freezing rain at the surface in P3_MOD compared to P3_ORIG.

2.4.3 Microphysical properties of precipitation aloft

An analysis of microphysical variables along two cross-sections (dotted and solid lines in Fig. 2.7a) is shown in Figs. 2.11 to 2.13. The variables are time-averaged over a time period during the second icing period. This time period was chosen when large differences are produced between P3_MOD and P3_ORIG. One cross-section extends from sub-region A to C (Fig. 2.11) and the other one is from sub-region B to D (Figs. 2.12-2.13).

Figures 2.11 and 2.12 show mass mixing ratios of hydrometeors of both simulations as well as their differences (P3_MOD–P3_ORIG). First, the ice entering the melting layer in sub-regions A (Fig. 2.11) and B (Fig. 2.12) melted completely to produce freezing rain at the surface. No melting layer aloft is present over sub-region C leading to mainly snow during that time period (Fig. 2.11). A mixture of freezing rain and ice pellets is obtained in sub-region D (Fig. 2.12). Second, the ice entering the melting layer aloft is highly rimed (~0.15) south of sub-region A (Fig. 2.11a: ~0-100 km) and south of sub-region B (Fig. 2.12a: ~60-120 km). The total ice mass mixing ratio above the melting layer is higher and more rimed over the sub-region B compared to D (Fig. 2.12). For both cross-sections, $q_{i,liq}$ (Figs. 2.11g and 2.12g) and q_{rain} (Figs. 2.11i-j and 2.12i-j) are higher in the melting layer when $q_{i,tot}$ above the melting layer is higher (~0.3 g kg^{-1}). Cloud is generally formed through supersaturated conditions produced by diabatic cooling of melting (Figs. 2.11l-m and 2.12l-m). Also, $q_{i,tot}$ (Figs. 2.11c and 2.12c) and $q_{i,rim}$ (Figs. 2.11f and 2.12f) aloft are smaller in P3_MOD compared to P3_ORIG, in particular over the sub-region B (Fig. 2.12c). The rain mass mixing ratio is always higher in P3_MOD compared to P3_ORIG for both cross-sections (Figs. 2.11k and 2.12k). Lastly, q_{cloud} (Figs. 2.11n and 2.12n) is smaller in P3_MOD compared to P3_ORIG into the melting layer.

Since P3_MOD and P3_ORIG used the same model configuration, the changes between the two simulations illustrated in Figs. 2.11 and 2.12 are assumed to be associated with the different microphysical formulations when the predicted $F_{i,liq}$ is used. Figure 2.13 shows the differences between P3_MOD and P3_ORIG in vertical structures of temperature (Fig. 2.13a), water vapour (Fig. 2.13b) as well as some microphysical properties (Figs. 2.13c-f) for the cross-section over the sub-regions B and D. Note that the melting and refreezing processes shown in Figs. 2.13d and 2.13f, respectively, are time-averaged and non-advected quantities, so there are located where temperatures are near 0°C, but refreezing (melting) is only computed when temperatures are <0°C (0°C).

The prediction of $F_{i,liq}$ in P3_MOD allows different representations of hydrometeor properties while they undergo melting in contrast to P3_ORIG. For instance, P3_MOD allows for a decrease in the diameter and an increase in both fall speed and density during melting, while these behaviours are not represented in P3_ORIG (Cholette et al. 2019). The increase in density (shown in Fig. 2.13c) and hence fall speed during melting induces a deeper melting depth in P3_MOD compared to P3_ORIG (Fig. 2.13d). This tends to produce ice pellets instead of freezing rain and wet snow instead of rain in P3_MOD, leading to higher accumulated solid precipitation (including ice pellets when they are mixed with freezing rain). Also, the partial melting explicitly treated in P3_MOD, combined with shedding of accumulated liquid water when the melting ice is partially or fully rimed (neglected in P3_ORIG), produces higher melting rates leading to greater rain mass (Fig. 2.12k) and number mixing ratios (not shown). In particular, the change in rain number mixing ratio from melting is scaled by a factor of 0.2 in P3_ORIG to account implicitly for evaporation of melting ice, while this is not done in P3_MOD. Thus, the melting process in P3_MOD affects the proportions of rain versus ice produced in the melting layer and induces a higher cooling rate from melting near the top of the melting layer compared to P3_ORIG (Fig. 2.13a). These differences are generally larger when the rime mass fraction aloft is greater associated with higher surface precipitation rates (>1.5-2 mm h^{-1}). These differences also lead to a smaller mass-weighted mean diameter of rain and freezing rain in P3_MOD compared to P3_ORIG (Fig. 2.13e). This, in turn, reduces the freezing rain rate, contributing to smaller freezing rate accumulations at the surface in P3_MOD compared to P3_ORIG.

Other processes within the melting layer include cloud water accretion by rain and condensation/evaporation (not shown). The larger q_{rain} in P3_MOD increases the cloud water accretion rate, which results in lower q_{cloud} in the melting layer (Figs. 2.11n and 2.12n). The condensation/evaporation of $q_{i,liq}$ acts as a source/sink term for water vapor in P3_MOD whereas it is neglected above 0°C in P3_ORIG, thus competing for available water vapour with q_{cloud} and q_{rain}. Condensation rates, in particular those for q_{cloud}, mostly depend on the thermodynamic and dynamics conditions (e.g., vertical velocity and temperature). However, for rain and P3_MOD's mixed-phase ice, the rates are more sensitive to the microphysical characteristics including mass content and number concentration. This is because the phase relaxation time for cloud condensation is usually small, of order 1-10 sec, regardless of the microphysical characteristics, whereas the phase relaxation timescale for rain and mixed-phase particles is usually much longer and is more sensitive to the microphysical properties. It is found that the rain condensation rate in P3_MOD associated with Figs. 2.11 and 2.12 is slightly greater compared to P3_ORIG, contributing to the higher air temperature in the melting layer.

Lastly, in the refreezing layer, the refreezing of partially-melted ice (Fig. 2.13f) in P3_MOD increases the air temperature near the top of the refreezing layer (Fig. 2.13a) and changes the ice properties gradually, such as the mean mass-weighted diameter, compared to P3_ORIG. For instance, refreezing of partially-melted ice increases the mean diameter of ice, which increases the solid precipitation rate and accumulation in region with ice pellets accumulation in P3_MOD in contrast to P3_ORIG. The differences between P3_MOD and P3_ORIG are greater when conditions of wet growth are met above the melting layer. It should be noted that wet growth (not shown) and refreezing rates near the upper 0°C height of the melting layer are small. In general, wet growth is associated with hail growth in a strong updraft. However, wet growth in P3, parameterized following Musil (1970), still can occur in non-hail conditions and this is the case here. In P3_ORIG, cloud droplets and raindrops collected during wet growth are directly transferred to $q_{i,rim}$ with some portion that is shed back to rain

(Morrison and Milbrandt 2015), whereas in P3_MOD they are transferred to $q_{i,liq}$ to form mixed-phase particles. These mixed-phase particles can refreeze if temperatures are below 0°C (Fig. 2.13f; near aloft the melting layer). In the example shown here, this impacts the cloud ice characteristics above the melting layer by decreasing the rime mass fraction (Fig. 2.12f), the number concentration and the total mass-mixing ratio (Fig. 2.12c). This is particularly important when southerly winds aloft bring higher amounts of water vapor above the melting layer as in ME during the second icing period.

2.5 Conclusions

Simulating winter precipitation types is challenging because it involves parameterizing key microphysical processes associated with mixed-phase particles, such as partial melting and refreezing. To account for this, a predicted bulk liquid fraction, $F_{i,liq}$, was recently implemented into the Predicted Particle Properties (P3) bulk microphysics scheme (Cholette *et al.* 2019). It allows the explicit representation of mixed-phase particles and their processes. The objective was to investigate the impacts of predicting the bulk liquid fraction on simulated precipitation types and characteristics produced during a winter storm. To this end, WRF simulations of the 1998 Ice Storm using the P3 scheme with (P3_MOD) and without (P3_ORIG) the predicted bulk liquid fraction were conducted.

Both simulations reasonably reproduced the observed storm meteorological conditions (e.g., temperature and winds). The prediction of $F_{i,liq}$ allowed P3_MOD to reproduce observed precipitation types of freezing rain, ice pellets and wet snow. An overall decrease of freezing rain accumulation occurred with the predicted $F_{i,liq}$ in P3_MOD compared to P3_ORIG, with decreases up to ~30% in some regions where ice pellets and freezing rain were mixed in P3_MOD. This led to a small but consistent improvement in bias and RMSE for P3_MOD compared to P3_ORIG, relative to observations. It was shown that partial melting and refreezing processes affect the simulated precipitation types obtained at the surface by changing bulk properties of hydrometeors as they fall through the melting and refreezing layers. In particular, the increase in mean density and hence fall speed, and the increase of mean particle size during refreezing led to an increase of solid and ice pellets precipitation accumulation in P3_MOD, while smaller mean raindrop size from melting led to a decrease in freezing rain rate compared to P3_ORIG.

This study has some limitations. First, it is challenging to validate the precipitation type during winter storms when temperatures are near 0°C (Ralph *et al.* 2005; Reeves *et al.* 2014), particularly because ice pellets are often not reported. Moreover, freezing rain and ice pellet events generally last only a few hours (e.g., Ressler *et al.* 2012; Matte *et al.* 2018). Therefore, high temporal resolution observations of surface precipitation type and measurements of the vertical temperature and relative humidity profiles are needed. Second, P3_MOD under-predicted the total solid accumulation (including ice pellets) in southern Quebec (near YUL) compared to hourly observed surface precipitation type. Other microphysical processes, such as the secondary ice production (Hallett and Mossop 1974) which was not included here, may have played an important role in the formation of ice pellets during the 1998 Ice Storm. This limitation could be investigated using the multiple category configuration of P3 (Milbrandt and Morrison 2016), which includes secondary ice production, combined with the prediction of bulk liquid fraction. Finally, the storm studied was extreme in terms of both duration and amount of precipitation. Indeed, strong warm air advection and the northeasterly cold winds near the surface contributed to maintaining favorable conditions for freezing rain and ice pellets for a very long duration (Henson *et al.* 2011). It would be interesting to compare P3_MOD and P3_ORIG when the vertical temperature structure is closer to

0°C (i.e., a weaker melting layer) and the diabatic cooling from melting and warming from refreezing rates are on the same order of magnitude as the warm/cold air advection.

Overall, this work is a step forward to a better understanding of the microphysical processes responsible for the formation of ice pellets and freezing rain during winter storms when temperatures are near 0°C. More complete atmospheric models can now be used to study the occurrences of winter precipitation types and their transitions as well as other physical processes that can lead to the production of freezing rain and ice pellets at the surface using the modified P3 scheme with the prediction of $F_{i,liq}$. Furthermore, P3_MOD could be useful for operational NWP since, usually, precipitation types are poorly diagnosed. For example, a sounding-based precipitation type diagnostic (Bourgouin 2000) is used to diagnose ice pellets in the High Resolution Deterministic Prediction System, the km-scale Canadian NWP system (Milbrandt *et al.* 2016). P3_MOD should also improve the simulated reflectivity in the bright band region due to the explicit parameterization of partial melting because particle properties for wet snowflakes are different than those of raindrops (Szyrmer and Zawadzki 1999; Henson *et al.* 2011). For instance, wet snowflakes have larger diameter, but smaller density and fall speed than raindrops, so the effect of predicting the liquid fraction of mixed-phase particles on the simulated bright band reflectivity should be examined in detail in a future study.

Acknowledgments

The authors would like to thank the funding agencies, Canadian Network for Regional Climate and Weather Processes (CNRCWP) funded by the Natural Sciences and Engineering Research Council of Canada (NSERC) as well as the NSERC Discovery grant and a Canadian Research Chair Tier 2. The first author (MC) would like to thank Fonds de recherche du Québec – Nature et technologies (FQRNT) for a fellowship. The computations were made on the supercomputer cedar managed by Calcul Québec and Compute Canada.

2.6 Appendix: P3_MOD simulated variables

2.6.1 Atmospheric fields

This appendix aims at illustrating the overall behavior of simulated atmospheric fields of P3_MOD. Fig. 2.14 shows same as Fig. 2.4 but for the lowest model level of P3_MOD. The locations of the 0°C-isotherms are well reproduced compared to observations with some small differences over Lake Ontario and New Hampshire (NH) during the second icing period. In general, there is a small warm bias in both icing periods: 0.67°C for the first icing period and 0.12°C for the second icing period. Sea-level pressures are smaller by about ~2 to 4 hPa in P3_MOD compared to observations. Low-level winds compared well with observations within the SLRV and are stronger during the second icing period compared to the first one as in Henson *et al.* (2011). The intensities of low-level horizontal winds are slightly higher (smaller) at YUL (YQB) with a northward rotation at both stations.

A comparison between simulations and the observed vertical temperatures at two times of each icing period and at two locations where soundings are available (WMJ and GYX) is shown in Fig. 2.15. The temperature profiles are in general well reproduced by P3_MOD, except for the temperatures in the refreezing layer, which are warmer (not for Fig. 2.15d). The simulated height of the melting layer is higher at both times included in the second icing period (Figs. 2.15c-d) compared to times within the first icing period (Figs. 2.15a-b) in agreement with Henson *et al.* (2011).

Figure 2.16 shows vertical structures of time-averaged during both icing periods P3_MOD temperature, horizontal wind speed and direction, and vertical wind speed over southern Quebec. The height of the melting layer was higher, and the melting layer was deeper during the second icing period (Fig. 2.16a) compared to the first icing one (Fig. 2.16b). The horizontal wind speed is generally stronger during the second icing period (Figs. 2.16c-d) and at lower levels in the SLRV. While south-westerly winds occurred aloft during the first icing period, they rotated to southerly during the second one (Figs. 2.16e-f). Vertical air motions (Figs. 2.16g-h) follow the topography of the Appalachians (-220 km to -100 km of YUL) and the Laurentians (110 km to 100 km of YUL). Upward vertical air motion and downward vertical air motion are obtained in the SLRV near the Appalachians and the Laurentians, respectively, in particular during the second icing period (Fig. 2.16f). The combination of southerly (instead of south-westerly) horizontal wind aloft into the melting layer, stronger surface north-easterly flow and vertical air motions, as well as warmer and deeper melting layer may have contributed to the higher differences between P3_MOD and P3_ORIG obtained during the second icing period compared to the first icing period. The simulated results of Fig. 2.16 agree well with Henson *et al.* (2011).

2.6.2 Precipitation fields

Simulated time evolution of surface precipitation rates is shown at six stations in Fig. 2.17. The two periods of significant freezing rain are well reproduced by the simulation. There is a south to north transition of precipitation types in P3_MOD and observations, such that there is more freezing rain in southern stations and more snow in northern stations. The mixture of wet snow (because surface temperature in observations in >0°C; not shown), ice pellets and rain at YOW (Fig. 2.17f) at around 1200 UTC 8 January is well captured by P3_MOD. Overall, the duration of ice pellets is lower in P3_MOD compared to observations for YMX, YUL, YHU, and YOW (Figs. 2.17c-f).

Lastly, Fig. 2.18 compares simulations and the observed total accumulated precipitation types with scatter diagrams. For all precipitation categories, except solid precipitation (Fig. 2.18c), the lower (higher) precipitation amounts are overestimated (underestimated). The accumulated liquid precipitation (Fig. 2.18b) is overestimated for accumulations >100 mm. Both freezing rain (Fig. 2.18d) and total (Fig. 2.18a) accumulations >80 mm are overestimated by P3_MOD. The bias and the root mean square error (RMSE) (Table 2.2) are of the same order of magnitude in P3_MOD and P3_ORIG. However, those of P3_MOD are systematically lower than P3_ORIG. For both simulations, the biases and the RMSE are larger for liquid and freezing rain than for solid accumulations. The mean bias and the RMSE for freezing rain accumulations are reduced by 14% and 9.4%, respectively, in P3_MOD compared to P3_ORIG. Also, for solid accumulations, P3_MOD improved by 87% the mean bias of P3_ORIG, though the biases for solid accumulations are very small for both simulations. The difference between both simulations and the observations is much larger than the difference between the two simulations, except for the solid accumulation bias, for which the differences are of the same order of magnitude.

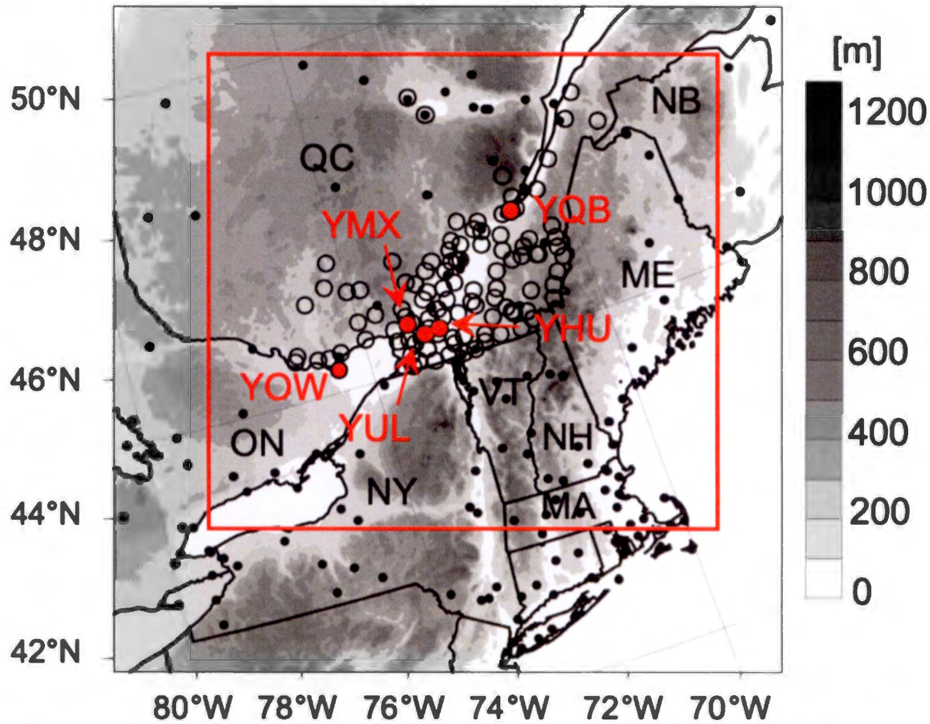

Figure 2.1 Simulation domain topography (grey tones, [m]) and location of the analysis domain (red square). Also shown are the locations of the observation stations for the 1998 Ice Storm meteorological overview of total accumulated precipitation types (circles) from Milton and Bourque (1999) and surface atmospheric variables (dots) from the University of Wyoming web site (http://weather.uwyo.edu/). Specific stations are highlighted: Montreal Pierre-Elliott-Trudeau international airport (YUL), Ottawa airport (YOW), Mirabel (YMX), Saint-Hubert (YHU) and Quebec Jean-Lesage airport (YQB). Canadian provinces and America States are listed in the list of acronyms.

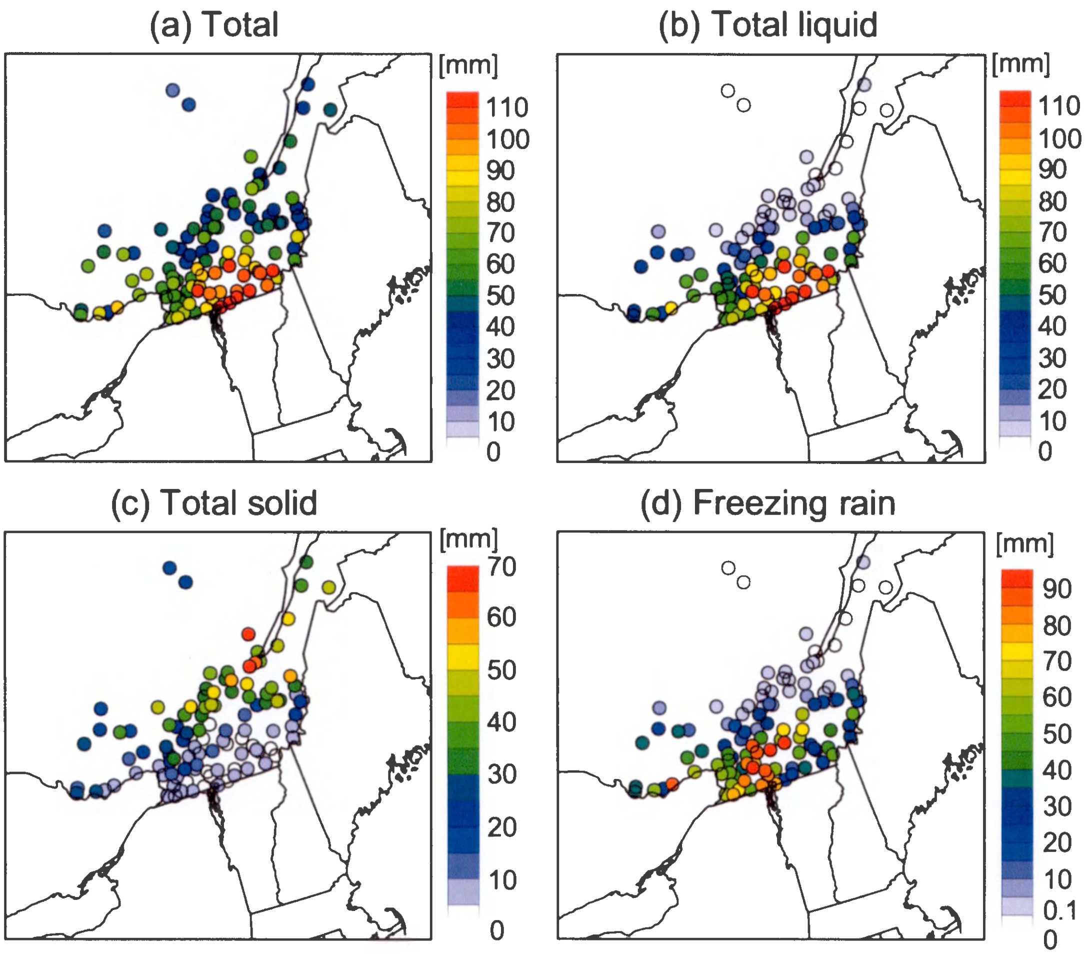

Figure 2.2 Observed total accumulated precipitation [mm] from 0600 UTC 4 January 1998 to 0600 UTC 10 January 1998 of (a) total, (b) total liquid, (c) total solid and (d) freezing rain. A 1 mm-to-1 cm ratio is assumed for (a) and (c) as in Milton and Bourque (1999).

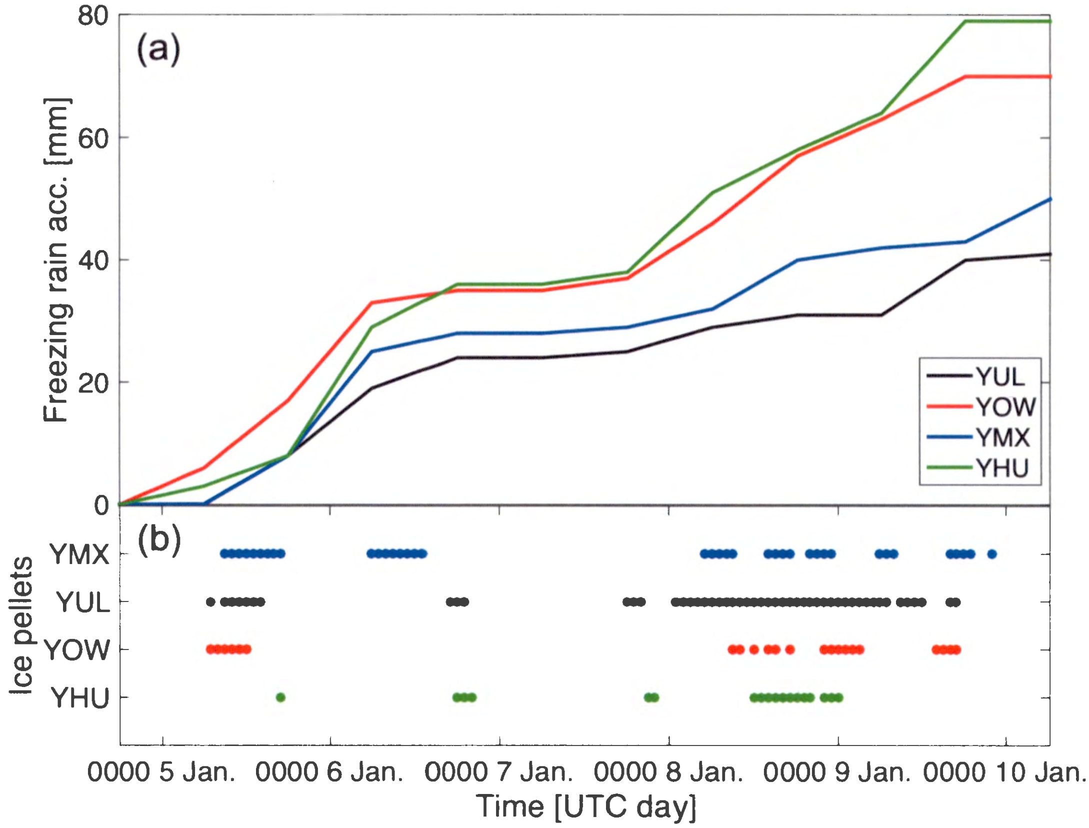

Figure 2.3 Temporal evolution of (a) 12-hourly accumulated freezing rain [mm] (Milton and Bourque 1999) and (b) hourly observed ice pellets (http://weather.uwyo.edu/) at YUL (black), YOW (red), YMX (blue) and YHU (green).

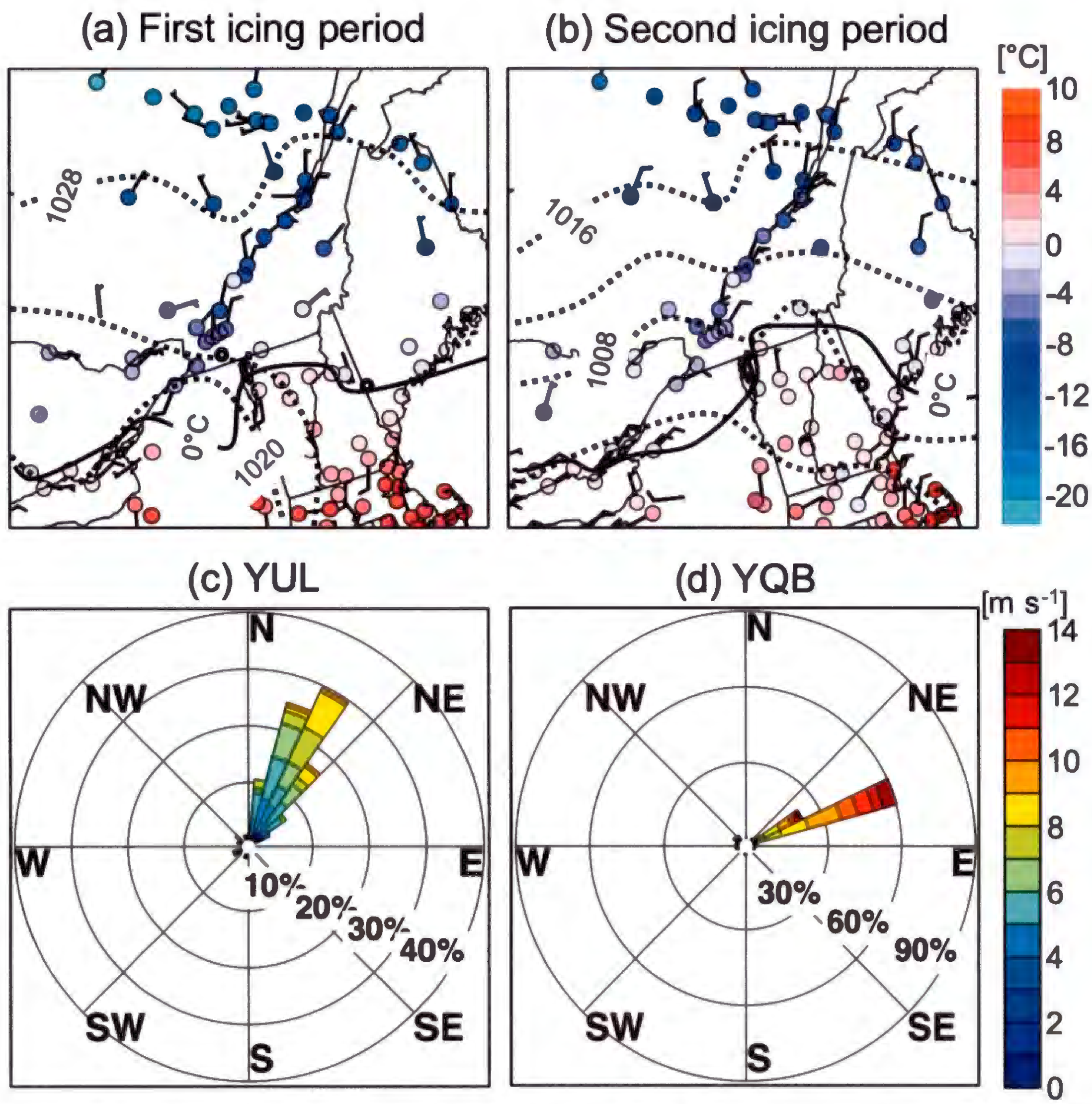

Figure 2.4 (a)-(b) Time-averaged over (a) the first icing period (from 0000 UTC 5 January 1998 to 0000 UTC 7 January 1998) and (b) the second icing period (from 0000 UTC 8 January 1998 to 0000 UTC 10 January 1998) of hourly observed 2 m temperature (colors, [°C]) and 0°C-isotherm (black). Also shown in (a)-(b) are the 10 m wind barbs (<0.1 m s^{-1} for no barb, <2.5 m s^{-1} for half-barb and <5 m s^{-1} for full-barb) and the sea-level pressure (dotted, every 4 hPa) on 0000 UTC 6 January 1998 for (a) and 0000 UTC 9 January 1998 for (b). (c)-(d) Time-averaged over the simulated period (from 0600 UTC 4 January 1998 to 0600 UTC 10 January 1998) 10 m wind rose diagrams at (c) YUL and (d) YQB. In (c)-(d), the colors represent the wind intensities [m s^{-1}] and the circles are the frequencies [%] of each intensity/direction combination. Data are taken from the University of Wyoming web site (http://weather.uwyo.edu/).

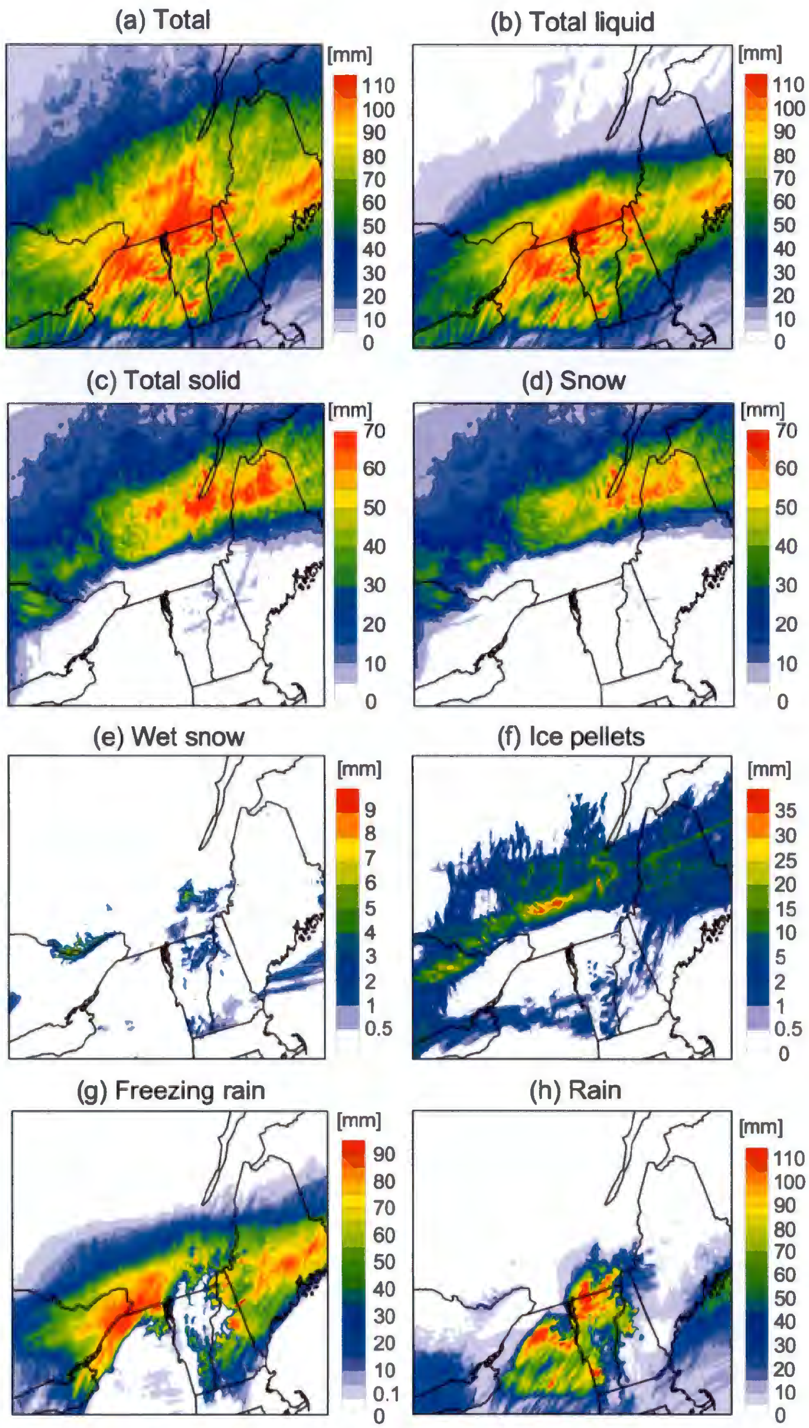

Figure 2.5 P3_MOD total accumulated precipitation [mm] from 0600 UTC 4 January 1998 to 0600 UTC 10 January 1998 of (a) total, (b) total liquid, (c) total solid, (d) snow, (e) wet snow, (f) ice pellets, (g) freezing rain and (h) rain.

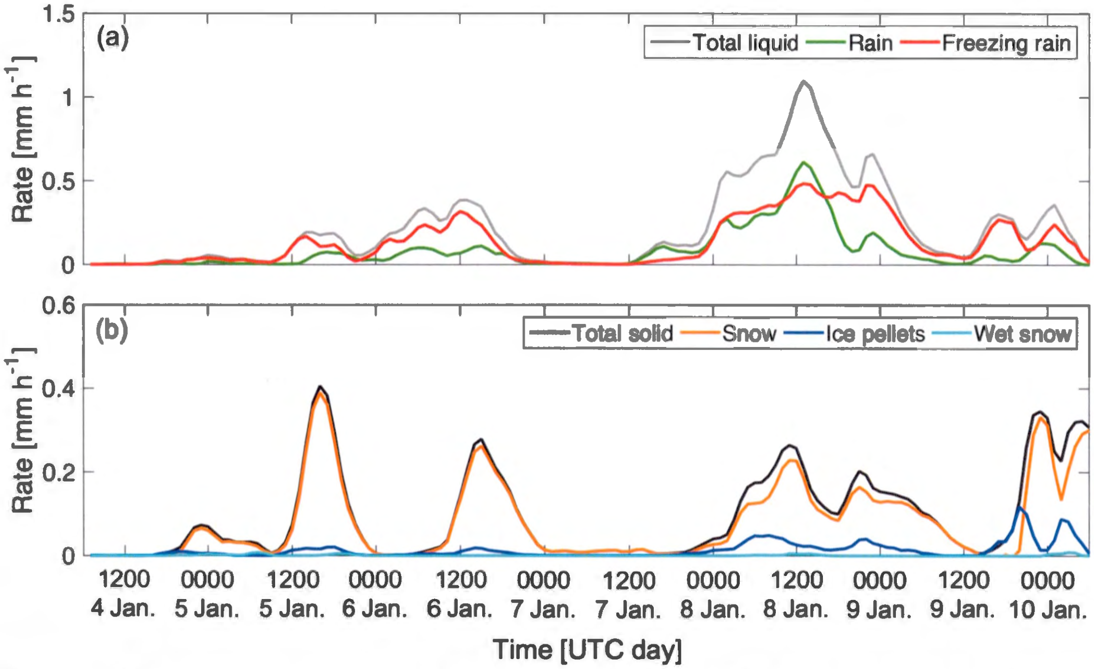

Figure 2.6 Temporal evolution of domain-averaged P3_MOD surface precipitation rate [mm h^{-1}] of (a) total liquid (grey), freezing rain (red) and rain (green), and (b) total solid (black), snow (orange), ice pellets (blue) and wet snow (light blue).

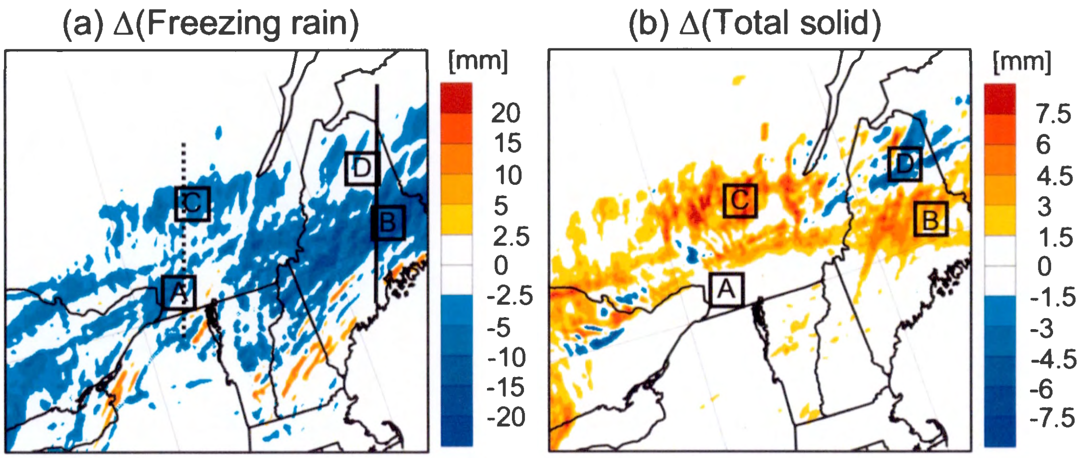

Figure 2.7 P3_MOD–P3_ORIG total accumulated precipitation [mm] from 0600 UTC 4 January 1998 to 0600 UTC 10 January 1998 of (a) freezing rain and (b) total solid. Also shown are the locations of the four sub-regions A, B, C and D (squares) and the two cross-sections for Figs. 2.11-2.13 (dotted and solid lines in a).

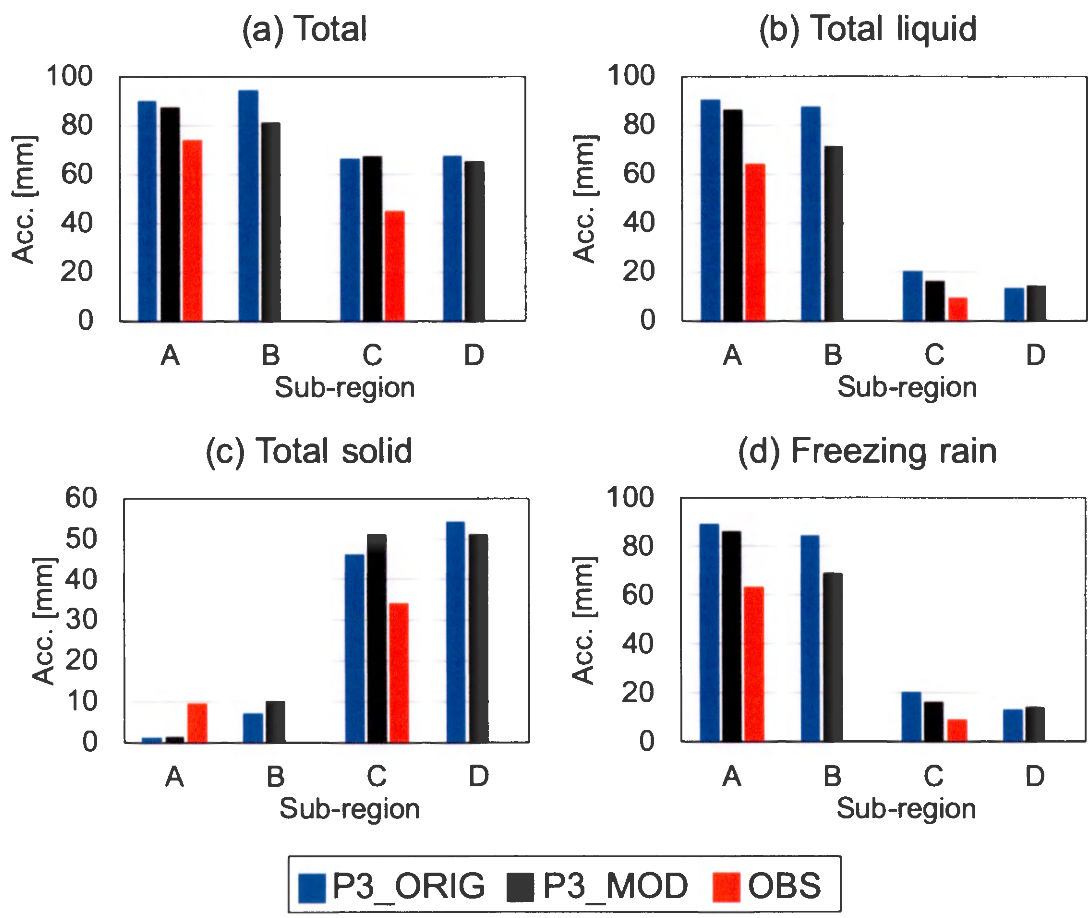

Figure 2.8 P3_ORIG (blue), P3_MOD (black) and observed (red, when available) sub-region-averaged total accumulated precipitation [Acc., mm] from 0600 UTC 4 January 1998 to 0600 UTC 10 January 1998 of (a) total, (b) total liquid, (c) total solid and (d) freezing rain.

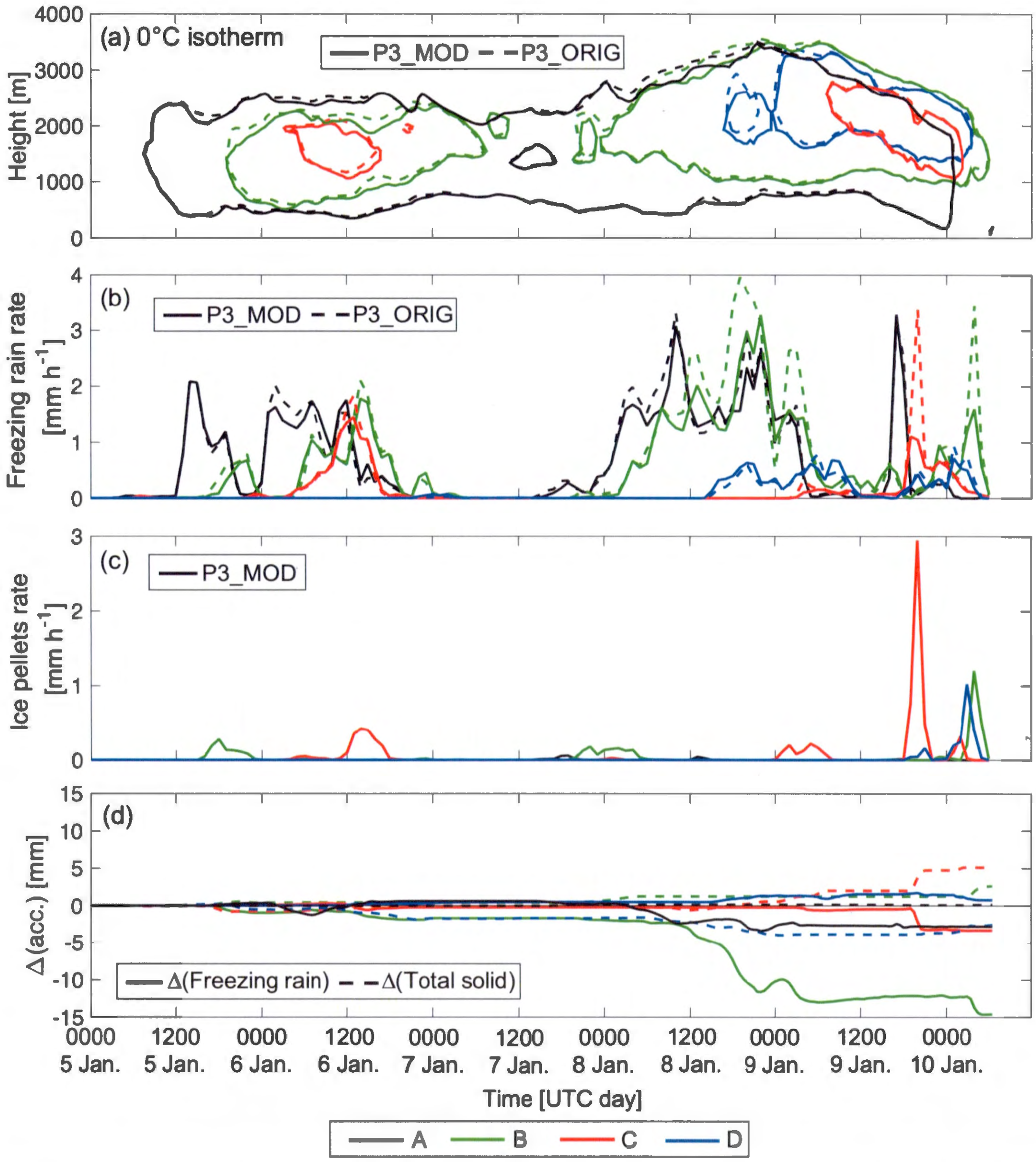

Figure 2.9 Temporal evolution of sub-region-averaged over A (black), B (green), C (red) and D (blue) (a) P3_MOD (solid) and P3_ORIG (dashed) 0°C-isotherm, (b) P3_MOD (solid) and P3_ORIG (dashed) freezing rain rate [mm h^{-1}], (c) P3_MOD ice pellets rate [mm h^{-1}] and (d) P3_MOD–P3_ORIG hourly accumulated precipitation [Δ(acc.), mm] of freezing rain (solid) and total solid (dashed).

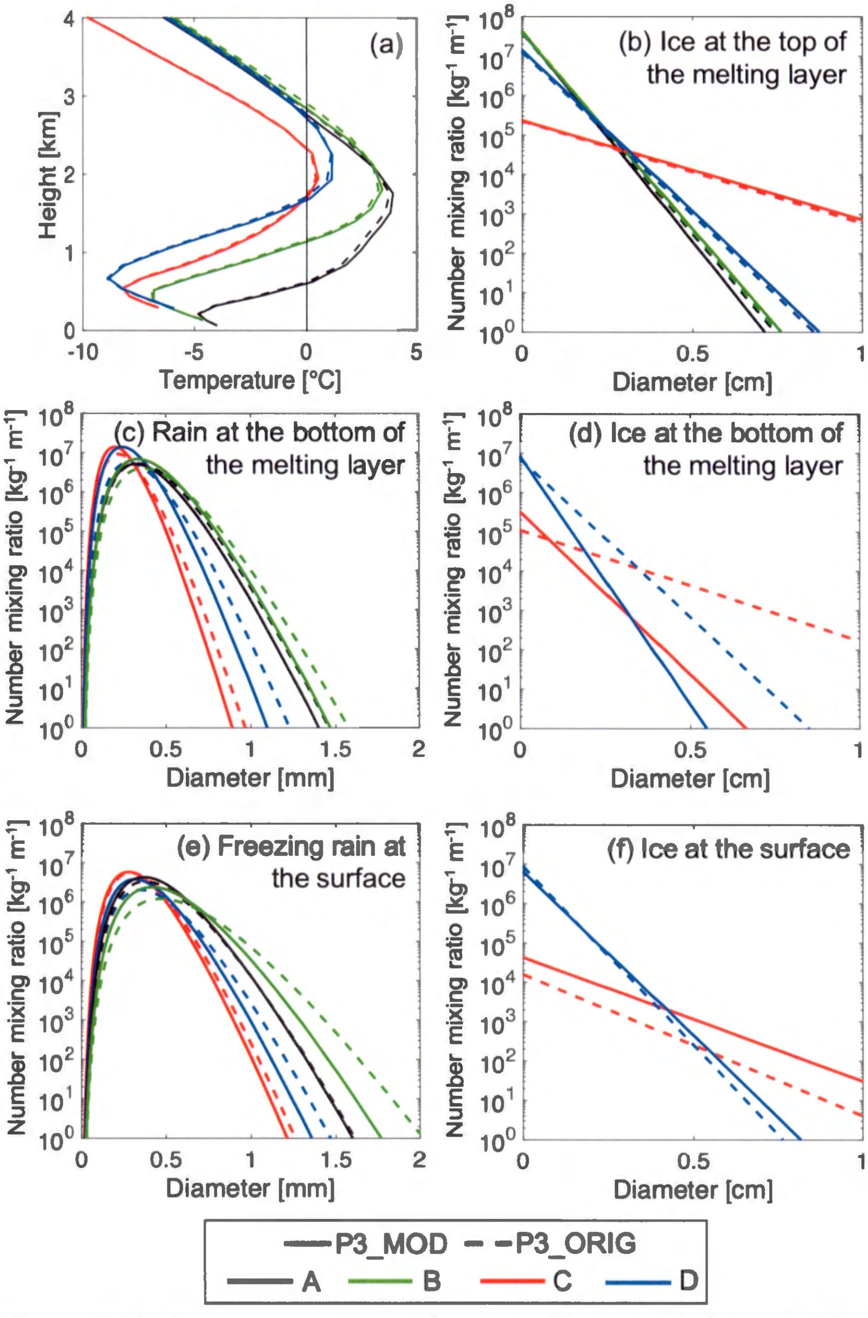

Figure 2.10 Time-averaged over the second icing period (see Table 2.1) of sub-region-averaged over A (black), B (green), C (red) and D (blue) P3_MOD (solid) and P3_ORIG (dashed) (a) vertical profiles of temperature [°C] and (b)-(f) particle size distributions [kg^{-1} m^{-1}] of (b) ice at temperature near -1.5°C just above the melting layer, (c) rain at the bottom of the melting layer, (d) ice at the bottom of the melting layer, (e) freezing rain at the surface and (f) ice at the surface.

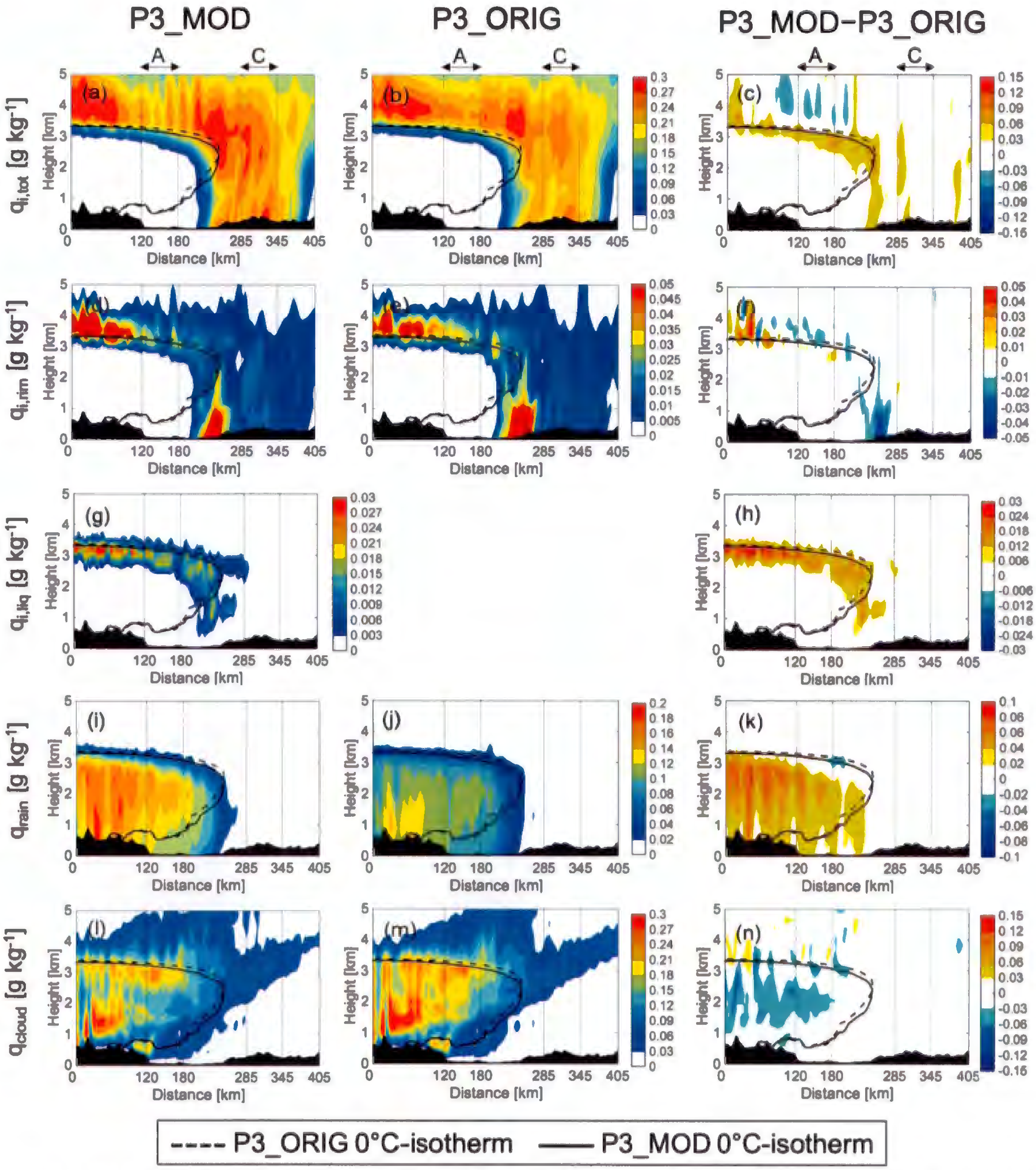

Figure 2.11 P3_MOD (left), P3_ORIG (middle) and P3_MOD–P3_ORIG (right) vertical structures along the cross-section over the sub-regions A and C (dotted line in Fig. 2.7a) of time-averaged from 0600 UTC 8 January 1998 to 0600 UTC 9 January 1998 P3_MOD (solid) and P3_ORIG (dashed) 0°C-isotherms superimposed on the mass mixing ratio (colors, [g kg^{-1}]) of (a)-(c) total ice [$q_{i,tot}$], (d)-(f) rime on ice [$q_{i,rim}$], (g)-(h) liquid on ice [$q_{i,liq}$], (i)-(k) rain [q_{rain}] and (l)-(n) cloud [q_{cloud}].

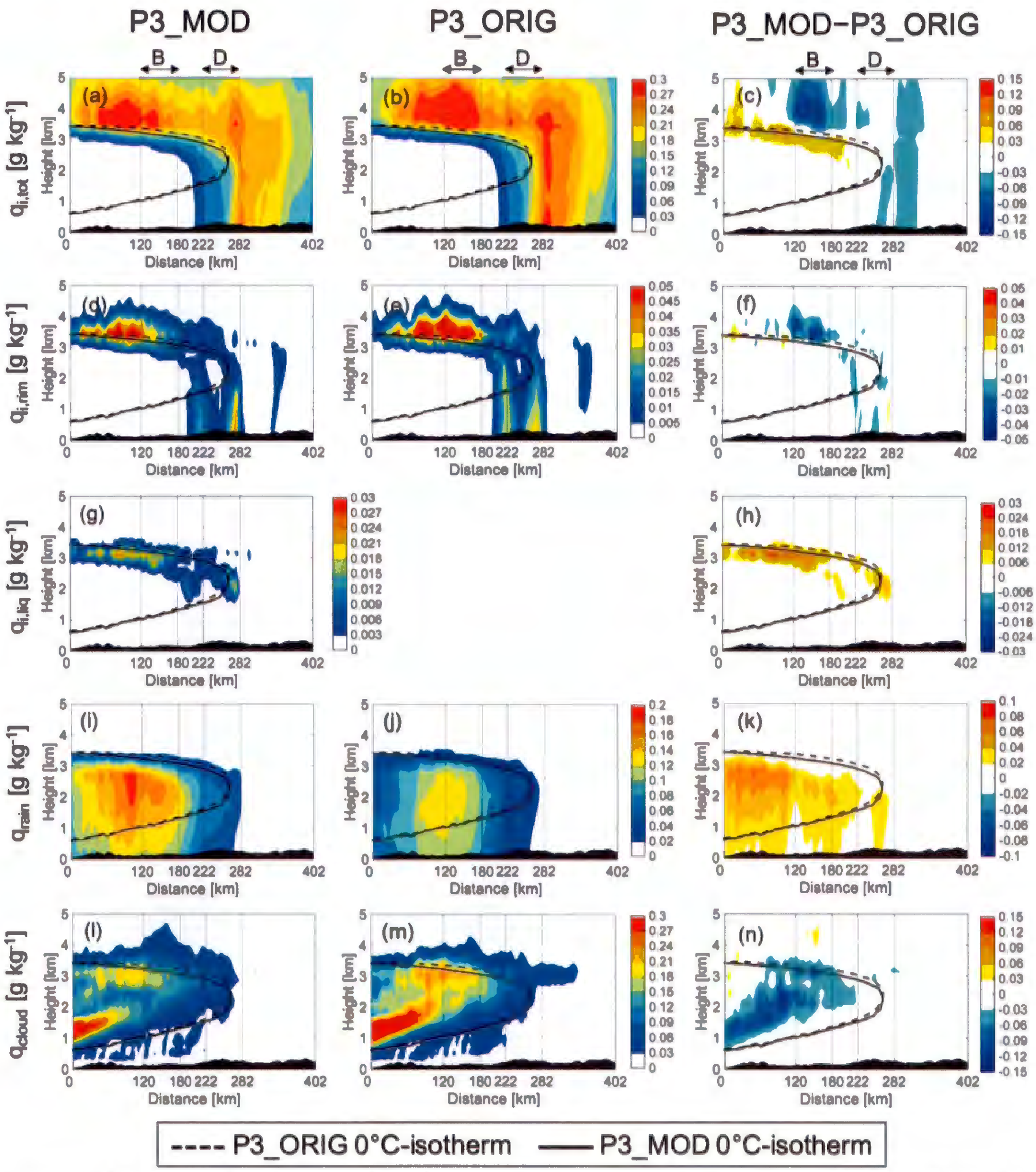

Figure 2.12 Same as Fig. 2.11 but for the cross-section over the sub-regions B and D (solid line in Fig. 2.7a).

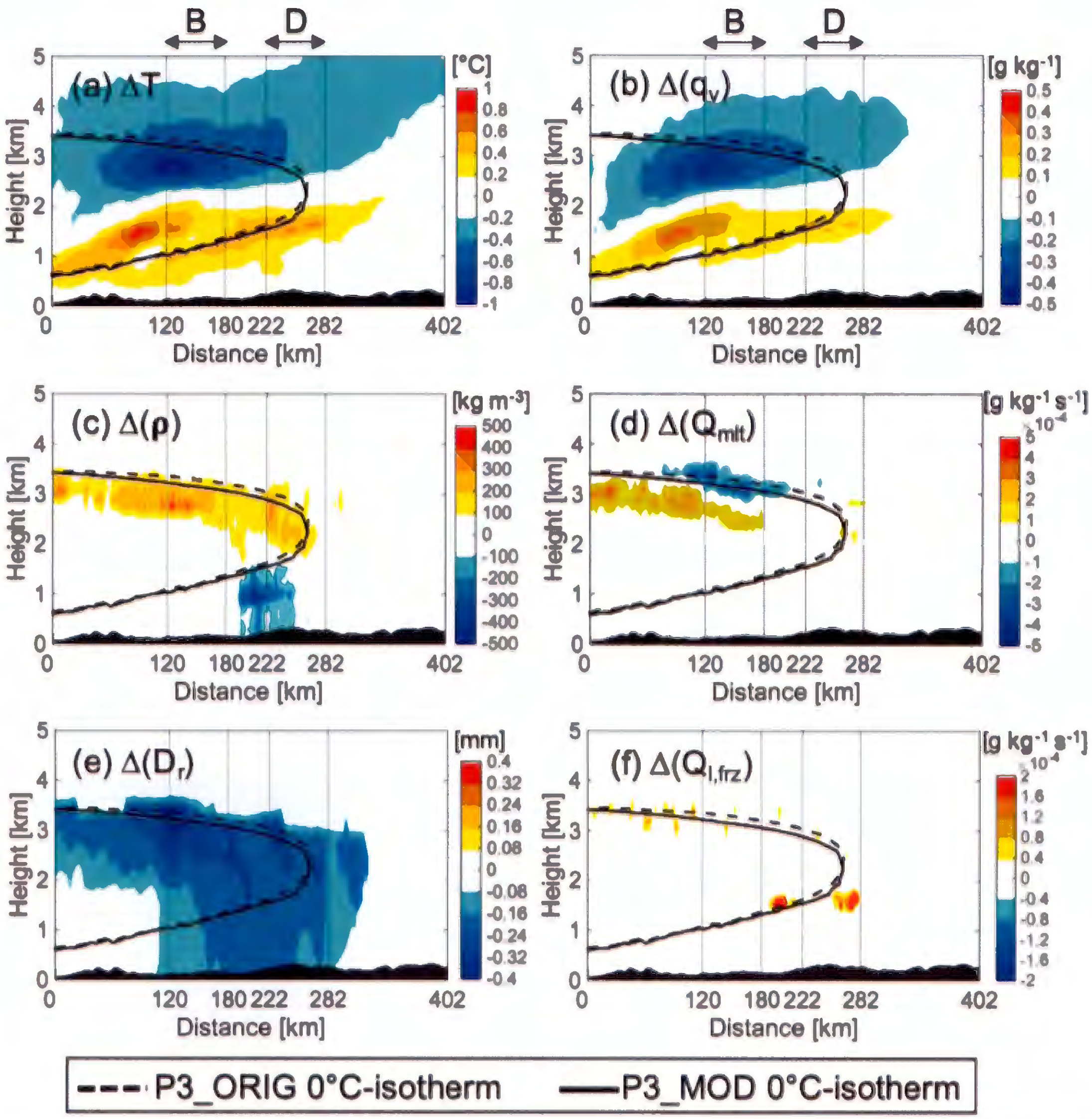

Figure 2.13 Vertical structures along the cross-section over the sub-regions B and D (solid line in Fig. 2.7a) of time-averaged from 0600 UTC 8 January 1998 to 0600 UTC 9 January 1998 P3_MOD (solid) and P3_ORIG (dashed) 0°C-isotherm superimposed on P3_MOD–P3_ORIG (colors) (a) temperature [ΔT, °C], (b) water vapor mixing ratio [$\Delta(q_v)$, g kg^{-1}], (c) mean mass-weighted density of ice [$\Delta(\rho)$, kg m^{-3}], (d) total melting process rate [$\Delta(Q_{mlt})$, g kg^{-1} s^{-1}], (e) mean mass-weighted diameter of rain/freezing rain [$\Delta(D_r)$, mm] and (f) refreezing process rate [$\Delta(Q_{l,frz})$, g kg^{-1} s^{-1}].

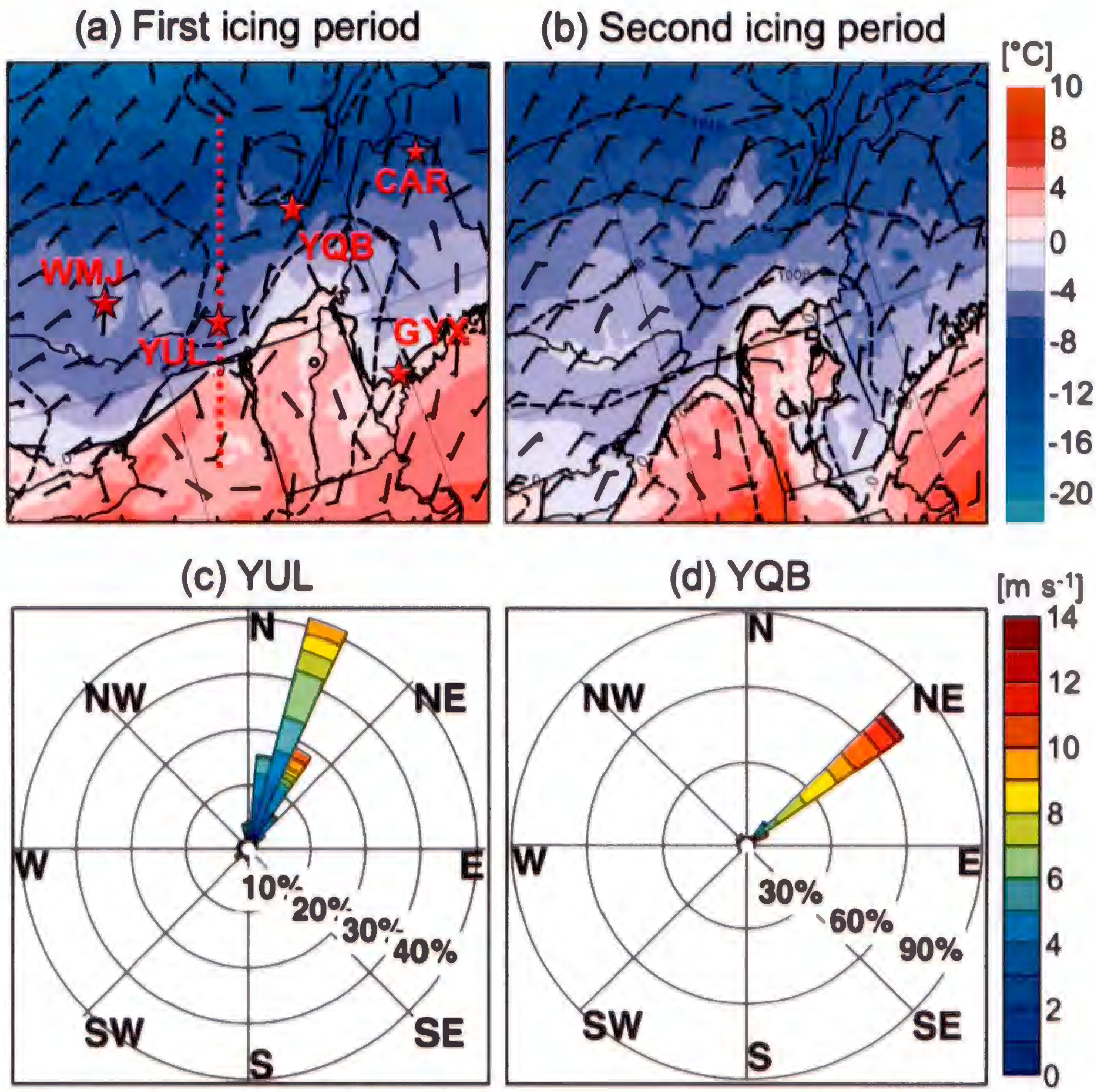

Figure 2.14 Same as Fig. 2.4 but for the lowest model level of P3_MOD. Also shown in (a) are the locations of the cross-section for Fig. 2.16 and the surface stations (red stars) of YUL, YQB, Caribou (CAR), Maniwaki (WMJ) and Gray (GYX).

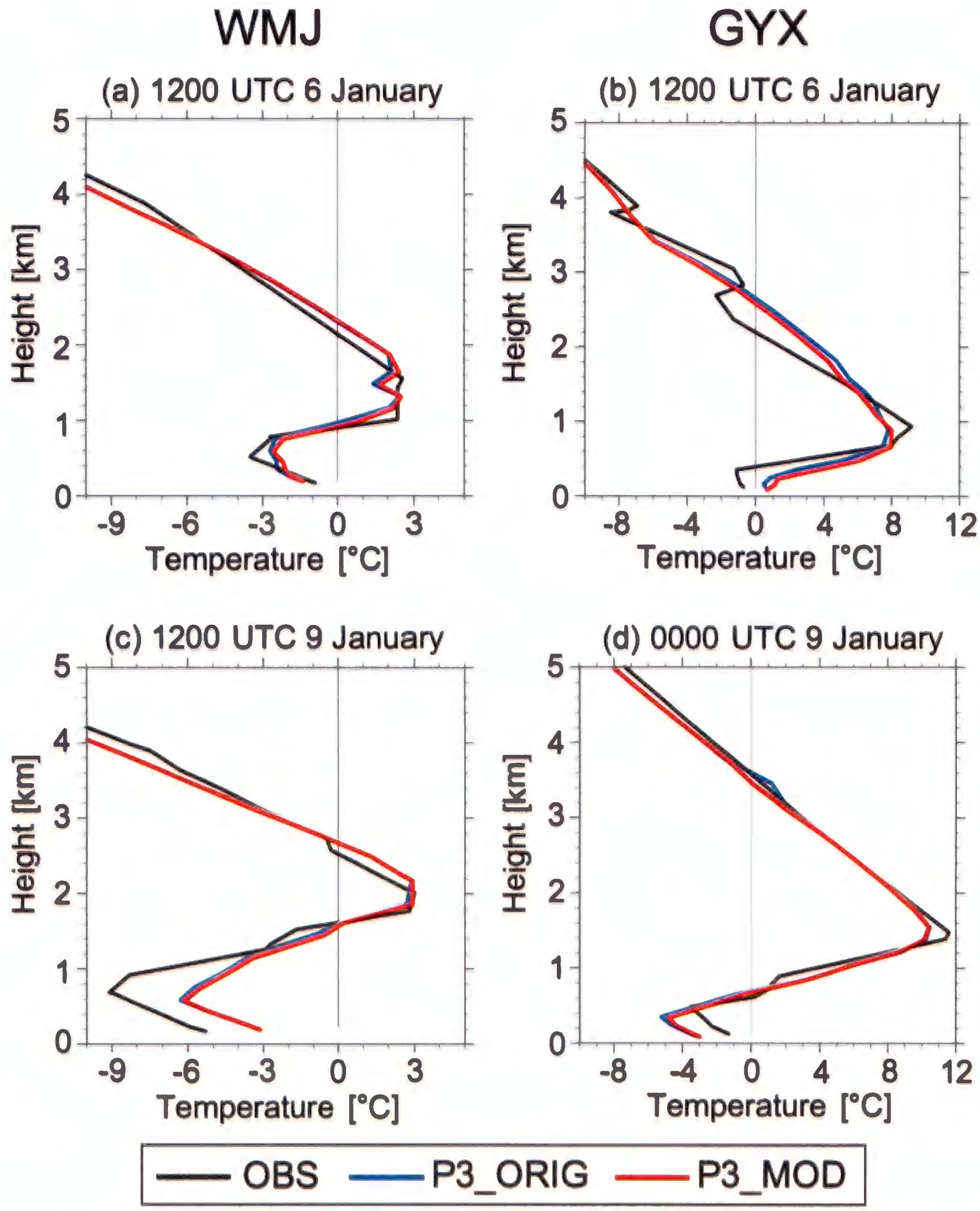

Figure 2.15 Observed (black), P3_ORIG (blue) and P3_MOD (red) vertical profiles of temperature [°C] on (a) 1200 UTC 6 January 1998 at WMJ, (b) 1200 UTC 6 January 1998 at GYX, (c) 1200 UTC 9 January 1998 at WMJ and (d) 0000 UTC 9 January 1998 at GYX. Simulated profiles are taken at the grid point closest to the observation stations and observed profiles are taken from the University of Wyoming web site (http://weather.uwyo.edu/).

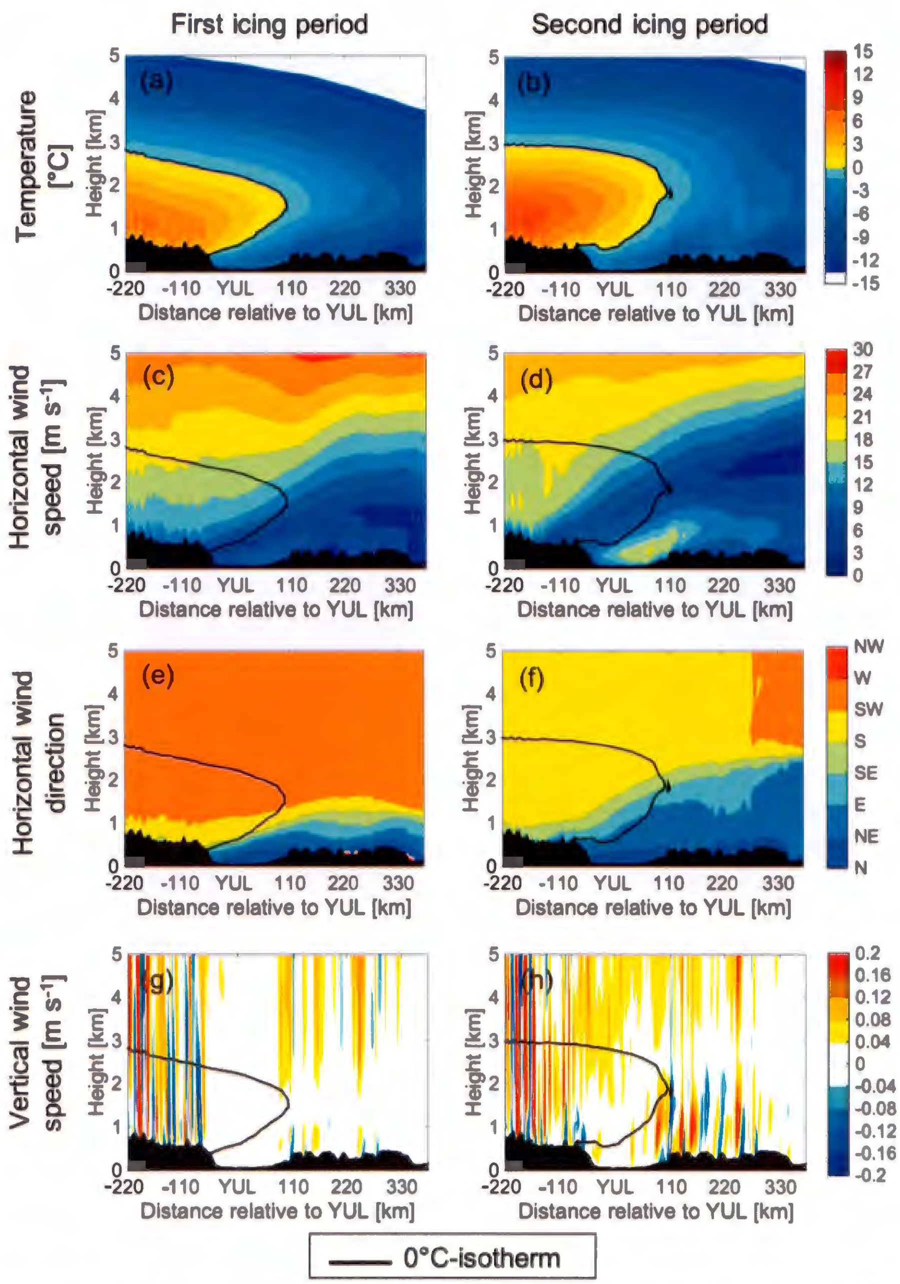

Figure 2.16 Time-averaged over (left) the first icing period (from 0000 UTC 5 January 1998 to 0000 UTC 7 January 1998) and (right) the second icing period (from 0000 UTC 8 January 1998 to 0000 UTC 10 January 1998) P3_MOD 0°C-isotherm (black line) superimposed on vertical structures (colors) of (a)-(b) temperature [°C], (c)-(d) horizontal wind speed [m s^{-1}], (e)-(f) horizontal wind direction and (g)-(h) vertical wind speed [m s^{-1}]. The location of the cross-section is shown in Fig. 2.14a (red dotted line).

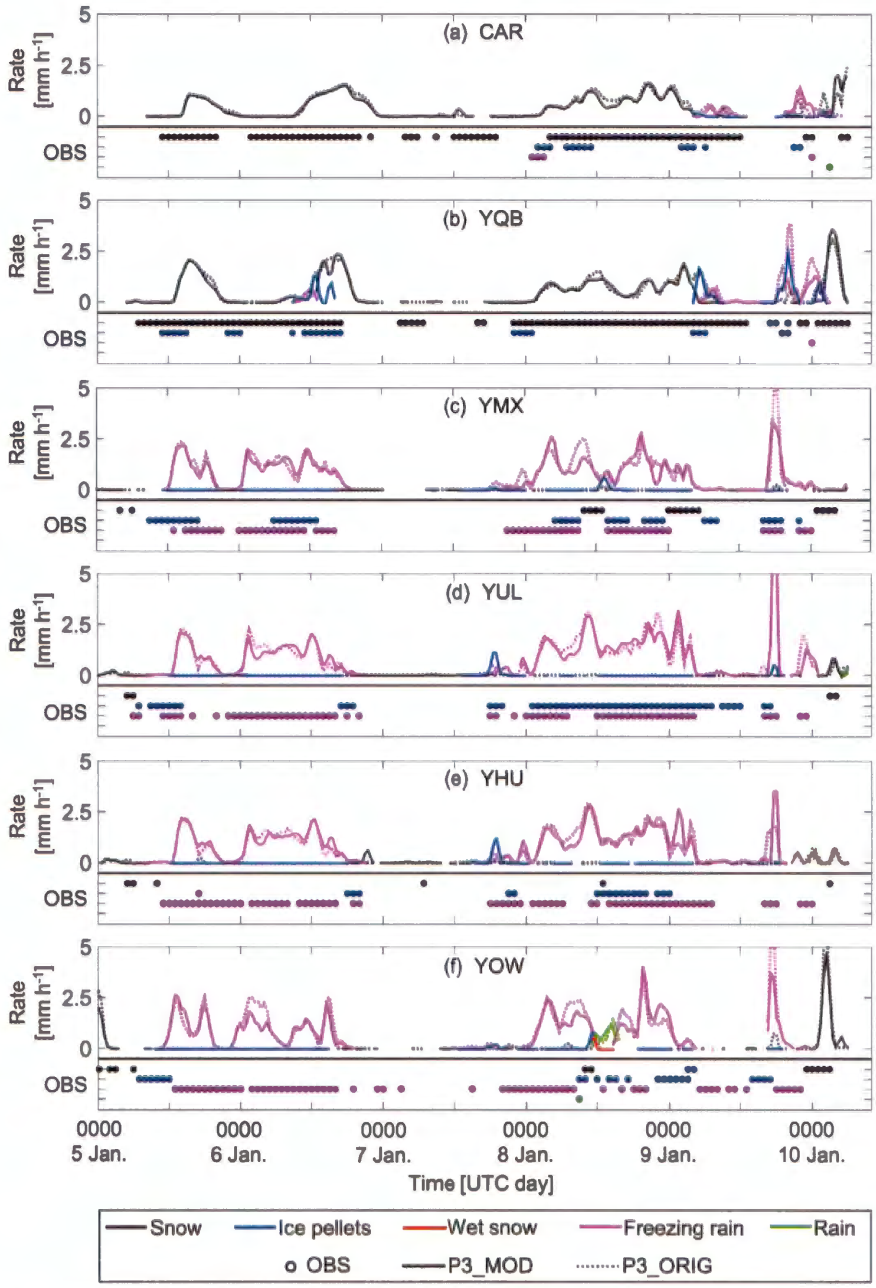

Figure 2.17 Time evolution of P3_MOD (solid) and P3_ORIG (dashed) surface precipitation rates [mm h^{-1}], and hourly observed precipitation types (dots) of snow (black), ice pellets (blue), wet snow (red), freezing rain (pink) and rain (green) at six stations: (a) CAR, (b) YQB, (c) YMX, (d) YUL, (e) YHU and (f) YOW.

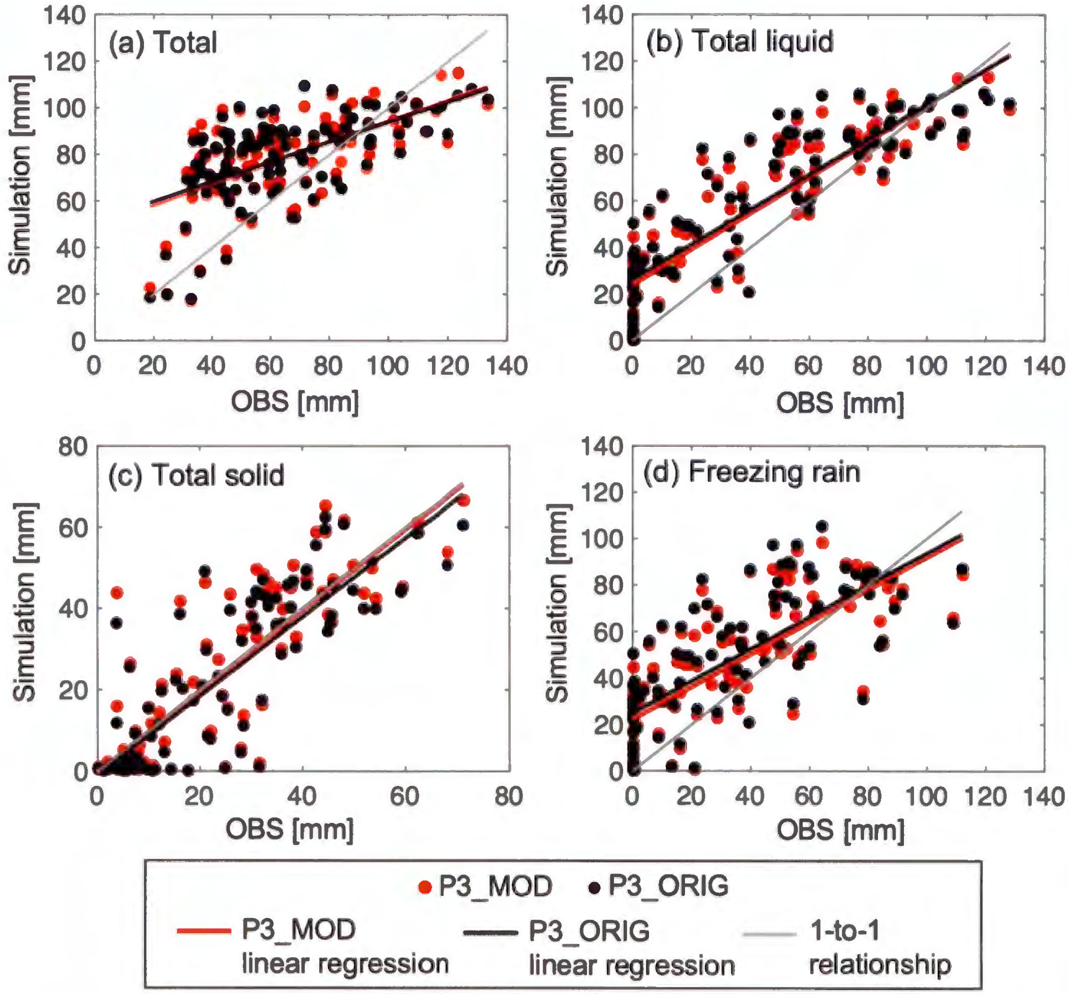

Figure 2.18 Scatter diagram between P3_MOD (red), P3_ORIG (black) and the observed total accumulated precipitation [mm] from 0600 UTC 4 January 1998 to 0600 UTC 10 January 1998 of (a) total, (b) total liquid, (c) total solid and (d) freezing rain. Simulated accumulations are taken at the grid point closest to the observation stations. The red, black and grey lines show the P3_MOD linear regression, the P3_ORIG linear regression and the 1-to-1 relationship, respectively.

Table 2.1 Icing periods for each sub-region.

Sub-region	First icing period	Second icing period
A	0000 5 Jan. to 1200 7 Jan.	2000 7 Jan. to 0600 10 Jan.
B	1800 5 Jan. to 1200 7 Jan.	2000 7 Jan. to 0600 10 Jan.
C	0300 6 Jan. to 1800 6 Jan.	0000 9 Jan. to 0600 10 Jan.
D	-	1200 8 Jan. to 0600 10 Jan.

Table 2.2 Biases and root mean square error (RMSE) [mm] between simulated and observed total accumulated precipitation of Fig. 2.18.

		P3_ORIG	P3_MOD
Total	Bias	14.2	14.1
	RMSE	25.4	24.8
Total liquid	Bias	15.7	14.4
	RMSE	24.5	22.7
Total solid	Bias	-1.5	-0.2
	RMSE	10.4	10.7
Freezing rain	Bias	14.5	12.4
	RMSE	25.6	23.2

CHAPITRE III

CHANGES IN PRECIPITATION TYPE DISTRIBUTIONS DURING THE 1998 ICE STORM SIMULATED UNDER WARMER CONDITIONS

This chapter is presented in the format of a scientific article that will be submitted to *Atmospheric Research*. The detailed reference is:

Cholette, M. and Thériault, J.M. (2019). Changes in precipitation type distributions during the 1998 Ice Storm simulated under warmer conditions. *To be submitted to Atmospheric Research.*

Abstract

Winter precipitation types commonly observed at the surface when the temperatures are near 0°C are snow, freezing rain, ice pellets, wet snow and rain. Damages to infrastructure can occur due to ice loading from freezing rain and wet snow accumulations. The intensity and the occurrence of winter storms will change in the future according to the global warming of the Earth system. The goal is to investigate the impacts of a warmer atmosphere on the simulation of winter precipitation types produced during a winter storm: the 1998 Ice Storm. To do that, simulations using the Weather Research and Forecasting (WRF) model coupled with a bulk microphysics scheme predicting the liquid fraction are conducted. The Pseudo-Global-Warming (PGW) approach is used to simulate the same storm under warmer conditions. A general northward-eastward migration of the rain-snow transition is produced and freezing rain is still produced southern Quebec despite warmer conditions. Snow is generally changed in freezing rain whereas ice pellets and freezing rain are generally changed to rain. The topography of southern Quebec affects the position of the melting and refreezing layers aloft as well as the surface precipitation type transition compared to, for example, over the state of Maine where terrain elevations are lower. An overall increase in maximum amounts of rain and freezing rain were produced under warmer conditions. This is a step forward to better understanding the impacts of warmer environmental conditions on the formation of many types of precipitation produced during a winter storm that could occur in the future.

3.1 Introduction

Several precipitation types can occur during winter storms, such as snow, wet snow, ice pellets, freezing rain and rain. Surface icing caused by freezing rain and wet snow can lead to major power outages, disruptions of ground and air transports and injuries to citizens (e.g., Lecompte *et al.* 1998; King and Laplante 2005; Chang *et al.* 2007; Kringlebotn Nygaard *et al.* 2013). Freezing rain and ice pellets are commonly observed in eastern Canada and southern Quebec (e.g., Cortinas *et al.* 2004; Bresson *et al.* 2017; McGray *et al.* 2019) and their occurrences will change in the future (e.g., Lambert and Hansen 2011; Matte *et al.* 2018).

Some studies on the future evolution of freezing rain occurrences with climate change have been conducted so far. First, Lambert and Hansen (2011) used a Global Circulation Model (GCM) with a diagnostic algorithm of freezing rain events. Their results showed a northward relocation of freezing rain occurrence as well as an overall decrease in freezing rain event by late 2100 over southern Quebec. Secondly, for the same period of time and region, results of Cheng *et al.* (2011) showed an overall increase in the frequency of freezing rain event using statistical downscaling of GCM simulations and a diagnostic algorithm to determine the surface precipitation types. Thirdly, Klima and Morgan (2015) conducted an idealized experiment by adding several perturbations on historical vertical profiles of temperature over the United States including those at Maniwaki in Quebec. Their results mainly showed a northward transition of freezing rain and an increase of freezing rain potential for winter months in southern Quebec. Lastly, results of Matte *et al.* (2018) showed a decrease of freezing rain occurrence by late 2100 in southern Quebec using multiple diagnostic algorithms to determine the precipitation types projected by the fifth generation of the Canadian Regional Climate Model (Hernández-Díaz *et al.* 2013). None of those studies conducted simulations with detailed microphysics parameterizations, an important issue for long-term projections of surface precipitation types (Matte *et al.* 2018) due to the increasing numerical cost when used.

More recent efforts have been made to study the impacts of climate change on precipitation types and their extremes with convection-permitting models (CPCM) (e.g., Chan *et al.* 2013; Prein *et al.* 2013; Ban *et al.* 2014; Fosser *et al.* 2014; Prein *et al.* 2015; Kendon *et al.* 2017). Those models are used at very high resolution (<4 km) and allow the use of microphysics parameterizations and deep explicit convection. Despite the main improvement of the winter precipitation pattern due to the better resolved orography in CPCMs (Prein *et al.* 2015) very few studies have been focusing on winter precipitation (Ikeda *et al.* 2010; Liu *et al.* 2011; Rasmussen *et al.* 2011) and none were conducting on freezing rain and ice pellets events in particular.

Freezing rain and ice pellets are formed during cold seasons when there is a melting layer (T>0°C) aloft and a refreezing layer (T<0°C) below it (e.g., Stewart 1992; Stewart 1985; Stewart and King 1987; Zerr 1997; Ressler *et al.* 2012). Depending on whether solid precipitation falling in the melting layer aloft melts partially or completely, it will lead to ice pellets or freezing rain at the surface, respectively (Stewart *et al.* 1990; Zerr 1997; Thériault *et al.* 2006). When those mixed-phase particles from partial melting (Fujiyoshi 1986) are formed they undergo phase changes, which alter the environmental temperature. The diabatic cooling of melting snow acts to cool the environmental air to 0°C (e.g., Stewart *et al.* 1984) whereas the refreezing of particles leads to an increase of the temperature to 0°C (e.g., Lackmann *et al.* 2002). This can alter the precipitation type of freezing rain or ice pellets by snow, wet snow or rain instead. Other microphysical processes such as the collection among particle types and phase can alter the type of precipitation at the surface.

To simulate explicit mixed-phase particles involved in formations of several precipitation types, such as ice pellets, freezing rain and wet snow, the bulk microphysics parameterization must include the prediction of the liquid fraction. The bulk liquid fraction is defined as the ratio of the liquid mass over the total mass of a mixed-phase particle. The implementation of the bulk liquid fraction on mixed-phase particles into the Predicted Particle Properties (P3; Morrison and Milbrandt 2015) microphysics scheme has been made and described in Cholette *et al.* (2019).

Given that a 1°C change can alter the precipitation types from liquid to solid or vice versa (Frick *et al.* 2013; IPCC 2013; Thériault *et al.* 2010) and changes the occurrences, intensities and phases of winter precipitation types (Cheng *et al.* 2007; Cheng *et al.* 2011; Lambert and Hansen 2011; Klima and Morgan 2015; Kämäräinen *et al.* 2018; Matte *et al.* 2018), the objective is to assess the impacts of warmer environmental conditions on the formation and distribution of various precipitation types during an extreme winter storm using the predicted bulk liquid fraction on mixed-phase particles of P3. To address this, the Pseudo-Global-Warming approach (Schär *et al.* 1996) is used to simulate, under warmer conditions, one of the costliest natural disaster in Canadian history, the 1998 Ice Storm using the P3 scheme and the predicted bulk liquid fraction (Cholette *et al.* 2019). This storm is well documented (Laflamme and Périard 1998; Lecompte *et al.* 1998; Milton and Bourque 1999; Cober *et al.* 2001; Gyakum and Roebber 2001; Roebber and Gyakum 2003; Henson *et al.* 2007; Henson *et al.* 2011; Cholette *et al.* 2019 in prep). To the best of our knowledge, this approach has never been used before to simulate a high-impact freezing rain and ice pellets winter storm, particularly with a detailed microphysics representation of mixed-phase particles.

This paper is organized as follows. Section 3.2 describes the experimental design including the case description of the 1998 Ice Storm, the model and the Pseudo-Global-Warming configurations. Section 3.3 compares the simulated precipitation type characteristics under current and warmer conditions both at the surface and at the vertical. Section 3.4 analyzes the influence of the topography on the precipitation type transition of the storm. Lastly, section 3.5 presents the conclusions.

3.2 Experimental Design

Two simulations of the 1998 Ice Storm using the configuration described below are performed. The first one is the simulation of the historical storm under its atmospheric conditions of the past, hereafter called CUR. The second one is the simulation of the storm under warmer and moister atmospheric conditions using the Pseudo-Global-Warming approach, hereafter called PGW. First an overview of the case study is made in the following section 3.2.1.

3.2.1 Overview of the 1998 Ice Storm

The 1998 Ice Storm occurred from 4 to 10 January 1998. The maximum accumulated freezing rain (~110 mm) was located in southern Quebec (Lecompte *et al.* 1998; Milton and Bourque 1999). The successive passages of low-pressure systems and the quasi-stationary front extending from southern Ontario to the Maritime Provinces led to relatively warmer and moister air flow aloft, which produced favourable conditions for freezing rain and ice pellets (Roebber and Gyakum 2003). The total accumulated freezing rain extended from southeastern Ontario to Nova Scotia, including southern Quebec, Maine and New Brunswick. Two periods of significant freezing rain accumulation occurred in southern Quebec (Henson *et al.* 2011). The first icing period was mainly between 0000 UTC 5 January and 0000 UTC 7 January, and the second was between 0000 UTC 8 January and 0000 UTC 10 January. The second icing period was characterized by a more widespread region of precipitation and higher precipitation accumulations including freezing rain and ice pellets (Roebber and Gyakum 2003). The height of the upper and lower 0°C-isotherms were lower during the first icing period compared to the second one (Henson *et al.* 2011). More details about the 1998 Ice Storm meteorological overview can be found in Milton and Bourque

(1999), Gyakum and Roebber (2001), Roebber and Gyakum (2003), Henson *et al.* (2007), Henson *et al.* (2011) et Cholette *et al.* (2019 in prep).

3.2.2 Model configuration

This study uses the Weather Research and Forecasting (WRF) model version 3.9.1.1 (Skamarock and Klemp 2008). WRF is a non-hydrostatic compressible atmospheric model. The domain of simulation, shown in Fig. 3.1, is the same as in Cholette *et al.* (2019 in prep) and covers the region of southern Quebec extending from Lake Ontario to almost all of New Brunswick. It has 352×352 horizontal grid points and 3 km horizontal grid spacing. The red square in Fig. 3.1 shows the analysis domain. The number of vertical levels is 56 with a vertical grid spacing varying from 60–320 m in the first 2 km and from 320–340 m between 2 km and 16 km height. The simulated period is from 0600 UTC 4 January 1998 to 0600 UTC 10 January 1998. The time step is 10 s and the model outputs are archived every 30 min. The North American Regional Reanalysis (NARR; Mesinger *et al.* 2006) are used as initial and boundary conditions for CUR. NARR are available every 3 h over North America at 32 km horizontal grid spacing.

Physics parameterizations include microphysics, radiation, planetary boundary layer/turbulent mixing, and surface processes. Short-wave and long-wave radiations are calculated using the General Circulation Model version of the Rapid Radiative Transfer Model (Iacono *et al.* 2008) with a 10 s radiation time step. The Yonsei University nonlocal planetary boundary layer scheme of Hong *et al.* (2006) is employed. Surface processes are calculated using the 5-layers thermal diffusion scheme of Dudhia (1996). The microphysics scheme is P3 including the predicted bulk liquid fraction (Cholette *et al.* 2019).

3.2.3 Pseudo-Global-Warming approach

The evolution of high-impact weather, such as freezing rain events, with climate change can be addressed using the Pseudo-Global-Warming approach. This approach was originally developed by Schär *et al.* (1996) followed by Hara *et al.* (2008) and Kawase *et al.* (2009). It consists of modifying the initial and lateral boundary reanalysis conditions used to simulate past weather events with climate perturbations from a GCM climate projection. For example, it has been used to investigate warmer and moister climate impacts on snow depth (Hara *et al.* 2008), rain bands (Kawase *et al.* 2009), snowfall (Rasmussen *et al.* 2011), water balance headwater (Liu *et al.* 2017; Rasmussen *et al.* 2014), heavy rain events (Taniguchi and Sho 2015; Prein *et al.* 2017), hurricanes (Gutmann *et al.* 2018), and convective population and thermodynamic environments (Liu *et al.* 2017; Prein *et al.* 2017; Rasmussen *et al.* 2017). The advantage of using the Pseudo-Global-Warming approach is that a detailed microphysics parameterization can be used to simulate precipitation characteristics in contrast to GCM projections.

To develop the climate perturbations for NARR driven data, a subtraction between the 30-yr monthly climatology of the past (1976–2005) and future (2071–2100) for the month of January was made. Both current and future climatologies were from the 6-hourly Community Climate System Model (CCSM4; Meehl *et al.* 2012) of the Coupled Model Intercomparison Project Phase 5 (CMIP5) simulations (available online: https://www.earthsystemgrid.org/) under the Representative Concentration Pathway (RCP) 8.5 scenario (Meinshausen *et al.* 2011). The NARR atmospheric variables that have been modified in PGW are air temperature, relative humidity, geopotential height, horizontal wind components, sea surface temperature, mean sea level pressure and soil layers temperature.

3.2.4 Results analysis

The simulated differences between CUR and PGW in atmospheric variables are given in Appendix (section 3.6) and the next section (3.3) analyzed the differences in precipitation type distributions. First, the changes in accumulated precipitation rates and types at the surface are compared in section 3.3.1. Second, the evolution of the precipitation type transition region along a cross-section is investigated in section 3.3.2. The location of the cross-section is shown in Fig. 3.1 (red dotted line). It passes over the St. Lawrence River Valley (SLRV; all acronyms are defined in the list of acronyms) and the Montreal Pierre-Elliott-Trudeau international airport (YUL). It covers a distance of ~575 km from the Appalachians (mountains south of the SLRV) to the Laurentians (mountains north of the SLRV).

The influence of the topography on the surface precipitation type transition is investigated in section 3.4. To do that, results of the distance associated with a melting layer aloft and a refreezing layer below it as well as the changes in precipitation type transition of the cross-section over southern Quebec (QC) (Fig. 3.1; red dotted line) are compared to those of the cross-section over Maine (ME) of smaller terrain elevations (Fig. 3.1; blue dotted line).

3.3 Comparison between CUR and PGW precipitation types

3.3.1 Changes in precipitation at the surface

The changes in amounts and location of precipitation maxima in PGW compared to CUR are shown in Fig. 3.2. The amount of liquid precipitation (Figs. 3.2d-f) increased by about ~50% whereas the amount of solid precipitation (Fig. 3.2g-i) decreased by about ~40% in PGW compared to CUR. The maximum amount of liquid precipitation is similarly located to CUR but it is higher, while the maximum amount of solid precipitation is lower and located north-eastward (~60 km eastward and ~105 km northward). There is a wider (narrower) north-south distribution of liquid (solid) precipitation by ~90 km (~105 km) in PGW compared to CUR. Similar results as for solid and liquid precipitations are obtained for snow (Figs. 3.3a-c) and rain (Figs. 3.3m-o), respectively. The maximum amount of ice pellets (Figs. 3.3g-i) decreased by ~20% cm in PGW and moved north-eastward near Quebec City (YQB) compared to CUR. An increase (by about ~35%) in the amount of wet snow is produced in PGW compared to CUR mainly due to surface temperatures above 0°C (see section 3.6). Maximum amounts of freezing rain (Figs. 3.3j-l) are mainly located north-eastward (near YQB) and in central ME in PGW compared to CUR. The maximum amount of freezing rain is higher of ~50% in PGW compared to CUR in ME. However, domain-averaged accumulated freezing rain is reduced by ~20% in PGW compared to CUR. Overall, there is an increase (decrease) of freezing precipitation (i.e., freezing rain and ice pellets) in northern (southern) regions in PGW.

The PGW percentage of each precipitation type relative to the total accumulation is compared to CUR accumulated precipitation types in Fig. 3.4. For each grid point of the analysis domain, PGW precipitation type percentage is calculated as a function of each CUR precipitation type and the mean values over every CUR 5 mm-bin are shown in Fig. 3.4. A mixture of precipitation types is common in PGW when snow is produced in CUR (Fig. 3.4a): snow accumulations <5 mm in CUR changed to rain whereas accumulated snow of >30 mm changed to freezing rain. Most of the accumulated rain in CUR remained mainly in rain in PGW (Fig. 3.4b). Also, high amounts of freezing rain (Fig. 3.4d; >20 mm) and ice pellets (Fig. 3.4c; >15 mm) in CUR changed to rain in PGW, while a mixture of precipitation types is obtained for smaller amounts, mainly freezing rain or rain. For instance, small relative amounts of snow, ice pellets and wet snow are obtained in PGW when ice pellets and freezing rain are smaller than 15 mm and 10 mm, respectively in CUR. Wet snow in CUR is changed in mainly rain and freezing rain (Fig. 3.4e). Overall, precipitation types composed of liquid or supercooled liquid, such as rain, freezing rain and wet snow changed to rain in PGW, while solid precipitation, such as snow and ice pellets, become a mixture of precipitation types with a higher relative amount of freezing rain.

The temporal evolution of domain-averaged surface precipitation rates of each precipitation type in CUR and PGW as well as their differences (PGW–CUR) are shown in Fig. 3.5. The timings of the two main freezing rain periods are similar in both simulations (Fig. 3.5a). The rainfall rate (Fig. 3.5a) is higher in PGW compared to CUR, while the snowfall rate (Fig. 3.5b) is lower (Fig. 3.5c) over the simulated period. Freezing rain and ice pellets rates are similar in both simulations with some variations during the event (Fig. 3.5c).

3.3.2 Changes in precipitation type transition along a cross-section

The precipitation type transition, microphysical variables as well as the mean 0°C-isotherm are analyzed over a north-south vertical cross-section passing through the SLRV (red dotted line in Fig. 3.1). The analysis is divided between the two icing periods because atmospheric conditions (see section 3.6) and precipitation accumulations were different (Henson *et al.* 2011; Cholette *et al.* 2019 in prep).

Figure 3.6 (Fig. 3.7) shows a comparison of the time-averaged precipitation mass mixing ratios between CUR and PGW over specific times within the first (second) icing period when the surface precipitation rates were relatively high (near 0.4 mm h^{-1} for the first icing period and ~0.5 mm h^{-1} for the second icing period according to Fig. 3.5). All mass mixing ratios are higher during the second icing period compared to the first one. In general, averaged maxima of all mass mixing ratios are higher in PGW compared to CUR. However, in PGW, less ice reaches the surface north of YUL due to the presence of a deep melting layer aloft that produced rain or freezing rain instead.

During the first icing period (Fig. 3.6), total and rime ice mass mixing ratios ($q_{i,tot}$ and $q_{i,rim}$, respectively) above the melting layer are higher where the surface precipitation type is mainly freezing rain (rain) in CUR (PGW) along the cross-section. For the second icing period (Fig. 3.7), $q_{i,tot}$ and $q_{i,rim}$ above the melting layer are higher where the surface precipitation type is rain (-220 km to -100 km from YUL) in both CUR and PGW. For both icing periods, the produced liquid on ice and rain mass mixing ratios ($q_{i,liq}$ and q_{rain}, respectively) in the melting layer are higher where $q_{i,tot}$ and $q_{i,rim}$ above the melting layer are higher. For both icing periods, the locations along the cross-section of ice pellets (Figs. 3.6m-o and 3.7m-o) moved northward in PGW compared to CUR. For example, during the second icing period in CUR (Fig. 3.7), the region of ice pellets is located over the SLRV (30 km<YUL<50 km), while it is located over the Laurentians (165 km<YUL<220 km) in PGW.

The general mean values of 12-hourly-averaged (for each icing period) temperature and microphysical variables over each grid point along the cross-section (Fig. 3.1; red dotted line) are computed to link the surface precipitation to the rime mass fraction at the model level above the melting layer and the temperature needed to melt ice completely (shown in Fig. 3.8). The mean temperature to melt ice completely (Figs. 3.8a-b; only for rain and freezing rain surface precipitation types) is related to the rime mass fraction and $q_{i,tot}$ (not shown) above the melting layer. In general, an increase in the rime mass fraction is associated with higher temperatures required to melt ice completely. However, the temperature to melt ice completely also depends on the values of $q_{i,tot}$. This is obtained during the second icing period compared to the first icing period and in PGW compared to CUR. The maximum mean temperature at which ice melted completely is 3.7°C when rain occurred at the surface in PGW and during the second icing period. The mean rime mass fraction just above the melting layer aloft is higher during the second icing period (Fig. 3.8d) compared to the first one (Fig. 3.8c) in both CUR and PGW when rain and freezing rain reaches the surface. The rime mass fraction aloft is higher when rain (freezing rain) reaches the surface in PGW (CUR) during the first icing period. For the second icing period, the rime mass fraction aloft is similar when both rain and freezing rain reach the surface along the cross-section in CUR. In general freezing rain in CUR along the cross-section is converted to rain in PGW and the maximum rime mass fraction aloft is when rain reaches the surface in PGW compared to freezing rain in CUR. For all surface precipitation types, the rime mass fraction aloft is higher in PGW compared to CUR due to more rime growth, also reported in Rasmussen *et al.* (2011).

3.4 Effect of the topography on precipitation type transition

3.4.1 Surface elevation and precipitation type

The topography can influence the surface temperature and then on the occurrence of freezing rain at the surface. Figures 3.9a-b show the domain time-averaged surface temperature as a function of the terrain elevation. The surface temperature distribution is similar between PGW and CUR but shifted towards warmer temperatures for a given elevation in PGW. While the covered range of surface temperatures is between -16.4°C to 7.6°C in CUR, it is between -10.3°C to 12.2°C in PGW. The mean percentage of elevations with surface temperatures above 0°C is 28% in CUR and 50% in PGW, leading to an increase (decrease) of 22% of the number of grid points with surface temperatures above (below) 0°C in PGW compared to CUR. This impacts, for example, the accumulated wet snow, which is higher in PGW compared to CUR, in particular at higher elevations (Fig. 3.3).

Figures 3.9c and 3.9e show CUR, PGW and Figs. 3.9d and 3.9f the difference between PGW and CUR domain-averaged accumulated precipitation types as a function of the terrain elevation (binned every 25 m). Accumulated liquid precipitation is higher in PGW compared to CUR at every elevation while solid precipitation, including snow, are lower at every elevation. Maximum amount of freezing rain occurs at ~75 m in CUR and ~175 m in PGW. At elevations <175 m, there is a decrease in freezing rain amount in PGW compared to CUR while there is a general increase at elevations >175 m. There is an increase in ice pellets amount in PGW compared to CUR at elevations >600 m. As seen with Fig. 3.3 this corresponds to the amount of ice pellets north of YQB.

3.4.2 Atmospheric conditions aloft and precipitation type transition

To show the impact of topography on the precipitation type transition, time-averaged of accumulated precipitation over two cross-sections are compared. These are passing over QC (Fig. 3.1; red dotted line) and ME (Fig. 3.1; blue dotted line) and they are chosen because the elevations along the cross-sections are different. Figures 3.10a-b show temporal evolution of 12-hourly-averaged distance along both cross-sections associated with a melting layer aloft and a refreezing layer near the surface for both CUR and PGW. This distance varies in time over QC while it is mainly increasing in time over ME for both simulations. Figures 3.10c-d show the 0°C-isotherm averaged over both icing periods for both simulations and both cross-sections. The melting layers are generally deeper over ME compared to QC for both icing periods and simulations. The depths of the refreezing layer are similar between QC and ME for the first icing period, while they are deeper over ME compared to QC for the second icing period. This affects the spatial distribution of freezing rain along the cross-section over ME in PGW compared to CUR and compared to QC.

The distance along the cross-section associated with a melting layer aloft and a refreezing layer near the surface is higher in PGW compared to CUR for both cross-sections, however, the difference is higher over QC than ME. For instance, the averaged distance is 156 km (262 km) in CUR (PGW) over QC, while it is 195 km (238 km) for CUR (PGW) over ME. Therefore, the mean distance along the cross-section generally covered by a melting layer aloft is longer in PGW compared to CUR of 43 km over ME and 106 km over QC. This increase along both cross-sections can be explained by the increased warming at lower levels (pressure levels <800 hPa) under the Pseudo-Global-Warming approach (see section 3.6). Those levels generally correspond to where the melting layer is formed and produce a deeper melting layer in PGW compared to CUR. The highest difference between PGW and CUR over QC compared to ME is mainly due to the topography differences of those regions. The refreezing layer near the surface is shallowed south of the SLRV due to the Appalachians in CUR, while this is not the case in PGW due to the northward migration of the melting layer aloft. Over ME, the lower terrain elevations resulted in similar characteristics of the melting layer aloft in PGW and CUR but slightly shifted northward. Lastly, the upward/downward air motions into the Laurentians over QC aided to form melting layers aloft, in particular during the second icing period (see section 3.6; Fig. 3.16) in PGW compared to CUR. This process can potentially lead to an increase in accumulated freezing rain and ice pellets into the Laurentians in warmer conditions.

Figure 3.11 shows time-averaged over the simulated period of CUR and PGW total accumulated precipitation (Figs. 3.11a-b) as well as their difference (PGW–CUR; Figs. 3.11c-d) along both cross-sections. Total accumulated liquid (solid) is higher (similar) over QC compared to ME (Figs. 3.11a-b). The maximum amount of liquid precipitation reached 150 mm (95 mm) over QC, and 122 mm (75 mm) over ME in PGW (CUR). More accumulated liquid and rain is produced in PGW compared to CUR, with less solid precipitation (Figs. 3.11c-d). More freezing rain occurred over QC in CUR but it decreases in PGW (Figs. 3.11a and c). In contrast, the amount of freezing rain increased over ME in PGW compared to CUR (Fig. 3.11d). There is a decrease in accumulated ice pellets in the SLRV (Fig. 3.11c) in PGW compared to CUR, while there are similar amounts between CUR and PGW over ME (Fig. 3.11b). The ice pellets transition extends over a longer distance in PGW compared to CUR along both cross-sections.

Accumulated freezing rain and ice pellets are shifted northward along both cross-sections in PGW compared to CUR. Over QC, the distance along the cross-section covered by the maximum amount of total accumulated precipitation in CUR (-55 km<YUL<55 km) shifted over the Appalachians in PGW (-165 km from YUL to -100 km). The CUR freezing rain surface precipitation type changed to rain in PGW. Over ME, the distance along the cross-section covered by the maximum amount of accumulated precipitation is similar between CUR and PGW (near 110 km to 220 km from ATL-O), with freezing rain as the main precipitation type in both simulations. Large amounts of freezing rain occurred over a common spatial distribution over ME (near 110 km to 220 km from ATL-O) between CUR and PGW.

3.5 Conclusions

Recently, the predicted liquid fraction has been implemented in the Predicted Particle Properties (P3) bulk microphysics scheme (Cholette *et al.* 2019) to allow the explicit simulations of mixed-phase particles and their microphysical processes. These particles are important to get feedback mechanisms between phase changes and air temperature involved in the formations of several winter precipitation types, such as wet snow, ice pellets and freezing rain (Cholette *et al.* 2019). As these precipitation types are generally formed at near 0°C, their occurrence and phase are expected to change under climate change. Investigating the impacts of warmer atmospheric conditions on freezing rain and ice pellets winter storms is challenging mainly because of they are related to small-scale processes at temperatures near 0°C.

The objective was to assess the impacts of warmer environmental conditions on the distribution of various precipitation types produced during a major winter storm using the predicted bulk liquid fraction on mixed-phase particles. To this end, WRF simulations of the extreme 1998 Ice Storm under its current climate and under warmer conditions simulated with the Pseudo-Global-Warming approach were compared.

Results showed a northward-eastward migration of the rain-snow transition under warmer conditions. In general, snow changed to freezing rain whereas ice pellets and freezing rain changed to rain. This, however, is when accumulated precipitations were >~20 mm in the current climate simulation related to change in size distribution as suggested by Thériault *et al.* (2010). In some regions, large amounts of freezing rain are obtained in both simulations. For example, in Maine ~70 mm (~130 mm) of freezing rain accumulated in current (warmer) conditions. More wet snow was produced in warmer conditions due to higher occurrence of surface temperatures near 0°C, in particular in mountainous regions. In general, all mass mixing ratios (rain/freezing rain, total of ice, rime and liquid on ice) increased under warmer conditions as in Rasmussen *et al.* (2011) according to moister environmental air. However, less solid precipitation ($q_{i,tot}$) reached the surface due to a deeper melting layer aloft leading to freezing rain instead. Both the rime mass fraction above the melting layer aloft and the temperature to melt ice completely were higher during the second icing period in the two simulations. The temperatures to melt ice completely have increased in warmer conditions, mainly because of the increased rime mass fraction of ice aloft.

Lastly, the topography affected the distance associated with a melting layer aloft and a refreezing layer below it and, therefore, the surface precipitation type transition of the storm along cross-sections. For instance, the topography of southern Quebec (the SLRV bordered by the Appalachians to the south and the Laurentians to the north) has led to a higher increase of this distance under warmer conditions when compared to the Maine region associated with smaller terrain elevations. The distance was 106 km longer over Quebec in contrast to 43 km over Maine under warmer conditions. This combined with a deep refreezing layer in Maine, especially during the second icing period, has resulted in a wide surface distance along the cross-section (~100 km) of increased freezing rain accumulations under warmer conditions.

Overall, this study addresses for the first time the changes in precipitation types during a major freezing rain event in warmer climate conditions. Further investigations should be conducted with a series of storm as well as with several other Pseudo-Global-Warming configurations, such as other RCP, the use of an ensemble of climate model as driven data and the use of many microphysics schemes. This is nevertheless a step towards a better understanding of the changes into small-scale processes leading to freezing rain and ice pellets in future warmer and moister conditions.

Acknowledgments

The authors would like to thank the funding agencies, Canadian Network for Regional Climate and Weather Processes (CNRCWP) funded by the Natural Sciences and Engineering Research Council of Canada (NSERC) as well as the NSERC Discovery grant and a Canadian Research Chair Tier 2. The first author (MC) would like to thank Fonds de recherche du Québec – Nature et technologies (FQRNT) for a fellowship. The computations were made on the supercomputer cedar managed by Calcul Québec and Compute Canada. The authors also want to thank Kyoko Ikeda and Changhai Liu from the National Center for Atmospheric Research for their help building the climate perturbations of the Pseudo-Global-Warming configuration.

3.6 Appendix: PGW and CUR simulated atmospheric variables

This appendix aims at illustrating the impacts of the Pseudo-Global-Warming approach on the simulated atmospheric variables, such as temperature and wind fields. Figure 3.12 shows time-averaged temperature, water vapor mixing ratio and horizontal wind speed over the simulated period of the lowest model level of CUR, PGW and their differences (PGW–CUR). The mean surface temperature is increased by about 3°C to 5°C over the analysis domain in PGW with a spatial mean temperature difference between PGW and CUR of +4.7°C. While mean temperature is below freezing into the entire SLRV in CUR, it is above freezing and less than 2°C in PGW for the half-southern portion of the SLRV. The warming is smaller in the Appalachians. The increase in mean temperature leads to an increase in water vapor mass mixing ratio of about 0.6 g kg^{-1} to 1.8 g kg^{-1} in PGW with a spatial mean difference between PGW and CUR of +1.3 g kg^{-1}. The increase of water vapor mass mixing ratio is higher in the south where the availability of water vapor is higher.

As shown in Figs. 3.12g-h, horizontal surface winds are generally stronger within the SLRV in PGW compared to CUR. An overall increase of the wind speed is obtained except in ME, in VT and over the Atlantic Ocean. The maximum increase of horizontal wind speed is obtained south-west of the analysis domain and over south-eastern Quebec. The mean difference between PGW and CUR in surface horizontal wind speed is +0.2 m s^{-1}. Low-level wind roses at three different locations along the SLRV are shown in Fig. 3.13. For YQB, winds are almost always from north-east, while they vary from north-northeast to north-east at YUL and YOW, respectively. In general, the low-level winds are stronger in PGW than in CUR, except at YUL, where they are similar.

Figure 3.14 shows the difference between PGW and CUR in domain-averaged vertical profiles of temperature, and water vapor, total ice and rain mass mixing ratios every

12 hours. Changes in temperature (Fig. 3.14a) and water vapor mixing ratio (Fig. 3.14b) between PGW and CUR are maximum at lower pressure levels (i.e., $<$800 hPa). In agreement with the CCSM4 projections (Meehl *et al.* 2012), there is cooling in PGW compared to CUR at pressure levels above 150 hPa. Changes in temperature are quasi-isothermal between 800 hPa to 250 hPa (+~3.5°C). Maximum changes in water vapor mixing ratio is around 900 hPa to 800 hPa, and then smaller above, until 100 hPa. While upper pressure levels (Fig. 3.14c; $<$600 hPa) get higher $q_{i,tot}$, lower pressure levels (Fig. 3.14c; $<$600 hPa) get lower $q_{i,tot}$ in PGW compared to CUR. Rain mass mixing ratio (Fig. 3.14d) is higher in PGW compared to CUR at any pressure $<$600 hPa. Differences in all variables are higher on 1200 UTC 8 January (blue dashed line), corresponding to the time of high surface precipitation rates (Cholette *et al.* 2019, in prep). Also seen with Figs. 3.14c-d, the melting height is higher during the second icing period (dashed lines) compared to the first icing period (solid lines).

Figure 3.15 shows vertical structures of PGW temperature and the difference between PGW and CUR as well as the surface temperature along the cross-section of Fig. 3.1 (red dotted line) time-averaged over both icing periods. In both CUR and PGW, the melting layer is deeper and the top of the melting layer is higher during the second icing period compared to the first one (Figs. 3.15a-b) (Henson *et al.* 2011; Cholette *et al.* 2019, in prep). The warming induced by the Pseudo-Global-Warming approach is higher at lower model levels. While there is a melting layer aloft across the SLRV (-50 km$<$YUL$<$100 km) in CUR (Figs. 3.15c-d), it is only present over half of the SLRV in PGW (from near YUL up to 100 km north of YUL). Also, the distance along the cross-section associated a melting layer aloft and a refreezing layer below it is longer in PGW compared to CUR. For instance, without the Appalachians Mountains, the presence of the refreezing layer near the surface would have been further south in CUR (near -165 km from YUL). The surface temperatures (Figs. 3.15e-f) are similar between the two icing periods, with generally warmer surface temperatures during the second icing period. South of the SLRV (<-50 km from YUL), the surface temperatures are above 0°C while north of the SLRV (>100 km from YUL) they are generally below 0°C. The differences between PGW and CUR in surface temperature are higher into the SLRV and north of the SLRV.

CUR and PGW vertical structures of the horizontal wind speed and direction as well as vertical air motions are shown in Fig. 3.16. The horizontal wind speed and direction (Figs. 3.16a-d and e-h, respectively) are similar between CUR and PGW, but different between the two icing periods. For instance, the horizontal wind speed is generally stronger during the second icing period (Cholette *et al.* 2019, in prep). At above 2 km, wind direction rotated from the south-west to the south from the first to the second icing period. Low-level horizontal winds from -55 km<YUL<up to 330 km are from the north and north-east for both icing periods, but stronger during the second icing period, in particular into the SLRV. The vertical air motions (Figs. 3.16i-l) are stronger during the second icing period, in particular over the Laurentians (from 90 km to 330 km of YUL). Also, during the second icing period, there are upward air motions aloft (>2 km height) over the Appalachians (from -50 km to -220 km of YUL) in both simulations, but they are stronger in PGW compared to CUR.

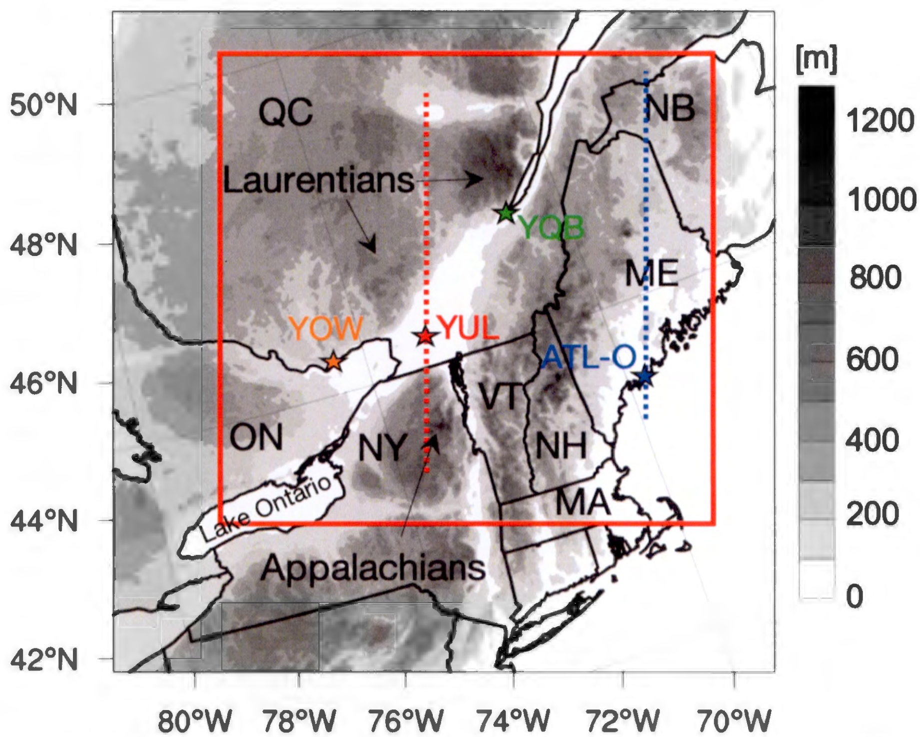

Figure 3.1 Simulation domain topography (grey tones, [m]) and location of the analysis domain (red square). Specific locations are highlighted: Montreal Pierre-Elliott-Trudeau international airport (YUL, red), Ottawa airport (YOW, orange), the point delimiting the American Coast from the Atlantic Ocean (ATL-O, blue) and Quebec Jean-Lesage airport (YQB, green). Canadian provinces and America States are listed in the list of acronyms.

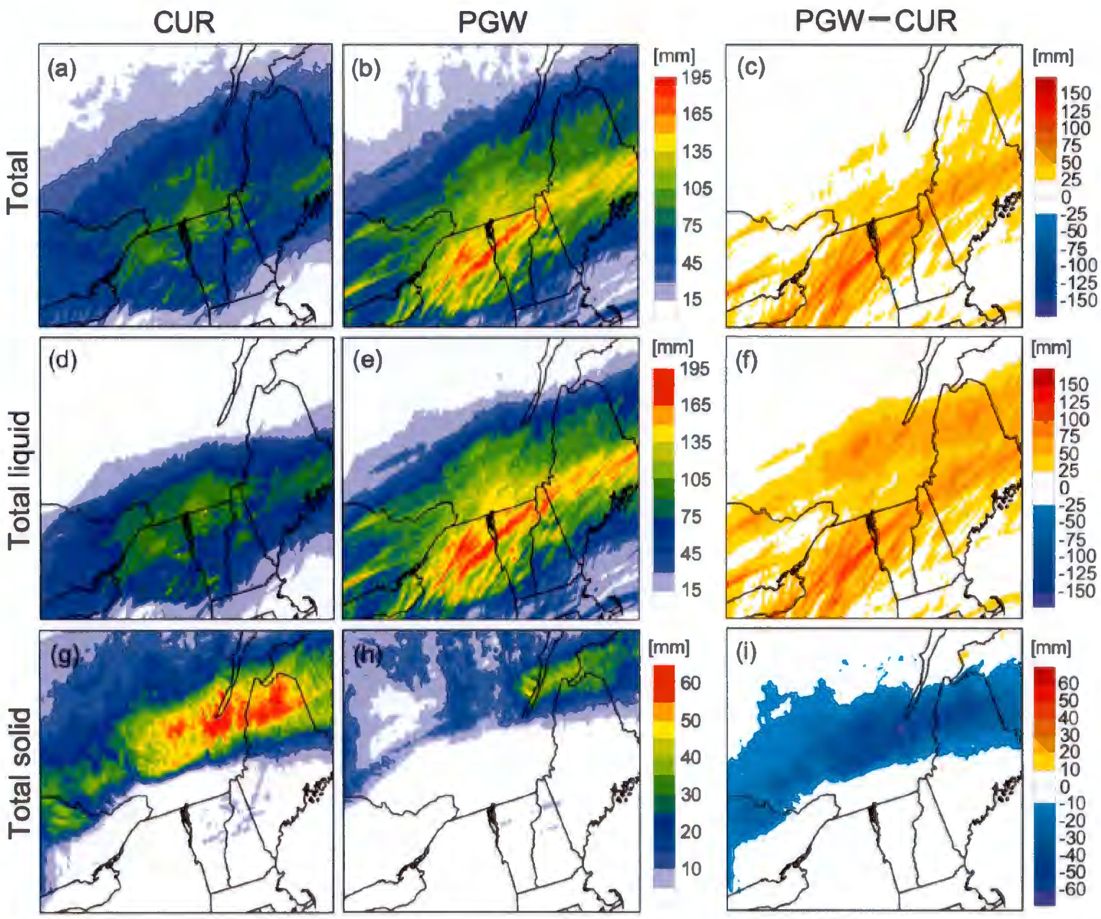

Figure 3.2 CUR (left), PGW (middle) and PGW–CUR (right) total accumulated precipitation [mm] from 0600 UTC 4 January 1998 to 0600 UTC 10 January 1998 of (a)-(c) total, (d)-(f) total liquid and (g)-(i) total solid.

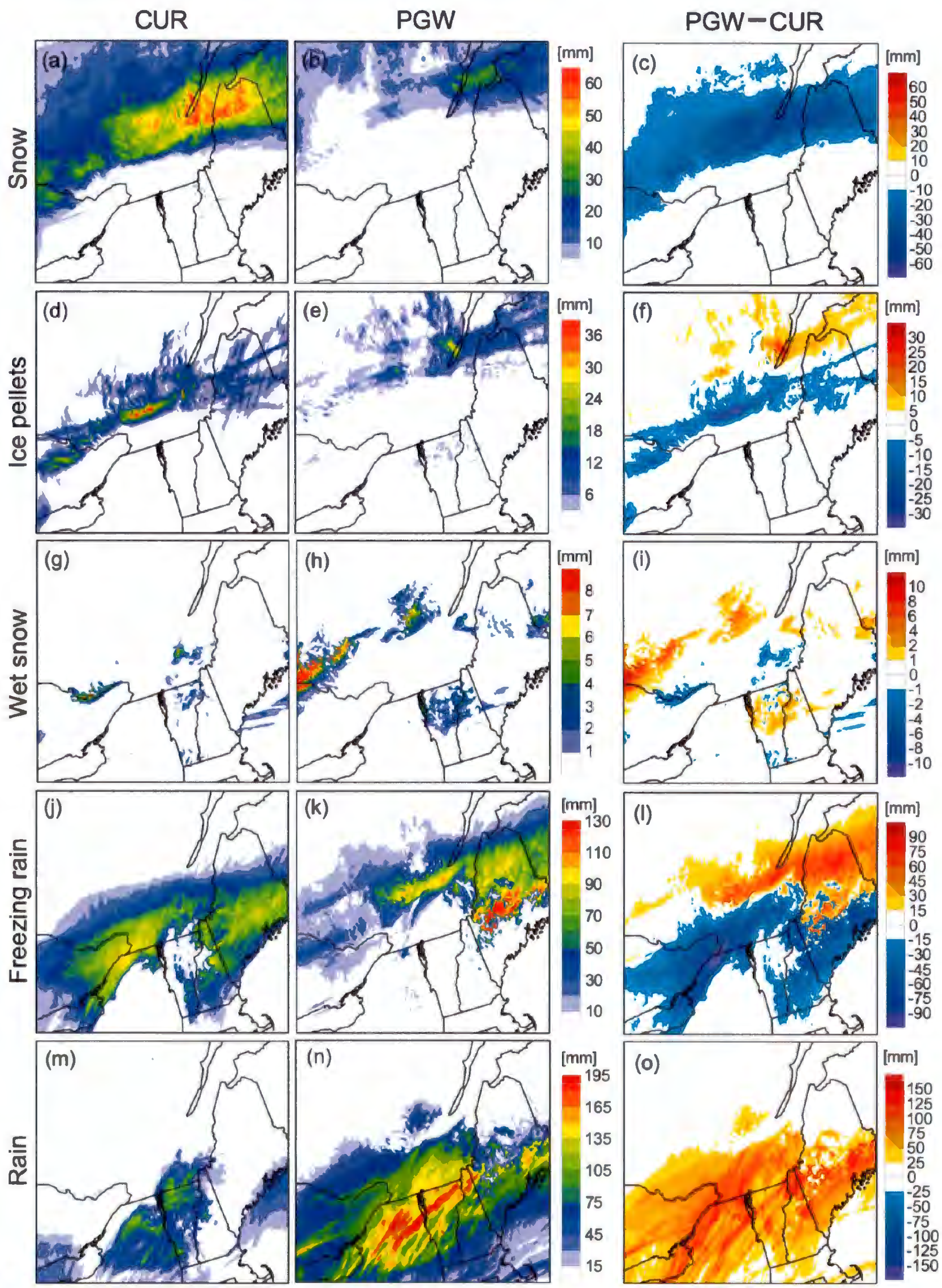

Figure 3.3 CUR (left), PGW (middle) and PGW–CUR (right) total accumulated precipitation [mm] from 0600 UTC 4 January 1998 to 0600 UTC 10 January 1998 of (a)-(c) snow, (d)-(f) ice pellets, (g)-(i) wet snow, (j)-(l) freezing rain and (m)-(o) rain.

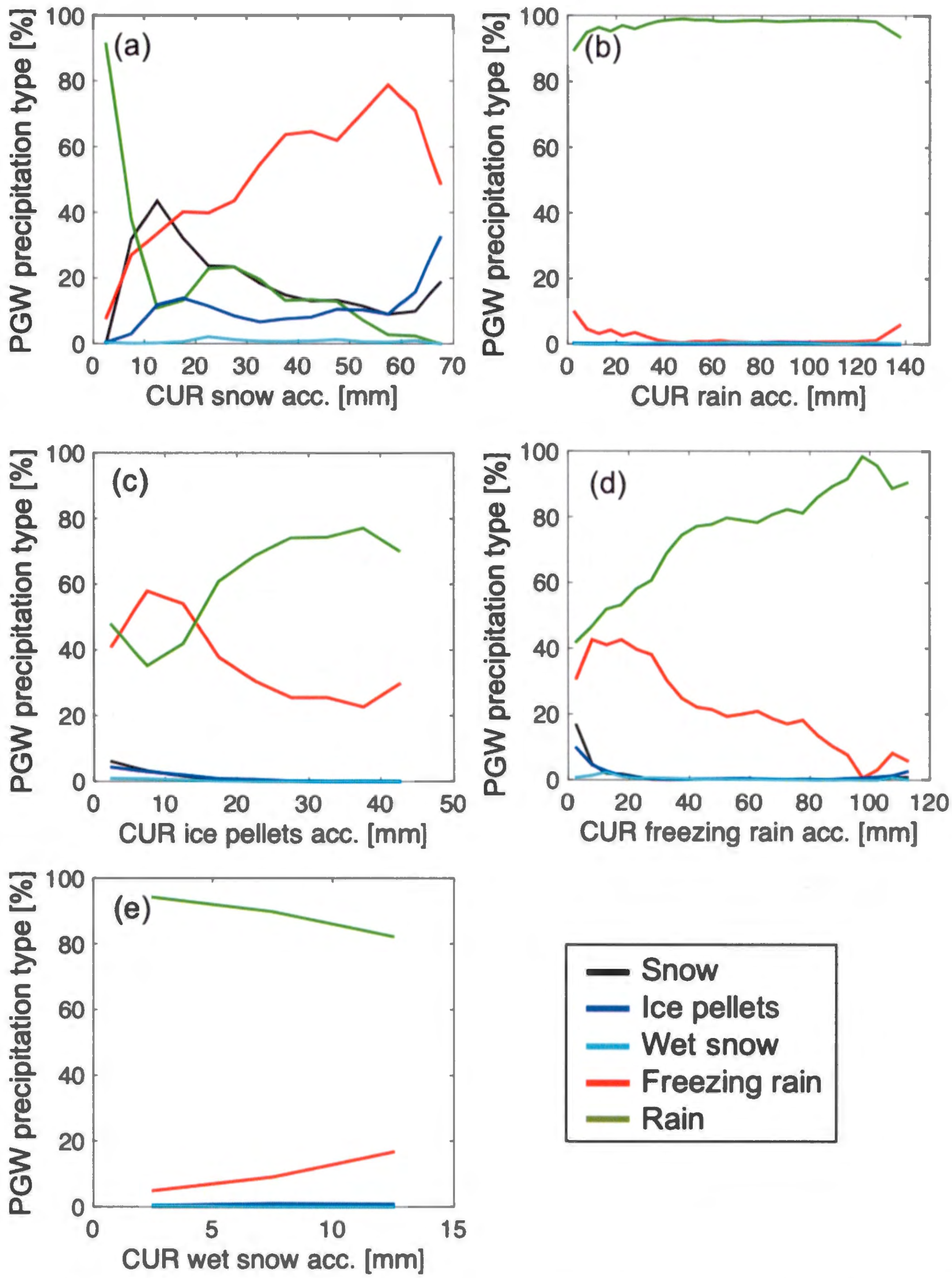

Figure 3.4 PGW total accumulated precipitation type relative to the total accumulation [in %] of snow (black), ice pellets (blue), wet snow (light blue), freezing rain (red) and rain (green) calculated at each grid point of the analysis domain as a function of CUR total accumulated precipitation type [mm] of (a) snow, (b) rain, (c) ice pellets, (d) freezing rain and (e) wet snow binned every 5 mm.

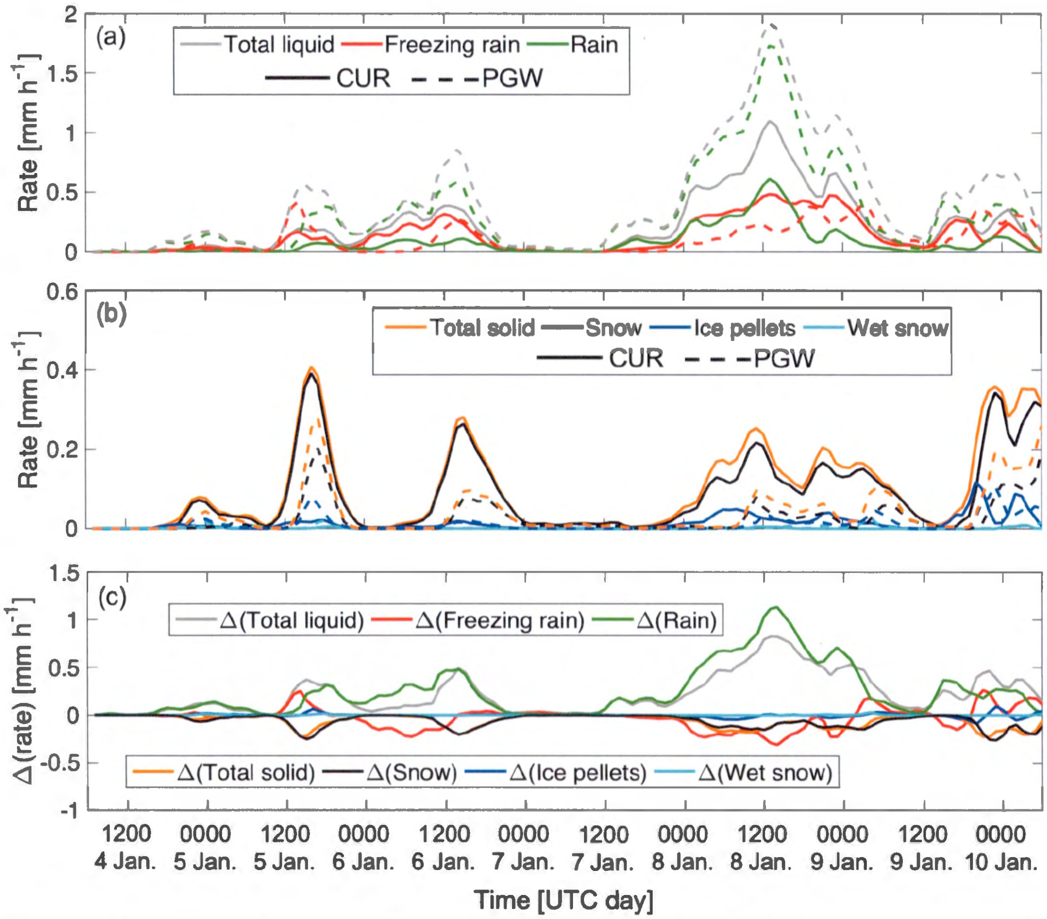

Figure 3.5 Temporal evolution of domain-averaged (a)-(b) CUR (solid) and PGW (dashed) and (c) PGW–CUR surface precipitation rate [mm h^{-1}] of (a), (c) total liquid (grey), freezing rain (red) and rain (green), and (b), (c) total solid (orange), snow (black), ice pellets (blue) and wet snow (light blue).

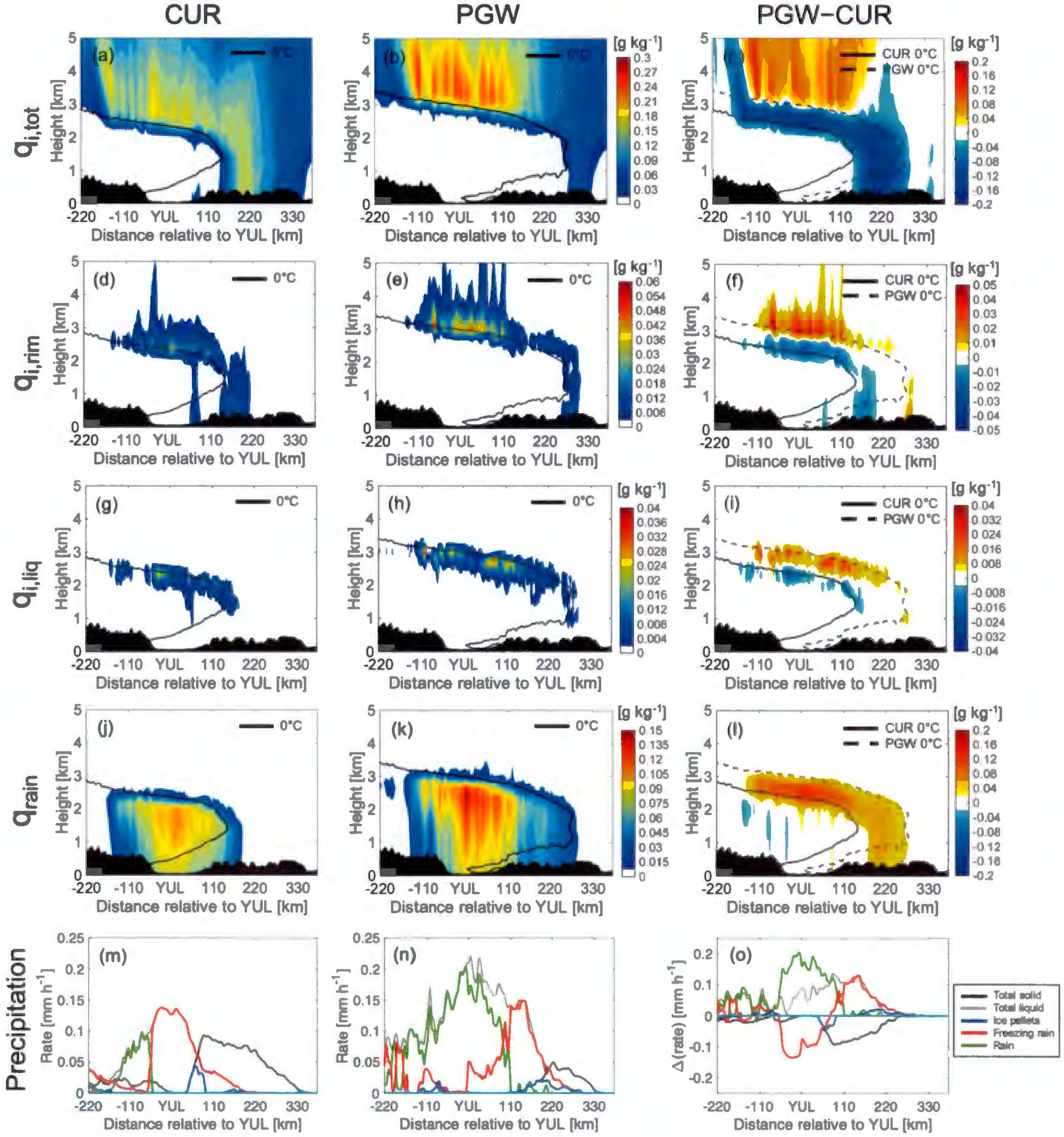

Figure 3.6 CUR (left), PGW (middle) and PGW–CUR (right) vertical structures along the cross-section (red dotted line in Fig. 3.1) of time-averaged from 1800 UTC 5 January 1998 to 1800 UTC 6 January 1998 (a)-(l) 0°C-isotherms (black) superimposed on the mass mixing ratio (colors, [g kg^{-1}]) of (a)-(c) total ice [$q_{i,tot}$], (d)-(f) rime on ice [$q_{i,rim}$], (g)-(i) liquid on ice [$q_{i,liq}$] and (j)-(l) rain [q_{rain}], and (m)-(o) surface precipitation rate [mm h^{-1}] of total solid (black), total liquid (grey), ice pellets (blue), freezing rain (red) and rain (green).

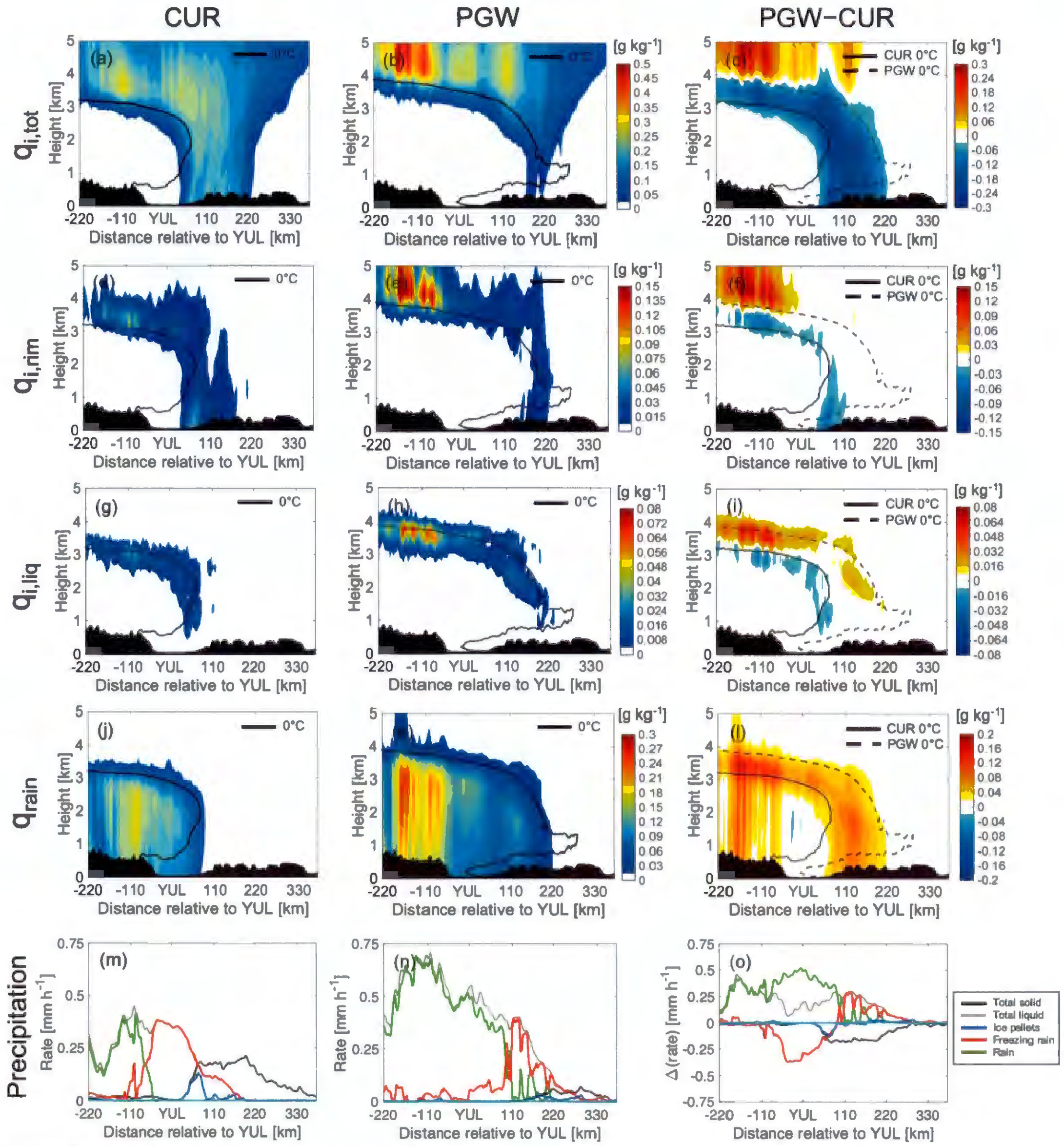

Figure 3.7 Same as Fig. 3.6 but time-averaged from 1800 UTC 7 January 1998 to 0600 UTC 9 January 1998.

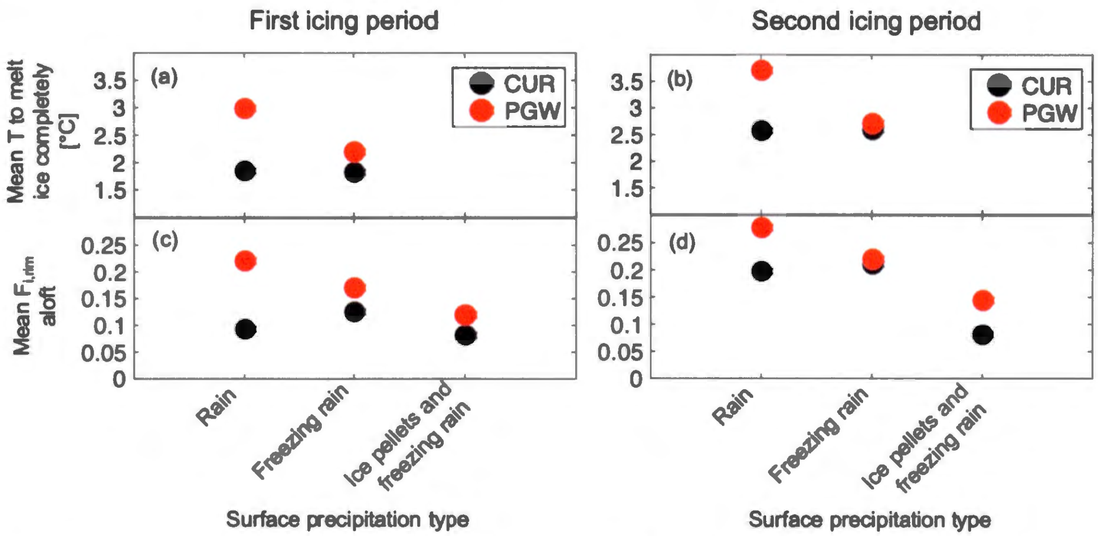

Figure 3.8 12-hourly-averaged over (a), (c) the first icing period (from 0000 UTC 5 January 1998 to 0000 UTC 7 January 1998) and (b), (d) the second icing period (from 0000 UTC 8 January 1998 to 0600 UTC 10 January 1998) CUR (black) and PGW (red) (a)-(b) mean temperature to melt ice completely [T, °C] and (c)-(d) mean rime mass fraction [$F_{i,rim}$] at the model level above the melting layer as a function of the surface precipitation type along the cross-section (red dotted line in Fig. 3.1).

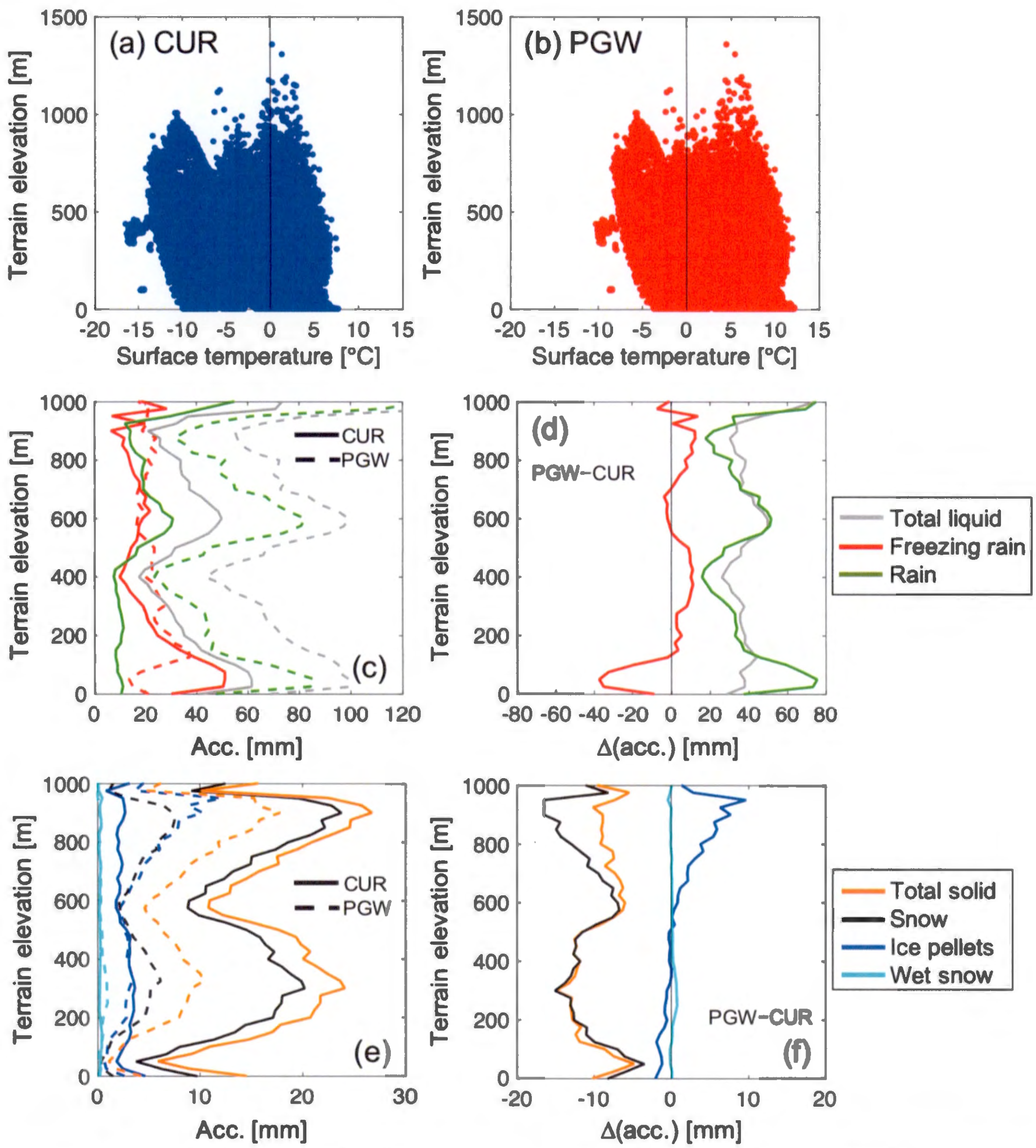

Figure 3.9 (a) CUR and (b) PGW temperature [°C] at the lowest model level time-averaged over the simulated period (from 0600 UTC 4 January 1998 to 0600 UTC 10 January 1998) as a function of the terrain elevation [m] for each grid point of the analysis domain. (c), (e) CUR (solid) and PGW (dashed), and (d), (f) PGW–CUR total accumulated precipitation [Acc., mm] from 0600 UTC 4 January 1998 to 0600 UTC 10 January 1998 of (c)-(d) total liquid (grey), freezing rain (red) and rain (green), and (e)-(f) total solid (orange), snow (black), ice pellets (blue) and wet snow (light blue) as a function of the terrain elevation [m] for each grid point of the analysis domain and averaged over every 25 m bin of elevation.

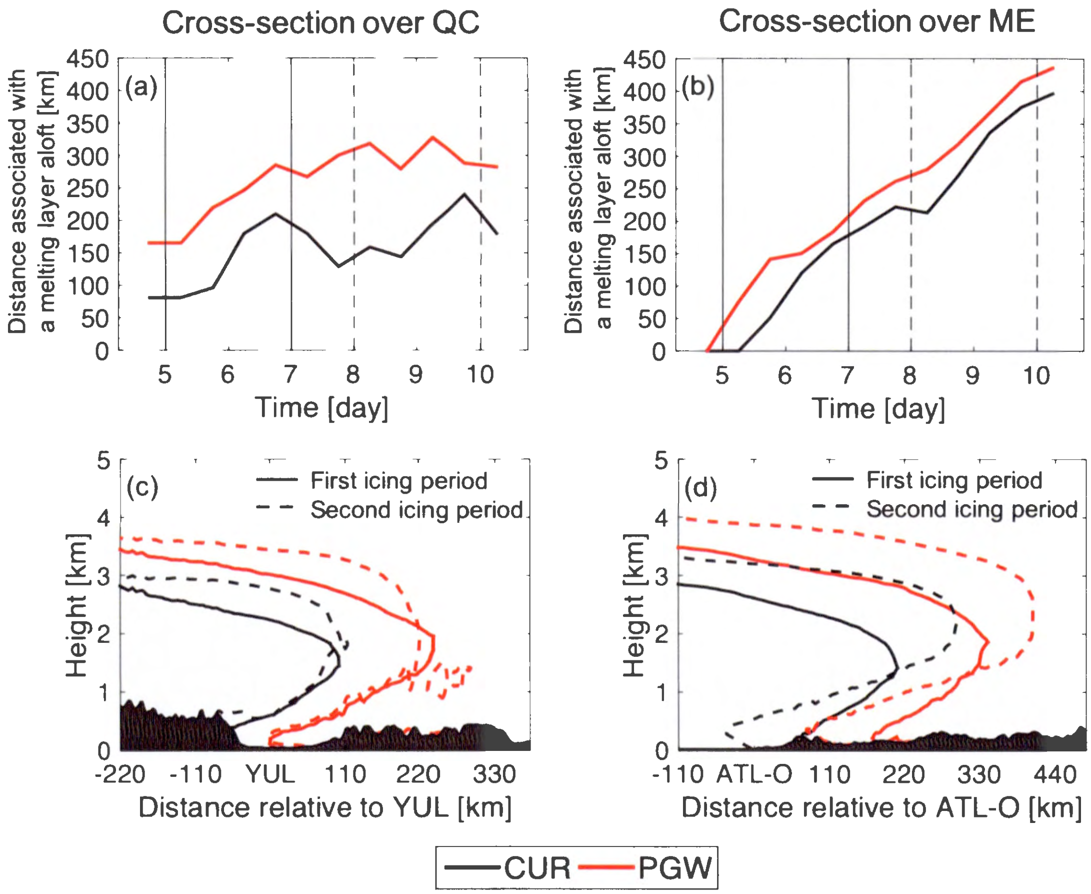

Figure 3.10 CUR (black) and PGW (red) (a)-(b) 12-hourly-averaged distance [km] along the cross-section associated with a melting layer aloft and a refreezing layer near the surface and (c)-(d) time-averaged over the first icing period (solid; from 0000 UTC 5 January 1998 to 0000 UTC 7 January 1998) and the second icing period (dashed; from 0000 UTC 8 January 1998 to 0000 UTC 10 January 1998) 0°C-isotherms along the cross-section over (a), (c) QC (red dotted line in Fig. 3.1) and (b), (d) ME (blue dotted line in Fig. 3.1).

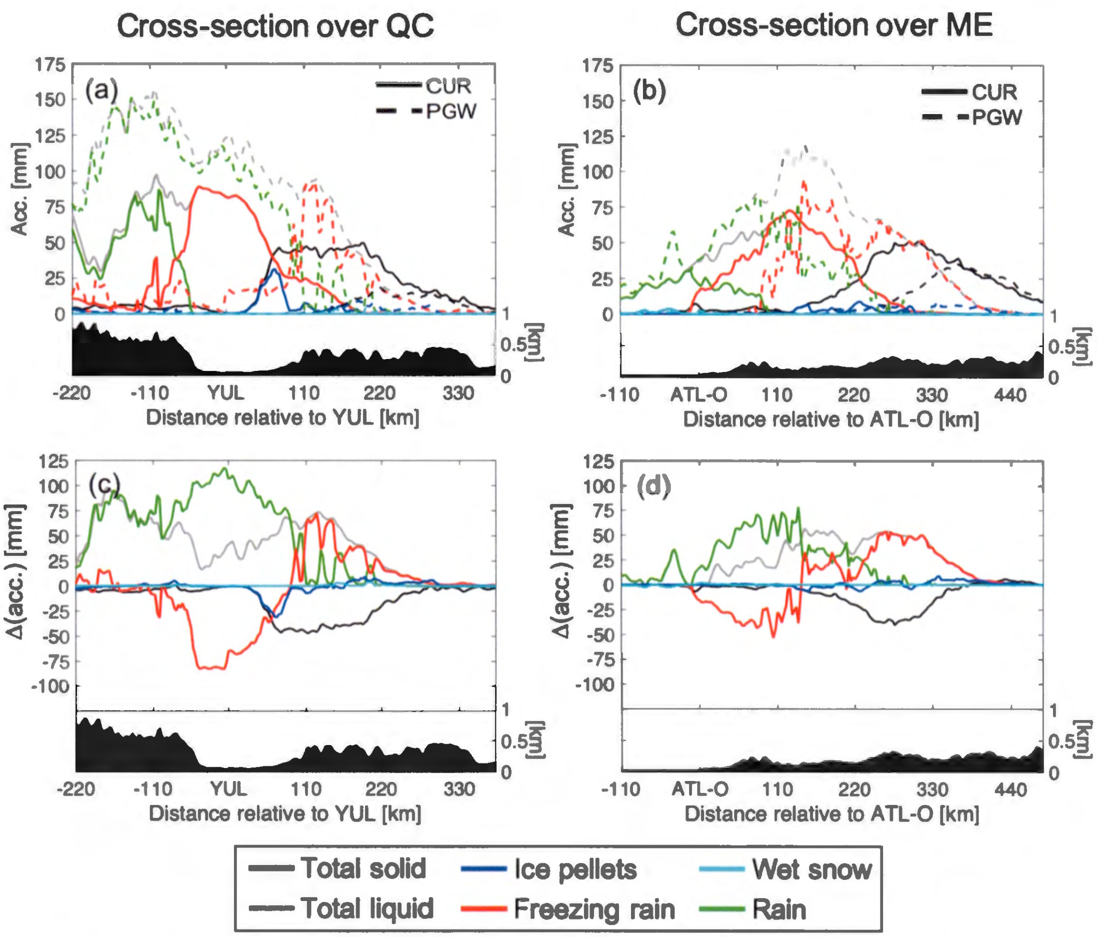

Figure 3.11 Time-averaged from 0600 UTC 4 January 1998 to 0600 UTC 10 January 1998 (a)-(b) CUR (solid) and PGW (dashed) and (c)-(d) PGW–CUR total accumulated precipitation [Acc., mm] of total solid (black), ice pellets (blue), wet snow (light blue), total liquid (grey), freezing rain (red) and rain (green) along the cross-section over (a), (c) QC (red dotted line in Fig. 3.1) and (b), (d) ME (blue dotted line in Fig. 3.1).

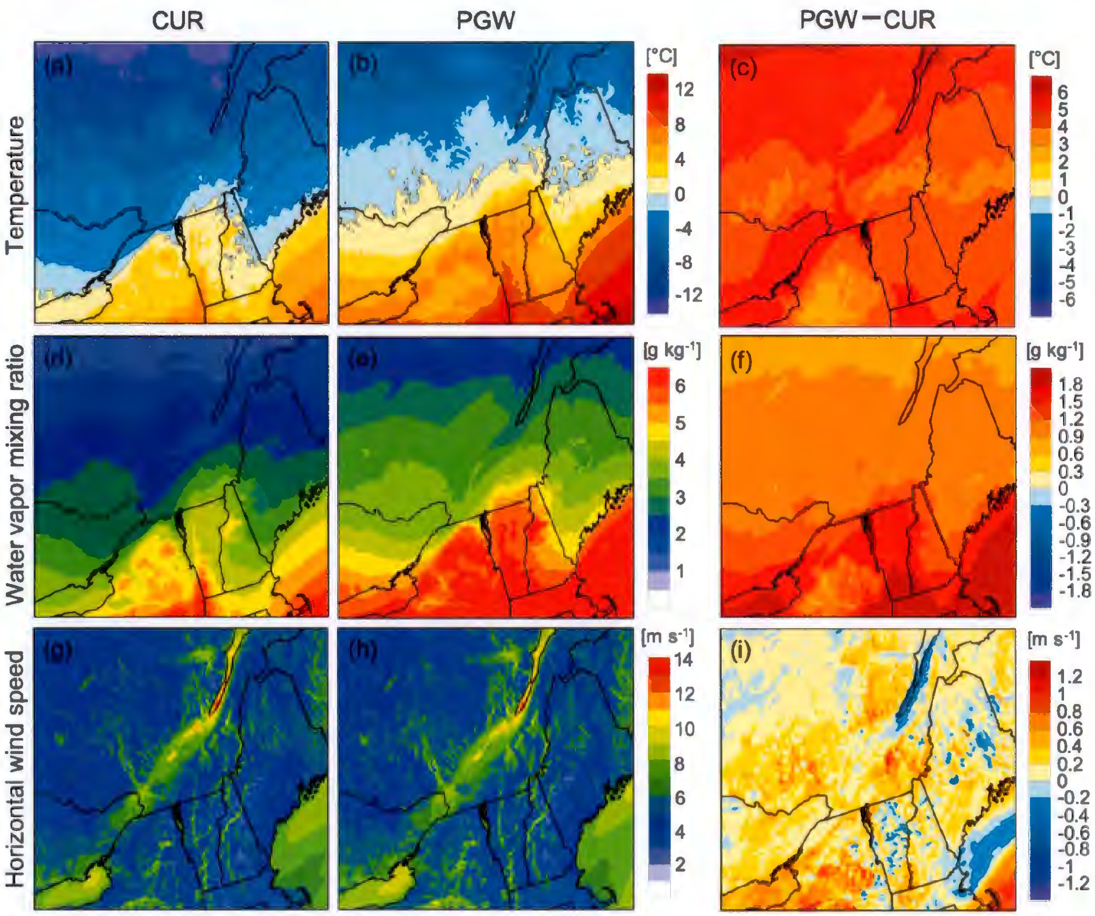

Figure 3.12 Time-averaged from 0600 UTC 4 January 1998 to 0600 UTC 10 January 1998 CUR (left), PGW (middle) and PGW–CUR (right) lowest model level (a)-(c) temperature [°C], (d)-(f) water vapor mixing ratio [g kg^{-1}] and (g)-(i) horizontal wind speed [m s^{-1}].

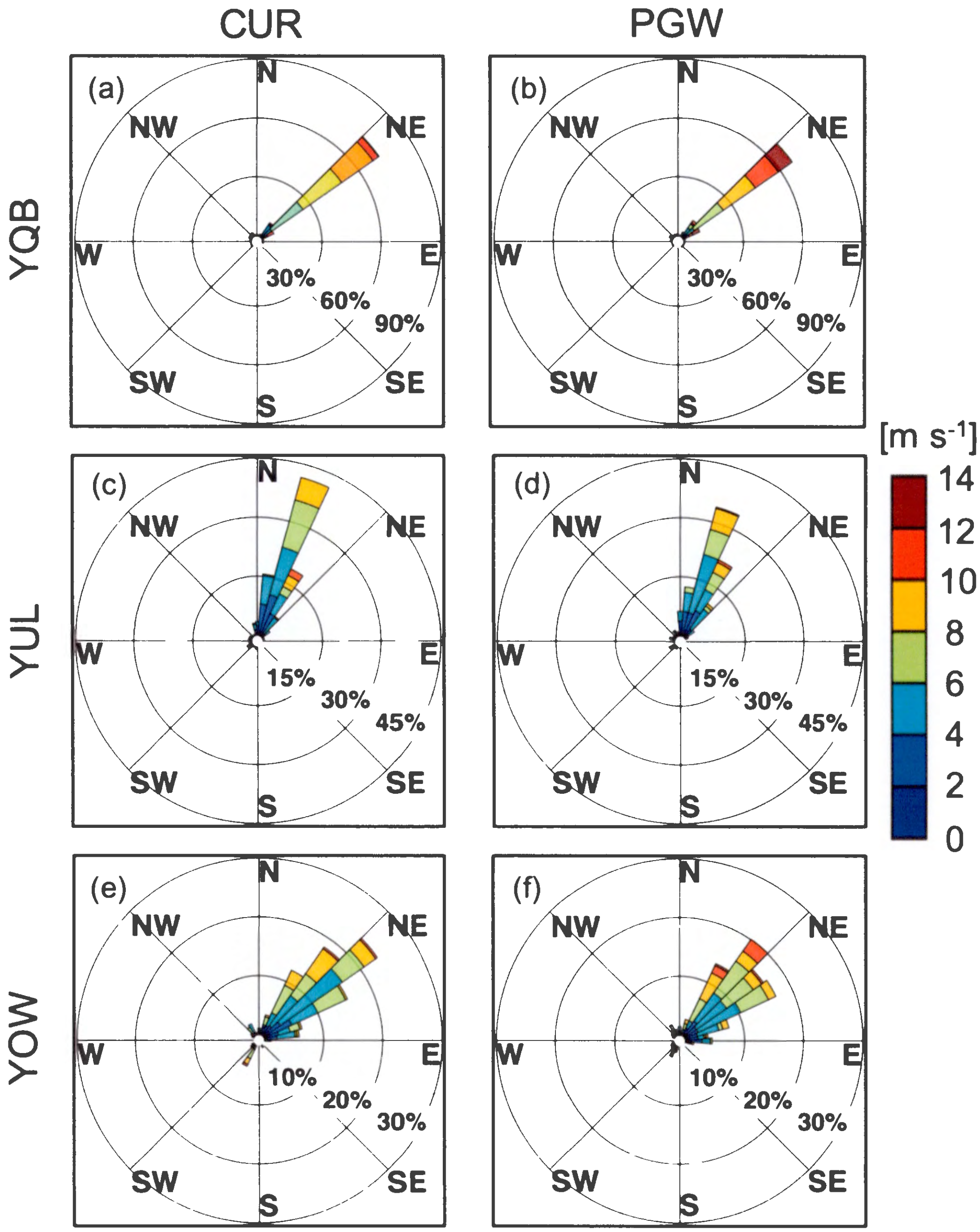

Figure 3.13 CUR (left) and PGW (right) wind rose diagrams of the horizontal wind at the lowest model level time-averaged over the simulated period (from 0600 UTC 4 January 1998 to 0600 UTC 10 January 1998) and at the grid point closest to (a)-(b) YQB, (c)-(d) YUL and (e)-(f) YOW. The colors represent the wind intensities [m s^{-1}] and the circles are the frequencies [%] of each intensity/direction combination.

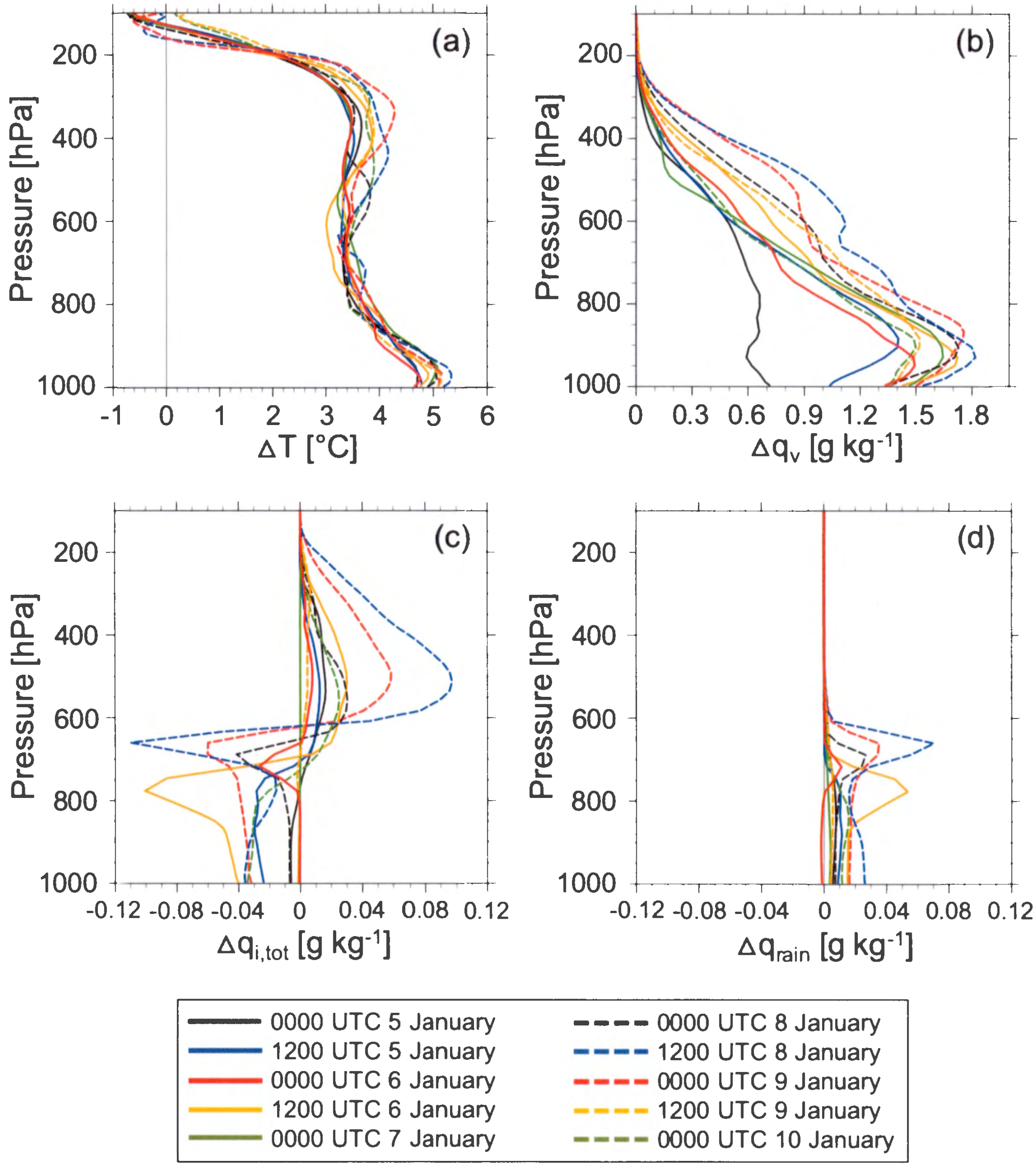

Figure 3.14 Vertical profiles every 12 hours of domain-averaged PGW–CUR (a) temperature [ΔT, °C], (b) water vapor mass mixing ratio [Δq_v, g kg^{-1}], (c) total ice mass mixing ratio [$\Delta q_{i,tot}$, g kg^{-1}] and (d) rain mass mixing ratio [Δq_{rain}, g kg^{-1}].

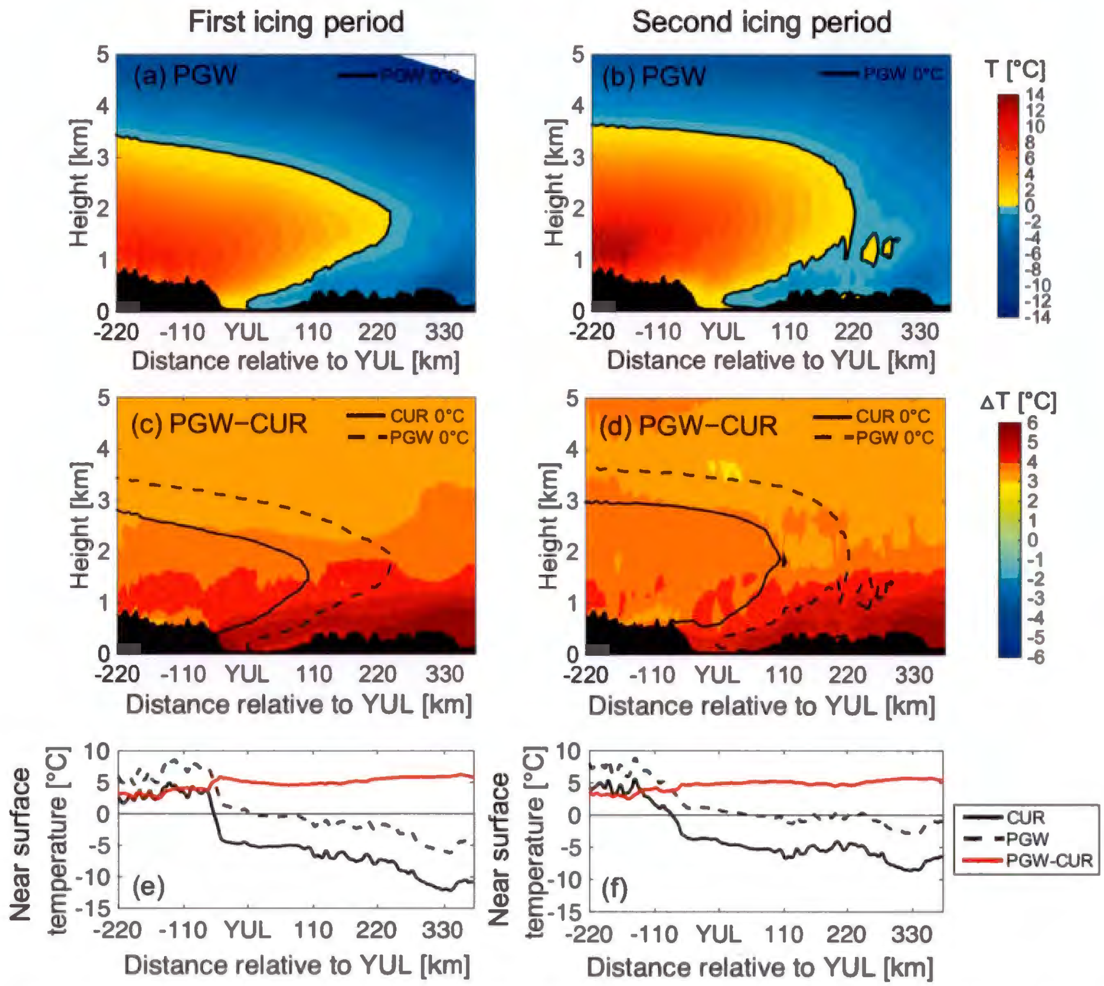

Figure 3.15 Vertical structures along the cross-section (red dotted line in Fig. 3.1) of time-averaged over (left) the first icing period from 0000 UTC 5 January 1998 to 000 UTC 7 January 1998 and (right) the second icing period from 0000 UTC 8 January 1998 to 0000 UTC 10 January 1998 (a)-(b) PGW 0°C-isotherm (solid) superimposed on temperature [T, °C], (c)-(d) CUR (solid) and PGW (dashed) 0°C-isotherms superimposed on PGW–CUR temperature [ΔT, °C] and (e)-(f) CUR (solid black), PGW (dashed black) and PGW–CUR (red) temperature [°C] of the lowest model level.

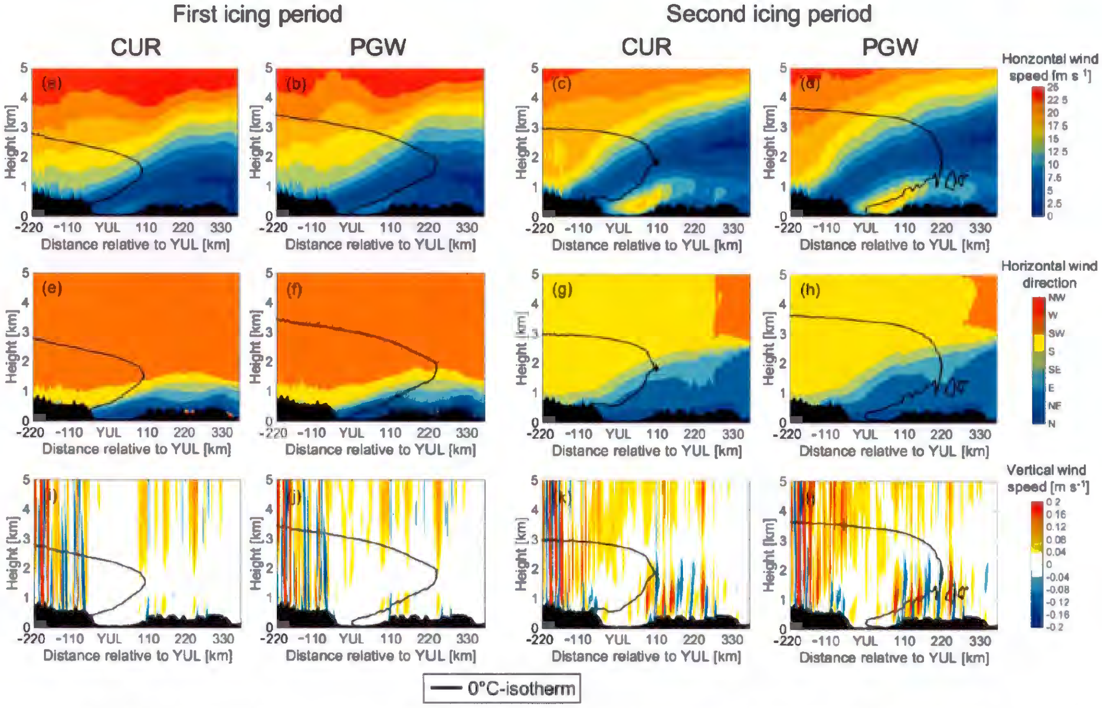

Figure 3.16 Vertical structures along the cross-section (red dotted line in Fig. 3.1) of time-averaged (two left columns) from 0000 UTC 5 January 1998 to 0000 UTC 7 January 1998 and (two right columns) from 0000 UTC 8 January 1998 to 0000 UTC 10 January 1998 0°C-isotherm (black line) superimposed on (a)-(d) horizontal wind speed [m s^{-1}], (e)-(h) horizontal wind direction and (i)-(l) vertical wind speed [m s^{-1}]. For the two icing periods, left is CUR and right is PGW.

CONCLUSION

4.1 Rappel de l'objectif et de l'approche empruntée

Les différents types de précipitations hivernales, comme la pluie verglaçante et le grésil, affectent de plusieurs façons la sécurité publique notamment à cause des interruptions des réseaux d'électricité et des moyens de transport, par exemple. Il est donc nécessaire de bien prévoir les transitions spatiales et temporelles des types de précipitations durant les passages de tempêtes hivernales. Sachant qu'il suffit d'un réchauffement de 1°C pour que le type de précipitation observé à la surface change de grésil à pluie verglaçante ou de neige à pluie (par exemple : Frick *et al.* 2013; Kämäräinen *et al.* 2018), il devient également important d'étudier les impacts du réchauffement climatique mondial sur l'occurrence de ces types de précipitation. Or, l'enjeu principal pour la simulation des types de précipitations hivernales est qu'il n'existe pas d'outils de paramétrisation pouvant être utilisés à la fois en prévision numérique du temps et à la fois en mode climat dans lesquels il y a la simulation explicite des processus microphysiques associés aux formations de ces types de précipitations. L'objectif principal de la thèse était d'étudier les processus microphysiques et les types de précipitations simulés lors d'une tempête hivernale dans le climat actuel, comme dans le contexte d'une atmosphère plus chaude, en utilisant la prévision de la fraction liquide ($F_{i,liq}$) des particules en phase mixte.

Dans le premier chapitre, une description rend compte de l'implantation de la $F_{i,liq}$ des particules en phase mixte dans le schéma P3 à l'aide d'approximations physiques basées sur la théorie et les observations de Fujyoshi (1986) et de Mitra *et al.* (1990).

Un modèle de nuage colonne (à une dimension) est utilisé pour comparer le processus de fonte partielle proposé avec un modèle de référence basé sur la littérature de Mitra *et al.* (1990). Le modèle colonne est également employé pour examiner les différences relatives à la prévision de $F_{i,liq}$ sur les simulations des propriétés des hydrométéores.

Dans les chapitres deux et trois, l'utilisation d'un modèle atmosphérique complet (Weather Research and Forecasting, WRF; Skamarock and Klemp 2008) a permis d'étudier les processus microphysiques et les types de précipitations simulés d'une tempête hivernale avec la prévision de $F_{i,liq}$. Le caractère météorologique extrême de la tempête de pluie verglaçante et de grésil du 4 au 10 janvier 1998 ainsi que le manque de littérature concernant la simulation de ces processus microphysiques ont justifié le choix de cette tempête comme étude de cas pour la thèse. Plus précisément, le deuxième chapitre a porté sur l'étude des différences obtenues entre les simulations des types de précipitations et de leurs propriétés avec et sans la prévision de $F_{i,liq}$. Quant à lui, le troisième chapitre a emprunté l'approche du *Pseudo-Global-Warming* (Schär *et al.* 1996) afin d'étudier les impacts d'une atmosphère plus chaude sur la simulation des types de précipitations de la tempête en utilisant la prévision de $F_{i,liq}$.

4.2 Principaux résultats de la recherche

Dans le premier chapitre de la recherche, il a d'abord été démontré que le processus de fonte partielle proposé par la prévision de $F_{i,liq}$ dans P3 se compare bien à un modèle de référence basé sur les observations de Mitra *et al.* (1990). Ensuite, il a été montré que la simulation explicite des particules en phase mixte affecte l'évolution verticale des propriétés des hydrométéores. Par exemple, une diminution du diamètre ainsi que des augmentations de la vitesse de chute et de la densité des hydrométéores en fonte sont obtenues avec la paramétrisation du processus de fonte partielle de la prévision de

$F_{i,liq}$. Cela représente mieux les comportements observés (Fujiyoshi 1986; Mitra *et al.* 1990) comparativement à la paramétrisation originale de ce processus. La fonte partielle affectait directement le taux de refroidissement de l'air induit par la fonte ainsi que les proportions en masse de pluie et de neige mouillée dans la couche de fonte. De plus, la prévision de $F_{i,liq}$ a permis d'ajouter de nouveaux processus microphysiques, comme le regel et le transfert de vapeur d'eau des particules en phase mixte. Avec ces derniers s'accompagnent de nouveaux termes d'échanges de chaleur latente avec l'environnement. La combinaison des processus de fonte partielle et de regel a eu pour effet de favoriser la formation de neige mouillée aux dépens de la pluie et de grésil aux dépens de la pluie verglaçante.

Dans le deuxième chapitre de la thèse, il a été démontré que l'utilisation de la $F_{i,liq}$ a eu pour effet général de diminuer l'accumulation totale de la pluie verglaçante et d'augmenter l'accumulation totale solide, comparativement à la simulation sans la prévision de $F_{i,liq}$ dans le cadre de l'épisode de verglas de janvier 1998. Dans certaines régions, comme le Maine, la diminution de pluie verglaçante a été de ~25 mm sur un total d'accumulation de ~85 mm, représentant une diminution de ~30%. La plupart de ces différences sont survenues durant la deuxième période de pluie verglaçante (dans l'intervalle du 8 janvier au 10 janvier), car cette période était notamment associée à des particules de glace plus givrée en altitude et à des couches de fonte et de regel plus épaisses en comparaison à la première période de pluie verglaçante (dans l'intervalle du 5 janvier au 7 janvier). La densification de la neige durant la fonte partielle entraînait une augmentation de la zone de fonte et favorisait l'accumulation de précipitations en phase solide aux dépens des précipitations en phase liquide (ou surfondue). La fonte partielle occasionnait aussi un refroidissement plus important dans la zone de fonte (de l'ordre de 0.5-1°C), comparativement à la simulation sans la prévision de $F_{i,liq}$. De plus, la fonte partielle produisait de plus grands rapports de mélange en masse et en nombre de pluie, diminuant le diamètre moyen des particules de pluie et réduisant le taux de précipitation (l'accumulation) de pluie verglaçante en surface. Le nouveau processus de regel des particules en phase mixte a, quant à lui, contribué à réchauffer le haut de la couche de regel et a augmenté le diamètre et l'accumulation des précipitations solides.

Dans le troisième chapitre de la thèse, les résultats ont montré que la tempête de verglas de janvier 1998 demeurerait un événement extrême avec des quantités abondantes de précipitations dans le contexte d'une atmosphère plus chaude et plus humide avec de l'approche du *Pseudo-Global-Warming*. Les maxima d'accumulation de précipitation totale, de pluie verglaçante et de neige mouillée ont augmenté, alors que ceux pour la précipitation solide et le grésil ont diminué. Les localisations des maxima de grésil et de pluie verglaçante ont été déplacées vers le nord-est. De plus, il existait des régions, comme dans le Maine et le nord-est de la Vallée-du-Saint-Laurent, où l'accumulation totale de pluie verglaçante était similaire, voire augmentée avec les conditions du réchauffement du *Pseudo-Global-Warming*. En général, les accumulations de pluie, de pluie verglaçante et de neige mouillée sont devenues de la pluie, tandis que les accumulations de neige se sont changées en un mélange de pluie verglaçante, pluie et grésil. Toutefois, les plus petites accumulations de pluie verglaçante et de grésil (20 mm et 15 mm, respectivement) sont demeurées des précipitations verglaçantes. Il a été démontré que la distance projetée au sol d'une couche de fonte en altitude superposant une couche de regel a augmenté dans la simulation avec le réchauffement comparativement à celle sans réchauffement atmosphérique, et cela, pour les deux régions analysées : le sud du Québec et le Maine. Toutefois, l'augmentation de cette distance avec le réchauffement était plus grande dans le sud du Québec notamment dû à la présence des Appalaches.

En résumé, les résultats obtenus dans cette recherche ont démontré que la prévision de $F_{i,liq}$ et des processus microphysiques associés aux particules en phase mixte ont des impacts sur la simulation des types de précipitations hivernales (diminution de l'accumulation de pluie verglaçante), de la température de l'air (refroidissement plus important dans la couche de fonte) et des propriétés des hydrométéores (densification de la glace avec la fonte partielle) lors de la tempête de verglas de janvier 1998.

4.3 Limitations et nouvelles pistes de recherche

La réalisation de cette recherche doctorale s'est accompagnée de plusieurs choix méthodologiques importants qui ont occasionné des limitations qu'il convient de rappeler. Premièrement, cette recherche s'est concentrée sur les types de précipitations hivernales et elle aurait ultérieurement avantage à être étendue à l'étude des précipitations estivales. Par exemple, le processus de croissance humide des particules en phase solide peut conduire à la formation de particules en phase mixte lorsque certaines conditions de température et d'humidité sont obtenues dans les tempêtes estivales (Musil 1970; Phillips *et al.* 2014). Cela peut être le cas durant les orages convectifs d'été lors desquels il y a formation de grêle (Pruppacher and Klett 1997). Ces orages peuvent, comme la pluie verglaçante, occasionner des dommages coûteux pour la société (par exemple : Hohl *et al.* 2002; Martius *et al.* 2018) et leur intensité est également appelée à changer dans le contexte du réchauffement climatique (Liu *et al.* 2017; Prein *et al.* 2017; Rasmussen *et al.* 2017). Ainsi, il pourrait être intéressant de prendre appui sur le travail de recherche fait dans les chapitres deux et trois de cette thèse pour utiliser la prévision de $F_{i,liq}$ de P3 pour l'étude d'un événement météorologique convectif.

Une deuxième limitation concerne le choix d'une seule tempête hivernale comme étude de cas. D'autant plus que cette tempête se qualifie d'extrême, car sa durée a largement dépassé celle obtenue par la moyenne des tempêtes de pluie verglaçante, qui est généralement de quelques heures (par exemple : Cortinas *et al.* 2004). En effet, il aurait été pertinent d'étudier plusieurs autres tempêtes hivernales de moins grandes intensités, de plus courtes durées et durant lesquelles les termes d'échanges de chaleur latente des processus microphysiques seraient de mêmes ordres de grandeur que les termes d'advection. À titre d'exemple, il serait intéressant d'étudier davantage le rôle de l'océan Atlantique et de son apport en humidité lors d'une tempête de verglas dans les provinces maritimes en utilisant la prévision de $F_{i,liq}$. Ou encore, il s'avérerait fort intéressant d'examiner la transition pluie-neige dans les régions montagneuses, par exemple de l'Ouest canadien. Cela afin de mieux comprendre les impacts de la topographie et de la simulation des propriétés des particules en phase mixte, comme la densité et la vitesse de chute, sur la transition verticale pluie-neige. Enfin, l'étude de tempêtes hivernales plus récentes permettrait certainement une meilleure validation des types de précipitations simulés par P3_MOD avec les observations. Toutefois, à cette fin, des observations des types de précipitations et des profils verticaux de température et d'humidité à plus haute résolution spatio-temporelle sont nécessaires, en particulier dans le sud du Québec.

Une troisième limitation concerne la configuration de l'expérimentation du *Pseudo-Global-Warming*. D'abord, bien que cette approche soit de plus en plus utilisée pour étudier les impacts du réchauffement climatique sur les phénomènes météorologiques locaux à potentiels dommageables, cette méthode ne peut pas être comparée à l'approche classique des projections climatiques. Or, en considérant les améliorations constantes de la performance des simulateurs et des précisions numériques des modèles climatiques, il se pourrait que des projections climatiques deviennent possibles dans un avenir rapproché en utilisant la prévision de $F_{i,liq}$. En attendant, différentes configurations de l'expérimentation du *Pseudo-Global-Warming* auraient avantage à être étudiées. À ce titre, les éléments suivants pourraient faire l'objet de recherches ultérieures : l'utilisation d'un autre ensemble de conditions aux frontières latérales que celui utilisé dans cette recherche; l'utilisation d'un modèle de température des lacs au lieu d'une extrapolation de la température de l'océan pour les Grands Lacs; l'évaluation des impacts d'autres scénarios climatiques que celui du RCP8.5 comme perturbations climatiques; et l'utilisation d'un ensemble de simulations de tempêtes hivernales.

4.4 Retombées scientifiques et mots de la fin

Dans l'ensemble, ce projet est un pas en avant vers une meilleure compréhension et une simulation plus réaliste des processus microphysiques associés aux formations des précipitations lorsque les températures sont près de 0°C. La simulation explicite de la fonte partielle permet d'obtenir la représentation des propriétés des particules en phase mixte. Ces propriétés diffèrent de celles des gouttes de pluie et, donc, leurs simulations auront certainement un impact sur la représentation de plusieurs variables atmosphériques importantes dans les modèles, comme la hauteur de l'isotherme 0°C (la transition pluie-neige) et la réflectivité radar.

De plus, ce travail doctoral contribue au développement des schémas de microphysiques des nuages et de la précipitation, car l'approche développée pour l'implantation de la $F_{i,liq}$ dans le schéma de microphysique P3 est unique et novatrice. La prévision de $F_{i,liq}$ par l'implantation de la nouvelle variable microphysique $q_{i,liq}$ dans P3 permet de suivre dans le temps et dans l'espace les particules en phase mixte, leurs propriétés et leurs processus microphysiques, alors que les particules en phase mixte sont généralement absentes des paramétrisations microphysiques.

Sachant que l'une des principales incertitudes est prévision numérique du temps hivernal est la détermination exacte du type de précipitation et de sa phase, P3_MOD pourrait être utile au système opérationnel de prévisions. Généralement, les types de précipitations sont diagnostiqués en utilisant des méthodes empiriques telles que celle de Bourgouin (2000). Cette méthode est utilisée pour prévoir les types de précipitations dans le système de prévision déterministe à haute résolution; le système opérationnel canadien de prévision numérique du temps à l'échelle du kilomètre (Milbrandt *et al.* 2016). Cet algorithme diagnostique utilise seulement le profil vertical de température et l'épaisseur des couches de fonte et de regel, alors que la formation de verglas et de grésil dépend étroitement de plusieurs processus microphysiques clés, comme la fonte et le regel. Ces méthodes ne considèrent également pas certaines caractéristiques, telles que la fraction de givrage et la densité, des types de particules solides en altitude qui permettent de déterminer le taux de fonte partielle. De plus, pour les schémas qui utilisent l'approche « bulk » traditionnelle, l'implantation de $q_{i,liq}$ demande d'ajouter une $F_{i,liq}$ pour chacune des catégories de précipitations en phase solide (glace, neige et neige roulée), ce qui entraîne une augmentation du coût numérique des simulations. Cela n'est pas idéal pour mener des simulations à très hautes résolutions spatiales (par exemple entre 3 km et 1 km). Toutefois, dans un schéma de microphysique utilisant une seule catégorie de glace, comme le schéma *Predicted Particle Properties* (P3; Morrison and Milbrandt 2015), cette approche s'avère abordable, car seulement une seule variable pronostique est ajoutée.

Finalement, davantage de modèles atmosphériques utilisant le schéma P3 et la prévision de $F_{i,liq}$ peuvent maintenant être utilisés pour étudier les occurrences, les transitions et les processus microphysique des types de précipitations pouvant avoir des impacts majeurs sur la société. Un exemple précis est la future utilisation de P3_MOD pour des projections climatiques à très hautes résolutions des événements de pluie verglaçante et de grésil au Canada.

APPENDIX A

COMPARISON BETWEEN P3_MOD AND P3_ORIG IN PRECIPITATION TYPE DISTRIBUTIONS PRODUCED DURING THE 1998 ICE STORM SIMULATED UNDER THE PSEUDO-GLOBAL-WARMING APPROACH

This appendix aims at illustrating the differences between P3_MOD and P3_ORIG in simulations of the precipitation types when the Pseudo-Global-Warming approach is used. The model configuration for P3_MOD and P3_ORIG is the one described in sections 3.2.2 and 3.2.3. The results analysis presented here is similar to section 2.4, which was comparing P3_MOD and P3_ORIG under current climate conditions.

A.1 Differences in accumulated precipitation

The differences between P3_MOD and P3_ORIG in total accumulated freezing rain, and solid (ice) precipitation are shown in Fig. A1. There is an overall decrease (increase) of freezing rain (total solid) accumulations in P3_MOD compared to P3_ORIG. The maximum decrease in freezing rain accumulation (~-40 mm) is obtained in Maine. The increase in total solid accumulation is nearly located where ice pellets are obtained in P3_MOD (see Fig. 3.3e).

An analysis of differences between P3_MOD and P3_ORIG is made over the same four sub-regions as in section 2.4. Sub-region A is associated with mainly rain whereas sub-region B is associated with a mixture of freezing rain and rain (Table A1). Sub-region C is located north of sub-region A and mainly freezing rain occurred with some rain. Finally, the fourth sub-region (D) is located north-west of sub-region B and mainly freezing rain occurred. The accumulated ice pellets in P3_MOD are small for the four sub-regions (Table A1). Except for the sub-region C, where all accumulated precipitation types were slightly higher in P3_MOD compared to P3_ORIG, freezing rain and rain (solid) precipitation accumulations decreased (increased) in P3_MOD compared to P3_ORIG.

The temporal evolution of the sub-regions-averaged 0°C-isotherm, freezing rain and ice pellets rates as well as the difference between P3_MOD and P3_ORIG in accumulated precipitation are shown in Fig. A2. For the sub-regions A and B, the first icing period is short-duration because surface temperature are above 0°C producing rain instead. Ice pellets are obtained in P3_MOD at the beginning of the first icing period in sub-regions B and C, and during the icing second period in the sub-regions C and D. Higher differences between P3_MOD and P3_ORIG are obtained during the first half of the second icing period for sub-regions B and D when freezing rain is the main precipitation type.

A.2 Microphysical properties of precipitation aloft

An analysis of microphysical properties along a cross-section (line in Fig. A1a) is made in Figs. A3 and A4. The cross-section is over the sub-regions B and D and variables are time-averaged over a selected time-period during the second icing period when differences between P3_MOD and P3_ORIG in accumulated freezing rain are higher (Fig. A2). Figure A3 shows mass mixing ratios of hydrometeors of both simulations as well as their differences (P3_MOD–P3_ORIG) similarly to Fig. 2.12. Figure A4 shows the differences between P3_MOD and P3_ORIG in vertical structures of temperature (Fig. A4a), water vapour (Fig. A4b) as well as some microphysical properties (Figs. A4c-f) similarly to Fig. 2.13.

First, the ice entering sub-regions B and D melted completely to produce freezing rain at the surface. A mixture of freezing rain and ice pellets is obtained north of the sub-region D (~342-402 km). Second, the ice entering the melting layer aloft is highly rimed (~0.25) south and in sub-region B (~60-180 km). The total ice mass mixing ratio above the melting layer is higher and more rimed over the sub-region B compared to D (Figs. A3a-b and d-e, respectively). Mass mixing ratios of liquid on ice (Fig. A3g) and rain (Figs. A3i-j) are higher in the melting layer when ice above the melting layer is higher (~0.4-0.45 g kg^{-1}). Cloud is generally formed through supersaturated conditions produced by diabatic cooling of melting (Figs. A3l-m). Also, $q_{i,tot}$ (Fig. A3c) and $q_{i,rim}$ (Fig. A3f) aloft are smaller in P3_MOD compared to P3_ORIG, in particular over the sub-region B. The rain mass mixing ratio is generally higher in P3_MOD compared to P3_ORIG (Fig. A3k). Lastly, cloud mass mixing ratio (Fig. A3n) is smaller in P3_MOD compared to P3_ORIG into the melting layer.

Overall, very similar results between P3_MOD and P3_ORIG are obtained under the Pseudo-Global-Warming approach (Figs. A3 and A4) compared to current conditions of Figs. 2.12 and 2.13, except that microphysical process rates are higher according to higher water vapour availability under warmer conditions. However, the changes between P3_MOD and P3_ORIG are similar in percentages and location through the storm in both current and warmer conditions except that under warmer conditions the spatial distribution of precipitation accumulation is shifted northward. The prediction of the bulk liquid fraction affected both the surface precipitation total accumulations and the air temperature in similar ways under warmer and current conditions. In particular, temperatures at the top of the melting layer were colder while temperatures at the bottom of the melting layer and below the refreezing layer were warmer in P3_MOD compared to P3_ORIG (Fig. A4a). That affects the water vapor distribution (Fig. A4b) and the deposition of water vapour process rates on $q_{i,liq}$ (neglected in P3_ORIG), q_{rain} and q_{cloud}. Overall, it is found that the partial melting (Fig. A4d) produced higher q_{rain} and N_{rain}, which tends to decrease the rain and freezing rain mean diameter (Fig. A4e), the freezing rain rate and then the freezing rain accumulation. On another hand, total solid precipitation is higher in P3_MOD compared to P3_ORIG due to two main reasons: an extended melting zone resulting in higher amount of ice reaching the refreezing layer due to the densification (Fig. A4c) of ice during melting (neglected in P3_ORIG) and the partial refreezing of ice process (neglected in P3_ORIG) (Fig. A4f) that produced an increase of ice particle diameter into the refreezing layer and then increase the total solid rate.

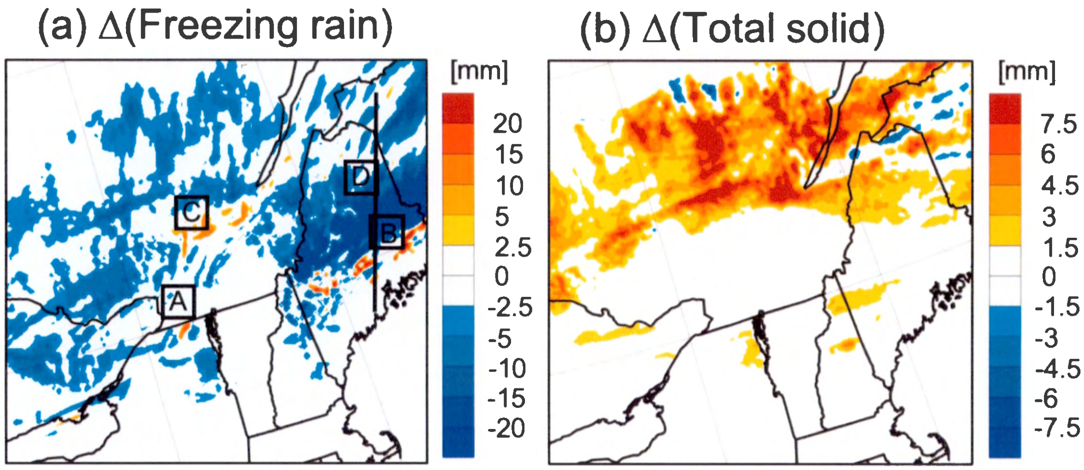

Figure A1 P3_MOD–P3_ORIG total accumulated precipitation [mm] from 0600 UTC 4 January 1998 to 0600 UTC 10 January 1998 of (a) freezing rain and (b) total solid. Also shown in (a) are the locations of the four sub-regions A, B, C and D (squares) and the cross-section for Figs. A3-A4 (black line).

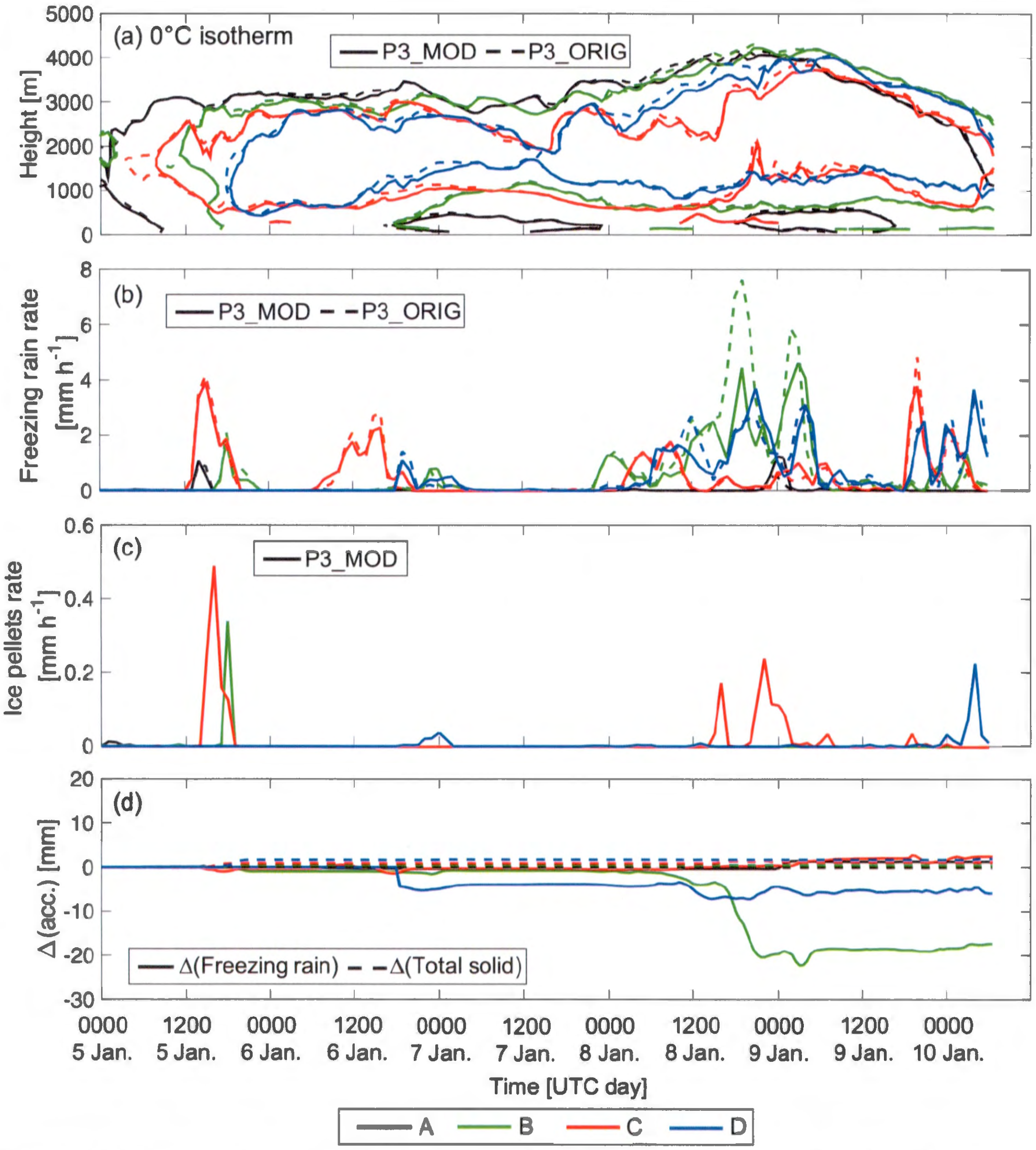

Figure A2 Temporal evolution of sub-region-averaged over A (black), B (green), C (red) and D (blue) (a) P3_MOD (solid) and P3_ORIG (dashed) 0°C-isotherm, (b) P3_MOD (solid) and P3_ORIG (dashed) freezing rain rate [mm h^{-1}], (c) P3_MOD ice pellets rate [mm h^{-1}] and (d) P3_MOD–P3_ORIG hourly accumulated precipitation [Δ(acc.), mm] of freezing rain (solid) and total solid (dashed).

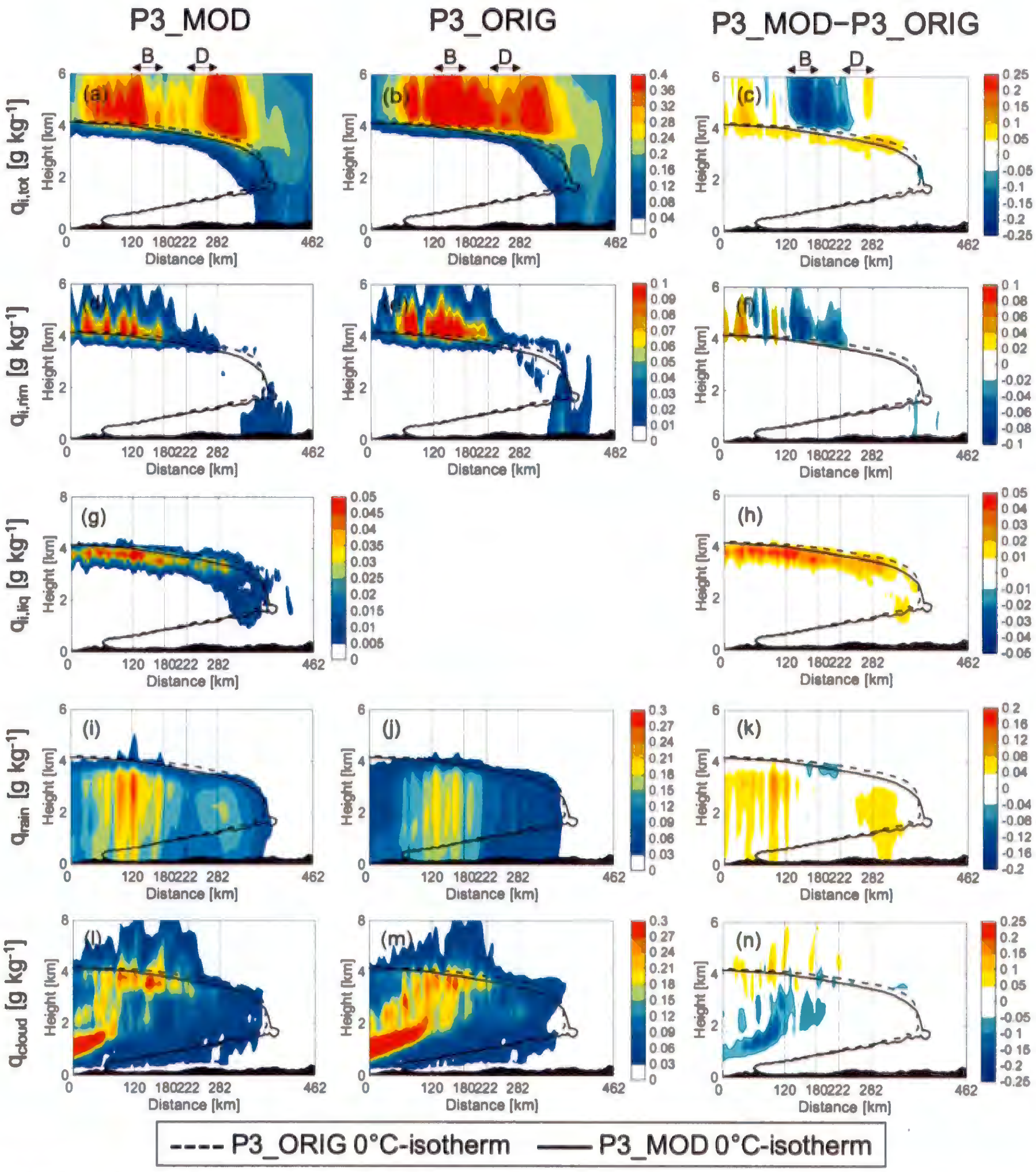

Figure A3 P3_MOD (left), P3_ORIG (middle) and P3_MOD–P3_ORIG (right) vertical structures along the cross-section over the sub-regions A and C (line in Fig. A1a) of time-averaged from 0600 UTC 8 January 1998 to 0600 UTC 9 January 1998 P3_MOD (solid) and P3_ORIG (dashed) 0°C-isotherms superimposed on the mass mixing ratio (colors, [g kg^{-1}]) of (a)-(c) total ice [$q_{i,tot}$], (d)-(f) rime on ice [$q_{i,rim}$], (g)-(h) liquid on ice [$q_{i,liq}$], (i)-(k) rain [q_{rain}] and (l)-(n) cloud [q_{cloud}].

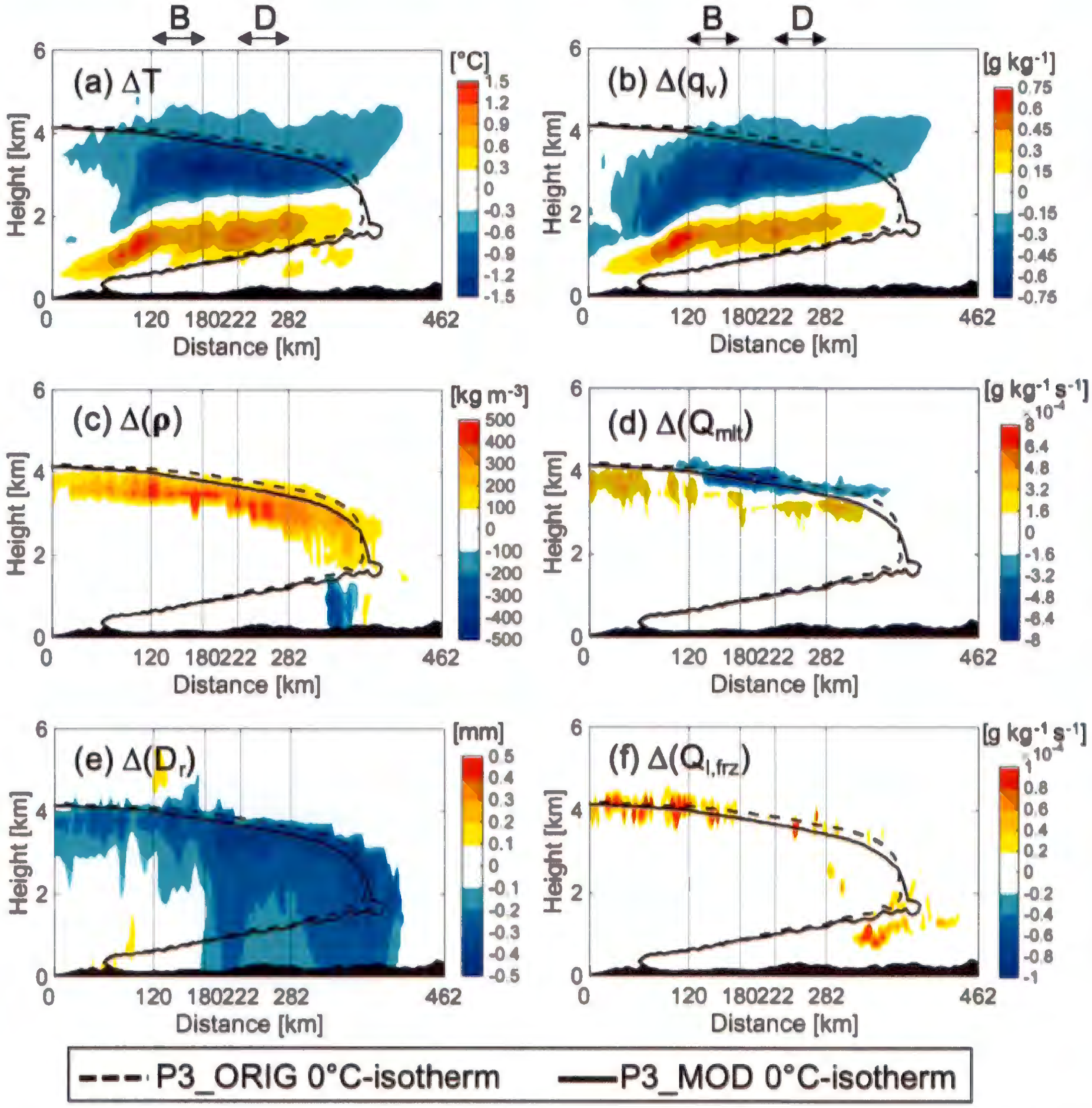

Figure A4 Vertical structures along the cross-section over the sub-regions B and D (line in Fig. A1a) of time-averaged from 0600 UTC 8 January 1998 to 0600 UTC 9 January 1998 P3_MOD (solid) and P3_ORIG (dashed) 0°C-isotherm superimposed on P3_MOD–P3_ORIG (colors) (a) temperature [ΔT, °C], (b) water vapor mixing ratio [$\Delta(q_v)$, g kg^{-1}], (c) mean mass-weighted density of ice [$\Delta(\rho)$, kg m^{-3}], (d) total melting process rate [$\Delta(Q_{mlt})$, g kg^{-1} s^{-1}], (e) mean mass-weighted diameter of rain/freezing rain [$\Delta(D_r)$, mm] and (f) refreezing process rate [$\Delta(Q_{l,frz})$, g kg^{-1} s^{-1}].

Table A.1 Sub-region-averaged total accumulated precipitation [mm] from 0600 UTC 4 January 1998 to 0600 UTC 10 January 1998 of total, total liquid, total solid, freezing rain, ice pellets, wet snow and rain for P3_MOD and P3_ORIG.

Sub-region		P3_ORIG	P3_MOD
A	Total	122	121
	Total liquid	122	121
	Total solid	0.2	0.1
	Freezing rain	5	6
	Ice pellets	-	0
	Wet snow	-	0
	Rain	117	115
B	Total	160	140
	Total liquid	160	139
	Total solid	0.2	0.6
	Freezing rain	86	69
	Ice pellets	-	0.4
	Wet snow	-	0.2
	Rain	74	70
C	Total	85	93
	Total liquid	82	89
	Total solid	3	4
	Freezing rain	65	67
	Ice pellets	-	2
	Wet snow	-	2
	Rain	17	22
D	Total	100	95
	Total liquid	95	88
	Total solid	5	7
	Freezing rain	92	86
	Ice pellets	-	3
	Wet snow	-	0.1
	Rain	3	2

RÉFÉRENCES

Arnott, J.M. and Chamberlain, J. (2014). Lake-effect freezing drizzle: A case-study analysis. *Journal of Operational Meteorology*, *2*(15), 180-190.

Austin, P.M. and Bemis, A.C. (1950). A quantitative study of the "bright band" in radar precipitation echoes. *Journal of Meteorology*, *7*(2), 145-151.

Baldwin, E.B. and Contorno, S.P. (1993). Development of a weather-type prediction system for NMC's mesoscale ETA model. In *Preprints, 13th Conf. on Weather Analysis and Forecasting, Vienna, VA, American Meteorological Society*, 86-87.

Ban, N., Schmidli, J. and Schär, C. (2014). Evaluation of the convection-resolving regional climate modeling approach in decade-long simulations. *Journal of Geophysical Research: Atmospheres*, *119*(13), 7889-7907.

Barszcz, A. (2017). *Impacts du gel par collision sur la production de pluie verglaçante*. [Mémoire de maîtrise]. Montréeal : Université du Québec à Montréal, 72 p. Récupéré de https://archipel.uqam.ca/9839/

Barszcz, A., Milbrandt, J.A. and Thériault, J.M. (2018). Improving the explicit prediction of freezing rain in a kilometer-scale numerical weather prediction model. *Weather and Forecasting*, *33*(3), 767-782.

Beard, K.V. (1976). Terminal velocity and shape of cloud and precipitation drops aloft. *Journal of the Atmospheric Sciences*, *33*(5), 851-864.

Benjamin, S.G., Brown, J.M. and Smirnova, T.G. (2016). Explicit precipitation-type diagnosis from a model using a mixed-phase bulk cloud–precipitation microphysics parameterization. *Weather and Forecasting*, *31*(2), 609-619.

Bourgouin, P. (2000). A method to determine precipitation types. *Weather and Forecasting*, *15*(5), 583-592.

Braun, S.A. and Houze Jr., R.A. (1995). Melting and freezing in a mesoscale convective system. *Quarterly Journal of the Royal Meteorological Society, 121*(521), 55-77.

Bresson, É., Laprise, R., Paquin, D., Thériault, J.M. and de Elía, R. (2017). Evaluating the ability of CRCM5 to simulate mixed precipitation. *Atmosphere-Ocean, 55*(2), 79-93.

Brown, P.R.A. and Francis, P.N. (1995). Improved measurments of the ice water content in cirrus using a total-water probe. *Journal of Atmospheric and Oceanic Technology, 12*(2), 410-414.

Browning, K.A., Ludlam, F.H. and Macklin, W.C. (1963). The density and structure of hailstones. *Quarterly Journal of the Royal Meteorological Society, 89*(379), 75-84.

Cantin, A. and Bachand, D. (1993). *Synoptic pattern recognition and partial thickness techniques as a tool for precipitation types forecasting associated with a winter storm*. [Rapport technique]. Service de l'environnement atmosphérique. Québec : Centre Météorologique du Québec, *93N-002*, 9 p.

Carmichael, H.E., Stewart, R.E., Henson, W. and Thériault, J.M. (2011). Environmental conditions favoring ice pellet aggregation. *Atmospheric Research, 101*(4), 844-851.

Carrera, M.L., Gyakum, J.R. and Lin, C.A. (2009). Observational study of wind channeling within the St-Lawrence River valley. *Journal of Applied Meteorology and Climatology, 48*(11), 2341-2361.

Chan, S.C., Kendon, E.J., Fowler, H.J., Blenkinsop, S., Ferro, C.A. and Stephenson, D.B. (2013). Does increasing the spatial resolution of a regional climate model improve the simulated daily precipitation? *Climate dynamics, 41*(5-6), 1475-1495.

Chang, S.E., McDaniels, T.L., Mikawoz, J. and Peterson, K. (2007). Infrastructure failure interdependencies in extreme events: power outage consequences in the 1998 Ice Storm. *Natural Hazards, 41*(2), 337-358.

Cheng, C.S., Li, G. and Auld, H. (2011). Possible impacts of climate change on freezing rain using downscaled future climate scenarios: Updated for Eastern Canada. *Atmosphere-Ocean, 49*(1), 8-21.

Cheng, C.S., Auld, H., Li, G., Klaassen, J. and Li, Q. (2007). Possible impacts of climate change on freezing rain in south-central Canada using downscaled future climate scenarios. *Natural Hazards and Earth System Science*, *7*(1), 71-87.

Cheng, C.S., Auld, H., Li, G., Klaassen, J., Tugwood, B. and Li, Q. (2004). An automated synoptic typing procedure to predict freezing rain: An application to Ottawa, Ontario, Canada. *Weather and Forecasting*, *19*(4), 751-768.

Cholette, M., Laprise, R. and Thériault, J. (2015). Perspectives for very high-resolution climate simulations with nested models: illustration of potential in simulating St. Lawrence River Valley channelling winds with the fifth-generation Canadian regional climate model. *Climate*, *3*(2), 283-307.

Cholette, M., Morrison, H., Milbrandt, J.A. and Thériault, J.M. (2019). Parameterization of the bulk liquid fraction on mixed-phase particles in the predicted particle properties (P3) scheme: Description and idealized simulations. *Journal of the Atmospheric Sciences*, *76*(2), 561-582.

Cober, C.G., Isaac, G.A. and Strapp, W. (2001). Characterizations of aircraft icing environments that include supercooled large drops. *Journal of Applied Meteorology*, *40*(11), 1984-2002.

Cortinas, Jr. J.V., Bernstein, B.C., Robbins, C.C. and Strapp, J.W. (2004). An analysis of freezing rain, freezing drizzle, and ice pellets across the United States and Canada. *Weather and Forecasting*, *19*(2), 377-390.

Czys, R.R., Scott, R.W., Tang, K.C., Przybylinski, R.W. and Sabones, M.E. (1996). A physically based, nondimensional parameter for discriminating between locations of freezing rain and ice pellets. *Weather and Forecasting*, *11*(4), 591-598.

Descurieux, J. (2010). Post Hoc evaluation of hazardous weather: snowstorms in the Montréal, Québec, area in March 2008. *Weather, Climate, and Society*, *2*(1), 36-43.

Dietlicher, R., Neubauer, D. and Lohmann, U. (2018). Prognostic parameterization of cloud ice with a single category in the aerosol-climate model ECHAM (v6.3.0)-HAM (v2.3). *Geoscientic Model Development*, *11*(4), 1557-1576.

Doms, G. and Schättler, U. (2002). A description of the nonhydrostatic regional model LM, Part I: Dynamics and numerics. *COSMO Newsletter*, *2*, 225-235.

Donaldson, N.R. and Stewart, R.E. (1993) Fog induced by mixed-phase precipitation. *Atmospheric Research*, *29*(1-2), 9-25.

Dudhia, J. (1996). A multi-layer soil temperature model for MM5. *The Sixth PSU/NCAR mesoscale model users' workshop*, Boulder, 22-24.

Fabry, F. and Szyrmer, W. (1999). Modeling of the melting layer. Part II: Electromagnetic. *Journal of the Atmospheric Sciences*, *56*(20), 3593-3600.

Fabry, F. and Zawadzki, I. (1995). Long-term radar observations of the melting layer of precipitation and their interpretation. *Journal of the Atmospheric Sciences*, *52*(7), 838-851.

Finch, Z. (2011). *Forecasting freezing drizzle: The 3-4 February 2011 ice storm event in Corpus Christi, Texas*. [Document non publié]. National Weather Service. Texas: Weather Forecast Office, 19 p. Récupéré de https://www.weather.gov/media/crp/Feb2011_IceStorm.pdf

Forbes, R., Tsonevsky, I., Hewson, T. and Leutbecher, M. (2014). Towards predicting high-impact freezing rain events. *ECMWF Newsletter*, *141*, 15-21.

Frick, C., Seifert, A. and Wernli, H. (2013). A bulk parameterization of melting snowflakes with explicit liquid water fraction for the COSMO model. *Geoscientific Model Development*, *6*(6), 1925-1939.

Fujiyoshi, Y. (1986). Melting snowflakes. *Journal of the Atmospheric Sciences*, *43*(3), 307-311.

Gascón, E., Hewson, T. and Haiden, T. (2018). Improving predictions of precipitation type at the surface: description and verification of two new products from the ECMWF ensemble. *Weather and Forecasting*, *33*(1), 89-108.

Geresdi, I., Sarkadi, N. and Thompson, G. (2014). Effect of the accretion by water drops on the melting of snowflakes. *Atmospheric Research*, *149*, 96-110.

Gibson, S.R. and Stewart, R.E. (2007). Observations of ice pellets during winter storm. *Atmospheric Research*, *85*(1), 64-76.

Groisman, P.Y., Bulygina, O.N., Yin, X., Vose, R.S., Gulev, S.K., Hanssen-Bauer, I. and Førland, E. (2016). Recent changes in the frequency of freezing precipitation in North America and Northern Eurasia. *Environmental Research Letters*, *11(4)*, 045007.

Gunn, R. and Kinzer, D.G. (1949). The terminal velocity of fall for water droplets in stagnant air. *Journal of Meteorology*, *6*(4), 243-248.

Gutmann, E.D., Rasmussen, R.M., Liu, C., Ikeda, K., Bruyere, C.L., Done, J.M., Garrè, L., Friis-Hansen, P. and Veldore, V. (2018). Changes in Hurricanes from a 13-Yr Convection-Permitting Pseudo–Global Warming Simulation. *Journal of Climate*, *31*(9), 3643-3657.

Gyakum, J.R. and Roebber, P.J. (2001). The 1998 ice storm - analysis of a planetary-scale event. *Monthly Weather Review*, *129*(12), 2983-2997.

Hallett, J. and Mossop, S.C. (1974). Production of secondary ice particles during the riming process. *Nature*, *249*(5452), 26-28.

Hanesiak, J.M. and Stewart, R.E. (1995). The mesoscale and microscale structure of a severe ice pellet storm. *Monthly Weather Review*, *123*(11), 3144-3162.

Hara, M., Yoshikane, T., Kawase, H. and Kimura, F. (2008). Estimation of the impact of global warming on snow depth in Japan by the pseudo-global-warming method. *Hydrological Research Letters*, *2*, 61-64.

Hashino, T. and Tripoli, G.J. (2007). The Spectral Ice Habit Prediction System (SHIPS). Part I: Model description and simulation of the vapor deposition process. *Journal of the Atmospheric Sciences*, *64*(7), 2210-2237.

Henson, W., Stewart, R.E. and Kochtubajda, B. (2007). On the precipitation and related features of the 1998 Ice Storm in the Montréal area. *Atmospheric Research*, *83*(1), 36-54.

Henson, W., Stewart, R.E., Kochtubajda, B. and Thériault, J.M. (2011). The 1998 Ice Storm: Local flow fields and linkages to precipitation. *Atmospheric Research*, *101*(4), 852-862.

Hernández-Díaz, L., Laprise, R., Sushama, L., Martynov, A., Winger, K. and Dugas, B. (2013). Climate simulation over CORDEX Africa domain using the fifth-generation Canadian Regional Climate Model (CRCM5). *Climate Dynamics*, *40*(5-6), 1415-1433.

Heymsfield, A.J. (2003). Properties of tropical and midlatitude ice cloud particle ensembles. Part II: Applications for mesascale and climate models. *Journal of the Atmospheric Sciences*, *60*(21), 2592-2611.

Hindmarsh, J.P., Russell, A.B. and Chen, X.D. (2003). Experimental and numerical analysis of the temperature transition of a suspended freezing water droplet. *International Journal of Heat and Mass Transfer*, *46*(7), 1199-1213.

Hogan, A.W. (1985). Is sleet a contact nucleation phenomenon. In *Proceedings 42nd Eastern Snow Conference, Montreal, QC/CAN*, *42*, 292-294.

Hogan, R.J., Tian, L., Brown, P.R.A., Westbrook, C.D., Heymsfield, A.J. and Eastment, J.D. (2012). Radar scattering from ice aggregates using the horizontally aligned oblate spheroid approximation. *Journal of Applied Meteorology and Climatology*, *51*(3), 655-671.

Hohl, R., Schiesser, H.H. and Aller, D. (2002). Hailfall: the relationship between radar-derived hail kinetic energy and hail damage to buildings. *Atmospheric Research*, *63*(3-4), 177-207.

Hong, S.-Y., Yign, N. and Dudhia, J. (2006). A new vertical diffusion package with an explicit treatment of entrainment processes. *Monthly Weather Review*, *134*(9), 2318-2341.

Hosek, J., Musilek, P., Lozowski, E. and Pytlak, P. (2011). Forecasting severe ice storms using numerical weather prediction: The March 2010 Newfoundland event. *Natural Hazards and Earth System Sciences*, *11*(2), 587-595.

Hux, J.D., Knappenberger, P.C., Michaels, P.J., Stenger, P.J., Cobb III, H.D. and Rusnak, M.P. (2001). Development of a discriminant analysis mixed precipitation (DAMP) forecast model for mid-Atlantic winter storms. *Weather and Forecasting*, *16*(2), 248-259.

Iacono, M.J., Delamere, J.S., Mlawer, E.J., Shephard, M.W., Clough, S.A. and Collins, W.D. (2008). Radiative forcing by long-lives greenhouse gases: calculations with the AER radiative transfer models. *Journal of Geophysical Research: Atmospheres*, *113*(D13), 1-8.

Ikeda, K., Rasmussen, R., Liu, C., Gochis, D., Yates, D., Chen, F., Tewari, M., Barlage, M., Dudhia, J., Miller, K. and Arsenault, K., (2010). Simulation of seasonal snowfall over Colorado. *Atmospheric Research*, *97*(4), 462-477.

Ikeda, K., Steiner, M. and Thompson, G. (2017). Examination of mixed-phase precipitation forecasts from the High-Resolution Rapid Refresh model using surface observations and sounding data. *Weather and Forecasting*, *32*(3), 949-967.

Isaac, G.A., Joe, P.I., Mailhot, J., Bailey, M., Bélair, S., Boudala, F.S., Brugman, M., Campos, E., Carpenter, R.L., Crawford, R.W. and Cober, S.G. (2014). Science of Nowcasting Olympic Weather for Vancouver 2010 (SNOW-V10): a world weather research programme project. *Pure and Applied Geophysics*, *171*(1-2), 1-24.

IPCC, 2013: *Climate change 2013: The physical science basis*. Contribution of working group I to the fifth assessment report of the intergovern-mental panel on climate change [Stocker, T.F., D. Qin, G.-K. Plattner, M. Tignor, S.K. Allen, J. Boschung, A. Nauels, Y. Xia, V. Bex and P.M. Midgley (eds.)]. Cambridge: Cambridge University Press, 1535 p. Récupéré de https://www.ipcc.ch/site/assets/uploads/2017/09/WG1AR5_Frontmatter_FINAL.pdf

Jeong, D.I. and Sushama, L. (2018). Rain-on-snow events over North America based on two Canadian regional climate models. *Climate Dynamics*, *50*(1-2), 303-316.

Kämäräinen, M., Hyvärinen, O., Vajda, A., Nikulin, G., Meijgaard, E.V., Teichmann, C., Jacob, D., Gregow, H. and Jylhä, K. (2018). Estimates of present-day and future climatologies of freezing rain in Europe based on CORDEX Regional Climate Models. *Journal of Geophysical Research: Atmospheres*, *123*(23), 13-291.

Kawase, H., Yoshikane, T., Hara, M., Kimura, F., Yasunari, T., Ailikun, B., Ueda, H. and Inoue, T. (2009). Intermodel variability of future changes in the Baiu rainband estimated by the pseudo global warming downscaling method. *Journal of Geophysical Research: Atmospheres*, *114*(D24), 1-14.

Kendon, E.J., Ban, B., Roberts, N.M., Fowler, H.J., Roberts, M.J., Chan, S.C., Evans, J.P., Fosser, G. and Wilkinson, J.M. (2017). Do convection-permitting regional climate models improve projections of future precipitation change? *Bulletin of the American Meteorological Society*, *98*(1), 79-93.

King, S. and Laplante, D.P. (2005). The effects of prenatal maternal stress on children's cognitive development: Project Ice Storm. *Stress*, *8*(1), 35-45.

Klima, K. and Morgan, M.G. (2015). Ice storm frequencies in a warmer climate. *Climatic Change*, *133*(2), 209-222.

Kringlebotn Nygaard, B.E., Ágústsson, H. and Somfalvi-Tóth, K. (2013). Modeling wet snow accretion on power lines: improvements to previous methods using 50 years of observations. *Journal of Applied Meteorology and Climatology, 52*(10), 2189-2203.

Kumjian, M.R. and Schenkman, A.D. (2014). The curious case of ice pellets over middle Tennessee on 1 March 2014. *Journal of Operational Meteorology, 2*, 209-213.

Lackmann, G.M., Keeter, K., Lee, L.G. and Ek, M.B. (2002). Model representation of freezing and melting precipitation: Implications for winter weather forecasting. *Weather and Forecasting, 17*(5), 1016-1033.

Laflamme, J.N. and Périard, G. (1998). The climate of freezing rain over the province of Québec in Canada: a preliminary analysis. *Atmospheric Research, 46*(1-2), 99-111.

Lambert, S.J. and Hansen, B.K. (2011). Simulated changes in the freezing rain climatology of North America under global warming using a coupled climate model. *Atmosphere-Ocean, 49*(3), 289-295.

Lecompte, E.L., Russell, J.W. and Pang, A.W. (1998). *La tempête de verglas de 1998.* [Document de recherche]. Toronto : Institut de Prévention des Sinistres Catastrophiques. 37 p. Récupéré de https://www.iclr.org/wp-content/uploads/PDFS/1998_ice_storm_report_french.pdf

Leinonen, J. and von Lerber, A. (2018). Snowflake melting simulation using smoothed particle hydrodynamics. *Journal of Geophysical Research: Atmospheres, 123*(3), 1811-1825.

Lin, C.A. and Stewart, R.E. (1986). Mesoscale circulations initiated by melting snow. *Journal of Geophysical Research: Atmospheres, 91*(D12), 299-302.

Liu, C., Ikeda, K., Rasmussen, R., Barlage, M., Newman, A.J., Prein, A.F., Chen, F., Chen, L., Clark, M., Dai, A. and Dudhia, J. (2017). Continental-scale convection-permitting modeling of the current and future climate of North America. *Climate Dynamics, 49*(1-2), 71-95.

Liu, C., Ikeda, K., Thompson, G., Rasmussen, R. and Dudhia, J. (2011). High-resolution simulations of wintertime precipitation in the Colorado Headwaters region: Sensitivity to physics parameterizations. *Monthly Weather Review, 139*(11), 3533-3553.

Macklin, W.C. (1962). The density and structure of ice formed by accretion. *Quarterly Journal of the Royal Meteorological Society*, *88*(375), 30-50.

Martius, O., Hering, A., Kunz, M., Manzato, A., Mohr, S., Nisi, L. and Trefalt, S. (2018). Challenges and Recent Advances in Hail Research. *Bulletin of the American Meteorological Society*, *99*(3), ES51-ES54.

Mason, B.J. (1956). On the melting of hailstones. *Quarterly Journal of the Royal Meteorological Society*, *82*(352), 209-216.

Matte, D., Thériault, J.M. and Laprise, R. (2018). Mixed precipitation occurrences over southern Québec, Canada, under warmer climate conditions using a regional climate model. *Climate Dynamics*, *53*(1-2), 1-17.

Matte, D., Laprise, R., Thériault, J.M. and Lucas-Picher, P. (2017). Spatial spin-up of fine scales in a regional climate model simulation driven by low-resolution boundary conditions. *Climate Dynamics*, *49*(1-2), 563-574.

Matsuo, T. and Sayso, Y. (1981). Melting of snowflakes below freezing level in the atmosphere. *Journal of the Meteorological Society of Japan*, *59*(1), 10-25.

McCray, C.D., Atallah, E.H. and Gyakum, J.R. (2019). Long-duration freezing rain events over North America: Regional climatology and thermodynamic evolution. *Weather and Forecasting*, *34*(3), 665-681.

Meehl, G.A., Washington, W.M., Arblaster, J.M., Hu, A., Teng, H., Tebaldi, C., Sanderson, B.N., Lamarque, J.F., Conley, A., Strand, W.G. and White III, J.B. (2012). Climate system response to external forcings and climate change projections in CCSM4. *Journal of Climate*, *25*(11), 3661-3683.

Meinshausen, M., Smith, S.J., Calvin, K., Daniel, J.S., Kainuma, M.L. T., Lamarque, J.-F., Matsumoto, K., Montzka, S.A., Raper, S.C.B., Riahi, K., Thomson, A., Velders, G.J.M. and van Vuuren, D.P.P. (2011). The RCP greenhouse gas concentrations and their extensions from 1765 to 2300. *Climatic Change*, *109*(1-2), 213.

Mesinger, F., G. DiMego, E. Kalnay, K. Mitchell, P. C. Shafran, W. Ebisuzaki, Jović, D., Woollen, J., Rogers, E., Berbery, E.H., Ek, M.B., Fan, Y., Grumbine, R., Higgins, W., Li, H., Lin, Y., Manikin, G., Parrish, D. and Shi, W. (2006). North American regional reanalysis. *Bulletin of the American Meteorological Society*, *87*(3), 343-360.

Milbrandt, J. A., Bélair, S., Faucher, M., Vallée, M., Carrera, M. L. and Glazer, A. (2016). The pan-Canadian high resolution (2.5 km) deterministic prediction system. *Weather and Forecasting*, *31*(6), 1791-1816.

Milbrandt, J.A., Glazer, A. and Jacob, D. (2012). Predicting the snow-to-liquid ratio of surface precipitation using a bulk microphysics scheme. *Monthly Weather Review*, *140*(8), 2461-2476.

Milbrandt, J.A. and Morrison, H. (2013). Prediction of graupel density in a bulk microphysics scheme. *Journal of the Atmospheric Sciences*, *70*(2), 410-429.

Milbrandt, J.A. and Morrison, H. (2016). Parameterization of cloud microphysics based on the prediction of bulk ice particle properties. Part III: Introduction of multiple free categories. *Journal of the Atmospheric Sciences*, *73*(3), 975-995.

Milbrandt, J.A. and Yau, M.K. (2005). A multimoment bulk microphysics parameterization. Part I: Analysis of the role of the spectral shape parameter. *Journal of the Atmospheric Sciences*, *62*(9), 3051-3064.

Milton, J. and Bourque, A. (1999). *A climatological account of the January 1998 Ice Storm in Quebec.* [Rapport Scientifique]. Québec : Envrionment Canada, Atmospheric Sciences and Environmental Issues Division, 92 p. Récupéré de http://publications.gc.ca/pub?id=9.614792&sl=0

Mitchell, D.L. and Heymsfield, A.J. (2005). Refinements in the treatment of ice particle terminal velocities, highlighting aggregates. *Journal of the Atmospheric Sciences*, *62*(5), 1637-1644.

Mitra, S.K., Vohl, O., Ahr, M. and Pruppacher, H.R. (1990). A wind tunnel and theoretical study of the melting behavior of atmospheric ice particles. Part IV: Experiment and theory for snowflakes. *Journal of the Atmospheric Sciences*, *47*(5), 584-591.

Morrison, H. and Grabowski, W.W. (2008a). Modeling supersaturation and subgrid-scale mixing with two-moment bulk warm microphysics. *Journal of the Atmospheric Sciences*, *65*(3), 792-812.

Morrison, H. and Grabowski, W.W. (2008b). A novel approach for representing ice microphysics in models: Description and tests using a kinematic framework. *Journal of the Atmospheric Sciences*, *65*(5), 1428-1548.

Morrison, H. and Milbrandt, J.A. (2015). Parameterization of cloud microphysics based on the prediction of the bulk ice particle properties. Part I: Scheme description and idealized tests. *Journal of the Atmospheric Sciences*, *72*(1), 287-311.

Morrison, H., Thompson, G. and Tatarskii, V. (2009). Impact of cloud microphysics on the development of trailing stratiform precipitation in a simulated squall line: Comparison of one- and two-moment schemes. *Monthly Weather Review*, *137*(3), 991-1007.

Musil, D.J. (1970). Computer modeling of hailstone growth in feeder clouds. *Journal of the Atmospheric Sciences*, *27*(3), 474-482.

Nagumo, N., Adachi, A. and Yamauchi, H. (2019). Geometrical properties of hydrometeors during the refreezing process and their effects on dual-polarized radar signals. *Monthly Weather Review*, *147*(5), 1753-1768.

Phillips, V.T.J., Khain, A., Benmoshe, N. and Ilotoviz, E. (2014). Theory of time-dependent freezing. Part I: Description of scheme for wet growth of hail. *Journal of the Atmospheric Sciences*, *71*(12), 4527-4557.

Phillips, V.T.J., Pokrovsky, A. and Khain, A. (2007). The influence of time-dependent melting on the dynamics and precipitation production in maritime and continental storm clouds. *Journal of the Atmospheric Sciences*, *64*(2), 338-359.

Prein, A.F., Gobiet, A., Suklitsch, M., Truhetz, H., Awan, N.K., Keuler, K. and Georgievski, G. (2013). Added value of convection permitting seasonal simulations. *Climate Dynamics*, *41*(9-10), 2655-2677.

Prein, A.F., Langhans, W., Fosser, G., Ferrone, A., Ban, N., Goergen, K., Keller, M., Tölle, M., Gutjahr, O., Feser, F., Brisson, E., Kollet, S., Schmidli, J., van Lipsig, N.P.M. and Leung, R. (2015). A review on regional convection-permitting climate modeling: Demonstrations, prospects, and challenges. *Reviews of Geophysics*, *53*(2), 323-361.

Prein, A.F., Rasmussen, R.M., Ikeda, K., Liu, C., Clark, M.P. and Holland, G.J. (2017). The future intensification of hourly precipitation extremes. *Nature Climate Change*, *7*(1), 48-52.

Petrolito, A.W. (2005). The 2-3 January 2002 winter storm across central South Carolina and east central Georgia: a precipitation type case study. *Eastern Region Technical Attachment*, *2*, 1-25.

Pruppacher, H.R. and Klett, J.D. (1997). *Microphysics of clouds and precipitation.* 2nd edition, Massachusetts: Kluwer Academic, Dordrecht, 954 p.

Ramer, J. (1993). An empirical technique for diagnosing precipitation type from model output. In *5th international conference on aviation weather systems. American Meteorological Society, Vienna, VA*, 227-230.

Ramos da Silva, R., Bohrer, G., Werth, D., Otte, M.J. and Avissar, R. (2006). Sensitivity of ice storms in the southeastern United States to Atlantic SST—Insights from a case study of the December 2002 storm. *Monthly Weather Review*, *134*(5), 1454-1464.

Ralph, F.M., Rauber, R.M., Jewett, B.F., Kingsmill, D.E., Pisano, P., Pugner, P., Rasmussen, R.M., Reynolds, D.W., Schlatter, W., Stewart, R.E. and Tracton, S. (2005). Improving short-term (0–48 h) cool-season quantitative precipitation forecasting: Recommendations from a USWRP workshop. *Bulletin of the American Meteorological Society*, *86*(11), 1619-1632.

Rasmussen, K.L., Prein, A.F., Rasmussen, R.M., Ikeda, K. and Liu, C. (2017). Changes in the convective population and thermodynamic environments in convection-permitting regional climate simulations over the United States. *Climate Dynamics*, 1-26.

Rasmussen, R., Ikeda, K., Liu, C., Gochis, D., Clark, M., Dai, A., Gutmann, E., Dudhia, J., Chen, F., Barlage, M. and Yates, D. (2014). Climate change impacts on the water balance of the Colorado headwaters: high-resolution regional climate model simulations. *Journal of Hydrometeorology*, *15*(3), 1091-1116.

Rasmussen, R., Liu, C., Ikeda, K., Gochis, D., Yates, D., Chen, F., Tewari, M., Barlage, M., Dudhia, J., Yu, W., Miller, K., Arsenault, K., Grubišić, V., Thompson, G. and Gutmann, E. (2011). High-resolution coupled climate runoff simulations of seasonal snowfall over Colorado: a process study of current and warmer climate. *Journal of Climate*, *24*(12), 3015-3048.

Rasmussen, R. and Pruppacher, H.R. (1982). A wind tunnel and theoretical study of the melting behavior of atmopheric ice particles. Part I: A wind tunnel study of frozen drops of radius < 500 um. *Journal of the Atmospheric Sciences*, *39*(1), 152-158.

Rasmussen, R.M., Levizzani, V. and Pruppacher, H.R. (1984a). A wind tunnel and theoretical study of the melting behavior of atmospheric ice particles. Part II: A theoretical study for frozen drops of radius < 500 um. *Journal of the Atmospheric Sciences*, *41*(3), 374-380.

Rasmussen, R.M., Levizzani, V. and Pruppacher, H.R. (1984b). A wind tunnel and theoretical study of the melting behavior of atmospheric ice particles. Part III: Experiment and theory for spherical ice particles of radius > 500 um. *Journal of the Atmospheric Sciences*, *41*(3), 381-388.

Rauber, R.M., Ramamurthy, M.K. and Tokay, A. (1994). Synoptic and mesoscale structure of a severe freezing rain event: The St. Valentine's Day ice storm. *Weather and Forecasting*, *9*(2), 183-208.

Ressler, G.M., Milrad, S.M., Atallah, E.H. and Gyakum, J.R. (2012). Synoptic-scale analysis of freezing rain events in Montreal, Quebec, Canada. *Weather and Forecasting*, *27*(2), 362-378.

Reeves, H.D. (2016). The uncertainty of precipitation-type observations and its effect on the validation of forecast precipitation type. *Weather and Forecasting*, *31*(6), 1961-1971.

Reeves, H.D., Elmore, K.L., Ryzhkov, A., Schuur, T. and Krause, J. (2014). Sources of uncertainty in precipitation-type forecasting. *Weather and Forecasting*, *29*(4), 936-953.

Reeves, H.D., Ryzhkov, A.V. and Krause, J. (2016). Discrimination between Winter Precipitation Types Based on Spectral-Bin Microphysical Modeling. *Journal of Applied Meteorology and Climatology*, *55*(8), 1747-1761.

Risk and Management Solutions, Inc. (2008). The 1998 ice storm: 10-year retrospective [RMS Special Report]. 13 p. Récupéré de https://forms2.rms.com/rs/729-DJX-565/images/wtr_1998_ice_storm_10_retrospective.pdf

Roebber, P.J. and Gyakum, J.R. (2003). Orographic influences on the mesoscale structure of the 1998 Ice Storm. *Monthly Weather Review*, *131*(1), 27-50.

Schär, C., Frei, C., Lüthi, D. and Davies, H.C. (1996). Surrogate climate-change scenarios for regional climate models. *Geophysical Research Letters*, *23*(6), 669-672.

Simmel, M., Trautmann, T. and Tetzlaff, G. (2002). Numerical solution of the stochastic collection equation - comparison of the linear discrete method with other methods. *Atmospheric Research*, *61*(2), 135-148.

Skamarock, W.C. and Klemp, J.B. (2008). A time-split nonhydrostatic atmospheric model for weather research and forecasting applications. *Journal of Computational Physics*, *227*(7), 3465-3485.

Stewart, R.E. (1992). Precipitation types in the transition region of winter storms. *Bulletin of the American Meteorological Society*, *73*(3), 287-296.

Stewart, R.E. (1985). Precipitation types in winter storm. *Pure and Applied Geophysics*, *123*(4), 597-609.

Stewart, R.E., Crawford, R.W., Donaldson, N.R., Low, T.B. and Sheppard, B.E. (1990). Precipitation and environmental conditions during accretion in Canadian east coast winter storms. *Journal of Applied Meteorology*, *29*(7), 525-538.

Stewart, R.E. and King, P. (1990). Precipitation type transition regions in winter storms over southern Ontario. *Journal of Geophysical Research: Atmospheres*, *95*(D13), 22355-22368.

Stewart, R.E. and King, P. (1987). Freezing precipitation in winter storms. *Monthly Weather Review*, *115*(7), 1270-1280.

Stewart, R.E., Marwitz, J.D., Pace, J.C. and Carbone, R.E. (1984). Characteristics through the melting layer of stratiform clouds. *Journal of the Atmospheric Sciences*, *41*(22), 3227-3237.

Stewart, R.E., Thériault, J.M. and Henson, W. (2015). On the characteristics of and processes producing winter precipitation types near 0°C. *Bulletin of the American Meteorology Society*, *96*(4), 623-639.

Stuart, R.A. and Isaac, G.A. (1999). Freezing precipitation in Canada. *Atmosphere-Ocean*, *37*(1), 87-102.

Szyrmer, W. and Zawadzki, I. (1999). Modeling of the melting layer. Part I: Dynamics and microphysics. *Journal of the Atmospheric Sciences*, *56*(20), 3573-3592.

Taniguchi, K. and Sho, K. (2015). Application of the pseudo global warming dynamic downscaling method to the Tokai Heavy Rain in 2000. *Journal of the Meteorological Society of Japan, Ser. II*, *93*(5), 551-570.

Thériault, J.M., Ramussen, K.L., Fisco, T., Stewart, R.E., Joe, P., Gultepe, I., Clément, M. and Isaac, G.A. (2014). Weather observations along whistler mountain in five storms during SNOW-V10. *Pure Applied Geophysics*, *171*(1-2), 129-155.

Thériault, J.M. and Stewart, R.E. (2010). A parameterization of the microphysical processes forming many types of winter precipitation. *Journal of the Atmospheric Sciences*, *67*(5), 1492-1508.

Thériault, J.M., Stewart, R.E. and Henson, W. (2010). On the dependence of winter precipitation types on temperature, precipitation rate and associated features. *Journal of Applied Meteorology and Climatology*, *49*(7), 1429-1442.

Thériault, J.M., Stewart, R.E., Milbrandt, J.A. and Yau, M.K. (2006). On the simulation of winter precipitation types. *Journal of Geophysical Research: Atmospheres (1984-2012)*, *111*(D18), 1-11.

Thielke, T. (2018). *Using advanced post-processing methods with the HRRR-TLE to improve the prediction of cold season precipitation type*. [Master Thesis]. Milwaukee: University of Wisconsin-Milwaukee, 38 p. Récupéré de https://dc.uwm.edu/etd/1928/

Thompson, G., Field, P.R., Rasmussen, R.M. and Hall, W.D. (2008). Explicit forecasts of winter precipitation using an improved bulk microphysics scheme. Part II: Implementation of a new snow parameterization. *Monthly Weaher Review*, *136*(12), 5095-5115.

Thorpe, A.D. and Mason, B.J. (1956). The evaporation of ice spheres and ice crystals. *British Journal of Applied Physics*, *17*(4), 541-548.

Walko, R.L., Cotton, W.R., Feingold, G. and Stevens, B. (2000). Efficient computation of vapor and heat diffusion between hydrometeors in numerical model. *Atmospheric Research*, *53*(1-3), 171-183.

Yokoyama, T. and Tanaka, H. (1984). Microphysical processes of melting snowflakes detected by 2-wavelength radar, Part I: Principle of measurement based on model calculation. *Journal of the Meteorological Society of Japan*, *62*(4), 650-667.

Zerr, R.J. (1997). Freezing rain: An observational and theoretical study. *Journal of Applied Meteorology*, *36*(12), 1647-1661.